Coupled approach to modelling damage in bonded composite structures

Robert Done

Imperial College London

Department of Aeronautics

This thesis is submitted for the degree of Doctor of
Philosophy and the Diploma of Imperial College London.

February 2014

Declaration of Originality

I hereby declare that the research described in this thesis is my own work. Where the ideas of others have influenced this work, this has been properly referenced.

Robert Done

Copyright Declaration

Robert Done

Abstract

A fully coupled global-local approach for structural analysis has been developed. It is motivated by the need to use a range of scales and modelling techniques when designing a structure in composite materials. These range from the microscale at which the interfaces between fibres and matrix, or buckling of fibres themselves may play a role in the material behaviour, through intermediate scales where delamination and debonding may have an influence up to the macroscale where entire structures may be modelled with service loads directly applied. The method is based on passing boundary conditions from larger to smaller length scale models while passing information about damage and stiffness degradation up through the scales. By using nested levels of submodel, a greater range of length scales may be included in a single set of coupled analyses.

Here an explanation of the methods of coupling two scales of solid models as well as coarse shell models to relatively refined solid models is presented. Each of these methods is validated against equivalent models using established modelling techniques, and are shown to produce results comparable to a complete model at the refined scale and preferable to other global-local approaches. Experimental tests have also been carried out on a stiffened panel with two stiffener runouts undergoing debonding. Not only did the coupling method model these tests accurately, but it was also shown to be more appropriate than simple submodelling in this case.

A further demonstration of the techniques is included. The largest scale consisting of a shell element mesh is coupled with an intermediate scale with a continuum shell mesh, which in turn is coupled to a refined scale solid model. This demonstration shows how the methods developed here could be used to unify various analyses in the composites design process which until now have remained separate.

Contents

List of Figures

14

List of Tables

Nomenclature

Roman symbols

Symbol	Definition
E_{11}	Young's modulus in the fibre direction
E_{22}	Young's modulus in plane and transverse to the fibre direction
E_{33}	Out of plane Young's modulus
E_N	Normal Young's modulus of a cohesive layer
F	Crack tip shape function
$\mathbf{F}$	Force vector
$\mathbf{F_M}$	Macroscale deformation gradient
$\overline{\mathbf{F}}_{\mathbf{R}}$	Averaged microscale deformation gradient
^{G}	Superscript denoting global domain
G_{12}	In plane shear modulus
G_{13}	Transverse shear modulus
G_{23}	Transverse shear modulus
G_N	Cohesive layer energy due to normal loading
G_{NC}	Opening fracture toughness
G_{NS1}	Shear modulus of a cohesive layer
G_{NS2}	Shear modulus of a cohesive layer
G_S	Cohesive layer energy due to shear loading
G_{S1C}	Fracture toughness under shear loading in the first shear direction
G_{S2C}	Fracture toughness under shear loading in the second shear direction
G_{SC}	Homogenised shear fracture toughness
G_{TC}	Combined mode I and mode II fracture energy
H	Heaviside function
i	Index or integer counter
j	Index or integer counter
k_N	Normal stiffness
K_{NN}	Normal elastic stiffness in a cohesive model
k_{S1}	Stiffness in the first shear direction

k_{S2}	Stiffness in the second shear direction
$\mathbf{k}_{SE}^{i}$	$i^{t}h$ column of the superelement stiffness matrix
K_{ss}, K_{tt}	Elastic shear stiffness in a cohesive model
L	Superscript denoting local domain
N	Normal strength or shape function
$\mathbf{n}$	Normal vector
$\tilde{\mathbf{N}}_{P}$	Shape functions defining the displacement of a point on the local boundary in terms of all global boundary degrees of freedom.
r	Radial coordinate
S	Critical shear strength
S_1	Shear strength in the first shear direction
S_2	Shear strength in the second shear direction
SE	Subscript denoting that a quantity, vector or matrix relates to a superelement
$\mathbf{T}$	Transformation matrix
t_N	Normal stress
t_S	Shear stress
$\mathbf{u}$	Displacement vector
$\mathbf{u}$	Displacement vector
$\mathbf{u}*$	Unit cell boundary displacements
$\mathbf{u}_{\delta}$	Vector of additional displacements at a point in the thickness of the global-local boundary due to global rotations.
$\mathbf{u}_{\Gamma}$	Vector of all global boundary displacements.
$\mathbf{u}_{\theta}$	Vector of components of rotation at a node
$\mathbf{v}*$	Shape functions on the global-local boundary
V_0	Undeformed volume
W_n	Work done deforming a superelement
W_p	Work done perturbing a superelement node at point p
$\hat{\mathbf{x}}_g$, $\hat{\mathbf{y}}_g$, $\hat{\mathbf{z}}_g$	Unit vectors in the global model coordinate directions
$\hat{\mathbf{x}}_l$, $\hat{\mathbf{y}}_l$, $\hat{\mathbf{z}}_l$	Unit vectors in the local model coordinate directions
$\mathbf{y_0}$	Undeformed position

Greek symbols

Symbol	Definition
β	Ratio of normal and shear relative displacement
δ	Relative displacement
δ_N	Normal relative displacement

δ_N^0	Critical normal relative displacement
δ_N^f	Normal relative displacement at failure
δ_S	Total shear relative displacement
δ_{S1}	Relative displacement in the first shear direction
δ_{S1}^0	Critical relative displacement in the first shear direction
δ_{S1}^f	Relative displacement in the first shear direction at failure
δ_{S2}	Relative displacement in the second shear direction
δ_{S2}^0	Critical relative displacement in the second shear direction
δ_{S2}^f	Relative displacement in the second shear direction at failure
ε_b	Bending measure
ε_s	Strain measured on the stiffened side of a panel
ε_u	Strain measured on the unstiffened side of a panel
Γ	Interface between global and local models
$_\Gamma$	Subscript denoting that a quantity
Θ	Angular coordinate
ν_{12}	In plane Poisson's ratio
ν_{13}	Transverse Poisson's ratio
ν_{23}	Transverse Poisson's ratio
ξ, η, ζ	Finite element basis coordinates
$\overline{\sigma}_R$	Volume averaged unit cell stress
τ	Shear stress
$_\Omega$	Subscript denoting that a quantity

1. Introduction

1.1. Motivation: composite materials and modelling large structures

Composite materials present a challenge to structural designers because the behaviour of the material is largely dependent on the microstructure [7–11], and even the micro-constituents' surface preparation [12–17]. This implies that the mesh used for a direct simulation of these materials must be of a refinement such that the elements are smaller than the microcsonstituents' typical dimensions (of the order of micrometres). Even if homogenised properties are used, in the case of laminates if the designer considers delam-ination or plasticity then the elements' maximum thickness is that of the ply [18, 19] (less than 0.25 mm). When reasonable use of computational resources is taken into account, this imposes a cap on the domain size of the finite element model. Generally only test coupons may be modelled with this level of refinement.

In order to apply appropriate boundary conditions, however, the model must be of a region whose boundaries have known loads or displacements. In the case of an airliner, the wing may be considered a separate structure, as it may generally be constrained at the fuselage junction. Even with this reduction in size of the domain, it is only affordable to model the structure with shell elements with in plane dimensions of up to 100 mm. This is 400 times the size of elements required to model at the ply level. Given that it is not unreasonable to use a laminate of 400 plies in a wing structure the cost of running models of a wing with ply-level refinement is 400^3 times more expensive than what is considered reasonable.

In order to make the best use of all levels of modelling, boundary conditions must be brought from the largest, coarsest models to the most refined, and data concerning material behaviour must be passed the other way. A combination of two techniques must be used in industry to obtain an acceptable set of models, as shown in Figure 1.1. The first involves using the periodic nature of fibre reinforced laminates to reduce the size of a microscale problem. This set of techniques is examined in detail in Section 2.3, and are often referred to as homogenisation, unit cell or relative volume element approaches.

The second technique is known as submodelling, and is discussed in more detail in Section 2.6. This entails dividing a global model into smaller local regions. Any region requiring closer scrutiny (which may be decided based on a range of criteria [20]) may be meshed at a more refined level in a local model with boundary conditions derived from the global solution. This technique is typically used on 4 or 5 nested levels of model [1],

although for clarity descriptions of such models will assume there are two scales; the global and the local scale.

The problem with many submodelling approaches is that no data is fed back from the local models to the global one. This means that the effect of damage or other nonlinearities is not seen at the global scale. As shown in Figure 1.1, a consequence of this is that, beyond a certain scale of local model, data ceases to be passed from the local to the global scale. This can be a drawback if, for example, damage tolerance in a structure is a concern. No measure of the effect of failure of one local region on its neighbours is available.

1.2. Context

By extending typical submodelling approaches so that the stiffness of regions of the global level are dictated by local models, the defficiency in information transfer highlighted in Figure 1.1 is removed. The work presented here concerns an implementation of such an approach using commercial FEA package Abaqus and Python scripting. The proposed approach is summarised in Figure 1.2

Much of this work focusses on bonded skin-stiffener assemblies, an area which submodelling is particularly applicable. Modelling debonding of bonded joints requires a relatively high level of refinement compared to full wing models, therefore bonded stiffener runouts are regions which would typically require submodelling. This type of feature will be submodelled in many of the examples presented within this document.

This PhD forms part of a project on analysis of bonded composites. Figure 1.3 shows the context of the PhD in terms of the rest of the project.

Global structure
(cutaway)

Material/damage data (not achieved via
conventional submodelling)

Submodel levels

Boundary conditions

Material data

Miniature mock components
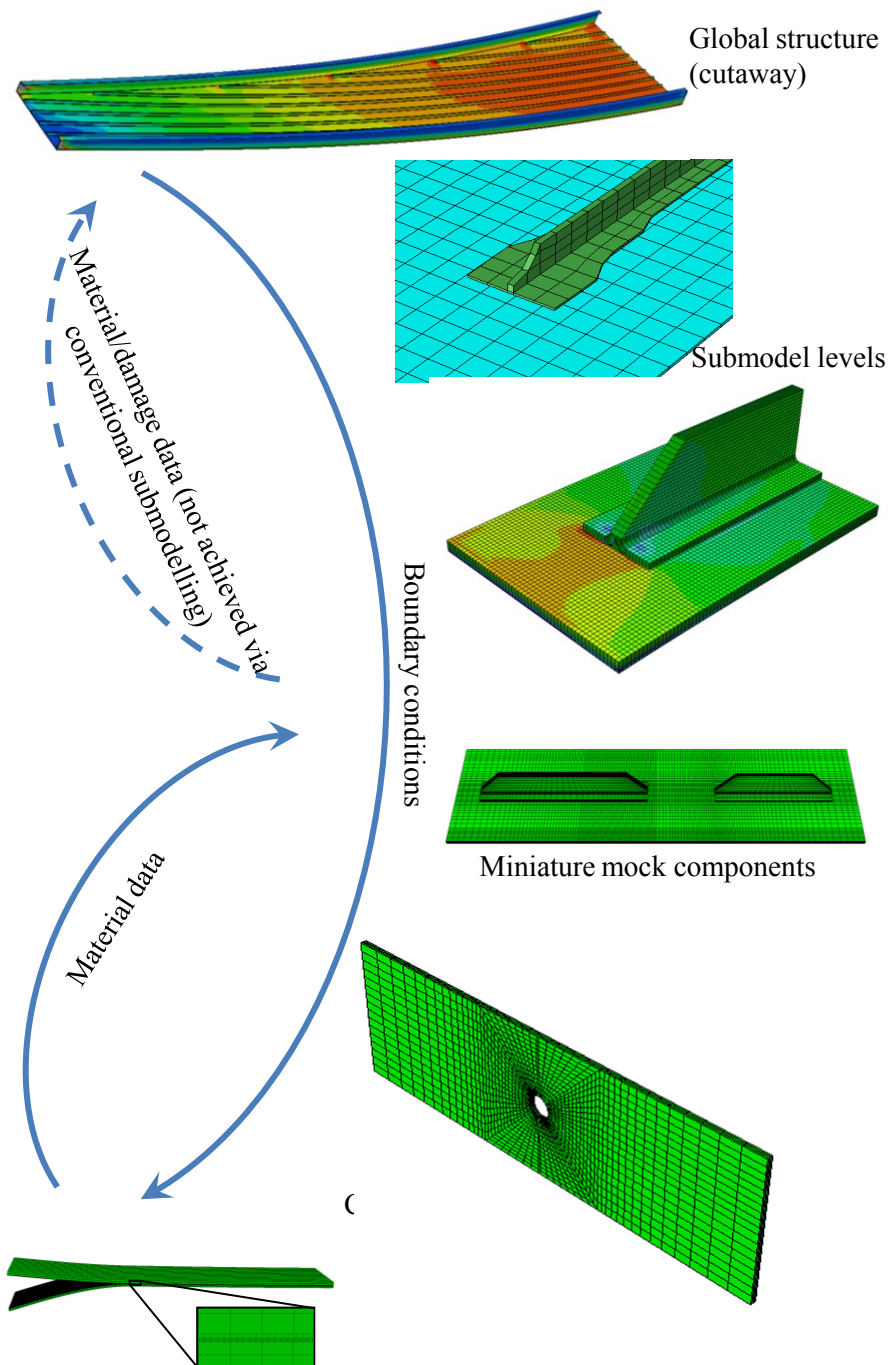
Figure 1.1.: The flow of information between the levels of model typically used in structural design from the microstructural to the global level. Defficiencies in transfer of information due to the use of one way submodelling are shown (After [1]).

Structural Model

Superelement

Γ

Transformed
component
stiffness,
$\mathbf{T^T K T}$

Interpolate
boundary
displacements
at component
nodes from
global
displacement
field,
$\mathbf{u}_\Gamma$

Component Model
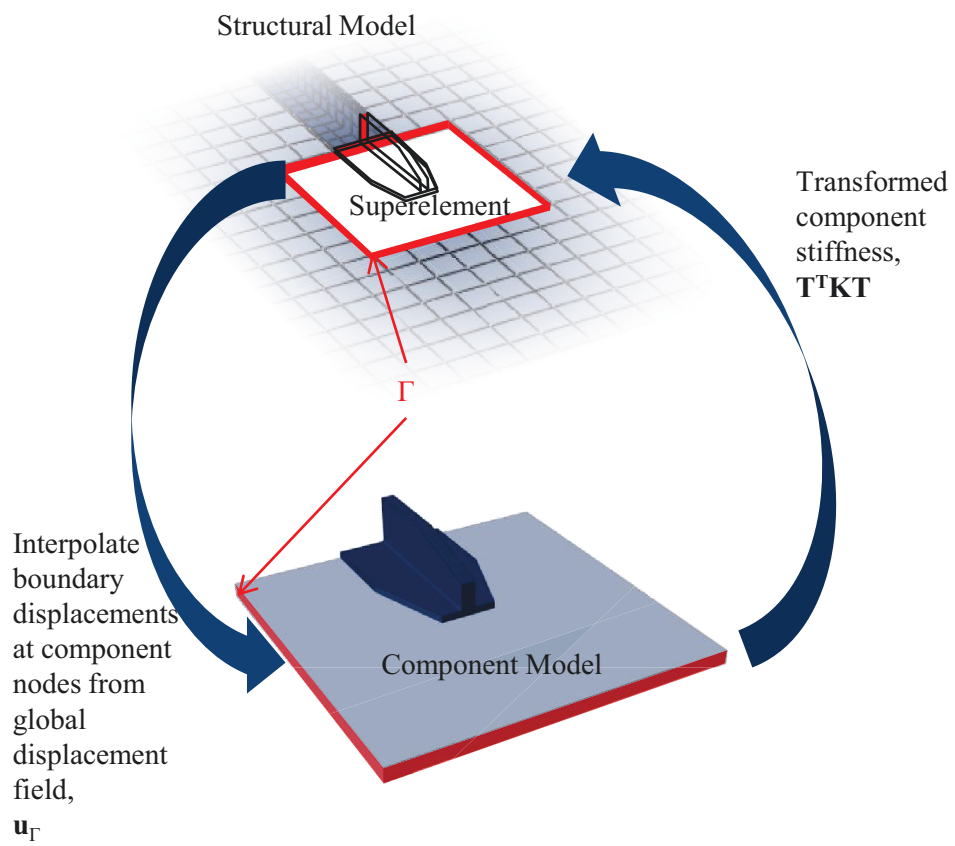
Figure 1.2.: The flow of information between scales in the proposed submodelling approach.
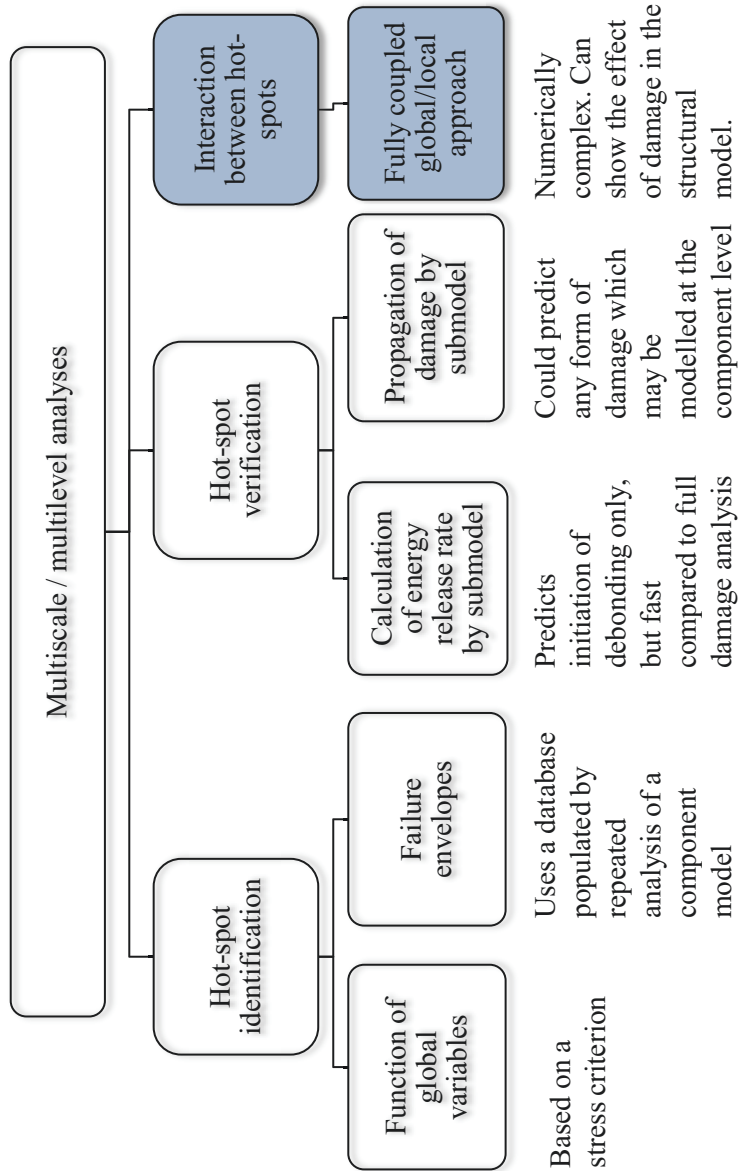
Figure 1.3.: The context of the PhD within a larger project.

2. Literature review

2.1. Introduction

Since bonded joints are central to this work, as discussed in Chapter 1, methods for analysing damage initiation and propagation will be reviewed in Section 2.2.2.

The Extended Finite Element Method and homogenisation by unit cell will also be studied Section 2.3.1 and Section 2.3.2 respectively. Both methods are used in modelling composite materials, and both may be considered multiscale approaches so they are particularly relevant to this work.

Cosimulation and global-local approaches are coupling approaches which are generally used at the larger scales of analyses. This range of scales encompasses the full wing and sub-component scales discussed in Chapter 1, which are central to this work. Cosimulation and global-local techniques are examined in Section 2.4 and Section 2.6 respectively.

2.2. Debonding and delamination

2.2.1. Introduction

Debonding and delamination in laminates are similar processes in that they concern the failure of a thin, resin rich layer between plies. In order to model these processes in finite elements a range of techniques have been developed, and are the focus of this section.

2.2.2. Debonding and delamination models

Delamination and debonding concern a thin resin rich layer or layer of adhesive. The small thickness means that rather than modelling these regions as a continuum, it is often desirable to use a traction-separation law as in [2]. This relates the relative displacement of two points in contact on the bonded surfaces to the traction forces, usually in terms of one normal and 2 in plane coordinates. In the simplest case where the adhesive layer is subjected to a pure loading mode, the behaviour may be described as follows.

$$\delta_N^0 = \frac{N}{k_N}, \ \delta_{S1}^0 = \frac{S_1}{k_{S1}}, \ \delta_{S2}^0 = \frac{S_2}{k_{S2}} \tag{2.1}$$

Where N, S_1, S_2 are the maximum normal and in plane traction forces, $\delta_N^0, \delta_{S1}^0, \delta_{S2}^0$ are the corresponding displacements and k_N, k_{S1}, k_{S2} are elastic constants. Assuming that the behaviour after the maximum load is also linear, the fracture toughness in the three
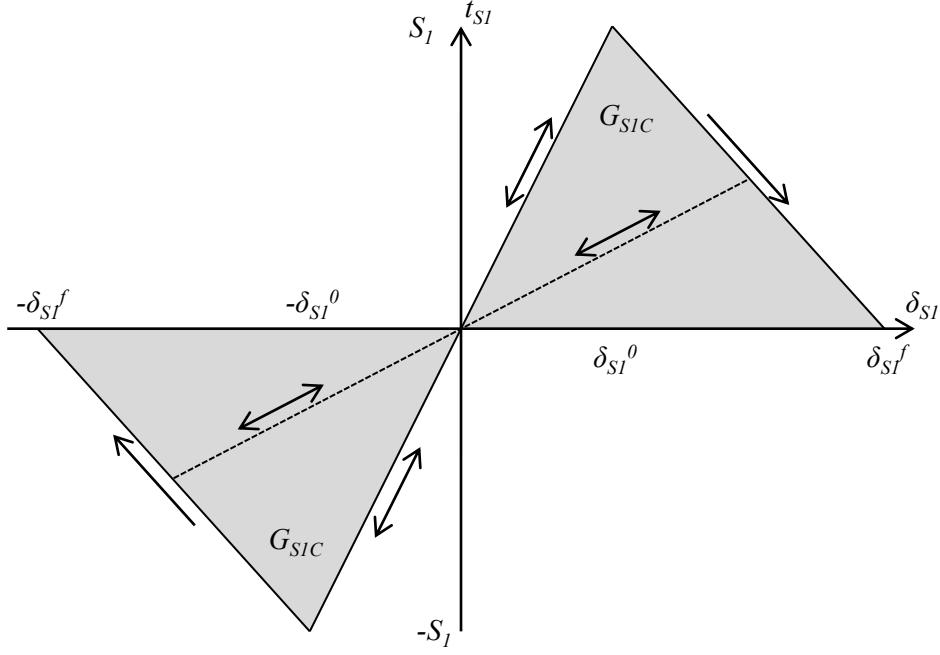
Figure 2.1.: A single mode constitutive law for a traction-separation model (after [2].

loading modes, G_{NC}, G_{S1C}, G_{S2C}, completes the constitutive definition of the adhesive layer.

$$\delta_N^f = \frac{2G_{NC}}{k_N \delta_N^0}, \ \delta_{S1}^f = \frac{2G_{S1C}}{k_{S1} \delta_{S1}^0}, \ \delta_{S2}^f = \frac{2G_{S2C}}{k_{S2} \delta_{S2}^0} \quad (2.2)$$

Figure 2.1 shows illustrates such a single mode constitutive law.

More commonly however, all the loading modes are active, and different damage initiation and propagation laws must be defined.Note that the bilinear shape of the traction-separation curves is only one of many possibilities. Other shapes have been proposed [21–23]. The initiation and propagation laws must be modified in the case of mixed mode loading. The in-plane behaviour may often be assumed to be independent of direction in debonding and delamination [2]. The displacements may therefore be reduced to two components, the normal component δ_N, and the shear component $\delta_S = \sqrt{\delta_{S1}^2 + \delta_{S2}^2}$. The relative displacement between the two points in contact is then;

$$\delta = \sqrt{\langle \delta_N \rangle^2 + (\delta_S)^2} \quad (2.3)$$

where $\langle x \rangle = \max 0, x \ x \in \Re$. The ratio of normal and shear relative displacement is;

$$\beta = \max \left\{ 0, \frac{\delta_S}{\delta_N} \right\} \quad (2.4)$$

Note that the mode mixture may also be defined in terms of energy rather than traction [24].

The following mixed mode initiation criterion suggested in [25] is now widely used in

delamination and debonding models [24]:

$$\left(\frac{\langle t_N \rangle}{N}\right)^2 + \left(\frac{t_S}{S}\right)^2 = 1 \tag{2.5}$$

where t_N is the normal contact stress, $\langle t_N \rangle = \max\{0, t_N\}$ and t_S is the resultant contact shear stress. N and S are the normal and shear strengths of the interface respectively.

This means that, in terms of normal and shear components, the displacement at which damage is initiated may be written as

$$\delta^0 = \begin{cases} \delta_S^0 \delta_N^0 \sqrt{\frac{1+\beta^2}{\left(\delta_S^0\right)^2 + \left(\beta\delta_N^0\right)^2}} & \delta_N > 0 \\ \delta_S^0 & \delta_N \leq 0 \end{cases} \tag{2.6}$$

Other criteria have also been proposed for initiation of delamination. These include the maximum stress criterion which states that damage is initiated when a single stress component reached its maximum value, but this has been shown to give poor results for delamination [26]. Maximum and quadratic strain criteria have also been used for delamination initiation. As with stress criteria, the quadratic forms give more satisfactory results than the maximum laws [27].

Similarly, a damage evolution criterion is required. A power law is commonly used [28], although others are also available and sometimes used in finite elements [24, 29]. The following is an example of a power law and assumes that shear behaviour is the same in any direction.

$$\left(\frac{G_N}{G_{NC}}\right)^\alpha + \left(\frac{G_S}{G_{SC}}\right)^\alpha = 1 \tag{2.7}$$

where α is a constant selected for a particular material/adhesive combination. The assumption is made that $G_{S1C} = G_{S2C} = G_{SC}$, and G_S represents the energy in the cohesive layer due to all shear components.

An alternative mixed mode law (the BK law) was shown to provide a good representation of debonding and delamination by Benzeggagh and Kenane [30, 31]. It has also been successfully applied in conjunction with bilinear damage models to simulate damage in bonded lap joints [32]. As a result it will be used in this work to model debonding of a stiffener from a panel - a problem with many similar characteristics to a lap joint. The BK law specifies the total fracture energy under combined mode I and II loading, G_{TC}, at a given mode mixture as:

$$G_{TC} = G_{NC} + (G_{S1C} - G_{NC})\left(\frac{G_{S1}}{G_T}\right)^m \tag{2.8}$$

Where $G_T = G_N + G_{S1}$, and m is a material parameter.

It has been remarked in [33] that in many cases the cohesive zone model parameters -the maximum traction and the fracture energy - are selected to match experimental data without any rigorous physical justification. In order to assess the impact of using

an unjustified pair of parameters which allow experimental results to be replicated for a single test the authors carried out a parametric study in which various parameter pairs were selected according to a mixed mode flexure (MMF) test. The test was then modelled using various mesh refinements and the previously determined parameter pairs. It was found that there was a range of maximum tractions within which the failure load of the joint was governed by the fracture energy. Below this range the maximum traction influenced the failure load strongly. Above this range both mesh refinement and maximum traction affected the failure load. It was concluded that a rigorous approach to determining the cohesive model parameters was required, and that the maximum traction values should be within the range where behaviour is governed by the fracture energy.

2.2.3. Discretising contact

Standard elements cannot be used with the damage models described in Section 2.2.2 due to the small in plane thickness of adhesive or ply interface layers and due to the discontinuous nature of contact problems (There is zero force if a particular pair of surfaces are not in contact, but there may be infinite force if they are). Cohesive elements and cohesive contact are often used in debonding and delamination modelling. Cohesive elements are very thin or even 2D elements which are used to represent the layer in which debonding or delamination may occur [2, 25]. Cohesive elements have the same topology as solid elements but the relative displacement of the top and bottom surfaces may be governed by traction separation laws, like those discussed in Section 2.2.2.

Cohesive contact does not require explicit definition of elements. Instead one of the two contact surfaces is designated a master, and the other a slave. For each node in the slave surface the opening or closure may be determined and thus the strain in the adhesive layer for the surrounding region is calculated. This in turn allows the calculation of the state of damage and the force transferred across that portion of the interface. Cohesive contact is convenient to use because the need to mesh the adhesive layer is removed. Only a pair of surfaces experiencing cohesive contact needs to be defined. For this reason, apart from when modelling particularly thick adhesive layers, cohesive contact is usually chosen over cohesive elements.

2.3. Modelling composite materials

2.3.1. The Extended Finite Element Method

The Extended Finite Element Method or XFEM allows discontinuities to be represented *within* elements. The method was first developed by Belytschko *et al.*[3, 34–36]. The shape of these discontinuities over time may be governed by any analytical or discretised solution to a mathematical problem. This makes XFEM a particularly useful tool in multiscale modelling of composite materials, since a crack modelled at a refined scale may be present in a coarse model. Many authors have used XFEM in such a way [37–42].
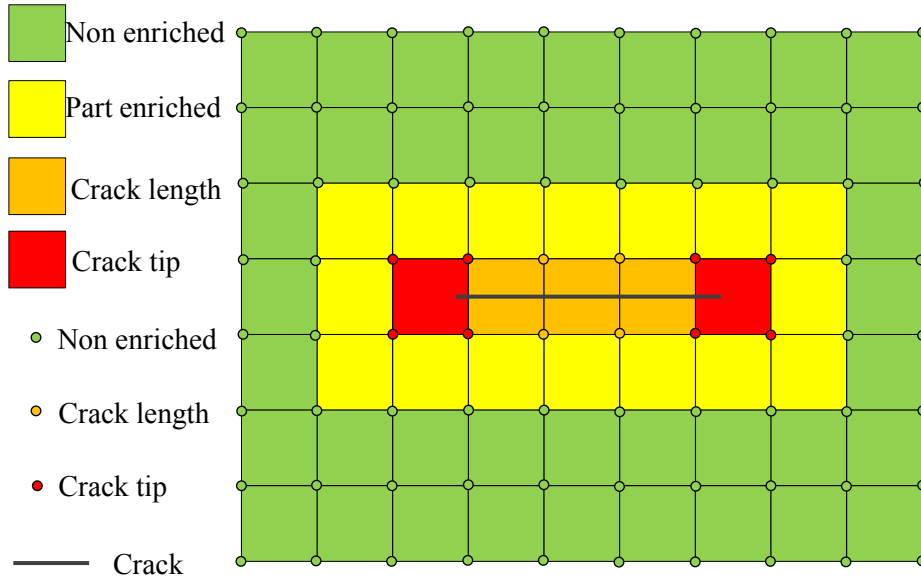
Figure 2.2.: The enrichment of nodes around an XFEM crack.

Consider Figure 2.2, which shows a crack in a 2D domain. XFEM does not dictate how the evolution of the crack must be defined, but the most common methods use fracture mechanics or a more refined discretised model [37–42] to define the displacement field close to the crack tip and the jump across the crack.

Given the shape of the crack at any given moment, the effect on the nodal displacements may be incorporated as follows, by a process known as enrichment [3, 34]. This can be explained using the 2D examples presented in [3] (see Figure 2.3). Consider mesh a. in which a crack is meshed explicitly. The displacement in the domain is given by the standard finite element shape functions,

$$\mathbf{u} = \sum_{i=1}^{10} \mathbf{u}_i N_i \tag{2.9}$$

Defining $\mathbf{a}$ and $\mathbf{b}$ as

$$\mathbf{a} = \frac{\mathbf{u}_9 + \mathbf{u}_{10}}{2}, \; \mathbf{b} = \frac{\mathbf{u}_9 - \mathbf{u}_{10}}{2} \tag{2.10}$$

hence

$$\mathbf{u}_9 = \mathbf{a} + \mathbf{b}, \; \mathbf{u}_{10} = \mathbf{a} - \mathbf{b} \tag{2.11}$$

Eq. 2.9 may then be written

$$\mathbf{u} = \sum_{i=1}^{8} \mathbf{u}_i N_i + \mathbf{a}(N_9 + N_{10}) + \mathbf{b}(N_9 + N_{10})H(\mathbf{x}) \tag{2.12}$$

where

$$H(x,y) = \begin{cases} 1 & \text{for } y > 0 \in j \\ -1 & \text{for } y < 0 \end{cases} \tag{2.13}$$

This allows $N_9 + N_{10}$ to be replaced by N_{11} and $\mathbf{a}$ by $\mathbf{u}_{11}$ (see Figure 2.3b);

$$\mathbf{u} = \sum_{i=1}^{8} \mathbf{u}_i N_i + \mathbf{u}_{11} N_{11} + \mathbf{b} N_{11} H(\mathbf{x}) \tag{2.14}$$

If, as in the case of Figure 2.3c, the crack is not aligned with the mesh, but only bisects complete elements, it is necessary to enrich more nodes;

$$\mathbf{u} = \sum_{i \in I} \mathbf{u}_i N_i + \sum_{j \in J} \mathbf{b}_j N_j H(\mathbf{x}) \tag{2.15}$$

where I is the set of all nodes and J are the circled nodes. Finally in the case where the crack tip is inside an element (Figure 2.3d)

$$\mathbf{u} = \sum_{i \in I} \mathbf{u}_i N_i + \sum_{j \in J} \mathbf{b}_j N_j H(\mathbf{x}) + \sum_{k \in K} N_k \left(\sum_{l=1}^{4} \mathbf{c}_k^l F_l(\mathbf{x}) \right) \tag{2.16}$$

where K are the squared nodes. $\{F_l(\mathbf{x})\}_{l=1}^{4}$ is a function used to define the shape of the displacement field around the crack tip. In the original paper this was defined in a polar coordinate system, centred at the crack tip and aligned with the crack:

$$\{F_l(r,\theta)\}_{l=1}^{4} = \left\{ \sqrt{r} \sin\left(\frac{\theta}{2}\right), \sqrt{r} \cos\left(\frac{\theta}{2}\right), \sqrt{r} \sin\left(\frac{\theta}{2}\right) \sin(\theta), \sqrt{r} \cos\left(\frac{\theta}{2}\right) \sin(\theta) \right\} \tag{2.17}$$

This is the equivalent of the Heaviside function used along the length of the crack. $\mathbf{c}_k^l$ is used to defined the magnitude of the crack jump. Note that this may be extended to 3D models [36], multiple cracks and cracks with multiple tips [3].

2.3.2. Homogenisation by unit cell

Homogenisation by unit cell aims to incorporate a representation of the microstructure of the composite material into a mesh where the elements may be much larger than the length scale of the microconstituents. This is achieved by modelling a small region of the composite on an extremely refined mesh, such that matrix and fibres may be meshed separately, and applying boundary conditions obtained using the coarse model. In turn the stress in the refined model defines the strain in the coarse.

A useful overview of this type of method was composed by Geers et al. [4]. They charted the methods through the following stages, towards being able to model heterogeneous materials under high gradients including nonlinear and even discontinuous behaviour:

- First order homogenisation

- Second order homogenisation

- Continuous-discontinuous homogenisation
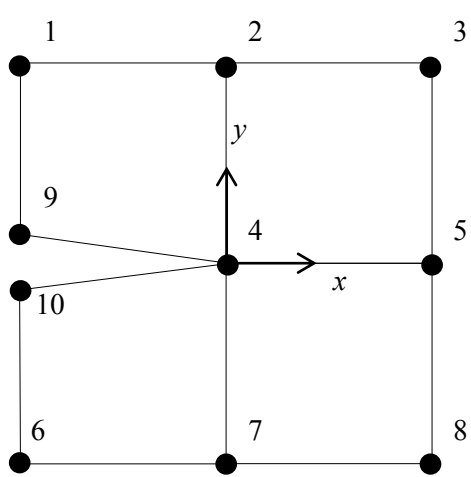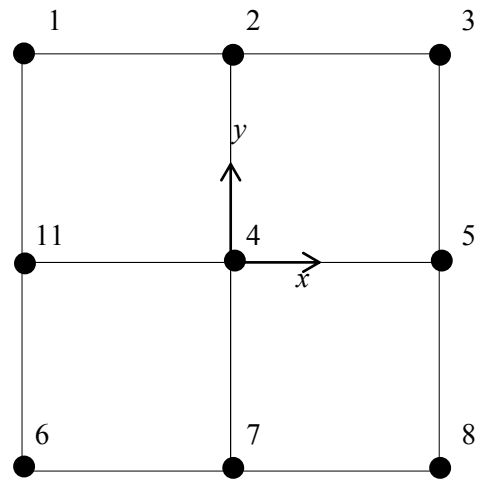
(a)   (b)
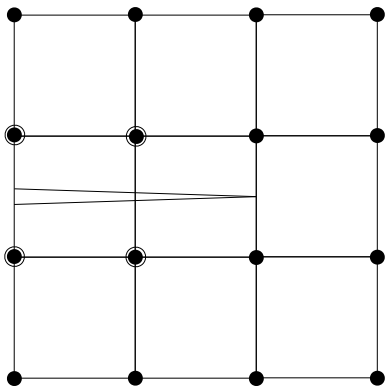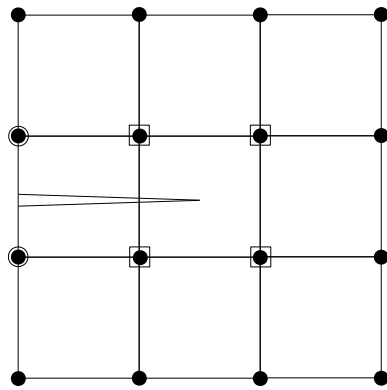
(c)   (d)

Figure 2.3.: 2D examples illustrating enrichment in the Extended Finite Element Method (after [3])

- Shells and beams

- Multiphysics problems

This section will concentrate on the first two items in this list since they are the most relevant to damage modelling in composite materials.

First order homogenisation

First order homogenisation was applied in Finite Element analyses to composite materials in [43]. The aim was to determine the properties of a composite material considering its microstructure, but in a form which could be applied in a mesh where the elements were much larger than the length scale of the microconstituents.

Figure 2.4 shows how the micro- and macro-scales are linked in a first order homogenisation process. The strain, or deformation gradient, $\mathbf{F_M}$ is computed at points in the macroscale (integration points in Finite Elements). This strain may be used to compute boundary conditions for the unit cell for that point in the macroscale. There are various ways of computing these boundary conditions, but they all ensure that the volume (or area in 2D) averaged deformation gradient, $\overline{\mathbf{F_R}}$, in the micro-scale unit cell is equivalent to that at the macroscale point (Eq. 2.18).

$$\overline{\mathbf{F_R}} = \frac{1}{V_0} \int_{\mathbf{y_0} \in V_0} \mathbf{F}(\mathbf{y_0}) dV_0 \tag{2.18}$$

where V_0 is the undeformed volume of the unit cell and $\mathbf{y_0}$ is any position within that volume. Once the volume averaged unit cell deformation gradient is known, it is possible to define boundary displacments $\mathbf{u}*$ using one of a variety of schemes, the most important of which will be discussed in Section 2.3.2. For the purposes of this section we can write:

$$\mathbf{u}* = \mathbf{f}(\mathbf{y_0}, \mathbf{F_M}) \tag{2.19}$$

Given the unit cell boundary conditions $\mathbf{u}*$, the unit cell boundary value problem may be solved. The volume averaged stress in the unit cell, $\overline{\sigma}_R$, may then be computed, giving the stress at the equivalent point in the macroscale via

$$\overline{\sigma}_R = \frac{1}{V} \int_{\mathbf{y} \in V} \sigma(\mathbf{y}) dV \tag{2.20}$$

where V is the deformed volume of the unit cell, and $\mathbf{y}$ is any point within it. This proces continues in an iterative loop until the volume averaged stress or deformation gradient has been deemed to converge within a specified limit, for example in the case of the deformation gradient being used as a convergence measure:

$$\tau > \frac{\overline{\mathbf{F_R}}^i - \overline{\mathbf{F_R}}^{i-1}}{\overline{\mathbf{F_R}}^i} \tag{2.21}$$
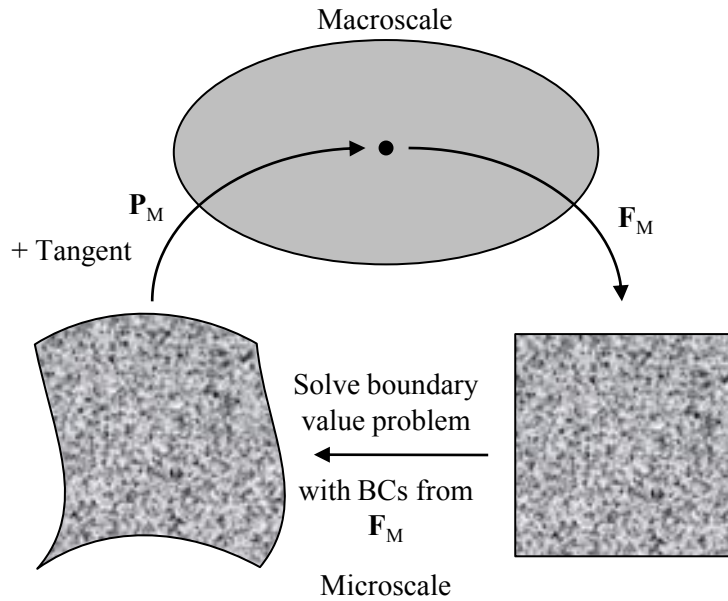
Figure 2.4.: An outline of the information passed between the unit cell and the global model in first order RVE approaches. After Geers et al [4].

Various authors have contributed to first order homogenisation. These include the use of digital microstructure images to construct the unit cells, where material properties are assigned according to the colour of each pixel in the micrograph [44]. A method of modelling inclusions or irregular microstructure was presented in [45]. This method allows microstructural meshes to be built around individual inclusions or microconstituents and then tesselated to make the full microstructural model. The advantage of using this technique is that fibres do not need to be regularly spaced. This allows the effect of matrix rich regions to be examined, for example. These tessalating elements, called Voronoi cells have been used as the basis of unit cells in homogenisation techniques [5]. This type of Voronoi cell constructed unit cell is illustrated in Figure 2.5. However, the application of boundary conditions is the area in which there is the most scope for innovation, and the remainder od this section deals with this topic.

The first order method assumes that the deformation gradient is constant within the unit cell. Hence the technique is limited to cases with no localised damage and small strain gradients. The higher order methods described later in this section have been developed in an attempt to bypass this limitation.

Unit cell boundary conditions in first order homogenisation

An early form of the first order method was presented by Guedes and Kikuchi [43]. Firstly, the macroscopic composite is assumed to be composed of a periodic repetition of a "base cell". In addition, there are two separate models. One macro model at which the general
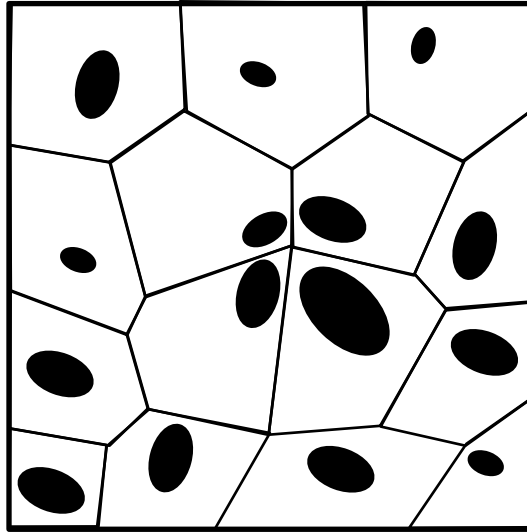
Figure 2.5.: A unit cell constructed of Voronoi cells to model irregular microstructures, after [5].

structure is represented, the other is the microscale model at which the microstructure is represented. The microscale model is a representation of the smallest unit of the material that is repeated to form the structure. This method uses the unit cell to determine the elastic properties of the homogenised material for the macroscale model. The solution at the macroscale is then obtained and the strains resulting may be used to determine the boundary conditions for the unit cell so that the local solution (displacements, stresses and strains) may be obtained.

First order periodic boundary conditions are often used to represent the repetition of a microstructure within a material [46]. The use of unit cells with periodic boundary conditions is restricted to periodic microstructures with small stress gradients [4], and hence are not applicable to the failure of a bonded joint. As a result they are not considered further here.

Second order homogenisation

With the aim of broadening the applicability of unit cell methods, second order homogenisation approaches, such as that presented by Geers et al. in [47, 48] have been developed. Second order periodic boundary conditions allow the use of unit cell methods in regions of moderate stress gradients. While in the first order approaches, the boundary conditions on the unit cell are based purely on the deformation gradient, $\mathbf{F}_M$, at the macroscale, in the second order method, they are based also on the gradient of $\mathbf{F}_M$.

It should be noted that the second order methods cannot deal with some forms of

cracking and localisation. This is because the second order displacement approximation at the microscale based on the first and second gradient of the deformation at the macroscale does not accurately capture deformations with discontinuities.

Summary of homogenisation techniques

While homogenisation techniques can reduce the computational cost of an analysis by reducing the number of degrees of freedom compared to a model meshed entirely at a micro-level refinement, they are still too costly to use on the whole domain of a large structure. They can, however, accurately capture the constitutive properties of a multiphase composite, and the most advanced techniques may even model localisation and damage within composite materials [49]. As a result of the recent advances, homogenisation methods are one of the most desirable ways to model composites in industry, and a way to break down large meshes into small regions where this technique would be managable would be useful.

2.4. Cosimulation

Techniques for dividing an analysis domain into regions with different time integration schemes have been shown to be conditionally stable [50]. This type of analysis is known as cosimulation. Cosimulation techniques were developed to improve the efficiency of fluid-structure and soil-structure interaction analyses, where different integration schemes were more applicable to different regions of a model [51]. Cosimulation may include implicit integration domains, explicit integration domains or a mixture of the two [50, 52]. It has also been shown that two domains may have different time increments [53].

Cosimulation techniques have more recently been implemented in commercial software to allow coupling of two structural domains where one used implicit and the other uses explicit time integration [24]. In the case of structural to structural coupling, the structural domain is divided into a implicit domain and an explicit domain. A boundary exists between these two domains. At this boundary forces and moments are transferred in one direction while displacments and rotations are passed in the opposite direction to be applied as boundary conditions. The data exchanges are made according to a rendezvousing scheme [75]. A common scheme is to exchange the data every standard increment, as a standard increment generally constitutes a larger time step, and to rendezvous every explicit increment would require a large increase in the number of costly standard increments required.

Cosimulation techniques are now used for problems like blast loading of offshore structures [54], where components which are exposed to blast loading are best modelled using an explicit scheme, while the response of the majority of the structure can be more efficiently calculated with implicit integration.

Cosimulation approaches generally require special treatment of the boundaries if mesh

refinement differs between models. If an appropriate treatment of the boundary could be devised, cosimulation may offer a means of achieving coupling of two scales of model.

Cosimulation techniques have been implemented to couple one implicit analysis to one explicit analysis [24]. The two analyses are closely linked and should ideally be run on the same computing node in order to avoid significant degradation in performance when exchanging data. Cosimulation techniques also require significant user input to make sure the interfaces between the implicit and explicit domain are compatible [24]. The methods developed here offer the following advantages over cosimulation:

- There is no restriction on the number of local regions, while in cosimulation the analyst is limited to one global and one local domain.

- Analyses may be distributed between available computational resources without degrading the performance, while both analyses in a cosimulation must be run on the same node.

- The methods developed here process the global and local models automatically to ensure the boundaries between modelling scales are compatible. This allows pre-existing models to be coupled automatically with minimal user input. In cosimulation approaches the user must ensure that this compatibility exists.

- The user is not restricted to running one implicit and one explicit analysis.

2.5. Mesh free methods

One of the significant challenges involved in analysing composite structures is the modelling of cracks and damage within a ply. For interlaminar damage, the methods discussed in Section 2.2.2 may be applied, since it is known in advance that, by definition, interlaminar cracks propagate within the interface between plies. This allows the analyst to include interlaminar damage modelling techniques between plies. However, composite structures are likely to be subject to intralaminar failure as well as delamination, and the path of an intralaminar crack is not generally known in advance. In the traditional finite element method, to model a crack, the analyst must choose whether to mesh the crack explicitly or smear the effect of a crack over a complete element through which it passes [24]. The former option decreases the value of the analysis as a truly predictive tool since the crack path is predefined, and the latter method removes stress concentrations from the analysis [55]. Capturing the stress concentrations accurately is important in predicting how a crack will grow, or initiate interlaminar damage.

As discussed in [56], mesh free methods are the focus of a significant amount of research with methods such as the Element Free Galerkin Method (EFG), the Diffuse Element Method and the Meshless Local Petrov-Galerkin method all being applied to solid mechanics.

Mesh free methods are being developed to model fracture without the need to ensure the mesh conforms to the crack geometry. In the Finite Element Method, the domain is discretised using elements within which the field variables are interpolated from the nodal values of that element. In contrast, mesh free methods represent the domain using a cloud of nodes, and at a point in the domain the field variable is an interpolation values at any node in the domain based on a weighting function of each node at that point [56]. This function is usually based on the proximity of the point at which values are being interpolated to a particular node [57]. In practice the weighting function of a particular node will only be nonzero within a certain distance from the node. A consequence of this is that each node has a domain of influence, or a subset of the whole domain upon which it has an effect of the interpolated field values at that point.

It has been shown in [58], that if the position of a crack within an EFG domain is known, then the weighting functions of each node may be specified such that the domain of influence of that node does not extend across a crack, and that this allows accurate representation of stress concentrations and field discontinuities due to cracks independent of the nodal distribution. In addition, cracks may initiate and evolve within an EFG domain during the course of an analysis based on stress criteria and linear elastic fracture mechanics, [55]. The authors of [55] have also demonstrated the applicability of EFG methods to modelling both delamination and microcracking.

Despite the advantages of mesh free methods for modelling damage in composite materials mentioned above, they have not been established for as long as the Finite Element Method and are not as widely available in commercial packages [56]. Since the focus of this work is to develop a multiscale approach to modelling bonded composite structures which is applicable in the short term it has been decided that the Finite Element Method is the most appropriate modelling technique, and the rest of this chapter will focus on modelling strategies available in commercial Finite Element packages. As discussed in Section 2.3.1, however, the Extended Finite Element Method allows Finite Element analyses to take advantage of some of the concepts of mesh free methods.

2.6. Global/local approaches

Many of the approaches described in Section 2.3 have been demonstrated to capture damage and nonlinear behaviour in composite materials very well. The benefits that would come with their implementation in a model of a very large structure, for example an airliner wing or even the whole aircraft, would be numerous. Not only would such a model be able to show which regions of the structure would be vulnerable at any point in the service envelope, but also whether the loads would be able to redistribute in the event of failure of one of these regions. Large scale physical testing of aircraft components, a costly and time consuming process, could also begin to be replaced by Finite Element Analyses.

A drawback of these approaches is the computational cost. The acceptable element size

in a mesh of the magnitude of an aircraft is of the order of 10 mm or higher. In order to implement the techniques in Section 2.3, however, the elements must often be of a length scale closer to 0.1 mm. Global/local approaches have been developed to overcome conflicts of length scales of exactly this kind, and there are a range of established techniques.

In the simplest form of the global local approach, the displacement field of the structural solution is simply used to provide boundary conditions for the component models. A limitation of this type of approach is that no information is passed from the component to the structural level. A consequence of this is that the effect of the damage or failure of a component on the complete structure is not evident. The structural solution does not benefit from the component analysis. These techniques are quite often used, however, when calculating stress intensity factors or modelling damage originating at a defect in composite pressure vessels [59–61], suggesting they are useful in providing a quick analysis of some localised, known damage.

Bogdanovich and Kizhakkethara have used this type of implementation to model failure of adhesively bonded double lap joints [62]. They applied the technique successively, using not only a global and a local level of refinement, but multiple levels of increasing refinement.

This form of global/local approaches has also been applied to bonded composite I-beams with an initial crack in order to predict failure [63]. In this work, the approach was compared to analytical fracture mechanics techniques, and experimental data. The potential computational savings associated with the use of this type of analysis on composite structures was shown by [64]

A slightly more complex form of global/local approaches involves applying residuals to the structural model, as suggested by Ransom and Knight [65]. The residuals are calculated based on the difference in stress at the component boundary and the equaivalent locations in the structural model. The residuals are applied as nodal forces in the global model. This allows the effect of component damage, for example, to be seen at the structural level. However, since the residuals are applied after the solution of the component models, one component solution will not have an effect on an adjacent one.

In order to allow component solutions to influence each other via the structural model, Whitcomb proposed an iterative approach [66]. In this method, when the residuals are calculated, if they differ beyond a set tolerance from the residuals calculated in the previous iteration, another iteration is performed. The boundary conditions for the components are obtained from the structural solution after application of the residuals. Even using an iterative approach, the residuals are valid only at one particular deformed state of the structural domain. Any change in the strain field in the structural model would render the residuals invalid.

Gendre *et al.* [67] attempt to address some limitations of the global/local approaches, first implemented over 20 years ago [65, 66], but still widely used today. They argue that in order to be useful in an industrial environment, a global/local approach must have the following features:

- The approach must be non-intrusive, in that remeshing is not required, and it may be used in conjunction with a finite element package without modifiying the calulations performed by that software. This ensures that minimal effort is required to perform a global/local analysis on existing models.

- There must be some feedback of information from the local solutions to the global model, for example via residuals [65, 66]. Simply passing boundary conditions from the global solution, as in [62], to the local models is not sufficient to see the effect of nonlinearity at the local level on the global structure.

In the method proposed by Gendre *et al.*, the boundary conditions are applied as in other global/local approaches; by interpolating displacements in a global solution.

$$\mathbf{u}^L = \mathbf{u}^G \text{ on } \Gamma \tag{2.22}$$

where Γ is the boundary between local and global regions, $\mathbf{u}^L$ represents the local boundary displacements and $\mathbf{u}^G$ the global ones. Residual forces are also applied to the global model on Γ such that:

$$\sigma^L \mathbf{n}_i + \sigma_c^G \mathbf{n}_c = 0 \text{ on } \Gamma \tag{2.23}$$

where $\sigma^L \mathbf{n}_i$ is the vector product of the outward normal and the local stress tensor on Γ, and $\sigma_c^G \mathbf{n}_c$ is the vector product of the outward normal and the global stress tensor on Γ. This equation may be written in the form of an integral along Γ in order that a measure of equilibrium between global and local models may be calculated.

$$r(\mathbf{v}^*) = - \int_\Gamma \left[\sigma^L \mathbf{n}_i + \sigma_c^G \mathbf{n}_c \right] \cdot \mathbf{v}^* \mathrm{d}\Gamma \tag{2.24}$$

The procedure used to update the global solution with the residuals is as follows:

- Solve the global problem, and, if this is not the first iteration the global problem with the original applied displacements and tractions set to zero, and the residual forces are applied on Γ. This yields $\Delta \mathbf{u}$, the residual global displacement field. This is superimposed on the original displacment field, $\mathbf{u}$.

- Interpolate the local boundary conditions from the superimposed global displacement field $\mathbf{u} + \Delta \mathbf{u}$.

- Quantify the lack of equilibrium in the models, using the criterion in Eq. 2.24. If the residual, $r(\mathbf{v}*)$, is of sufficiently small magnitude, the solution is deemed to have converged.

- Calculate the residual forces using Eq. 2.24, but writing $\mathbf{v}^*$ in terms of the basis functions on Γ.

- Solve the local problem, and return to the first step.
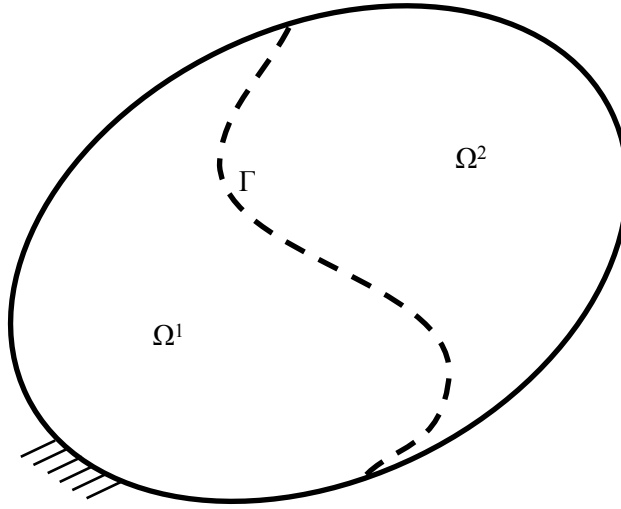
Figure 2.6.: The separation of the problem domain into multiple domains in a non-overlapping domain decomposition approach

This technique has been applied and shown to work effectively on a complex set of global and local models, similar to those used in the aerospace industry [68]

Yet another similar method, referred to as domain decomposition, and a summary of these techniques is given in [69]. In general the technique uses a global level and multiple local levels. The global level is used to ensure compatibility and equilibrium by iteration using linear finite elements. The principle of these techniques is illustrated in Figure 2.6. On the boundary, Γ, there should be compatibility of displacements,

$$\mathbf{u}^1 = \mathbf{u}^2 \text{ on } \Gamma \tag{2.25}$$

The stresses on Γ should also be in equilibrium,

$$\sigma^1 \mathbf{n}^1 + \sigma^2 \mathbf{n}^2 = 0 \tag{2.26}$$

It has been used to capture buckling in large structures [70], and in plate bending and structures composed of heterogeneous materials [71]. The local levels are more refined and account for geometric nonlinearities. The component models are completely separate, allowing the analyses to be sent to different processors. Transforming the boundary forces from the components, which may undergo significant rotations in the deformed state, into the global system means that geometric nonlinearity is also accounted for in the global model. A domain decomposition method has been demonstrated where the elements which are not sufficiently small are chosen based on strain gradient magnitude [72]. The procedure works with quadrilateral and triangular elements, which are divided into similarly

shaped smaller elements. The new nodes formed on the old element boundary are grouped to a pair of nodes formerly belonging to the old element via multi point constraints. The analysis is re-run and if necessary further elements may be sub divided again, leading to nested multigrid approaches. A limitation of this method is that only the refinement of the mesh may be updated. Different material models and details too small to be captured at the global scale are not dealt with as the mesh is refined.

A similar approach to [72] is proposed in [73, 74], in order to model damage growth in heterogeneous materials. In this case the refined component models are connected in gaps in the global model by multi point constraints, and all global and local problems are solved in a single analysis.

2.7. Objectives

As discussed in Chapter 1, this work is motivated by the need to model local regions of a large structure at a refinement which is too computationally intesive to be used throughout the domain. This must be done in such a way that the global solution influences the local solution via boundary conditions, and the damage modelled in the local analyses is reflected in the global analyses.

In this chapter, a range of multiscale techniques have been examined to asses how applicable they are to the conflict of scale issue in bonded composite structures. Homogenisation techniques work very well for modelling the microscale behaviour of fibre reinforced polymers in a mesoscale mesh. However they rely on the periodic nature of the microscale and therefore cannot be extended to the problem in question, where the local regions are not arranged in a periodic way.

XFEM can also be viewed as a multiscale approach - damage may propagate independently of the mesh as long as an appropriate model for crack propagation may be determined. The model for damage propagation may be viewed as the local model. Due to the complexity of implementation of XFEM, it is not considered a practical approach in this work.

Cosimulation techniques do not require periodic features within the global domain. Any feature may be selected and isolated as a separate domain. With correct treatement of the global and local boundaries, a cosimulation would provide a convenient means of coupling a global and a local scale of models. However, as a cosimulation requires regular communication between the two domains at what are known as rendez-vousing points where data are exchanged between domains it is necessary to run these jobs on the same computer node in order to avoid decreases in efficiency due to slow communication between global and local analyses.

Global-local techniques allow the global and local analyses to be run separately. This means that each model may be analysed wherever computational resources are available. This becomes a particularly important advantage when running a multiscale analysis containing many local models. Traditional global-local analysis, however only passes infor-

mation from the global to the local models. In Chapter 1, the need to be able to represent local damage and nonlinearity at the global scale was discussed. In order to do this a means of extracting damaged properties from a local model to be used at the global scale is required. The focus of this work is therefore:

1. To develop an appropriate method of extracting damaged properties from a local analysis, such that they may be used in a global analysis

2. To show that this technique provides results comparable to those obtained by benchmark problems.

3. To justify the use of fully coupled global local approaches over traditional global-local or submodelling processes.

The methods developed in this work also overcome some of the difficulties in global-local methods such as the one proposed in [67], which arise due to the fact that the stiffness of the local region in the global model is not updated according to damage or a more accurate geometrical representation at the local scale of modelling. As the deformation in the local region increases, and the difference between the solutions in this region in the global and local representations become more significant, then the applied residual forces and associated stresses also increase. As these residual forces become more significant compared to the element forces acting on the nodes, the global representation of the local region becomes less accurate. By updating the stiffness of the local region in the global model, as discussed in Chapter 4, these issues are avoided.

3. Design, manufacture, testing and analysis of a benchmark specimen for global/local models

3.1. Aims

Specimens were designed to demonstrate the applicability of various numerical damage prediction tools for bonded joints to structures exhibiting sequential failure of multiple joints. This lead to the following design conditions:

1. There should be more than one vulnerable adhesive joint in each specimen.

2. Each joint should fail at different loads/displacements.

3. The failure of one joint should have an effect on the failure of another, i.e. the failure of the second joint would have occurred at a different load/displacement had the first joint remained undamaged.

4. All vulnerable joints should fail below an applied load of 9kN since a 10kN load cell was to be used.

A further condition that the specimens should resemble a typical sub-structure of an aircraft wing was also added to make the results more industrially relevant.

3.2. Material

Materials used were T800/M21 high grade pre-preg and FM300K film adhesive. Their properties, as required by the Finite Element models discussed in Section 3.3.1, are summarised in Table 3.1 and Table 3.2 respectively. The nominal ply thickness of the adhesive is $13\mu m$.

3.3. Numerical design

3.3.1. Preliminary designs

A number of preliminary designs were assessed to determine which best met the criteria set out in Section 3.1 [20]. Finite element analyses were performed for each of the designs

Table 3.1.: Elastic properties of T800/M21 carbon fibre reinforced epoxy.

Material property	Value
Longitudinal modulus, E_{11} (GPa)	160.4
Transverse modulus, E_{22} (GPa)	9.29
Out of plane modulus, E_{33} (GPa)	9.29
In plane shear modulus, G_{23} (GPa)	4.81
Out of plane shear modulus, G_{12}, G_{13} (GPa)	4.81
Poisson's ratio, $\nu_{12}, \nu_{13}, \nu_{23}$	0.33

Table 3.2.: Mechanical properties of FM300K [6].

Material property	Value
Normal modulus, E_N (GPa)	2.38
Normal shear modulus, G_{NS1}, G_{NS2} (GPa)	0.68
Normal tensile strength, N (MPa)	48.9
Shear strength, S_1, S_2 (MPa)	61.0
Normal fracture toughness, G_{NC} (kJm^{-2})	0.9
Shear fracture toughness, G_{S1C}, G_{S2C} (kJm^{-2})	2.5

to predict the sequence of and load to failure. In each case, debonding was taken to initiate at a stiffener runout at the displacement at which the damage variable first reached 1.0 at a single contact node (see Section 2.2.2 for details on debonding models).

Stiffeners bonded to flat plates were quickly identified as suitable specimens because they are representative of wing components in aircraft making them industrially relevant. The arrangement of stiffeners on the plate could readily be modified as they must only be held in place during bonding by wooden moulds which are relatively simple to manufacture. This allowed the design to be tailored so that the criteria set out in Section 3.1 could be met.

A single layer of solid, linear, reduced integration elements was used to model each ply in the layup. Each layer of elements was given the properties of a T800/M21 ply as summarised in Table 3.1, and the orientation of the fibre direction was defined in accordance with the layup angle. Once input into the Finite Element model, the preprocessor used the data in Table 3.1 to calculate the elastic stiffness matrix for each element [75]. Linear elastic behaviour was assumed in the laminates. For the stiffeners, local directions had to be assigned for each element in the curved regions. This was achieved using a discrete coordinate system [75]. For each element, the normal or 3 direcion of a ply was taken as the normal of the top surface of the stiffener geometry, while the 0° angle was defined by the outside top edge of each stiffener half. Additional rotations about the 3 direction for each element in each ply were applied according to the angle of that ply.

Short stiffener
70 mm long
1.25 mm thick
Lay-up: (0,45,-45,90,0)

ENCASTRE

Long stiffener
100 mm long
1.25 mm thick
Lay-up: (0,45,-45,90,0)

Skin
100 mm x 150 mm
2 mm thick
Lay-up: (0,45,-45,90)s

APPLIED
DISPLACEMENT
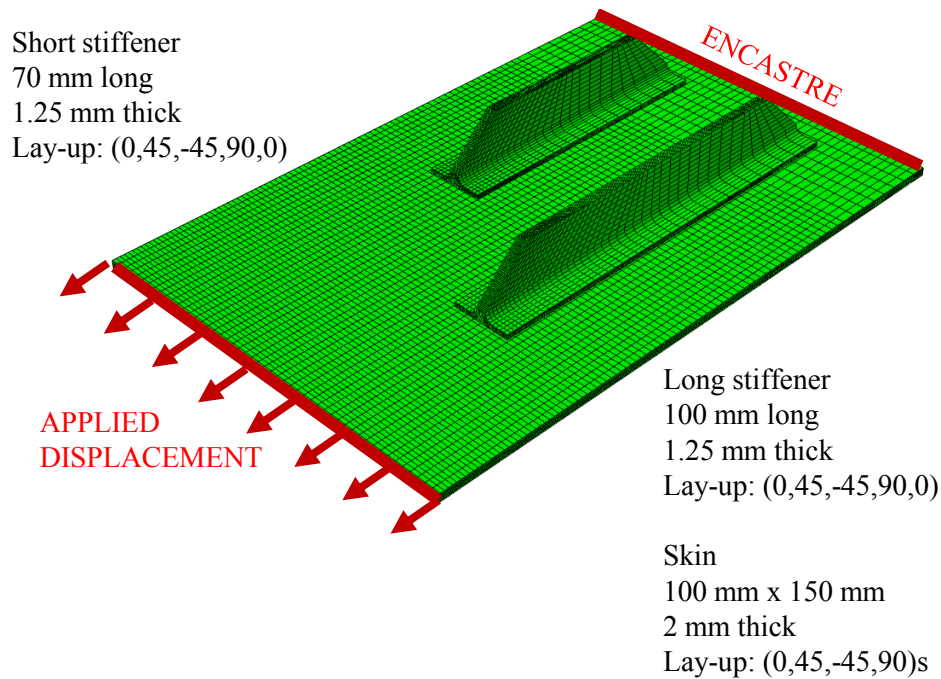
Figure 3.1.: Preliminary design: side by side configuration loaded in tension.

To model the interaction between the plate and stiffeners, a cohesive contact model was used, as discussed in Section 2.2.2. The properties required for a cohesive contact model and the values used in the analyses in this chapter are summarised in Table 3.2 [6]. The damage initiation model used was the quadratic traction criterion (see Section 2.2.2). A linear softening model was used for damage evolution and rate of softening under each loading mode was defined based on the fracture energy for that mode (see Section 2.2.2).

In each of the configurations considered in this chapter, debonding initiation was taken as the point where the damage variable (see Section 2.2.2) reached one for a single node on a particular runout. This point has been marked on the load-displacement curves obtained from the Finite Element analysis of each configuration (Figure 3.2, Figure 3.4, Figure 3.6).

The first configuration which was considered was a plate loaded in tension and stiffened by two parallel stiffeners side by side (Figure 3.1).

Finite element analysis was used to determine the sequence of failure of the two runouts and the loads at which these occured. The long stiffener debonded at 40kN and the short stiffener at 70kN, as shown in the load displacement curve in Figure 3.2. While there was a clearly defined sequence of failure the test machines had a load capacity of 10kN so this configuration was disregarded.

The next configuration to be considered used the same specimen geometry (Figure 3.1), but the specimen was to be loaded in bending as shown in Figure 3.3.

Debonding had initiated in both stiffeners at loads below 300N, as shown in Figure 3.4. This was within the capabilities of the testing machine. The long stiffener began to debond at an applied displacement of 13.6mm and the short stiffener at 16.3mm. However, the
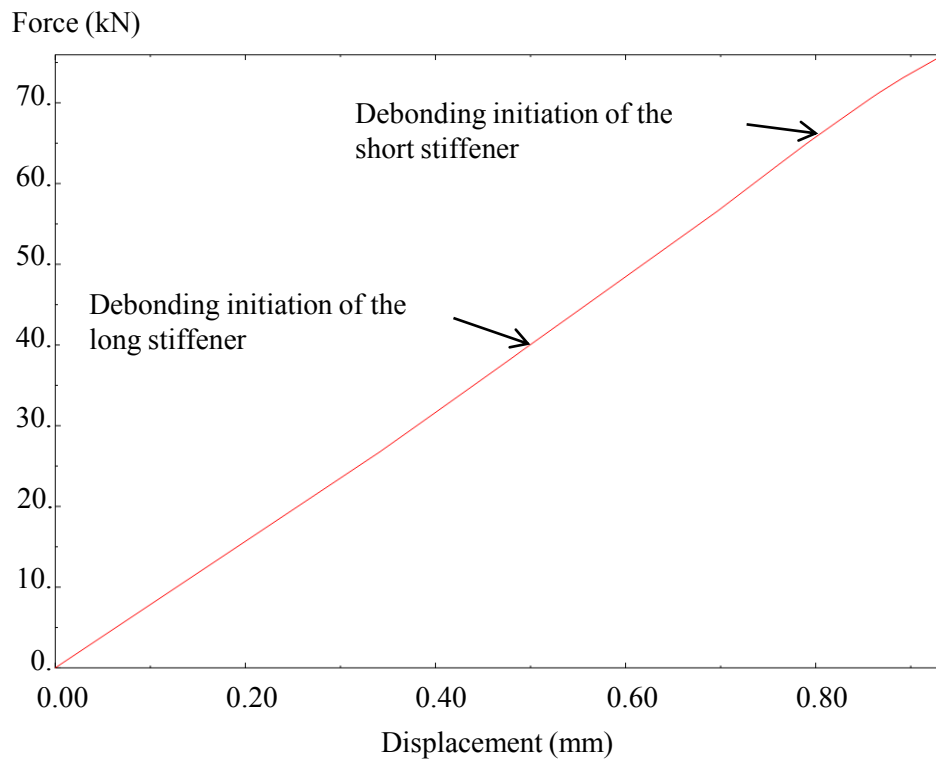
Figure 3.2.: Load displacement curve for the side by side configuration loaded in tension. The points at which debonding initiated at the long and short stiffeners are marked.
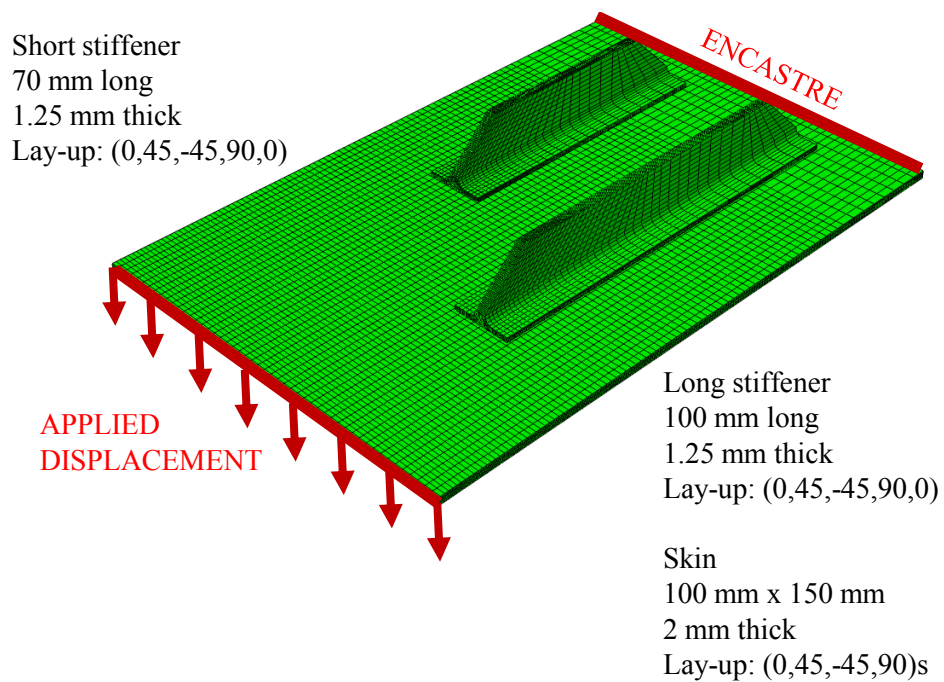
Figure 3.3.: Preliminary design: side by side configuration loaded in bending.
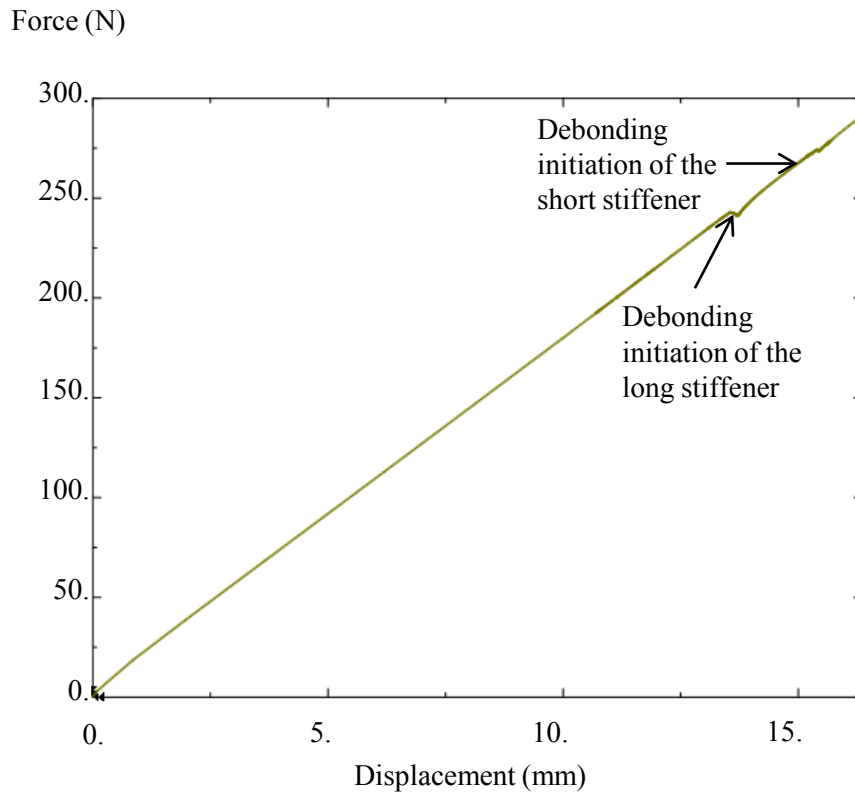
Figure 3.4.: Load displacement curve for the parallel stiffeners configuration loaded in bending. The points at which debonding initiated in each runout are marked.

extent of debonding in the long stiffener was minimal at the onset of debonding in the short stiffener. The effect of damage in the long stiffener bondline on the stress state in the short stiffener runout was therefore not significant, and this configuration was deemed not to satisfy the aims set out in Section 3.1.

Since the specimen with parallel stiffeners was deemed unsuitable, a plate loaded in bending stiffened by two aligned stiffeners (Figure 3.5) was considered.

The onset of debonding (taken as the displacement at which the damage variable first reaches 1.0 for a contact node on each stiffener) occured at applied displacements of 6mm and 9mm for the long and short runouts respectively Figure 3.5. Furthermore, the extent of debonding in the long runout predicted at the onset of debonding in the short runout was deemed significant enough to delay debonding in the short runout. The load-displacement curve for this configuration is shown in Figure 3.6. The features relating to the first significant debond jump at each runout are marked. These points were determined by comparing the displacements at which the discontinuities in the curve are present to the displacements at which sudden changes in the damage variable at each plate-stiffener interface occurred.

The aims set out in Section 3.1 were satisfied and this was selected as the configuration for the experimental specimens.
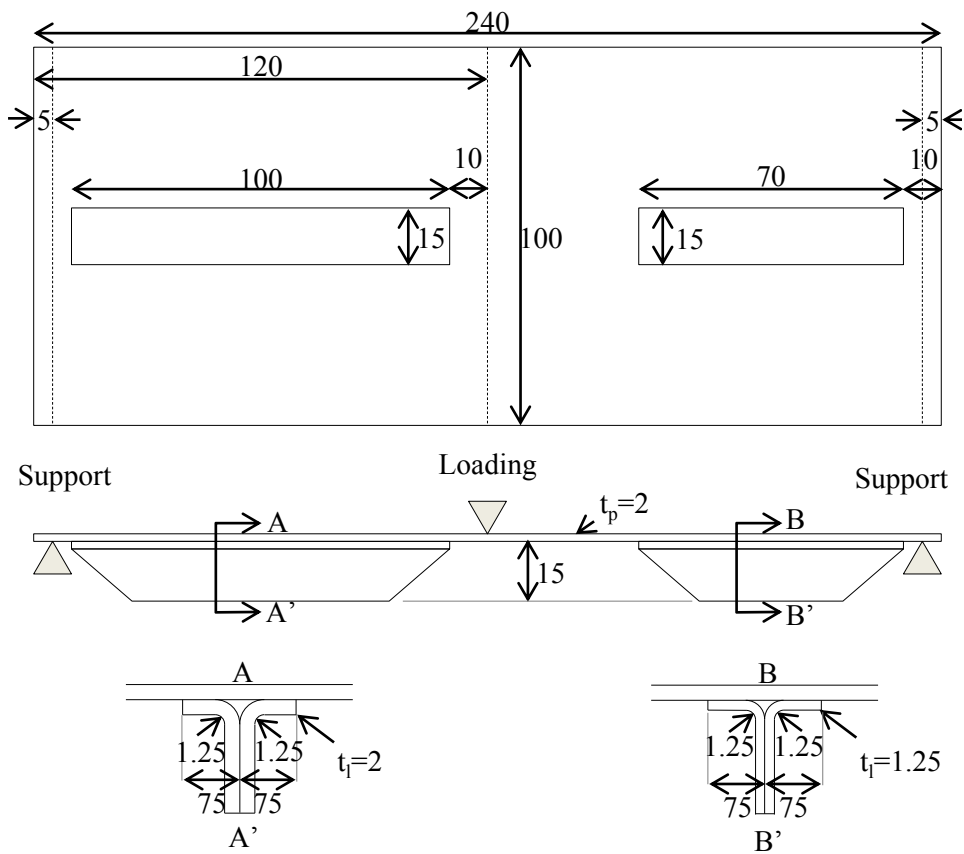
Figure 3.5.: Details of specimen design, dimensions in mm.
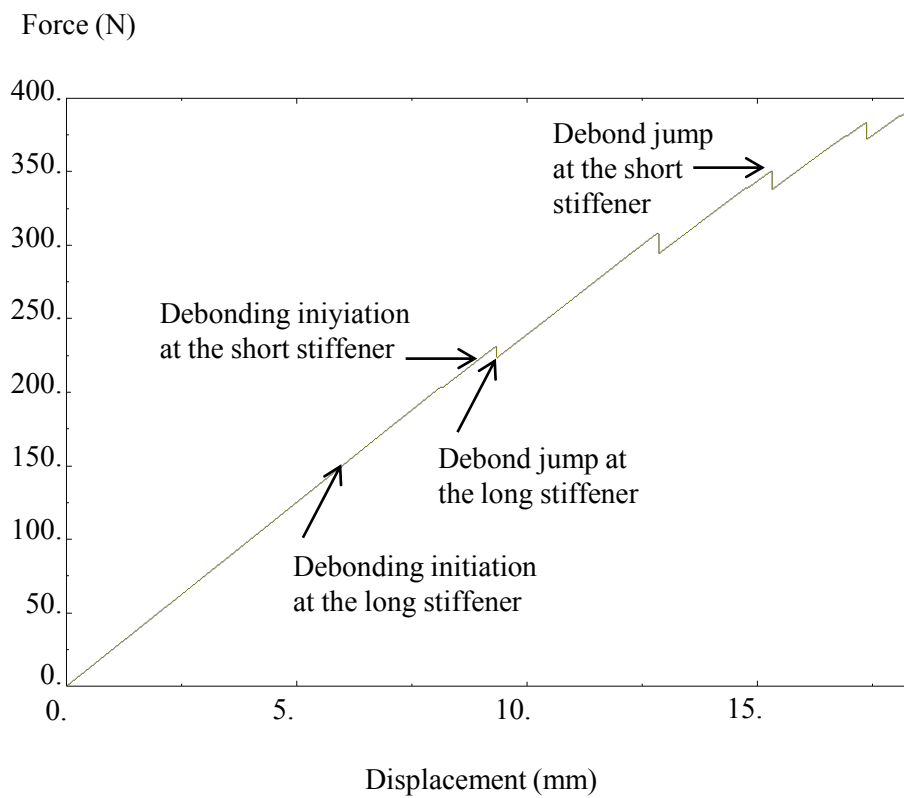
Figure 3.6.: Load displacement curve for the aligned configuration with the points at which debonding initiated at each runout marked.

Table 3.3.: Summary of layups in high grade T800/M21 for each component of the specimens.

Component	Layup
1. Plate	[45,-45,0,90]$_s$
2. Long stiffener	[0,45,-45,90]$_s$
3. Short stiffener	[90,90,0,-45,45]

3.3.2. Final design

Figure 3.5 shows the geometry of the specimens selected based on the findings of Section 3.3.1. A flat plate with two parallel runouts of different thicknesses, loaded in 3 point bending was used. Table 3.3 shows the layup of each component. Note that stiffener layups are given for one L-shaped stiffener half.

3.4. Manufacture

3.4.1. Layup

The layups for the plate and stiffeners was performed as summarised in Table 3.3. All the specimen plates were cut with a dry saw from a larger plate. A 30mm border was added at the edge of the larger plate to allow defects more common in this region to be avoided.

Stiffeners were laid up on a mould with 3 parts, as shown in figure 3.7. The first ply in the layup definition in Table 3.3 was the last to be placed on the mould. Each half of the stiffener was laid up on the curved parts of the mould. The two stiffener halves were then placed together. Ten 3mm strips of the pre-preg were gently twisted together with a drill, and placed in the cavity at the radii of the stiffener halves. Finally, the lid of the mould was placed on top. Stiffeners 700mm in length were cured, and all 5 of each thickness were cut from these.

3.4.2. Curing and bonding

The plates and stiffeners were cured according to the cure cycle shown in Figure 3.8. After all the curing and the cutting of the stiffeners had been completed, the plates, stiffeners and adhesive were placed in moulds as shown in figure 3.9, and the film adhesive was cured. Note that the mould came in four sections, with one pair of moulds for each stiffener. This was due to the difference in thickness of stiffeners.

3.4.3. Defects

A detailed inspection of manufacturing defects in the bondline was carried out. While these defects were not intentional they were important since they were representative of defects in real engineering structures. X-ray investigation was not possible as penetrant
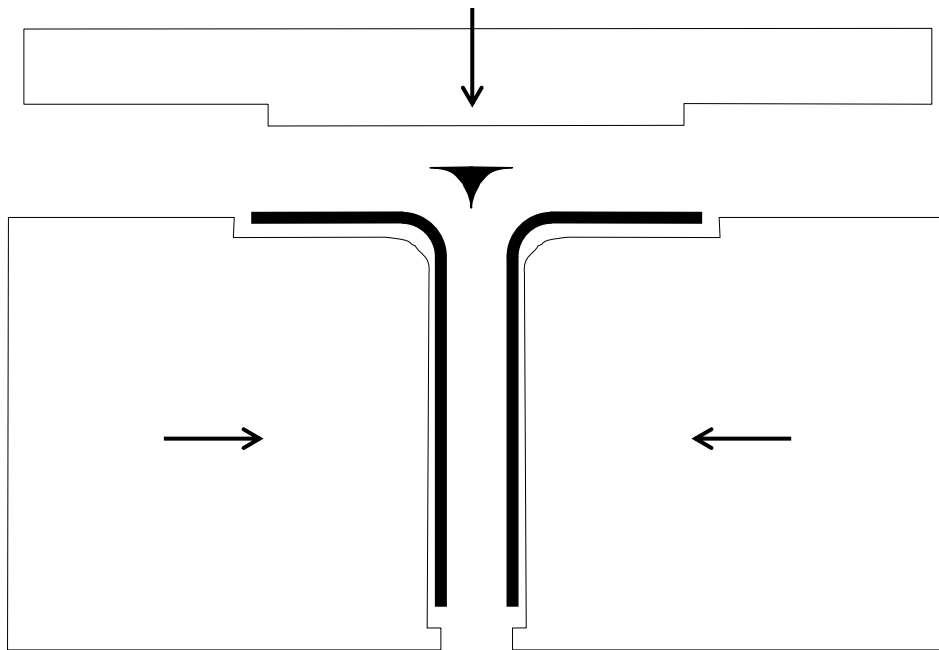
Figure 3.7.: The mould used in the manufacture of the stiffeners.
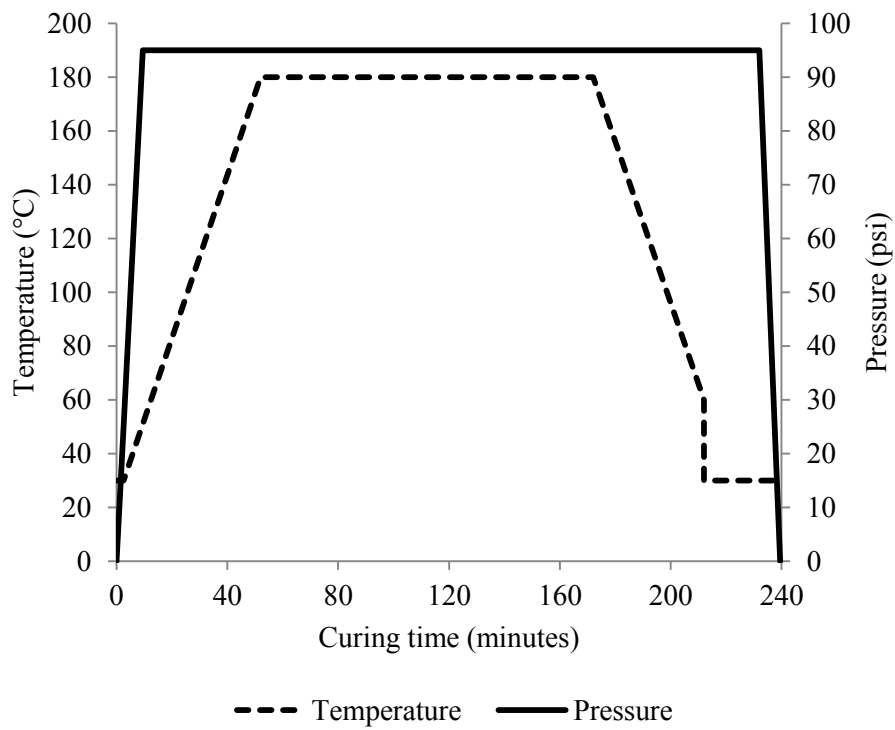
Figure 3.8.: Cure cycle used in preparing all components

Adhesive film
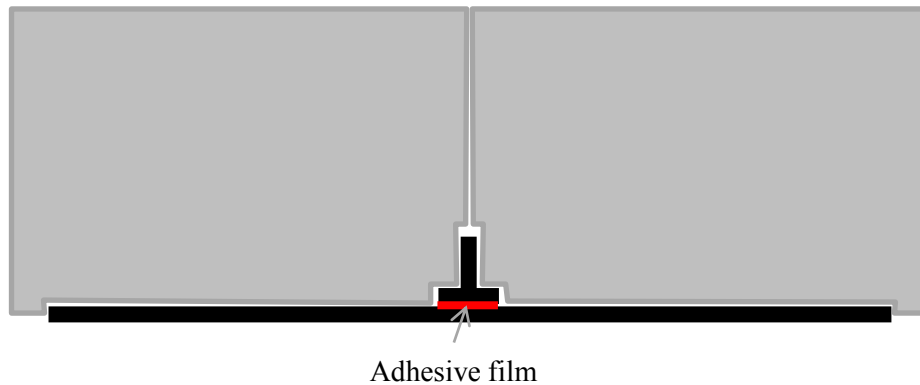
Figure 3.9.: The mould used in the bonding of the stiffeners to the plate.

fluid would have damaged the bonding prior to testing. C-scan investigations, both at Airbus UK and in the Department of Aeronautics were inconclusive. Measurements were taken by probing the edge of the bond with the corner of a small piece of paper and recording how far the probe could be inserted. Note that internal defects could not be detected. Fracture surfaces would be inspected after the tests for information on internal defects. Figure 3.10 gives a summary of the defects discovered by this probing technique.

3.5. Testing

3.5.1. Test rig

The specimens were loaded under 3 point bending at the mid-point using a 10T Instron machine fitted with a 10kN load cell. The loading rig consisted of 2 cylindrical supports, in parallel and fixed at a separation of 220 mm. The plates were placed, stiffener down and centred on these supports. Load was applied at the mid-span line via another cylindrical load fixture, as shown in Figure 3.11. The loading rate was 0.5 mm/min.

It should be mentioned here that when the photographs of the specimen in the test rig were taken, the specimen was not directly in front of the lens. As a result the photographs may be misleading as to the point of application of the load. In particular the central loading line seems to be directly above the long stiffener runout. This visual effect is due
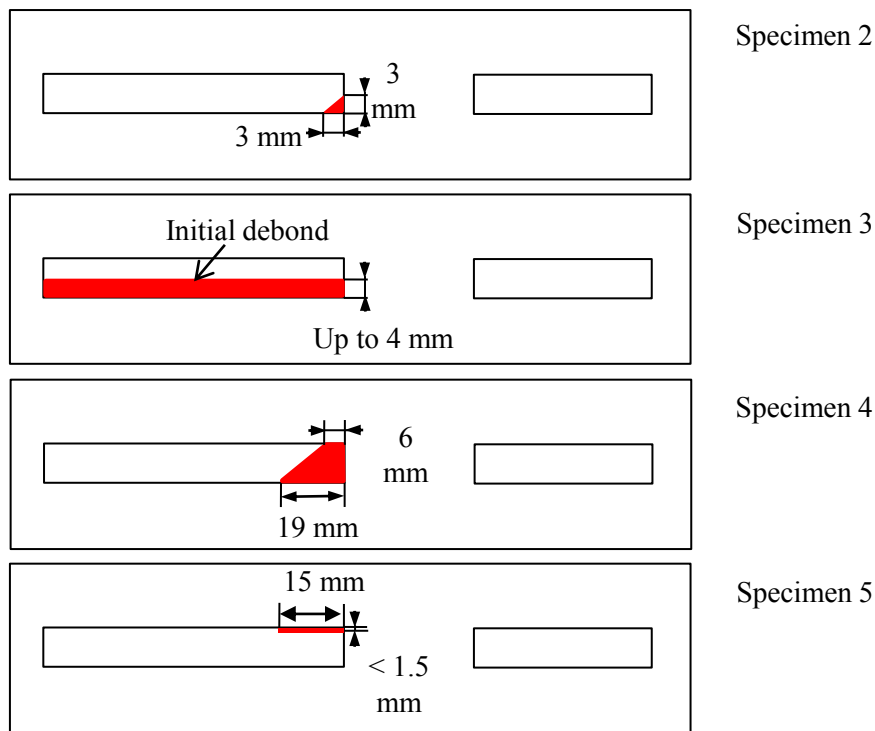
Figure 3.10.: Summary of bondline defects detected by probing with the corner of a piece of paper. No defects were detected in Specimen 1.

to the fact that the front of the loading cylinder lies in a different plane parallel to the lens than the closest face of the stiffener. As a result the photographs in this section may not be considered as 2D side views. For confirmation that this is the case, note that the internal vertical face of the left hand support is visible in Figure 3.11. Loads were applied as specified in Figure 3.5. In fact, the loading line was further to the right compared to the long stiffener runout than it appears in the photograph.

3.5.2. Data collection

Data were recorded by the following methods during the tests.

Load Cell: Load applied to the specimen was recorded every 0.5 s via a 10 kN load cell.

Strain Gauges: Two pairs of linear strain gauges were placed at the end of each stiffener, on both sides of the panel (See Figure 3.12). This gave an indication of the bending of the specimen at the runouts. Their location was a consequence of the numerical design process and was selected so that the onset of debonding would be accompanied by a change in slope of bending strain plotted against applied displacement (see Section 3.6).

High resolution digital camera: Photographs were taken after each 1 mm of displacement. This allowed the displacement rate of the load point to be verified, and the
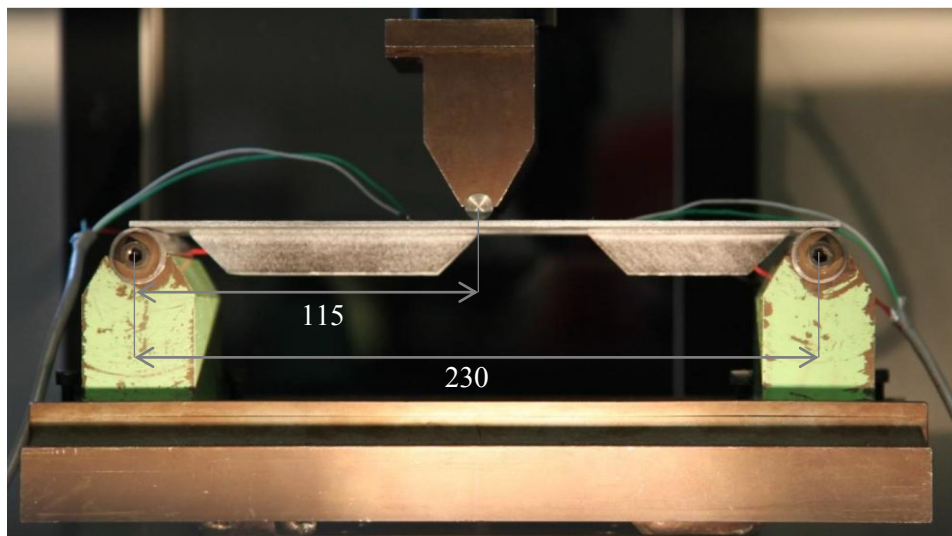
Figure 3.11.: A specimen in place in the 3 point bending rig (dimensions in mm). Note that the dimensions specified are loading rig dimensions. In the photograph the perspective distorts the position of objects at different distances from the plane of the camera lens relative to one another, so the dimensions of the runouts relative to the rig could not be marked. See Figure 3.5 for deatils on the loading points.
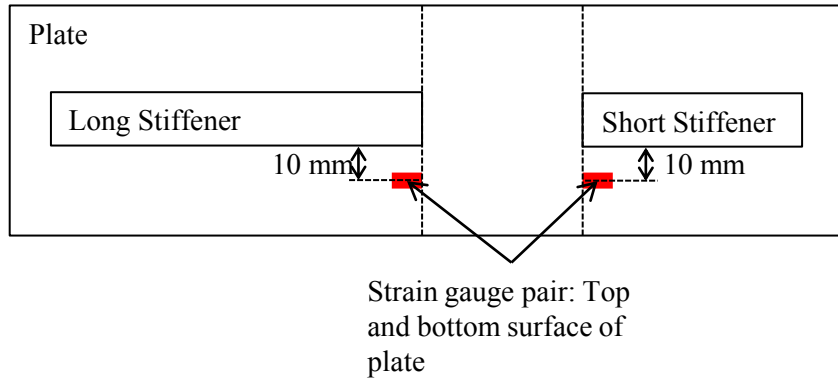
Figure 3.12.: Strain gauge locations in the tests.

damage in the bondline to be recorded visually.

3.6. Calculations

In order to highlight jumps in bending strain at the two runouts due to failure, pairs of strain gauges were used on either side of the plate near the stiffener's end as previously discussed. A bending measure, ε_b, is calculated by;

$$\varepsilon_b = \frac{\varepsilon_s - \varepsilon_u}{2} \tag{3.1}$$

where ε_s is the strain recorded on the stiffened side of the plate, and ε_u the strain recorded on the unstiffened side.

This bending measure could be used as an indicator of a debond passing the strain gauge locations. Consider the following simplified example; the panel may be represented as a beam of varying bending stiffness along the length (Figure 3.13). Clearly the curvature and hence ε_b is greatest in region 2 where the bending stiffness is lowest. Debonding of the long stiffener may be represented by the extension of region 2 to the crack tip. Hence the bending measure at the long runout is measured in region 2, and would be expected to increase. Simultaneously, the extension of relatively flexible region 2 would decrease the bending coefficient measured in regions 1 and 3. The displacements at which sudden

(a)

(b)
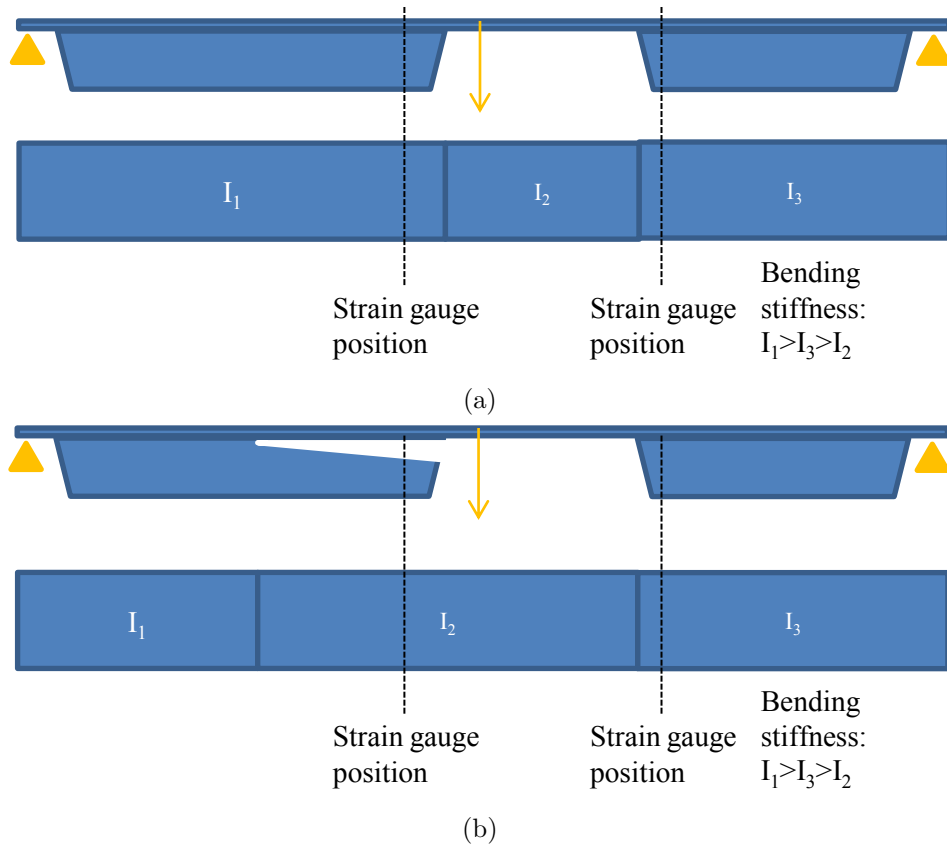
Figure 3.13.: Simplified representation of the debonding of a panel as a beam of varying bending stiffness.

changes in ε_b occur are taken to correspond to the debond passing a strain gauge (i.e. the onset of debonding).

3.7. Results

3.7.1. Strain-displacement

A bending measure, as discussed in Section 3.6, was plotted at the runout of each stiffener for each specimen (Figure 3.14) as an indicator that the stiffener had begun to debond. As shown in Figure 3.13, the stiffened panel may represented in a simplified form as a beam with three regions, each with a different bending stiffness. The highest bending stiffness is in the region to which the long stiffener is bonded, the lowest is in regions where there is no stiffener and the stiffness of the region where the short stiffener is bonded is between the two. As a debond grows beyond a location where the bending measure is recorded, the bending stiffness of this region decreases to that of the plate alone leading to an increase in bending measure gradient, $\frac{\partial \varepsilon_b}{\partial u}$ for that location. This also decreases the overall bending stiffness of the plate and thus the bending moment at any particular location in the beam representation of the specimen. This means that any debond growth in one stiffener leads

Table 3.4.: Summary of displacements at which measured bending measures exhibit opposing trends.

Specimen	Long stiffener ε_b increasing	Short stiffener ε_b increasing
1	8.7-9.3 mm	17.8-18.2 mm
2	4.0 mm	25.8-26.1 mm
3	4.0 mm	13.5-15.5 mm
5	1.8 mm	15.5-16.0 mm

to a decrease in $\frac{\partial \varepsilon_b}{\partial u}$ at the other location. Hence to identify debonding growth at one stiffener runout an increase in , $\frac{\partial \varepsilon_b}{\partial u}$ at that location with a corresponding decrease in , $\frac{\partial \varepsilon_b}{\partial u}$ at the other stiffener is sought.

Due to a strain gauge malfunction, the bending measure for specimen 4 could only be calculated near the long stiffener runout during the early stages of the testing. The location at which the bending measure was calculated is shown in Figure 3.12.

The bending measure for specimen 1 (the initially undebonded specimen) shows the clearest effect of debonding. The bending measure is initially highest near the short, thinner stiffener. After debonding of the long stiffener, the bending in the debonded region increases beyond that at the still bonded short stiffener. The gradient of these curves, $\frac{\partial \varepsilon_b}{\partial u}$, in Figure 3.14 should be considered. With the exception of specimen 4 (for which a strain gauge failed) it is possible to locate displacements at which $\frac{\partial \varepsilon_b}{\partial u}$ increases at one runout, while it decreases at another. For example, in Figure 3.14a, between 8.7 mm and 9.7 mm $\frac{\partial \varepsilon_b}{\partial u}$ increases for the location close to the long stiffener, while it decreases at the location close to the short stiffener. Similarly, between 17.8 mm and 18.2 mm $\frac{\partial \varepsilon_b}{\partial u}$ decreases for the location close to the long stiffener, while it increases at the location close to the short stiffener. These regions are summarised in Table 3.4.

Appendix A contains abridged experimental data. The value for applied displacement, load and each of the 4 strain gauge readings for every 25th sampling point in time is presented .

3.7.2. Load-displacement

Load-displacement plots are shown in Figure 3.16. Due to separate load cell malfunctions, the curves are not available for specimens 1 and 2.

3.7.3. High resolution photographs

Figures 3.17-3.21 show photographs of each specimen before debonding is visually detected, after the first debond is visually detected and after the second debond is visually detected (or at the end of the loading if no second debond is seen). Table 3.5 summarises the
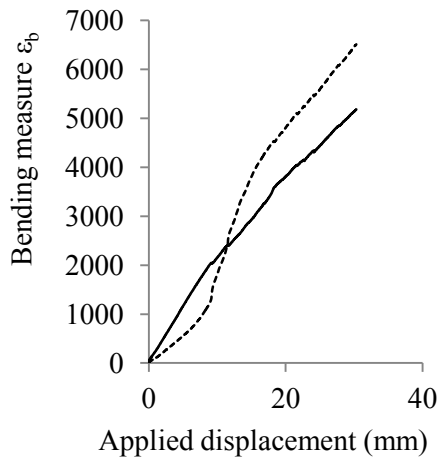
(a) Specimen 1.
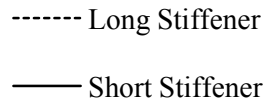
(b) Key.
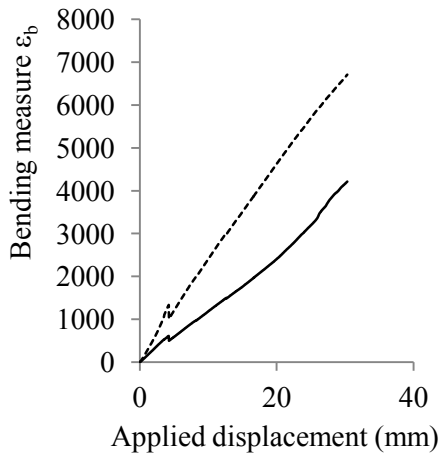
(c) Specimen 2.
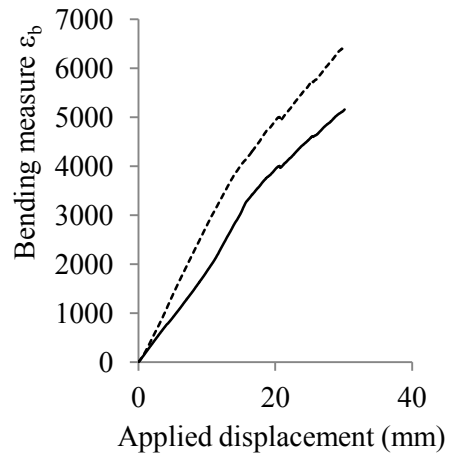
(d) Specimen 3.
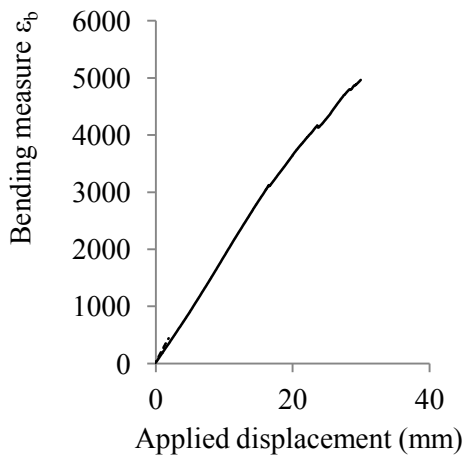
(e) Specimen 4.
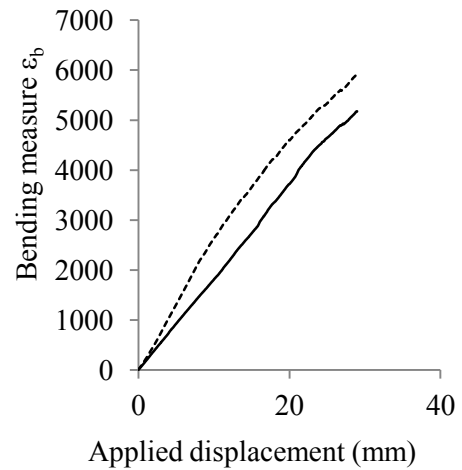
(f) Specimen 5.

Figure 3.14.: Bending measure (see Chapter 3.6) at the runout of the long and short stiffeners for each specimen.
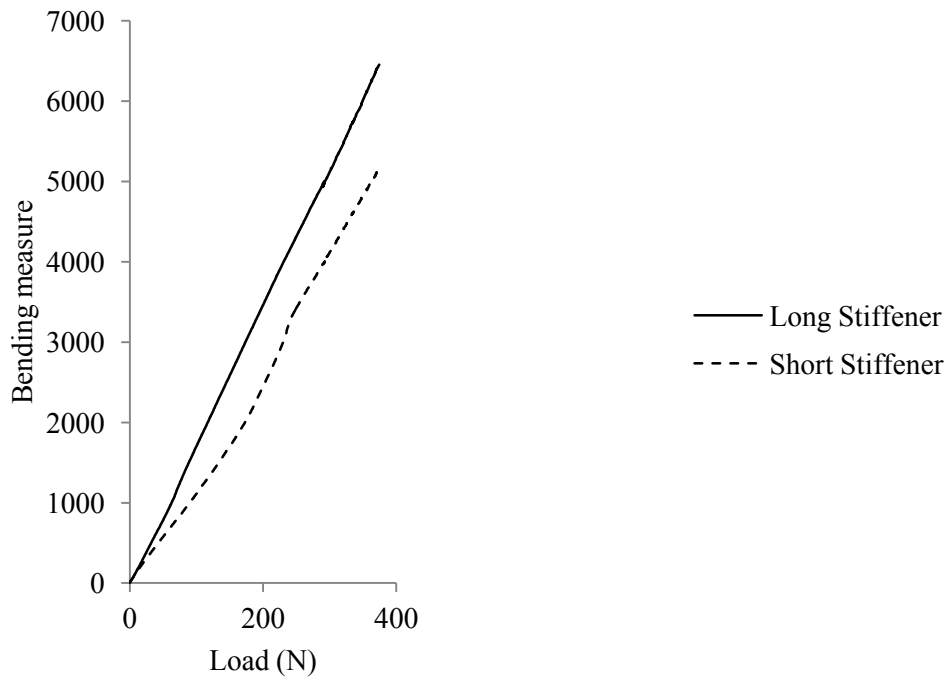
(a) Specimen 3.

(b) Key.
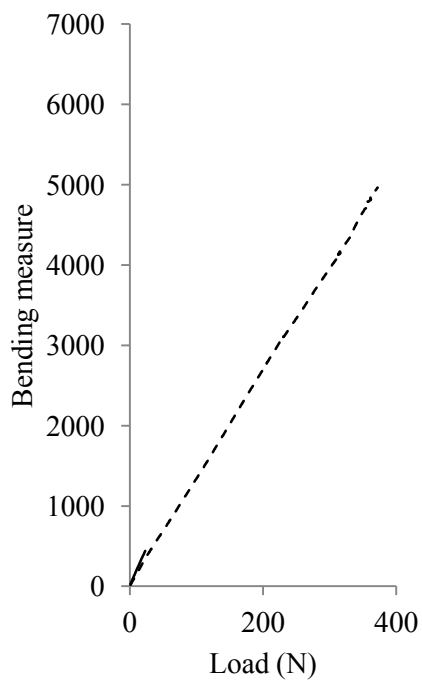
(c) Specimen 4.
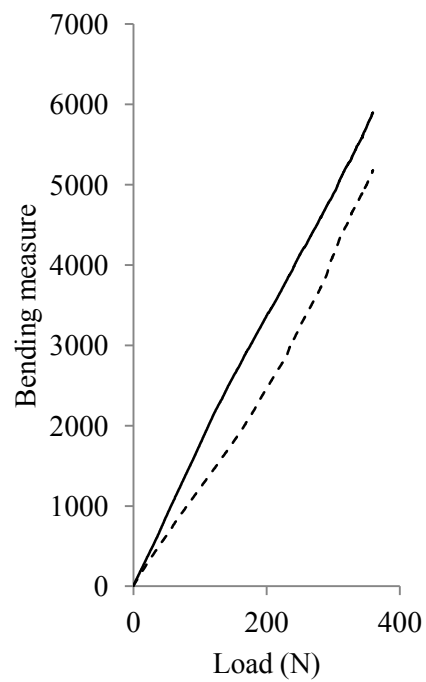
(d) Specimen 5.

Figure 3.15.: Bending measure (see Section 3.6) at the runout of the long and short stiffeners plotted against applied load.
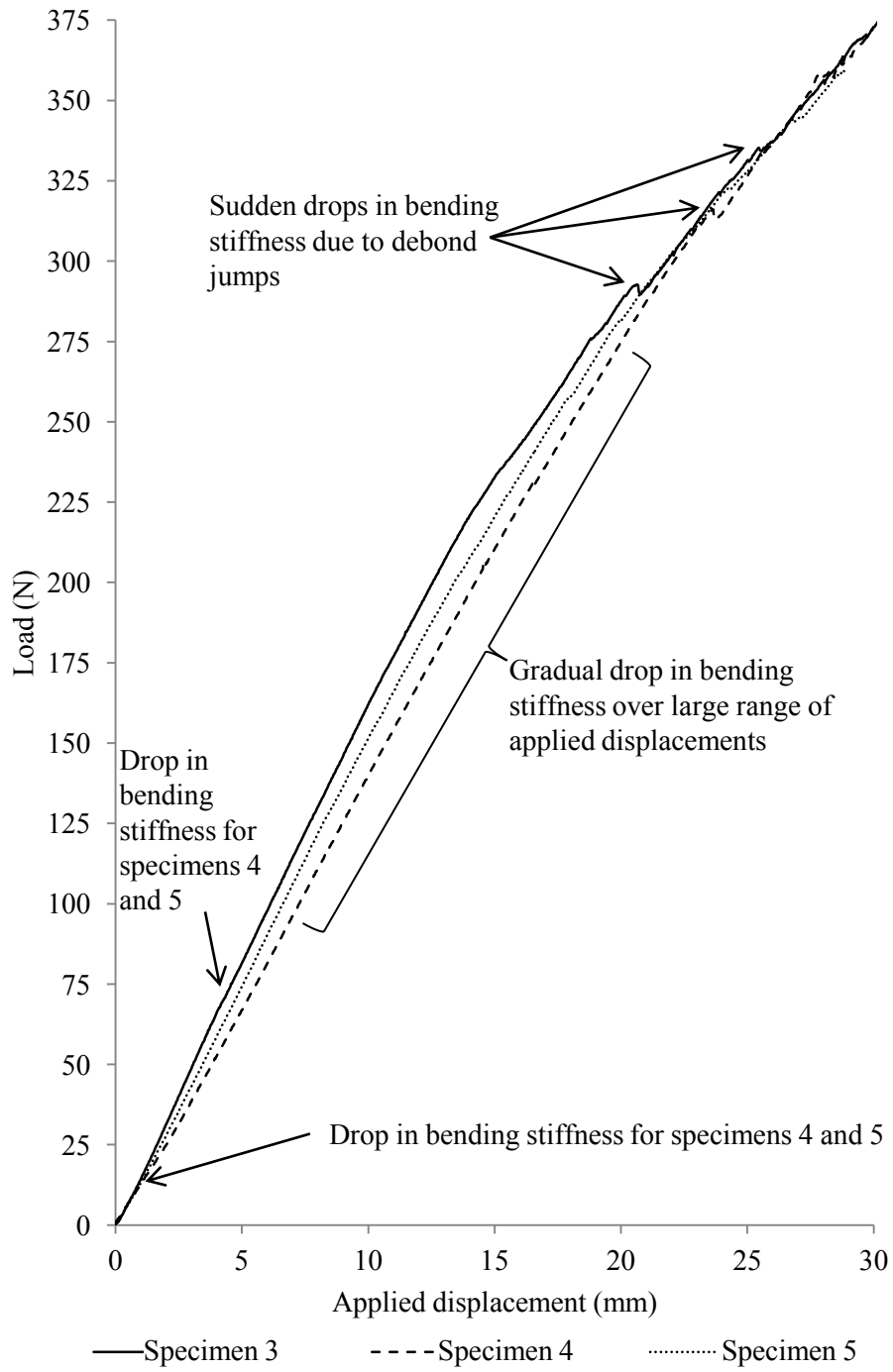
Figure 3.16.: Load-displacement curves for specimens 3-5.

Table 3.5.: Summary of displacements at which debonding at each runout as recorded on by high resolution photographs.

Specimen	Long stiffener	Short stiffener
1	11.3-11.9 mm	18.3-20.6 mm
2	3.1-4.0 mm	No debond visible
3	4.4-5.2 mm	16.7-17.9 mm
4	1.0-1.7 mm	8.3-8.8 mm
5	3.1-4.0 mm	20.4-21.5 mm

applied displacements at which debonding occurs visibly as recorded by the high resolution photographs.

3.7.4. Visually determined crack length

The high resolution photographs were used to determine the propagation of the crack as the specimen was loaded. For each photograph, the crack length was measured at each runout, and the loading point displacement was measured. For each measured length, a reference length in the same plane parallel to the camera lens was also recorded (see Figure 3.22). This was to allow the crack lengths and displacements measured in the photograph to be scaled. Crack lengths could then be plotted against applied displacement (Figure 3.23).

3.7.5. Stiffener cross sections

Primarily to investigate the quality of the filler region, selected stiffeners were debonded from the specimens after testing by clamping the web in a vice and peeling it away from the plate. A cut was then made through the cross section. An example is shown in Figure 3.24. The photograph shows a section through a longer, thicker stiffener. The short, thin stiffeners did not remain attached to the filler material upon removal from the pannel. The short stiffener fillers lost more resin during curing than the long ones leaving the the fibres more exposed. A cross section was not taken as the filler region did not remain intact.

3.8. Discussion

The components of the specimens manufactured by hand layup were acceptable. C-scan investigations showed no internal defects and the technique used was determined to be appropriate. The filler regions in the short stiffeners were found to have lost a significant amount of resin during curing. The filler in the long stiffeners (with a thicker layup and hence a larger filler region) did not lose as much resin. Since the same amount of material

Specimen 1: No debond

Specimen 1: Long stiffener debonded

Specimen 1: Both stiffeners debonded
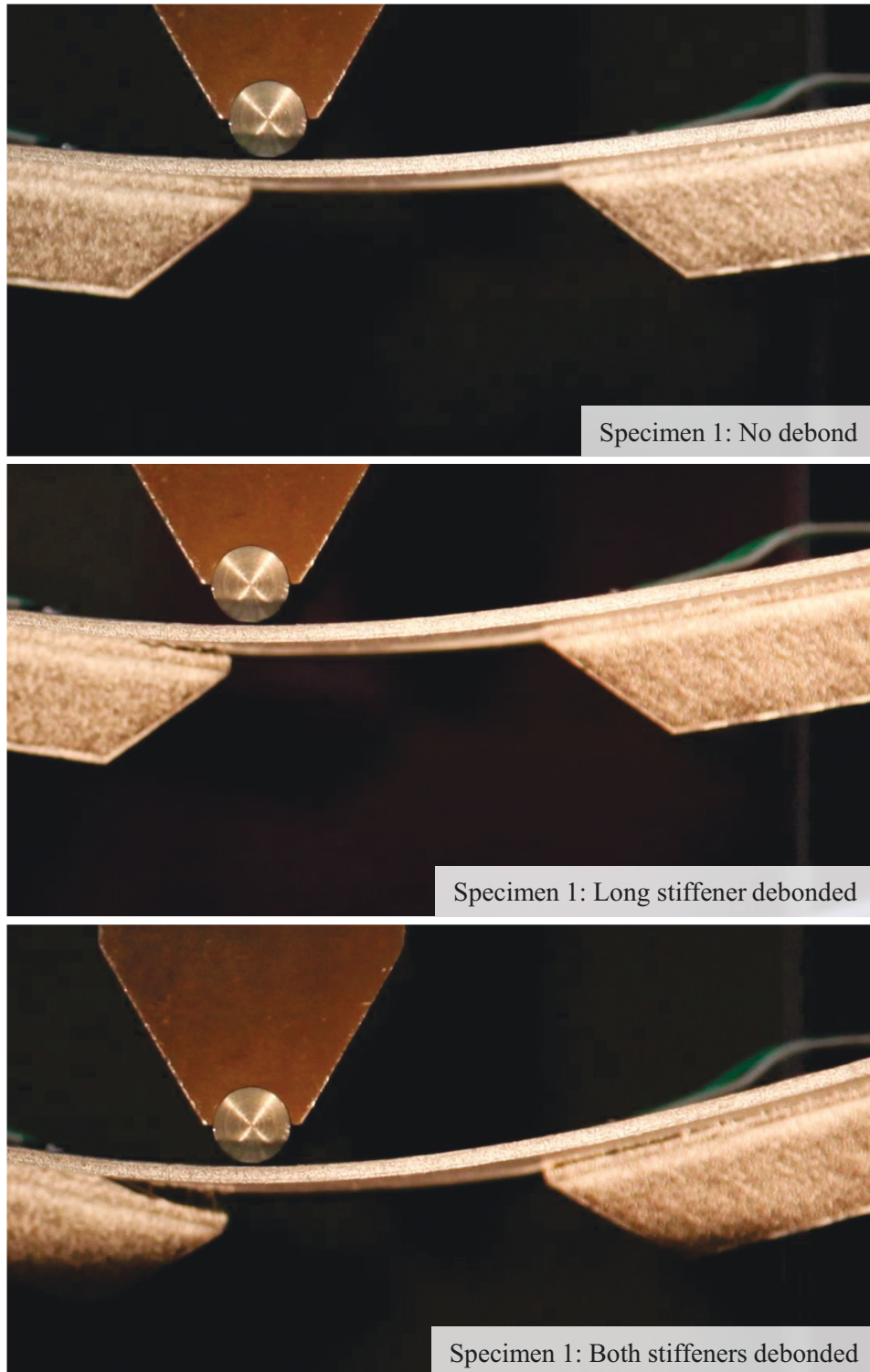
Figure 3.17.: Photographs of specimen 1 under testing. Earlier photographs towards the top of the figure, long stiffener on the left, short on the right.

Specimen 2: No debond

Specimen 2: Long stiffener debonded

Specimen 2: End of loading, short stiffener not debonded
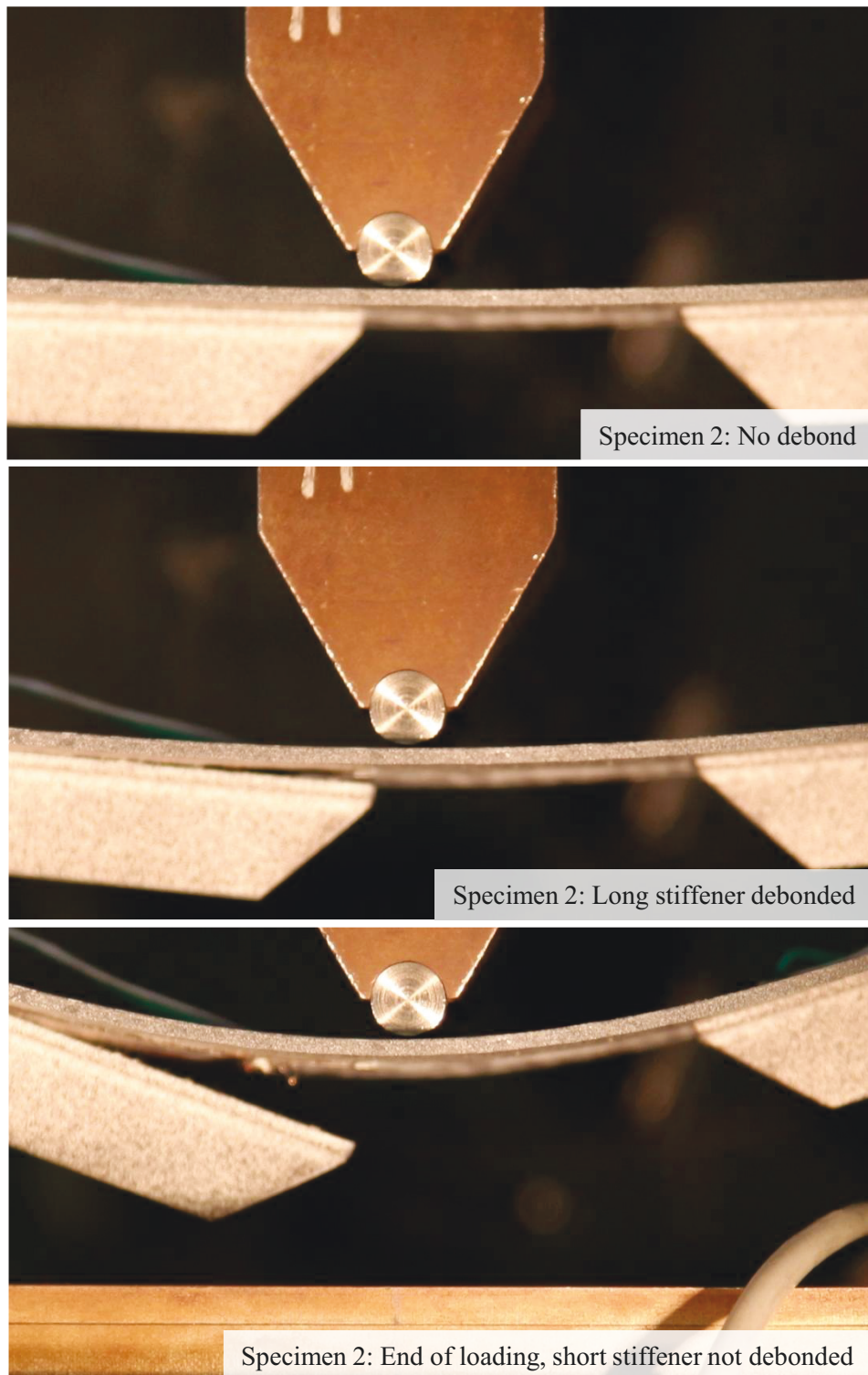
Figure 3.18.: Photographs of specimen 2 under testing. Earlier photographs towards the top of the figure, long stiffener on the left, short on the right.

Specimen 3: No debond

Specimen 3: Long stiffener debonded

Specimen 3: Both stiffeners debonded
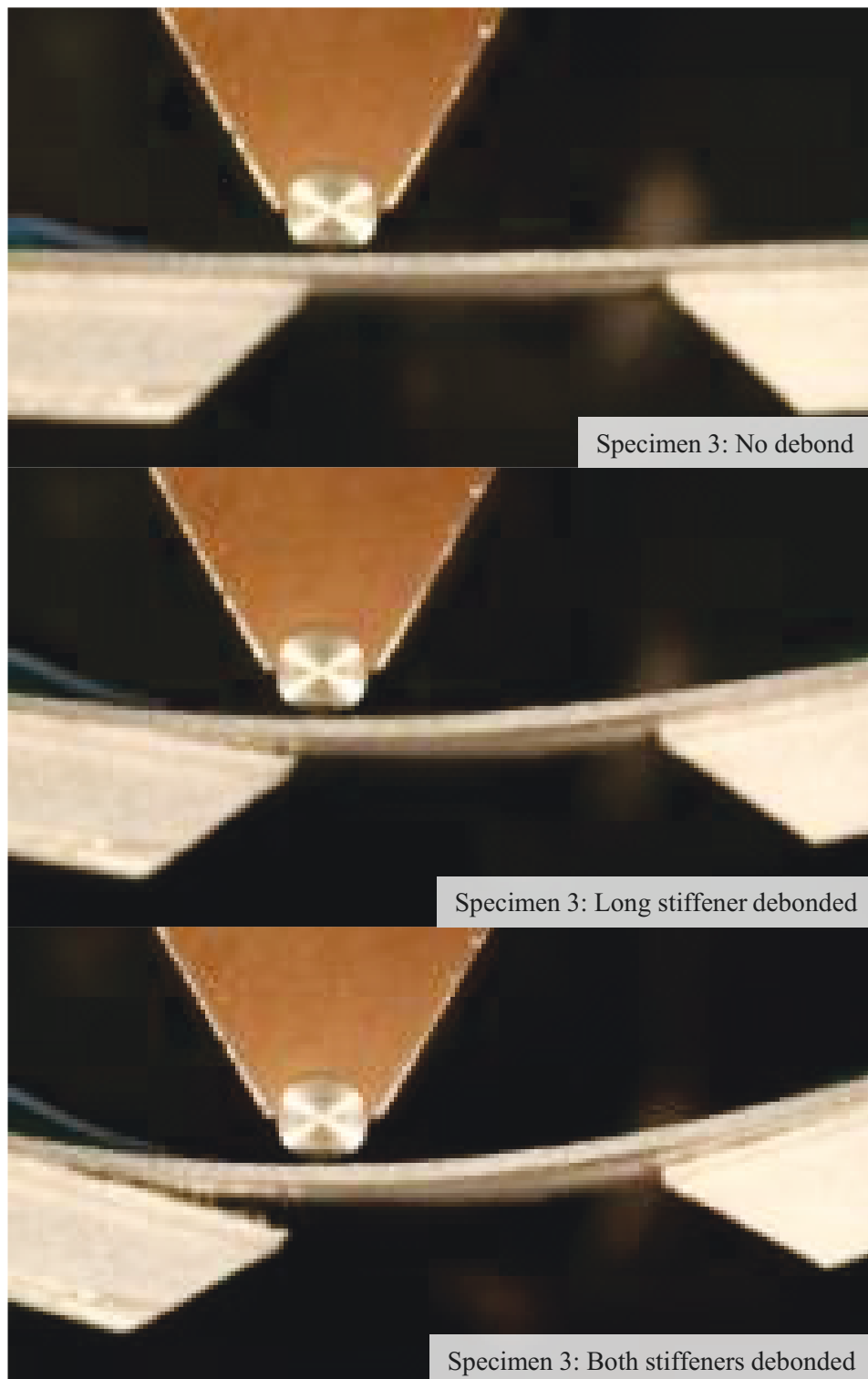
Figure 3.19.: Photographs of specimen 3 under testing. Earlier photographs towards the top of the figure, long stiffener on the left, short on the right.

Specimen 4: No debond

Specimen 4: Long stiffener debonded

Specimen 4: Both stiffeners debonded
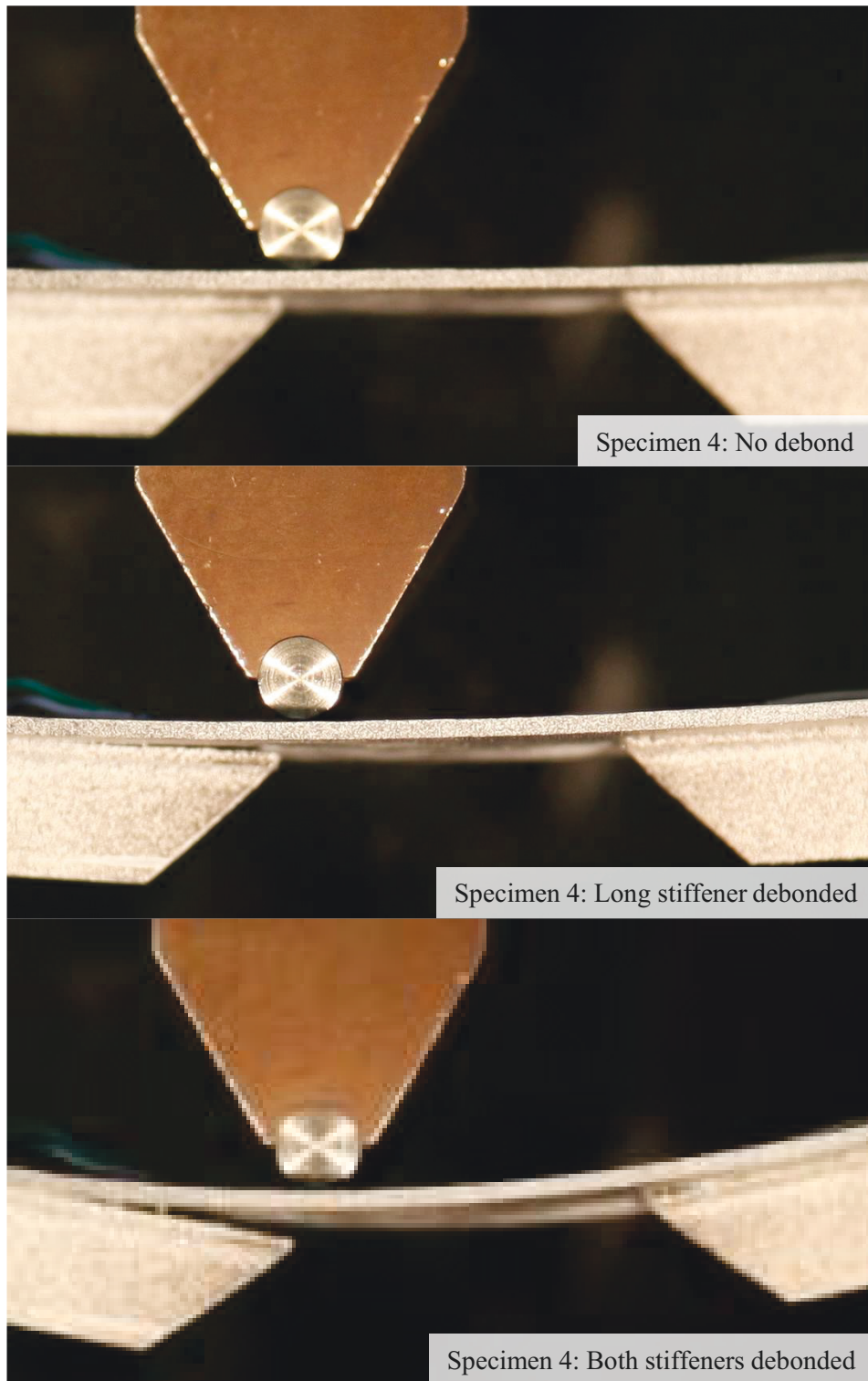
Figure 3.20.: Photographs of specimen 4 under testing. Earlier photographs towards the top of the figure, long stiffener on the left, short on the right.

Specimen 5: No debond

Specimen 5: Long stiffener debonded

Specimen 5: Both stiffeners debonded
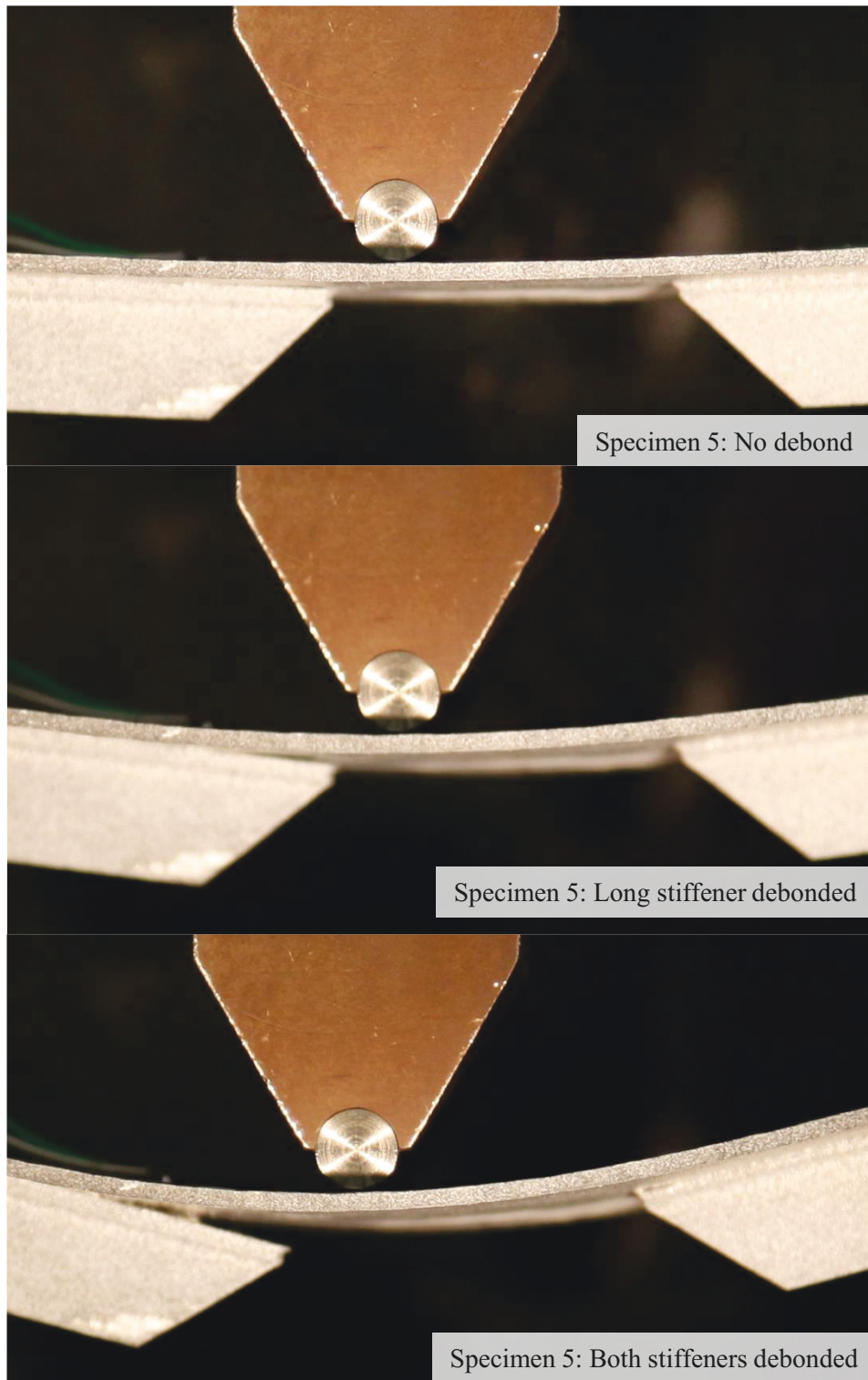
Figure 3.21.: Photographs of specimen 5 under testing. Earlier photographs towards the top of the figure, long stiffener on the left, short on the right.
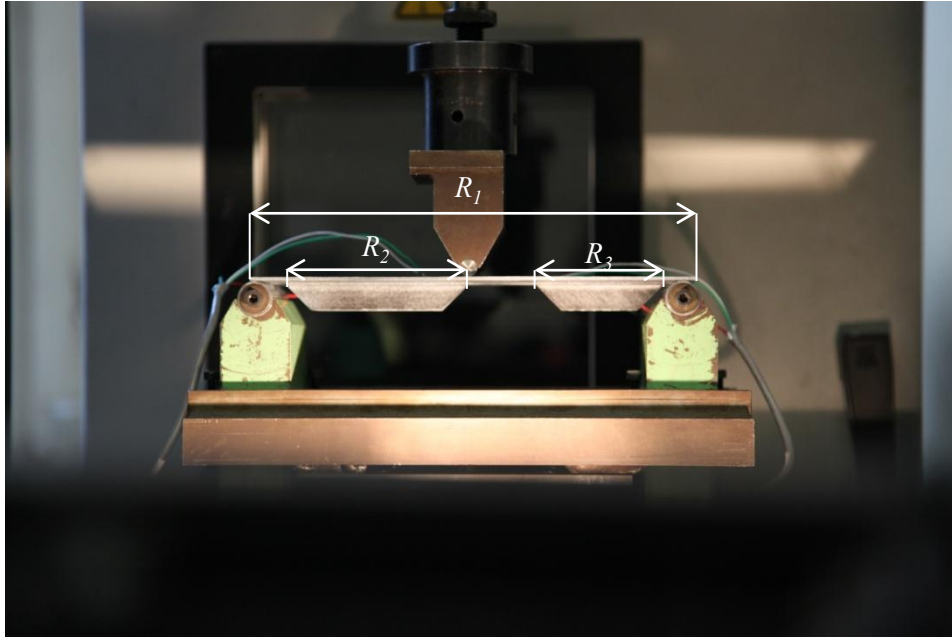
Figure 3.22.: Reference dimensions measured from photographs. R_1 =240 mm, R_2 =100 mm, R_3 =70 mm

per mm of filler was used for both long and short stiffeners, using less for the short stiffeners may improve the manufacturing process.

The defects in the bond summarised in Figure 3.10 were significant compared to the size of the bond. These defects were possibly due to the very low thickness (13 μm) of the film adhesive and the abundance of routes through which the adhesive could be lost during curing. These routes include the edges of the bond and the boundary between stiffener L-sections and the filler. The small size of the stiffeners makes these routes of leakage more significant compared to the bonding area. Using a larger specimen, and developing a smeared defect model or scaling the material properties used in analysis appropriately could help eliminate the effects of these defects when comparing experimental to numerical data. However the specimens used were already at the upper limit of the length and width imposed by the test rig.

In Figure 3.14, the plots of bending measure against applied load are significantly different for specimen 1 (Figure 3.14a) than for the others. While for specimen 1 the initial gradient of bending measure against displacement, $\frac{\partial \varepsilon_b}{\partial u}$, was highest for the location close to the long stiffener for the other specimens $\frac{\partial \varepsilon_b}{\partial u}$ was initially highest near the long stiffener. The strain gauges recording ε_b for the long stiffener runout were closer to the centre of the plate and the loading point than those recording ε_b at the short runout. Hence the bending moment for the section of the plate at the long stiffener location was higher. However the long stiffener was thicker than the short and so had a greater bending stiffness, so for specimen 1, which had the best quality of bond, the bending measure is initially highest
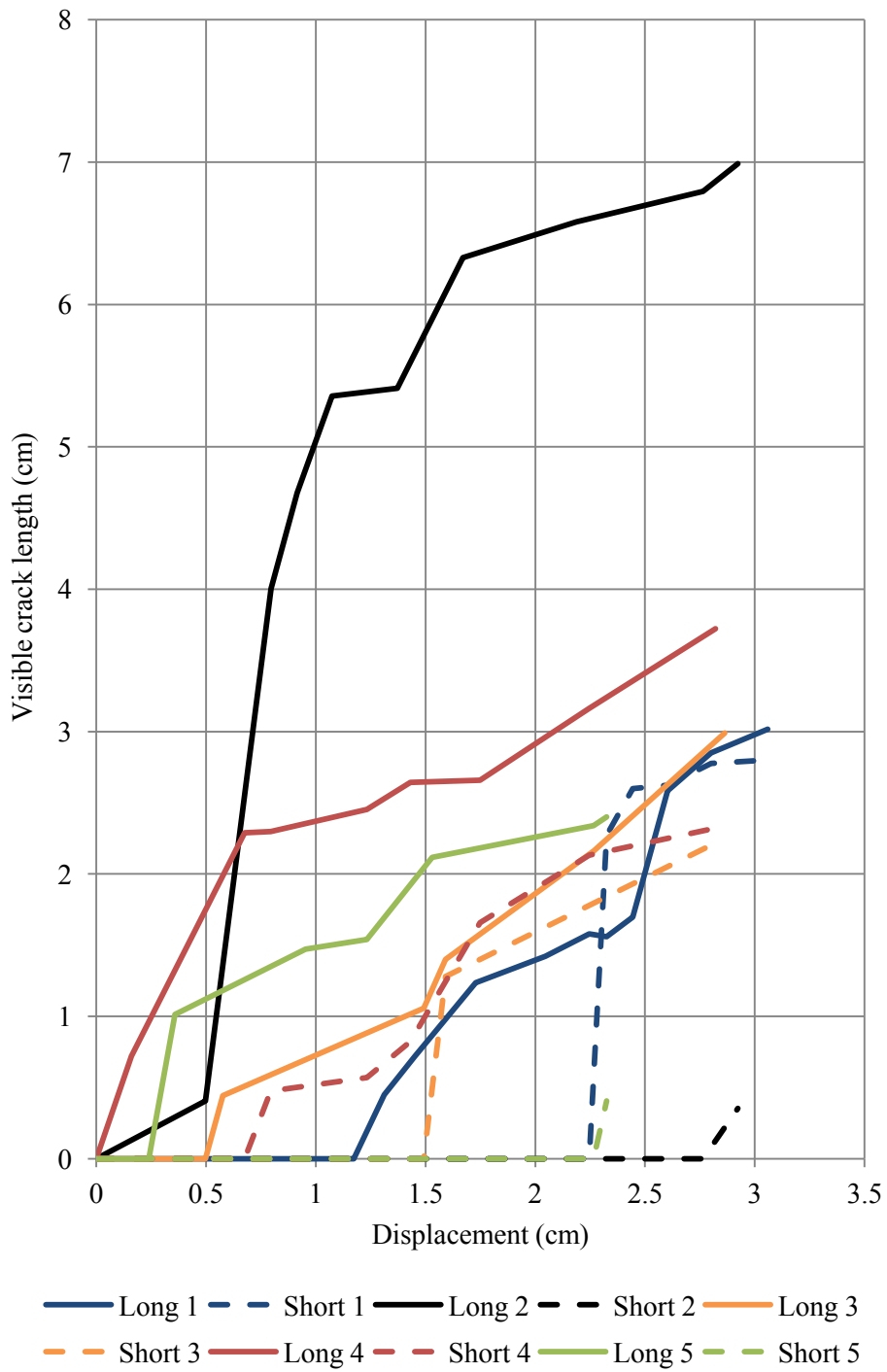
Figure 3.23.: Visible crack length against displacement measured from the photographs.

Figure 3.24.: A cross section through a long stiffener after testing appears to show a filler region with no voids or defects at the junction with the stiffener.

for the short stiffener location. In all other cases where the bond was of lower quality the long stiffener was not able to contribute as much bending stiffness to the plate and so the fact that the bending moment was higher at the long stiffener runout dominated and the bending measure recorded here was higher. In the case of specimen 1, once the long stiffener began to debond, the bending measure at this location increased beyond that at the short stiffener.

In Figure 3.16, load displacement curves for specimens 3, 4 and 5 are shown. Initially all three curves have the same gradient, up to the point marked on the graph where the gradients of the curves for specimens 4 and 5 begin to decrease. This is due to the onset of debonding at the long stiffener resulting in a loss of bending stiffness. The bending stiffness at the long stiffener runout does not begin to decrease until a displacement of approximately 4 mm, corresponding to the later onset of debonding in this specimen observed visually.

From a displacement of 4 mm until approximately 20 mm, the gradient of each specimen's curve continues to decrease gradually, corresponding to stable growth of the debonds and resulting in a gradual decrease in bending stiffness. Throughout this range of displacements, the load applied to specimen 3 remains higher than the load applied to the other two specimens, implying specimen 3 has the highest bending stiffness. This is corroborated by the visual observations summarised in Figure 3.23, which shows that the long stiffener

Table 3.6.: Summary of debonding implied by bending measure.

Panel	Long stiffener	Short stiffener
1	8.7-9.3 mm	17.8-18.2 mm
2	4.0 mm	25.8-26.1 mm
3	4.0 mm	13.5-15.5 mm
5	1.8 mm	15.5-16.0 mm

of specimen 3 exhibited a consistently shorter debond than that of specimens 4 and 5, although this debond in specimen 3 began to grow more rapidly beyond 15 mm applied displacement. This was accompanied by the onset of debonding in the short stiffener of specimen 3, which resulted in the gradient of the load-displacement curve beginning to decrease more rapidly and for the curve to converge with those of specimens 4 and 5.

Beyond a displacement of 20 mm, sudden drops in the load-displacement curves in Figure 3.16 can be seen. These are marked on the graph and correspond to sudden jumps in debonds at either stiffener. Due to the dynamic nature of crack jumps, it was not possible to record the displacement at which a crack jump occurred in a particular bond visually.

Table 3.6 contains a summary of the displacement at which debonding was determined to initiate at each runout based on bending measure. In each case the long stiffener was found to begin to debond before the short one, qualitatively matching the predictions given in Section 3.3.

The models used in the numerical design process predicted that debonding of the long stiffener and short stiffener would initiate at an applied displacement of 9mm and 18mm respectively. Comparison of these values to those observed in the tests (summarised in Table 3.6) shows the predicted debonding of the first stiffener was within the experimental range. The experimentally observed debonding of the second stiffener was later than predicted. This could be accounted for by the manufacturing defects in the long stiffener causing more extensive propagation of the debond, delaying the onset of debonding in the short stiffener.

Given that the failure sequence of the specimens matches that of the numerical design models, and that the failure of the short stiffener bond appears to be affected by that of the long stiffener these results will be useful in the validation of the coupled approach presented in Chapter 4.

3.9. Conclusions

The results of these tests have 2 clear uses:

1. To demonstrate the use of screening techniques used to assess the vulnerability of joints to damage, and to determine the order of failure under given boundary conditions.

2. To demonstrate the use of multiscale approaches in structural modelling.

The following useful data have been obtained and may be compared to numerical simulations:

1. Displacement values at which debonding occurs

2. Bending measures

3. Load-displacement curves.

The complexity of the specimens and their small physical size meant that defects were significant. As a result, the variability between specimens was high. This however provided a broader spectrum of experimental data against which screening and multiscale modelling techniques may be compared, incorporating initial defects.

4. Coupling local solid meshes with global solid meshes

4.1. Introduction

The method discussed in this chapter has been implemented in a series of Python scripts, used to modify models and drive Abaqus analyses. For reference the top level python script used to call the main modules in the implemented coupling technique is included in Appendix B. It is intended to provide an overview of the interfaces with commercially available software and the main steps in the coupling process. A flowchart outlining the coupling process discussed in the remainder of this chapter and Chapter 6 is shown in Figure 4.1. It shows the flow of data between global and local analyses and also where modifications to global and local models are necessary.

This section describes the coupling method for coarse and refined solid models which has been developed. Before considering the mathematics and implementation of the method the requirements and challenges are discussed.

Since the method is designed to couple the analysis of different pre-existing models, the case where all meshes have been constructed in the same coordinate system is a rare one. A means of transforming all models into the same coordinate system is therefore required.

As the main purpose of the method is to couple models with inconsistent mesh refinement at their interfaces, there must be an acceptable technique to relate displacements at the interface in the coarser mesh with displacements at the interface on the more refined one. This obviously implies that a displacement at a degree of freedom in the coarser mesh is related to the displacements at many degrees of freedom in the more refined meshes. Note that it is not adequate to simply select the nearest degree of freedom on the local interface and make it equivalent to one at the global interface. To understand why this is the case, consider Figure 4.2 which shows the deformation of a cube with a displacement applied at a corner where the cube's mesh has a varying refinement. The additional degrees of freedom on the more refined cubes allow the top face to assume a more concave shape, and thus the strain energy is lower. As a result the force required to displace the corner node is lower. The length of the arrows in Figure 4.2 are proportional to the force magnitude (also given numerically).

The coupling procedure also requires a means of matching each boundary node in the local model to a subset of the boundary nodes in the global model (i.e. the nodes of one global element face). An algorithm has been implemented to perform this matching.
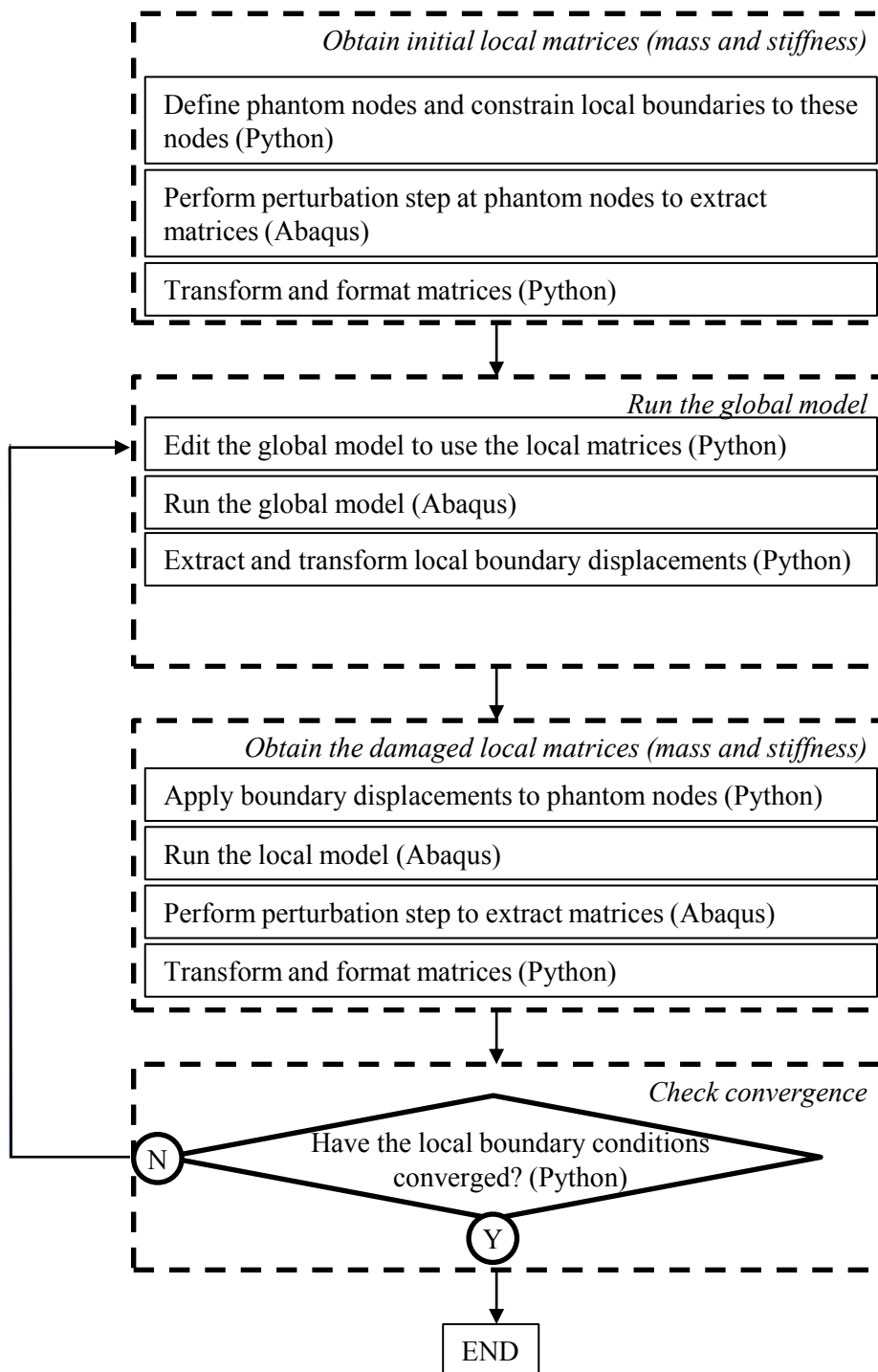
Figure 4.1.: An outline of the coupling processes developed in this work. Scripted components are labelled (Python) and Finite Element components are labelled (Abaqus).
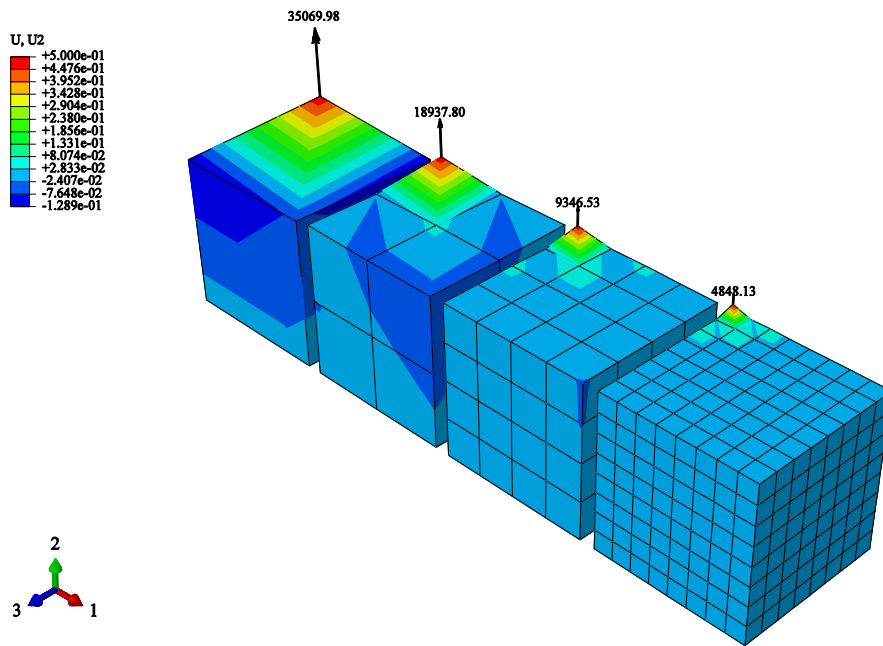
Figure 4.2.: Contour plots of displacement in the 2 direction for identical cubes with meshes of varying refinement with a unit upwards load applied at one corner. The cubes are fixed at the bottom faces. Reaction forces in the 2 direction at the displaced nodes are plotted numerically. The reaction force decreases as the refinement increases, as the cube is less confined.

The matching is achieved using basic geometric principles and so it is not discussed here. Details are provided in Appendix C.

4.2. An example of coupled models

Consider the test specimen shown in Figure 4.3. This is a small scale version of a stiffened skin panel, which is commonly used in the aerospace industry. Its construction is described in Chapter 3. As discussed in Section 3.7, when loaded under three point bending the behaviour of the specimen may be broadly distributed into two categories. The bulk of the specimen behaves in an elastic manner, and because the laminate may be homogenised using laminate theory, these parts of the panel may be represented by a coarse mesh built of single layers of shell or continuum shell elements. However, debonding takes place at the runouts. This means that in plane refinement is required to model damage initiation and propagation. Furthermore, the stresses in the plies joined at the bondline are important in debonding so a ply by ply modelling strategy is needed. These differing mesh requirements make this an good example to illustrate the coupled approach described in this chapter.

Consider the set of models shown in Figure 4.3. These represent the bulk of a stiffened laminate panel using a coarse mesh and homogenised material properties. Two vulnerable regions at the runouts are modelled at a more refined level, including adhesive debonding

and ply-by-ply material definition. The two levels of model, referred to as global and local levels from now on, are defined separately. Each region of the global domain corresponding to a local model is meshed with a superelement. The behaviour of the latter is governed by linear stiffness and mass matrices. The remainder of this section will focus on the necessary features of the local models, such that they provide appropriate matrices for the superelements.

Consider the boundaries, Γ formed when the local region elements are removed from the global model, and replaced with superelements (Figure 4.3). The compatibility of the superelement matrices with the global and local models is ensured by:

1. Enforcing compatibility of displacements over the global boundary between standard elements and superelements, and on the boundary of the local model.

2. Iterating between global and local solutions until convergence so that the energy required to deform the superelement is equal to the energy to deform the local model, such that for a given iteration:

$$\sum_{i=1}^{M} \mathbf{F}_g^i \mathbf{u}_g^i = \sum_{j=1}^{N} \mathbf{F}_l^j \mathbf{u}_l^j \tag{4.1}$$

$\mathbf{F}_g^i$ is the force acting on the ith superelement node due to stresses in adjacent elements. $\mathbf{F}_l^j$ is the reaction force on the jth boundary node of the local model where a displacement is enforced. $\mathbf{u}_g^i$ is the displacement of the ith superelement node and $\mathbf{u}_l^j$ is the boundary condition enforced at the jth local boundary node. M and N are the number of superelement and local boundary nodes respectively.

4.3. Transformation of vectors into a single coordinate system

Since the global and local coordinate systems are defined separately they may not be aligned. The first step in the coupling process must be to transform the global and local models into the same coordinate system. This will allow the local boundary nodes to be matched with the correct point on the global boundary, Γ.

A coordinate system is defined relative to the part being modelled using 3 points. These points are an origin, a point on the x-axis and a point in the xy plane. For each of the 3 points, 2 sets of coordinates are required by the coupling routine. One set in the global coordinate system, and one in the local coordinate system. This allows unit vectors for each coordinate axis to be expressed in terms of the global ($\hat{\mathbf{x}}_g$, $\hat{\mathbf{y}}_g$, $\hat{\mathbf{z}}_g$) and local coordinate systems ($\hat{\mathbf{x}}_l$, $\hat{\mathbf{y}}_l$, $\hat{\mathbf{z}}_l$).

Noting that the angle θ between two unit vectors $\mathbf{a}$ and $\mathbf{b}$ is related to the unit vectors by:

$$\mathbf{a} \cdot \mathbf{b} = cos\theta \tag{4.2}$$

Most of the domain represented by the coarse "structural model"

Γ

Vulnerable component regions represented by "user defined elements"

Γ
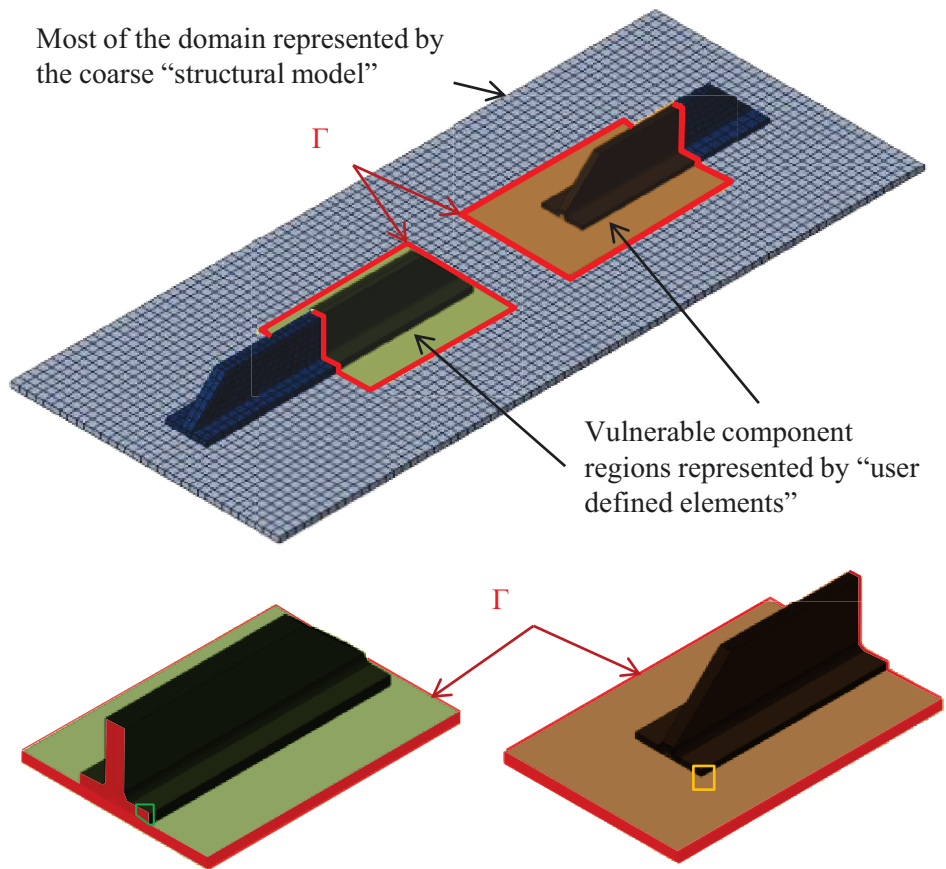
Increased mesh refinement in component models
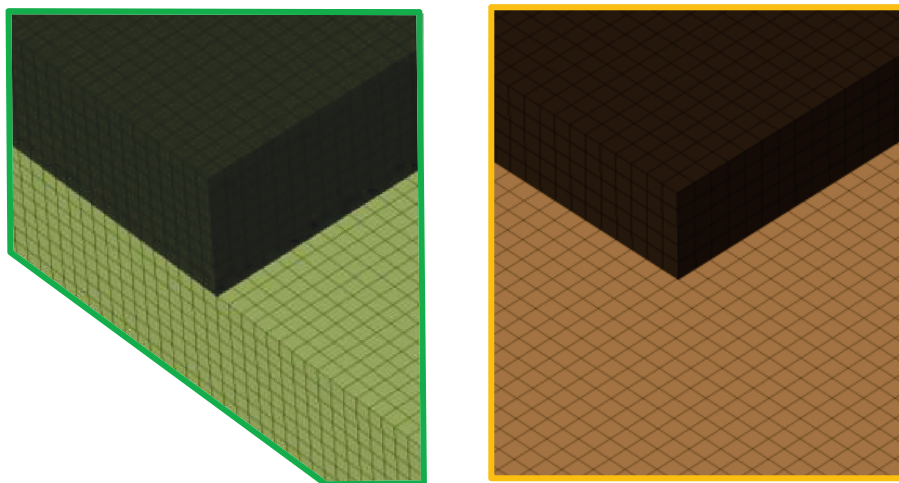
Figure 4.3.: Division of the domain into global and local level regions. Local regions are modelled with a higher mesh refinement. They are represented in the global models using "superelements".

It can be seen that a vector in the local coordinate system, $\mathbf{u}_l$, may be transformed into the global coordinate system as $\mathbf{u}_g$:

$$
\left\{
\begin{array}{c}
u_g \\
v_g \\
w_g
\end{array}
\right\}
=
\left[
\begin{array}{ccc}
\hat{\mathbf{x}}_l \cdot \hat{\mathbf{x}}_g & \hat{\mathbf{y}}_l \cdot \hat{\mathbf{x}}_g & \hat{\mathbf{z}}_l \cdot \hat{\mathbf{x}}_g \\
\hat{\mathbf{x}}_l \cdot \hat{\mathbf{y}}_g & \hat{\mathbf{y}}_l \cdot \hat{\mathbf{y}}_g & \hat{\mathbf{z}}_l \cdot \hat{\mathbf{y}}_g \\
\hat{\mathbf{x}}_l \cdot \hat{\mathbf{z}}_g & \hat{\mathbf{y}}_l \cdot \hat{\mathbf{z}}_g & \hat{\mathbf{z}}_l \cdot \hat{\mathbf{z}}_g
\end{array}
\right]
\left\{
\begin{array}{c}
u_l \\
v_l \\
w_l
\end{array}
\right\}
= \mathbf{T} \mathbf{u}_l
\tag{4.3}
$$

Note that the transformation matrix, $\mathbf{T}$ has the following properties:

$$
\mathbf{T} = \mathbf{T}^T = \mathbf{T}^{-1}
\tag{4.4}
$$

4.4. Shape of the deformed boundary

At the global level, the displacement at all points on the boundary Γ is defined by the nodal displacements on Γ. At intermediate points the displacements are calculated in terms of the Finite Element shape functions, determined in the element's natural coordinate system (Figure 4.4 a)), and the element nodal displacements. Because all points on the boundary also lie on one face of an element, one of the natural coordinates on this surface has a constant value, thus the number of shape functions required to define the displacement is reduced from 8 to 4 in an 8 node hexahedral element (Figure 4.4 b)).

Where the displacement at point P is $\mathbf{u}_P$, and the nodal displacements at node i are $\mathbf{u}_i$ (with $i = 1, 2, 3, 4$), the shape functions at point P based on the nodal displacement at node n, $\mathbf{N}_P^i$, may be written in matrix form as

$$
\mathbf{u}_P =
\left[
\begin{array}{cccc}
\mathbf{N}_P^1 & \mathbf{N}_P^2 & \mathbf{N}_P^3 & \mathbf{N}_P^4
\end{array}
\right]
\left\{
\begin{array}{c}
\mathbf{u}_1 \\
\mathbf{u}_2 \\
\mathbf{u}_3 \\
\mathbf{u}_4
\end{array}
\right\}
\tag{4.5}
$$

where

$$
\mathbf{N}_P^i =
\left[
\begin{array}{ccc}
N_P^i & 0 & 0 \\
0 & N_P^i & 0 \\
0 & 0 & N_P^i
\end{array}
\right]
\tag{4.6}
$$

Eq. 4.5 defines the shape of a patch of the boundary Γ on the local model, equivalent to a standard element face in the global model. In order to define the displacement at any point on Γ, the shape function at point P must be rewritten

$$
\tilde{\mathbf{N}}_P =
\left[
\begin{array}{cccccccccc}
N_P^1 & 0 & 0 & \cdots & N_P^i & 0 & 0 & \cdots & N_P^n & 0 & 0 \\
0 & N_P^1 & 0 & \cdots & 0 & N_P^i & 0 & \cdots & 0 & N_P^n & 0 \\
0 & 0 & N_P^1 & \cdots & 0 & 0 & N_P^i & \cdots & 0 & 0 & N_P^n
\end{array}
\right]
\tag{4.7}
$$

Where i now includes all nodes of the local model on the boundary Γ. If the nodes on the
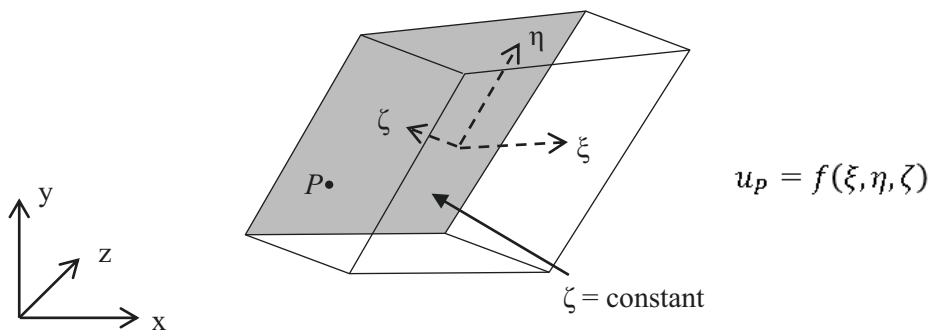
(a) 3D element
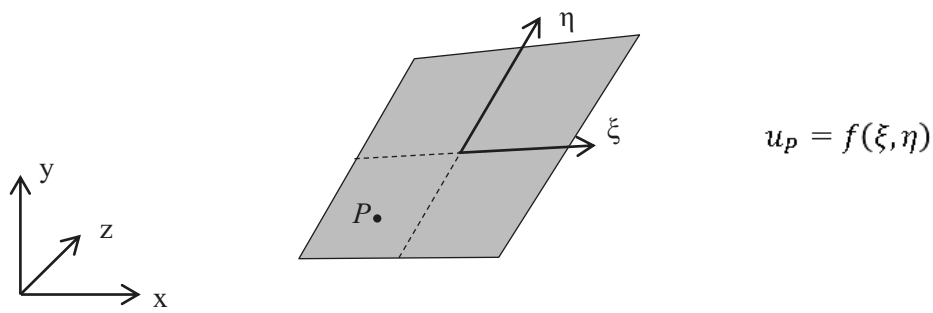
(b) 2D element face

Figure 4.4.: The natural coordinates in a 3D element and a 2D face of an element.

element face containing the point P are A,

$$
N_P^i = \begin{cases} N_P^i & i \in A \\ 0 & otherwise \end{cases}
\tag{4.8}
$$

The displacement of any point P on the boundary Γ may now be written

$$
\mathbf{u}_P = \tilde{\mathbf{N}}_P \mathbf{u}_\Gamma
\tag{4.9}
$$

where $\mathbf{u}_\Gamma$ are the displacement vectors at all nodes on Γ.

Given the deformed shape of the boundary, Γ, in terms of the global nodal displacements, boundary conditions for the local models may be determined from the nodal displacements in the global solution. It remains to generate stiffness and mass matrices for the superelements using the relevant local models.

Note that the displacement at each local node is calculated in terms of its natural coordinates on the global element face. Natural coordinates for a 4 node quadrilateral may be calculated exactly from the nodal coordinates and those of the point of interest, as described in [76]. As there are only 4 nodes on the element face, there are only 2 natural coordinates to be determined while there are 3 coordinates in 3D space. This problem is circumvented using the assumption that the global and local boundaries are perfectly coincident. If this is true then the same two natural coordinates would be calculated no matter which two coordinate directions were used to determine the natural coordinates. Thus neglecting one coordinate direction would not introduce an error. For the purposes of this work, the direction selected to be neglected is the one in which there is the least variation over the global element face.

4.5. Forces on the component boundary

Consider the work done in deforming the superelement, W_n, by forces $\mathbf{F}_n$ at the superelement nodes due to stresses in the adjacent global elements (Figure 4.5). The resulting displacements of the superelement nodes are $\mathbf{u}_n$;

$$
W_n = \frac{1}{2} \mathbf{u}_n^t \mathbf{F}_n
\tag{4.10}
$$

Or, expanding the displacement and force vectors with zeros for the rest of the superelement degrees of freedom;

$$
W_n = \frac{1}{2} \mathbf{u}_\Gamma^t \mathbf{F}_\Gamma
\tag{4.11}
$$

At a single local boundary node, also within the area of the same global element, the work done, W_P, by a force $\mathbf{F}_P$ at this node, causing a displacement $\mathbf{u}_P$ is;

$$
W_p = \frac{1}{2} \mathbf{u}_P^t \mathbf{F}_P
\tag{4.12}
$$

But the displacement $\mathbf{u}_P$ has already been defined in terms of $\mathbf{u}_n$ in Eq. 4.5, and hence,

$$W_P = \frac{1}{2}\mathbf{u}_n^t \mathbf{N}_P^t \mathbf{F}_P \tag{4.13}$$

Which, is equivalent to writing

$$W_P = \frac{1}{2}\mathbf{u}_\Gamma^t \tilde{\mathbf{N}}_P^t \mathbf{F}_P \tag{4.14}$$

following the same arguments as Eqs. 4.5-4.9. The force at the local boundary node P should be redistributed to the surrounding superelement nodes in such a way that the redistributed forces do an equal amount of work to the original force, i.e.

$$W_n = \frac{1}{2}\mathbf{u}_\Gamma^t \mathbf{F}_\Gamma = \frac{1}{2}\mathbf{u}_\Gamma^t \tilde{\mathbf{N}}_P^t \mathbf{F}_P = W_P \tag{4.15}$$

So the correct redistribution of forces to superelement nodes must satisfy

$$\mathbf{F}_\Gamma = \tilde{\mathbf{N}}_P^t \mathbf{F}_P \tag{4.16}$$

4.6. The superelement stiffness matrix

The role of the stiffness matrix is to define the change in force exerted on each superelement node, corresponding to a change in displacement at each degree of freedom of these nodes. Let the stiffness matrix of the superelement be $\mathbf{K}_{SE}$.

$$\mathbf{K}_{SE}\mathbf{u}_{SE} = \mathbf{F}_{SE} \tag{4.17}$$

where $\mathbf{u}_{SE}$ and $\mathbf{F}_{SE}$ are the nodal displacements and forces on the superelement at its nodes. Let $\mathbf{k}_{SE}^i$ be the ith column of $\mathbf{K}_{SE}$.

One column of $\mathbf{k}_{SE}^i$ is equal to the change in forces experienced at all degrees of freedom in the superelement, $\delta\mathbf{F}^i$, when a unit displacement is applied to degree of freedom i;

$$\delta\mathbf{F}^i = \mathbf{k}_{SE}^i = \mathbf{K}_{SE}\delta\mathbf{u}^i \tag{4.18}$$

where

$$\delta\mathbf{u}^i = \left\{ \begin{array}{c} u_1 \\ \vdots \\ u_j \\ \vdots \\ u_n \end{array} \right\} \tag{4.19}$$

if

$$u_j = \left\{ \begin{array}{l} 1, \ j = i \\ 0, \ j \neq i \end{array} \right. \tag{4.20}$$

In what shall be referred to as a "perturbation step" from now on, for a small dis-
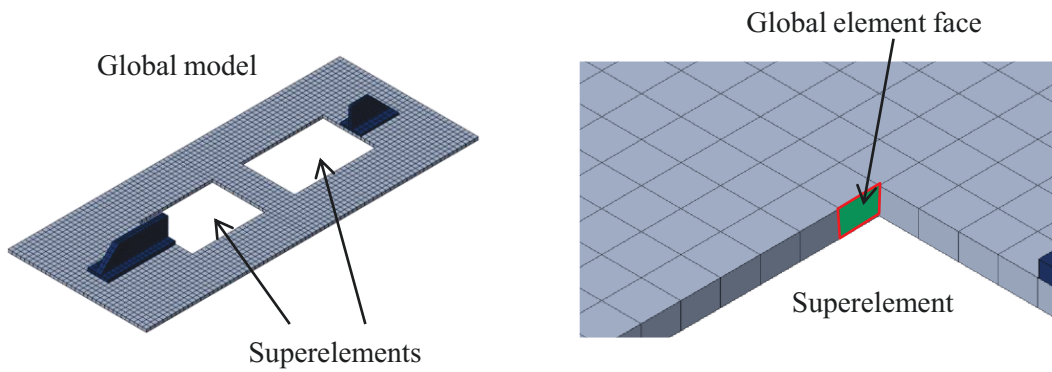
(a) The global model

(b) Zoomed view of an element face at the global boundary. A global element face is highlighted.

Global superelement node projected onto local boundary
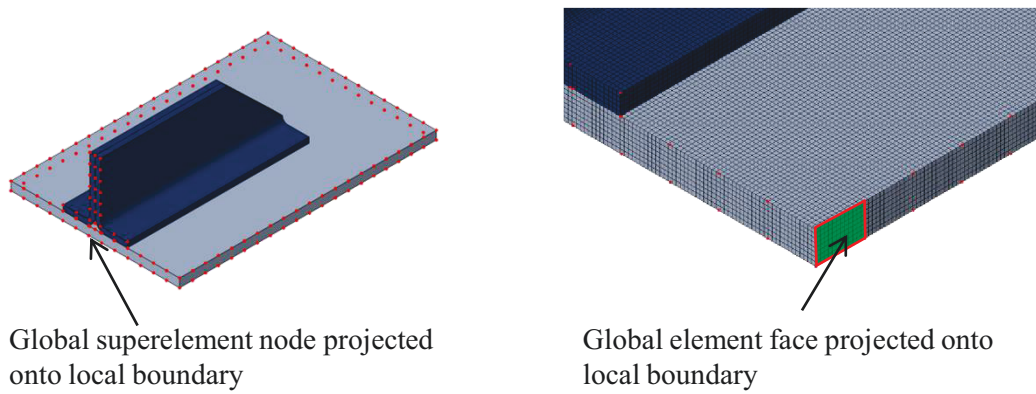
(c) A local model with global superelement nodes projected onto the boundary.

Global element face projected onto local boundary

(d) Zoomed view of a global element face projected onto a global model boundary.

Figure 4.5.: Projection of global model element faces and nodes onto the local model boundary

placement at each superelement degree of freedom, the corresponding displacements (i.e. the local boundary displacements for which the local boundary shape matches the global boundary shape) may be applied to the local boundary nodes. These are calculated according to Eq. 4.9. When applied, the nodal reaction forces to the displacements for the local boundary are calculated in the Finite Element Method. For each node on the local boundary, the resultant forces should be redistributed to a set of nodes equal to the number of superelement nodes using Eq. 4.16. These distributed forces will form a column of $\mathbf{K}_{SE}$. Application of the displacements via "virtual" nodes in the local model (one for each node on the global boundary). These "virtual" nodes are attached to the local boundary nodes using Transformation Method (TM) constraints which satisfy Eq. 4.9 perform the redistribution of forces required by Eq. 4.16. TM constraints are discussed in Appendix D.

4.7. Transformation of the superelement stiffness matrix

Since the perturbation step described in Section 4.6 is performed on the local model, the resulting matrix $\mathbf{K}_{SE}$ is defined in the local coordinate system. However, the superelements are part of the global model, and a coordinate transformation is required to put the matrix into its final form. As was seen in Section 4.3, a 3 dimensional vector may be transformed between two coordinate systems using a transformation matrix, $\mathbf{T}$. The same matrix may be used as follows to transform the matrix $\mathbf{K}_{SE}$ into the structural coordinate system.

In the local coordinate system, the displacements at the global degrees of freedom, $\mathbf{u}_{\Gamma l}$, are related to the reaction forces, $\mathbf{F}_{\Gamma l}$, by:

$$\mathbf{F}_{\Gamma l} = \mathbf{K}_{SE}\mathbf{u}_{\Gamma l} \tag{4.21}$$

The forces and displacements may also be expressed in the global coordinate system, and Eq. 4.21 may be written as:

$$\mathbf{T}^{-1}\mathbf{F}_{\Gamma g} = \mathbf{K}_{SE}\mathbf{T}^{-1}\mathbf{u}_{\Gamma g} \tag{4.22}$$

This means that, in the global coordinate system, the superelement behaviour must be defined by:

$$\mathbf{F}_{\Gamma g} = \mathbf{T}\mathbf{K}_{SE}\mathbf{T}^{-1}\mathbf{u}_{\Gamma g} = \mathbf{K}_{SEs}\mathbf{u}_{\Gamma g} \tag{4.23}$$

4.8. The superelement mass matrix

If a dynamic analysis of the global model is desired, then it is necessary to provide a mass matrix for the superelement. This may be approximated by assuming that the only forces acting on the local model are at the boundary degrees of freedom, and that the local model is static. Where Γ denotes "virtual" boundary degrees of freedom (as discussed in Section 4.6) and Ω represents all other degrees of freedom of the local model, the static

equilibrium equation may be written:

$$\left\{ \begin{array}{c} \mathbf{F}_\Gamma \\ \mathbf{F}_\Omega \end{array} \right\} = \left[\begin{array}{cc} \mathbf{K}_{\Gamma\Gamma} & \mathbf{K}_{\Gamma\Omega} \\ \mathbf{K}_{\Omega\Gamma} & \mathbf{K}_{\Omega\Omega} \end{array} \right] \left\{ \begin{array}{c} \mathbf{u}_\Gamma \\ \mathbf{u}_\Omega \end{array} \right\} \tag{4.24}$$

u_Ω may be eliminated:

$$\mathbf{u}_\Omega = -\mathbf{K}_{\Omega\Gamma}^{-1}\mathbf{K}_{\Omega\Omega}\mathbf{u}_\Gamma \tag{4.25}$$

This allows the acceleration of internal to be written in terms of the boundary accelerations:

$$\ddot{\mathbf{u}}_\Omega = -\mathbf{K}_{\Omega\Gamma}^{-1}\mathbf{K}_{\Omega\Omega}\ddot{\mathbf{u}}_\Gamma \tag{4.26}$$

The inertial forces at the boundary degrees of freedom are then:

$$\mathbf{F}_\Gamma^I = \mathbf{M}_\Gamma\ddot{\mathbf{u}}_\Gamma + \mathbf{M}_\Omega\mathbf{K}_{\Omega\Omega}^{-1}\mathbf{K}_{\Omega\Gamma}\ddot{\mathbf{u}}_\Gamma = \mathbf{M}_{SE}\ddot{\mathbf{u}}_\Gamma \tag{4.27}$$

where $\mathbf{M}_{SE}$ is the superelement mass matrix in the local coordinate system.

This matrix must undergo the same transformation operation described in Section 4.7 for the stiffness matrix, if it is to be used in the global model.

4.9. Convergence criterion

An iterative procedure is used to ensure the solution is converged. In the examples which follow, superelement nodal displacement is used as the convergence criterion. The maximum allowable percentage change in displacement at any given superelement degree of freedom, δ_{tol}, is 1%, and the solution is considered converged if the following criterion is met:

$$\max_j \left(\frac{abs\left(u_j^n - u_j^{n-1}\right)}{min\left(abs(u_j^n), abs(u_j^{n-1})\right)} \right) < \delta_{tol} \tag{4.28}$$

where superscripts denote the completed iteration number and j represents the degrees of freedom of the superelement.

5. Validation of method of coupling solid meshes

5.1. Numerical validation

5.1.1. Test cases

In order to evaluate how effective the approach described in Chapter 4 is in various applications, some test cases were designed. In some of these cases there was a known solution, such as a unidirectional plate loaded uniaxially. Other cases were more complex, and there was not an analytically calculable solution. For these cases, another approach was required to model the global-local problem, in order to provide some results for comparison. In this approach, the global and local models were reproduced exactly, including mesh and material properties and boundary conditions at the local scale. Instead of using the multiscale approach, however, the local region elements in the global model were removed, and the local mesh was fixed in their place using tie constraints.

The properties of the global and local meshes used for this validation are summarised in Figure 5.1. In order to evaluate the performance of the global-local approach in as wide a variety of applications as possible, and to highlight areas in which difficulties occur, a range of validation cases were run. They were designed to cover a range of boundary conditions, stress states, material and geometric nonlinearities and composite layups. The latter is of particular importance since the global mesh represents the laminate using homogenised properties and the local mesh considers each ply individually. It was therefore envisaged that the redistribution of stresses in the thickness direction at the boundary Γ could create difficulties.

For each case, boundary conditions were applied to the outer boundary of the global mesh. In the case where compression or tension was to be applied to the model, all boundary nodes had the appropriate direction of displacement applied to them, with a magnitude increasing linearly in the relevant coordinate direction. This will be referred to as uniform compression or tension.

In each case, the plate was 2mm thick, consisting of 8 plies, orientations measured from the x-axis. The ply properties are given in Table 5.1. The list of test cases studied in this section is as follows:

Table 5.1.: Elastic properties of T800/M21 carbon fibre reinforced epoxy. Table 3.1 has been repeated here for convenience.

Material property	Value
Longitudinal modulus, E_{11} (GPa)	160.4
Transverse modulus, E_{22} (GPa)	9.29
Out of plane modulus, E_{33} (GPa)	9.29
In plane shear modulus, G_{23} (GPa)	4.81
Out of plane shear modulus, G_{12}, G_{13} (GPa)	4.81
Poisson's ratio, $\nu_{12}, \nu_{13}, \nu_{23}$	0.33

1. Unidirectional plate in uniform longitudinal tension, linear geometry (Figure 5.4)

2. Unidirectional plate in uniform longitudinal compression, linear geometry (Figure 5.8)

3. $\pm45_{2S}$ plate in uniform longitudinal tension, linear geometry (Figure 5.12)

4. $[45_4, -45_4]$ plate in uniform longitudinal tension, linear geometry (Figure 5.16)

5. $[45_4, -45_4]$ plate in uniform longitudinal tension, nonlinear geometry (Figure 5.20)

For each validation case, contour plots of the direct stress in the $0°$ direction are presented. The red line AB in Figure 5.1 passes through the mid-thickness of the validation models. Further plots of various stress components against distance from Point A along this line are shown for three cases, tied models, the multiscale approach described in Chapter 4 and a direct application of the Abaqus substructuring technique combined with user elements at the global level (more details of this technique are given in Section 5.1.2). In addition, plots of various stress components are plotted at a selection of points along ab. The positions of these points, labelled A-D, are shown in Figure 5.2.

5.1.2. Direct application of Abaqus substructuring and superelements

The work presented in Chapter 4 makes use of an Abaqus analysis step known as substructuring to extract reduced stiffness and mass matrices for a model, and incorporates Abaqus user elements [75]. The technique for extracting the matrices is described in Chapter 4, and if it is to generate appropriate matrices for use in an Abaqus user element (referred to as a superelement here) special treatment of the boundaries in the substructure analysis is required.

To demonstrate the importance of proper treatment of the boundaries of the substructure analysis, as described in Chapter 4, the validation models presented in this work using the multiscale modelling techniques developed will be compared to a direct application of

Structural mesh

Thickness:	2mm
	1 element
Element type:	SC8R
	continuum shell
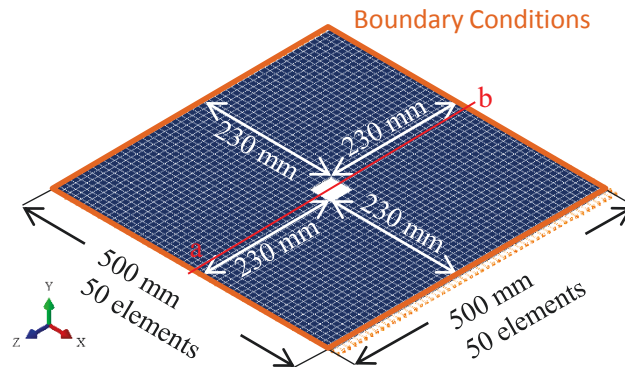
Component mesh

Thickness:	2mm
	8 elements
Element type:	C3D8
	solid brick
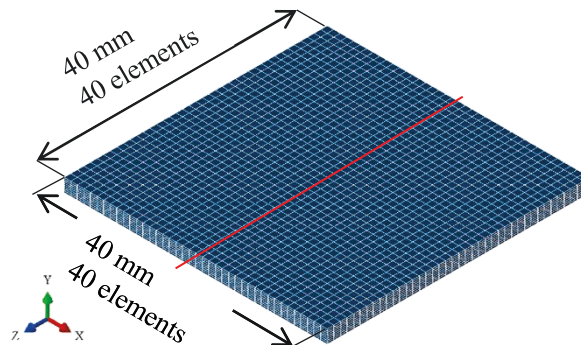
Figure 5.1.: Global (top) and local (bottom) models used in the numerical validation of the multiscale method for coupling continuum shell to solid models. These two problems were solved both by the multiscale approach and by tying the local region to the appropriate surfaces of the global model in order that the two sets of results may be compared.
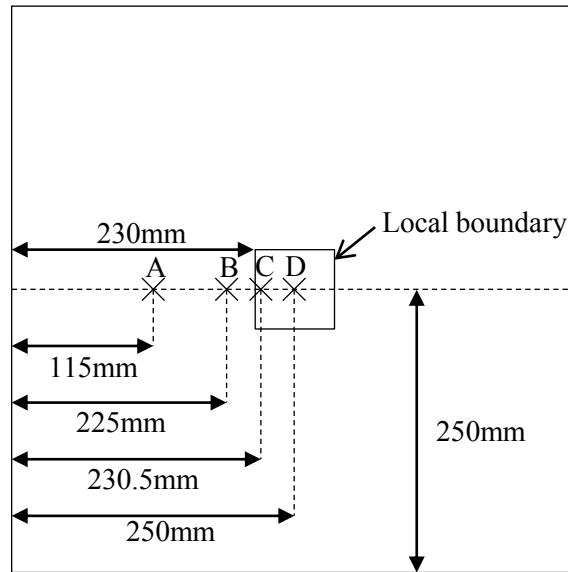
Figure 5.2.: The positions of points A-D, at which through thickness plots of various stress components are presented in this chapter. Point C is 0.5 mm inside the local region.

Abaqus substructuring and submodelling. This direct application of the techniques consists of running a substructuring analysis on a refined model where for each superelement node a single refined model node is "retained" in the substructure analysis. Perturbations are applied at each retained node in the substructuring step to generate mass and stiffness matrices, as discussed in Chapter 4 [75]. The closest refined node to the superelement node is retained. There is no special treatment of the refined model boundary and the resulting mass and stiffness matrices are used to define the superelement properties in the global model.

A direct application of substructuring and superelements is expected to result in superelement behaviour which is significantly less stiff than that of the surrounding material. This is because, without appropriate treatment of the local model boundary, the perturbation of a single degree of freedom of the local boundary provides the stiffness at a single degree of freedom of the superelement. However, due to the higher refinement of the local model, a unit displacement at a single degree of freedom results in a much smaller change in elastic energy than a unit displacement at a superelement degree of freedom. This is illustrated in Figure 4.2.

In order to make running the direct application of substructuring and superelements more efficient, the Python scripts used to implement the multiscale approach developed during this work were modified such that only the nearest boundary node to each phantom node described in Chapter 4 was included in the constraints. Assuming that each local model has a boundary node close to each phantom node then this is equivalent to a

direct application of substructuring and submodelling. The high refinement of the local compared to the global mesh ensures that there is always a local node in close proximity to a phantom node. In order to demonstrate that this is the case, an analysis on a unidirectional plate in uniform longitudinal tension is presented here using two methods. This model is identical to the first validation case described in Section 5.1.1. In the first method a direct application of Abaqus substructuring and superelements is used. The iterative procedure described in Chapter 4 is performed manually, with boundary conditions being updated in the input file of the local model based on global model results, and stiffness and mass matrices for the global model being updated after a new local model execution. In addition, the retained nodes for the stubstructuiring step were also defined manually such that the nearest local node to each global boundary node was retained. In the second approach, the modified scripts are used.

As can be seen in Figure 5.3, the stress values plotted along the path shown in Figure 5.1 are identical for the two approaches. Thus it was concluded that use of the modified scripts was equivalent to direct application of Abaqus substructuring and submodelling, and the scripts were used to generate all results for the direct application of substructuring and submodelling in this document.

5.2. Discussion

In Section 5.1.1, flat panels under uniaxial loading were modelled, with increased mesh refinement in the centre. Models with the central region coupled to the outer region via a tie constraint were taken as the control solution. The fully coupled global-local approach and a direct application of substructuring and superelements were evaluated against the control solution.

The results of the coupling approach matched the control solutions well, while the direct application of substructuring and superelements resulted in less stiff superelement behaviour and stress concentrations around global nodal positions in both the global and local models. This was the expected outcome, as discussed in Section 5.1.2.

In each of the stress component plots along the path ab, the curves obtained using the multiscale approach match the control solution generated using tied models very well. For the unbalanced laminates, both in the geometrically linear and nonlinear cases, the multiscale plot for σ_{22} deviates from the tied solution just inside the local boundary. This can be seen in Figure 5.17 and Figure 5.21. The deviation from the control solution is small in terms of the region of the local model affected. A possible explanation for the difference between the control and the multiscale solution is that the extent of constraints on the boundary of the local model due to the multiscale approach is slightly greater than that due to the tie constraint in the control solution. Within an iteration of the multiscale approach, the shape of a patch of the local boundary is fully defined by the shape of the corresponding global element face during that iteration. However in the tied approach the shape of a patch on the local boundary is solved at the same time as that

(a) σ_{11}.

(b) τ_{12}.

(c) σ_{22}.
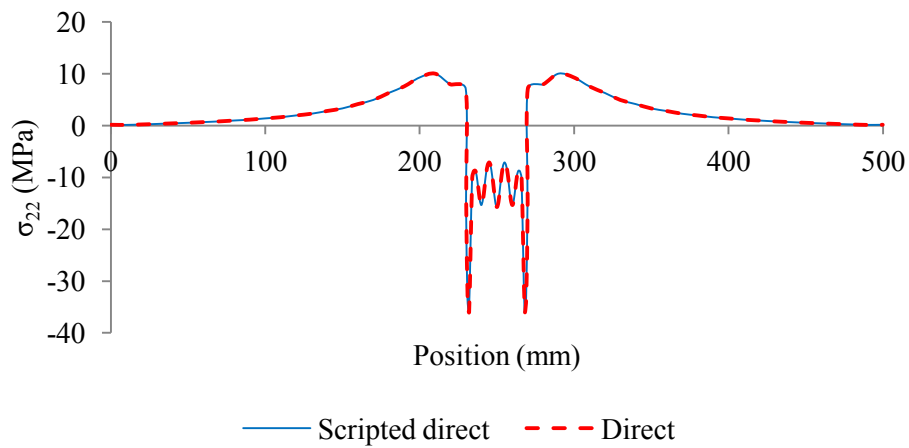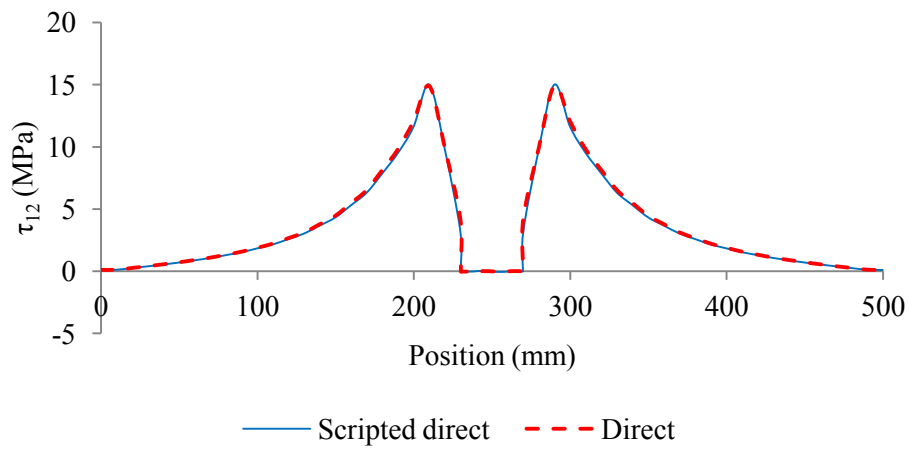
Figure 5.3.: Plots of midplane stress components along the path shown in Figure 5.1 for a direct application of substructuring and submodelling and for a multiscale approach for a 0_8 layup under the boundary conditions shown in Figure 5.4.
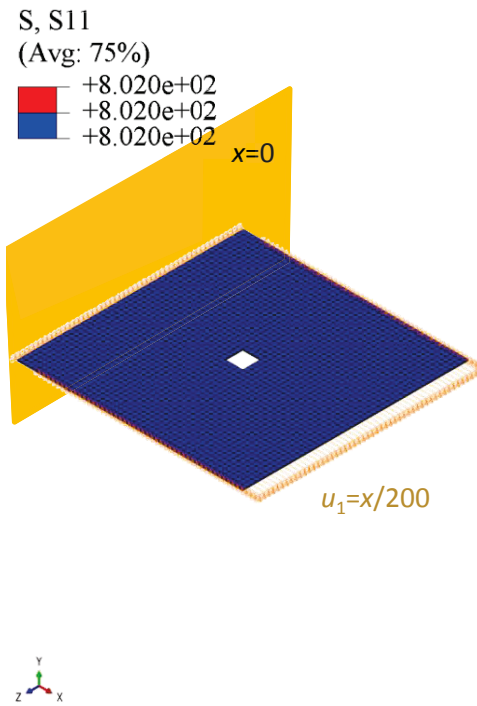
(a) Global model in the multiscale approach.
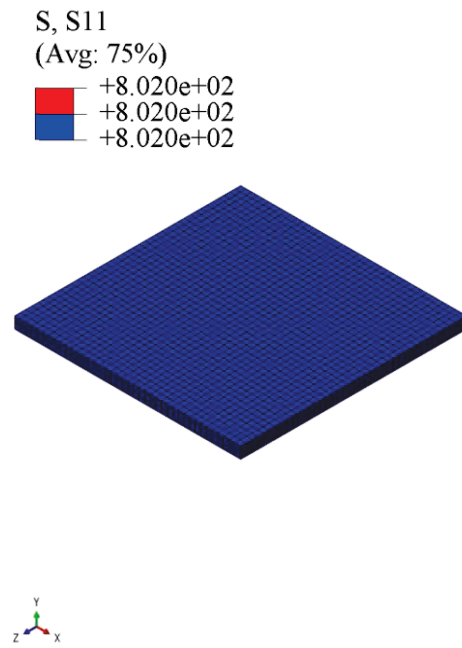
(b) Local model in the multiscale approach.
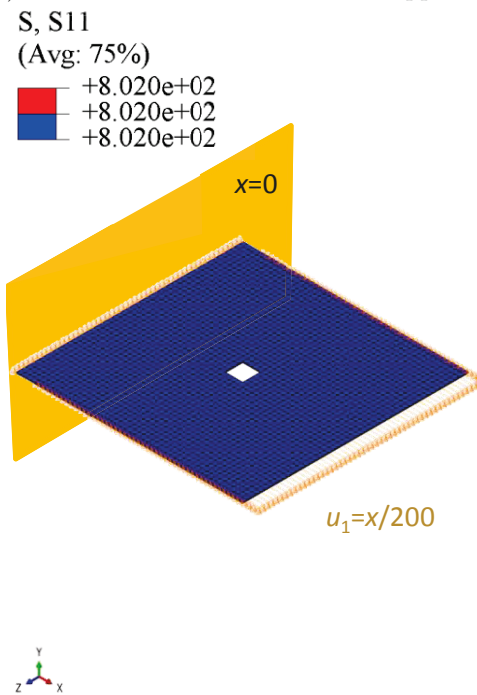
(c) Global model in the tied approach.

(d) Local model in the tied approach.

Figure 5.4.: Contour plots of σ_{11} using a layup of 0_8 under the boundary conditions shown.

(a) σ_{11}.

(b) τ_{12}.
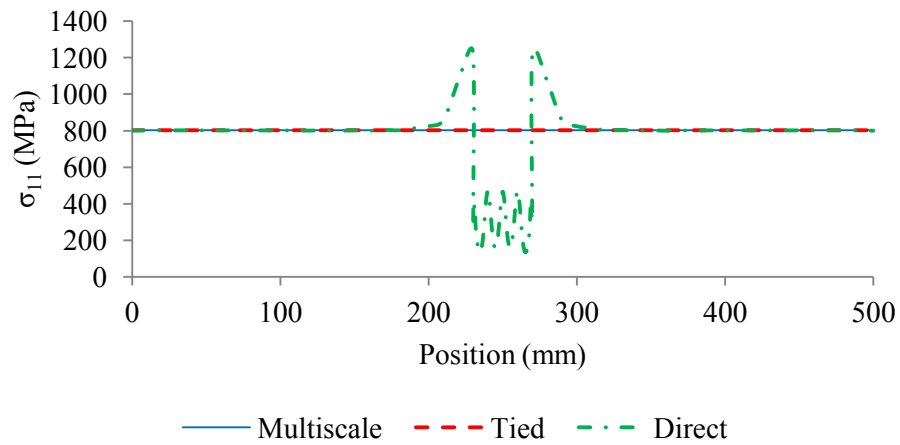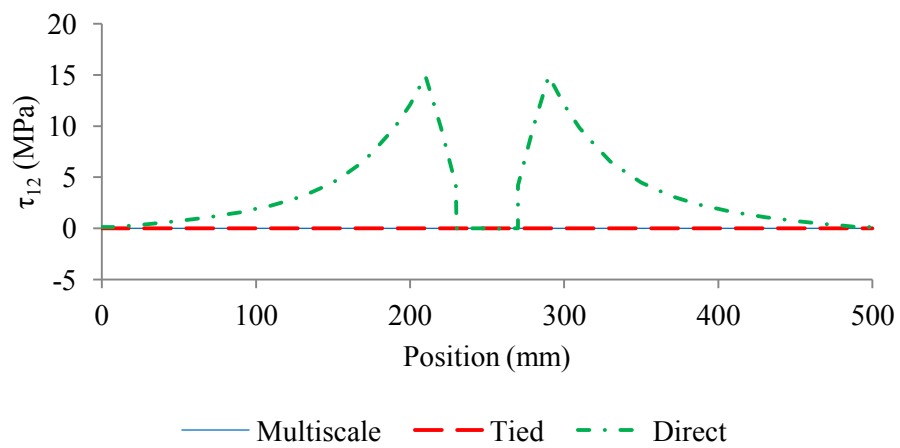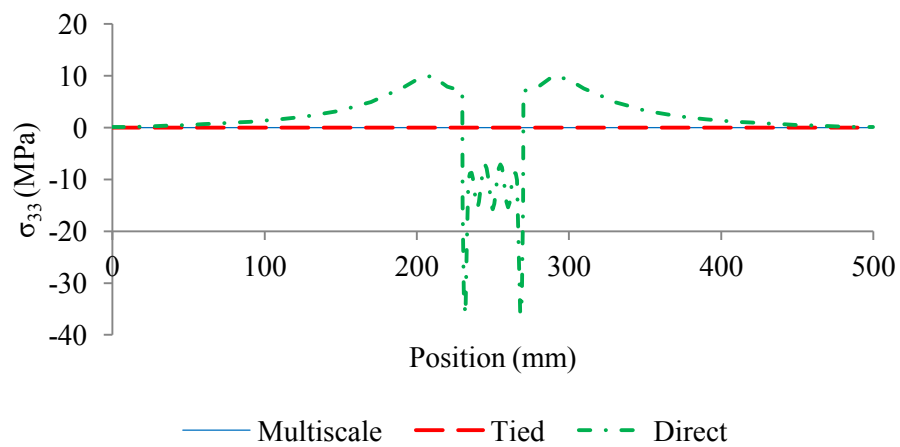
(c) σ_{22}.

Figure 5.5.: Plots of midplane stress components along the path shown in Figure 5.1 for tied and multiscale approaches for a 0_8 layup under the boundary conditions shown in Figure 5.4.

(a) σ_{11}.

(b) τ_{12}.
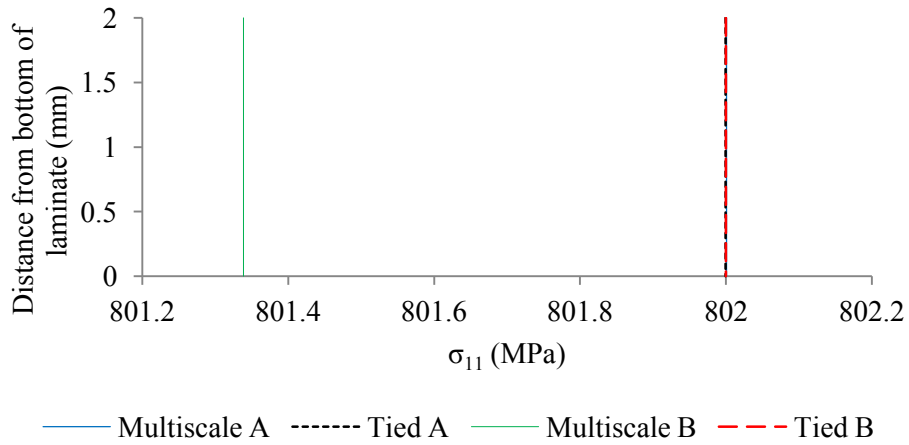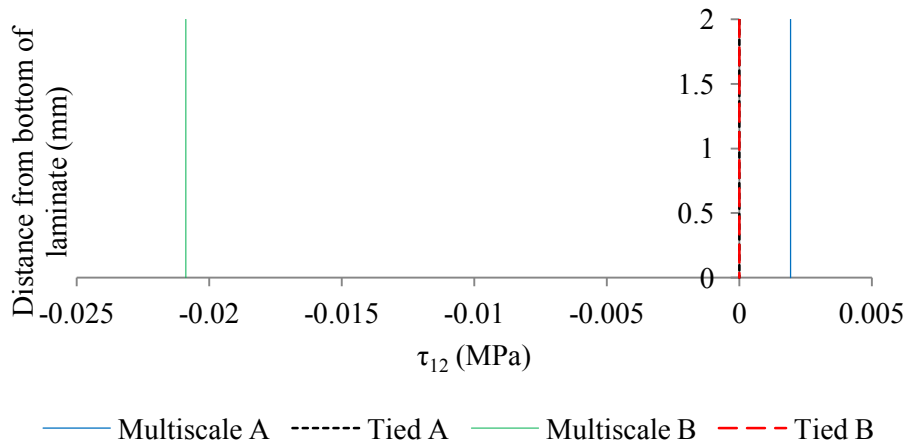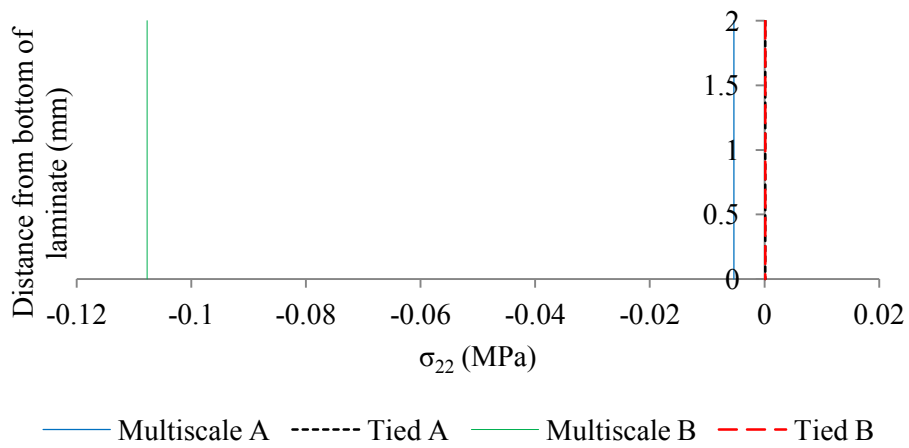
(c) σ_{22}.

Figure 5.6.: Through thickness plots of stress components at selected points (see Figure 5.2) in a 0_8 laminate under the boundary conditions shown in Figure 5.4.

(a) σ_{11}.

(b) τ_{12}.

(c) σ_{33}.

Figure 5.7.: Through thickness plots of stress components at selected points (see Figure 5.2) in a 0_8 laminate under the boundary conditions shown in Figure 5.4.

S, S11
(Avg: 75%)
-8.020e+02
-8.020e+02
-8.020e+02

S, S11
(Avg: 75%)
-8.020e+02
-8.020e+02
-8.020e+02

x=0

$u_1 = -x/200$

(a) Global model in the multiscale approach.

(b) Local model in the multiscale approach.

S, S11
(Avg: 75%)
-8.020e+02
-8.020e+02
-8.020e+02

S, S11
(Avg: 75%)
-8.020e+02
-8.020e+02
-8.020e+02

x=0

$u_1 = -x/200$

(c) Global model in the tied approach.
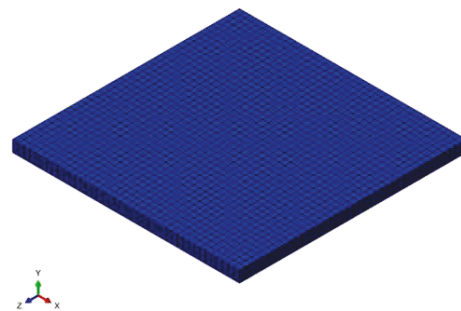
(d) Local model in the tied approach.

Figure 5.8.: Contour plots of σ_{11} using a layup of 0_8 under the boundary conditions shown.
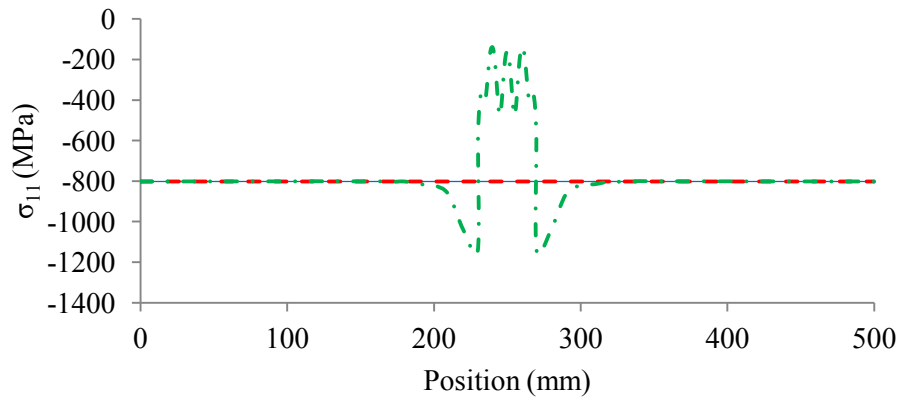
(a) σ_{11}.

(b) τ_{12}.
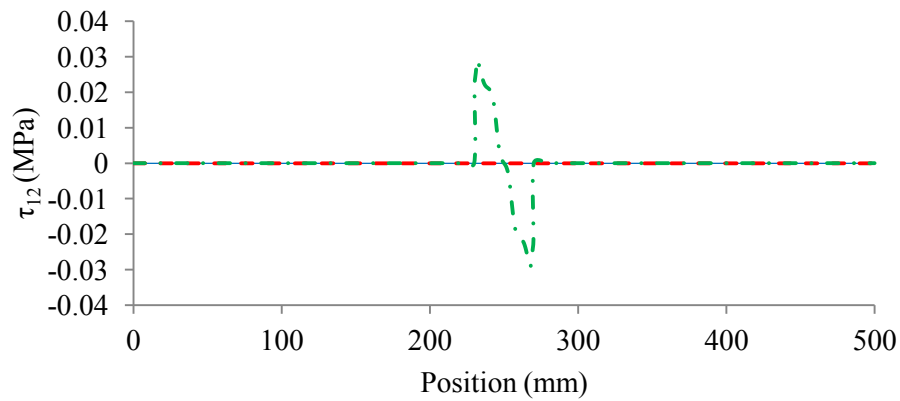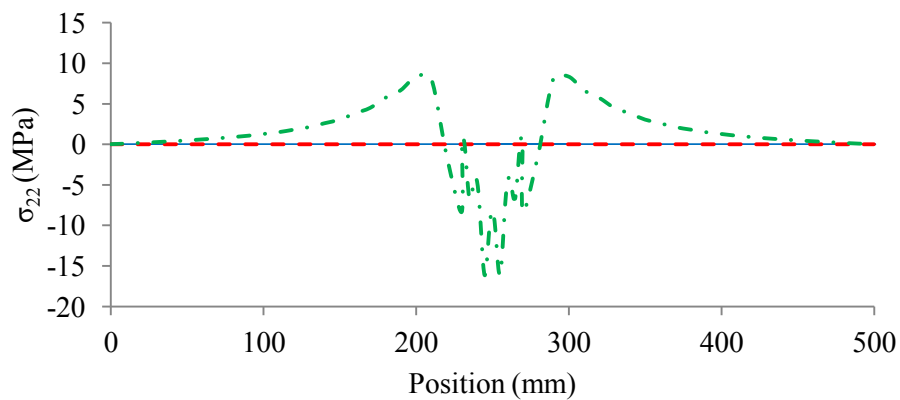
(c) σ_{22}.

Figure 5.9.: Plots of midplane stress components along the path shown in Figure 5.1 for tied and multiscale approaches for a 0_8 layup under the boundary conditions shown in Figure 5.8.

(a) σ_{11}.

(b) τ_{12}.
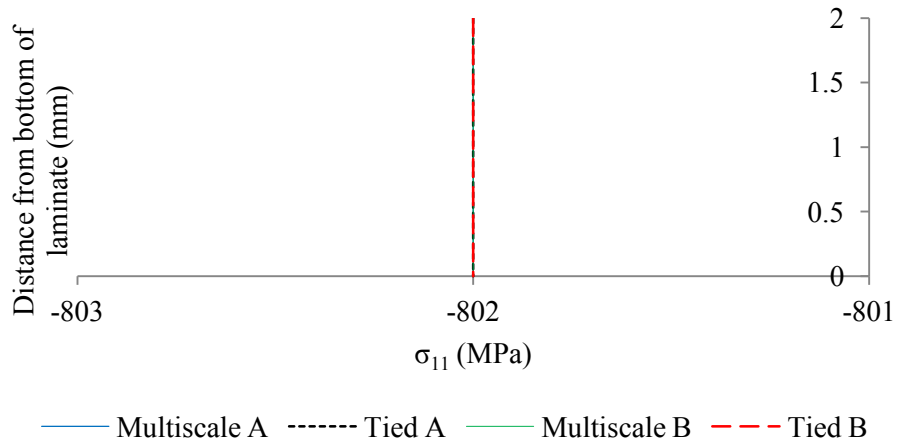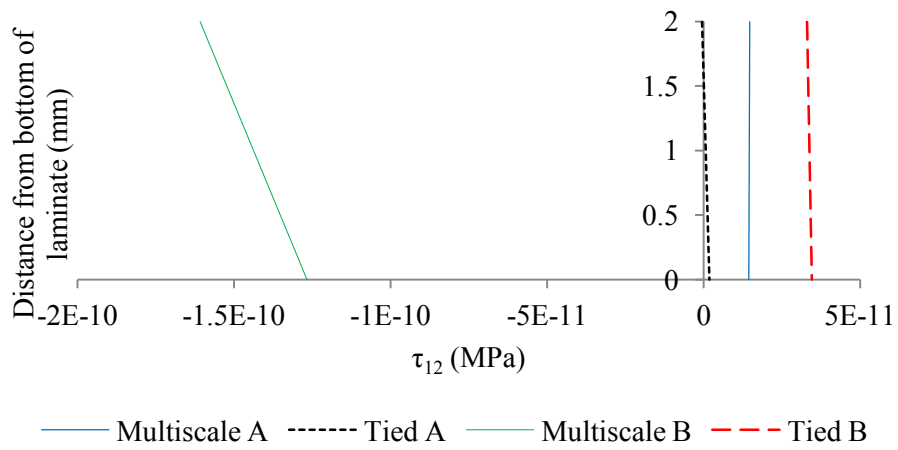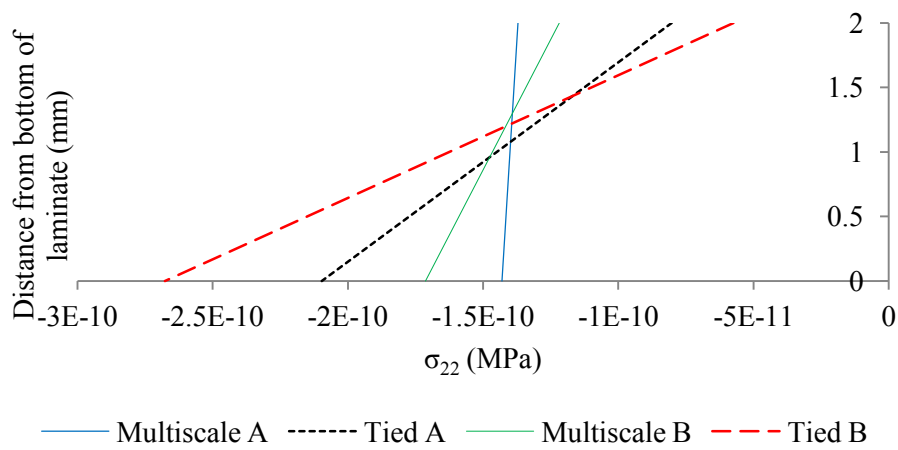
(c) σ_{22}.

Figure 5.10.: Through thickness plots of stress components at selected points (see Figure 5.2) in a 0_8 laminate under the boundary conditions shown in Figure 5.8.

(a) σ_{11}.

(b) τ_{12}.
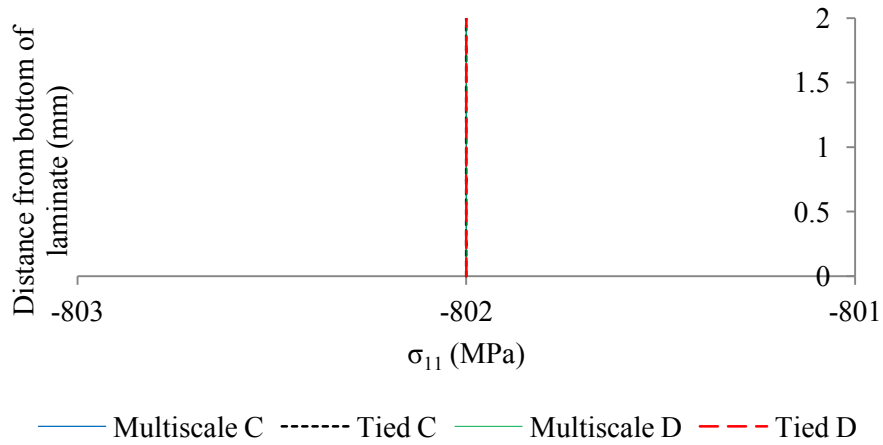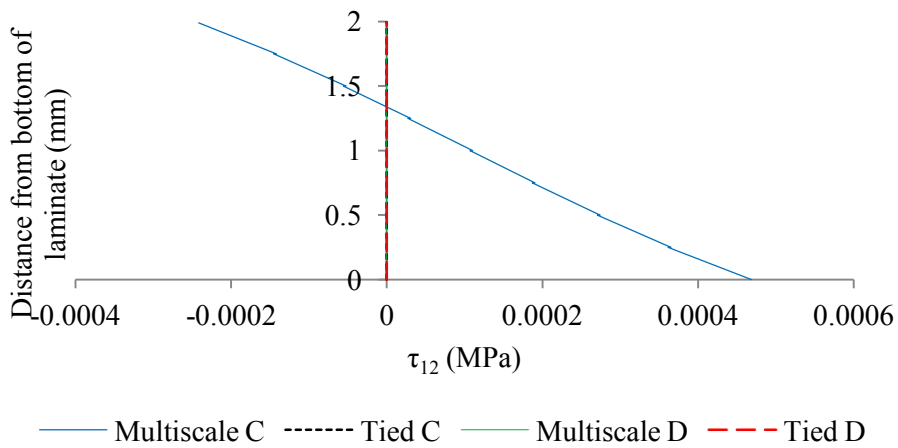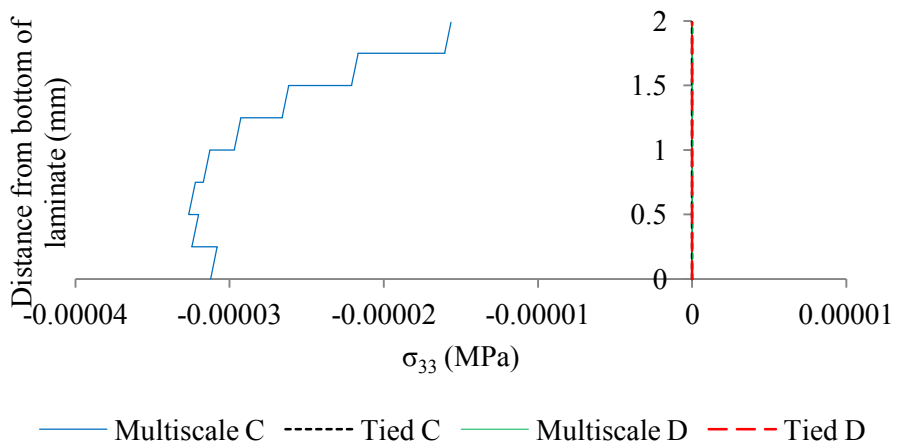
(c) σ_{33}.

Figure 5.11.: Through thickness plots of stress components at selected points (see Figure 5.2) in a 0_8 laminate under the boundary conditions shown in Figure 5.8.
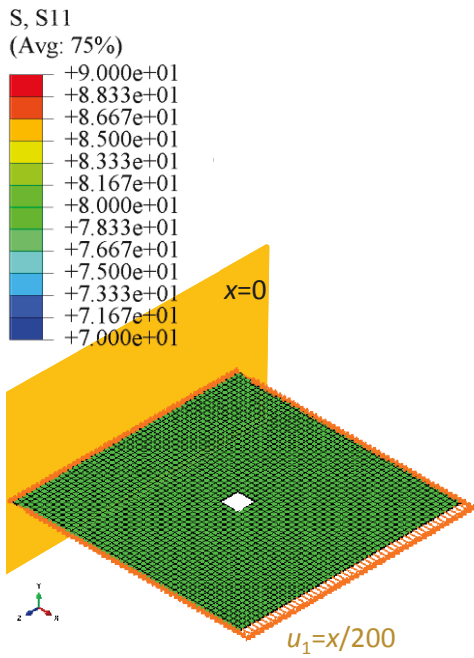
(a) Global model in the multiscale approach.
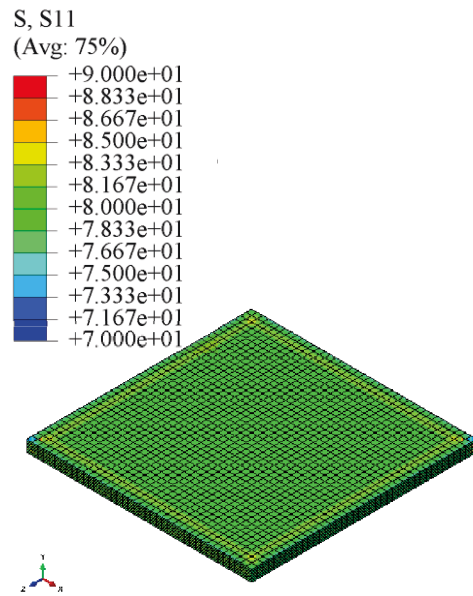
(b) Local model in the multiscale approach.
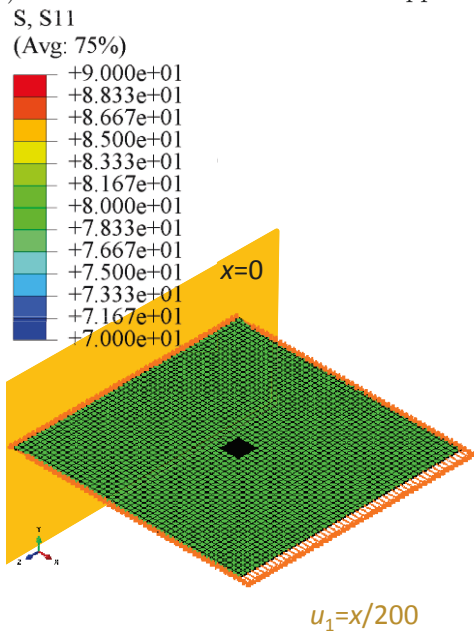
(c) Global model in the tied approach.
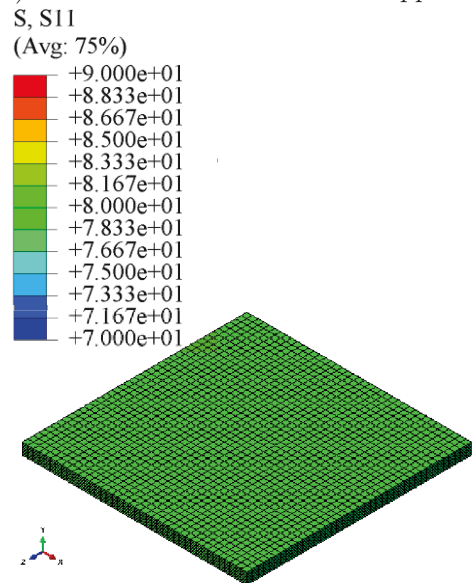
(d) Local model in the tied approach.

Figure 5.12.: Contour plots of σ_{11} using a layup of $\pm 45_{2S}$ under the boundary conditions shown.

(a) σ_{11}.
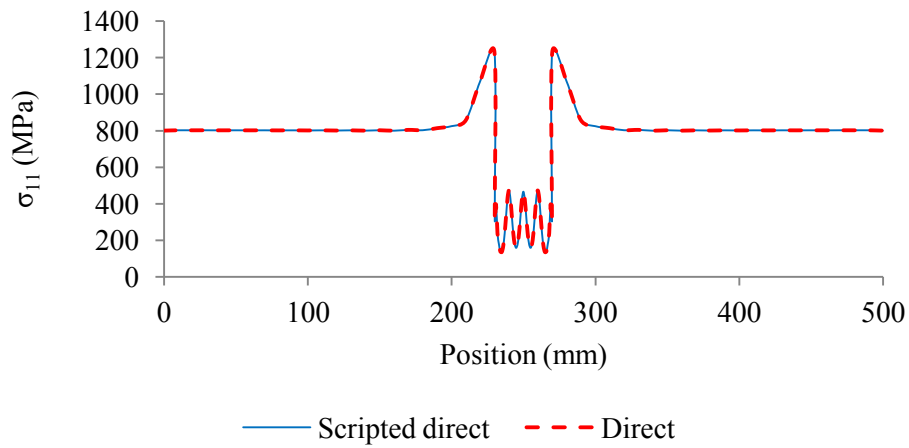

(b) τ_{12}.

(c) σ_{22}.
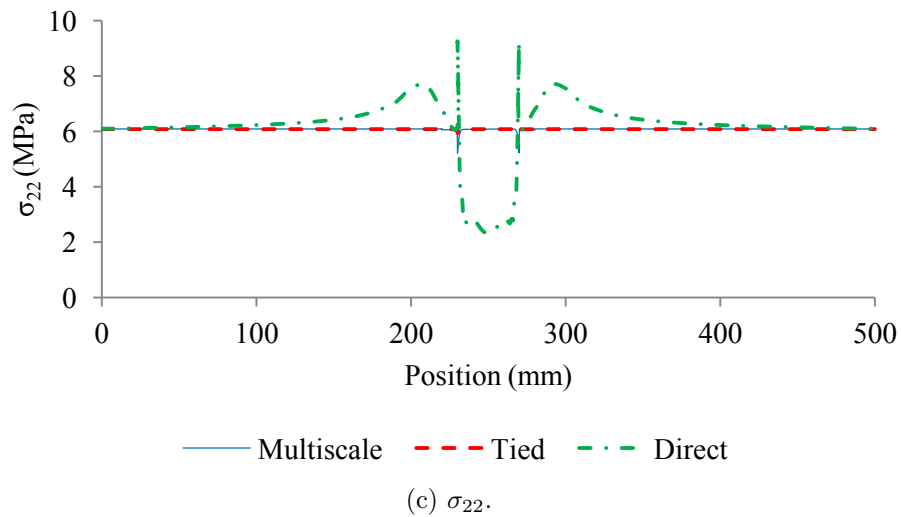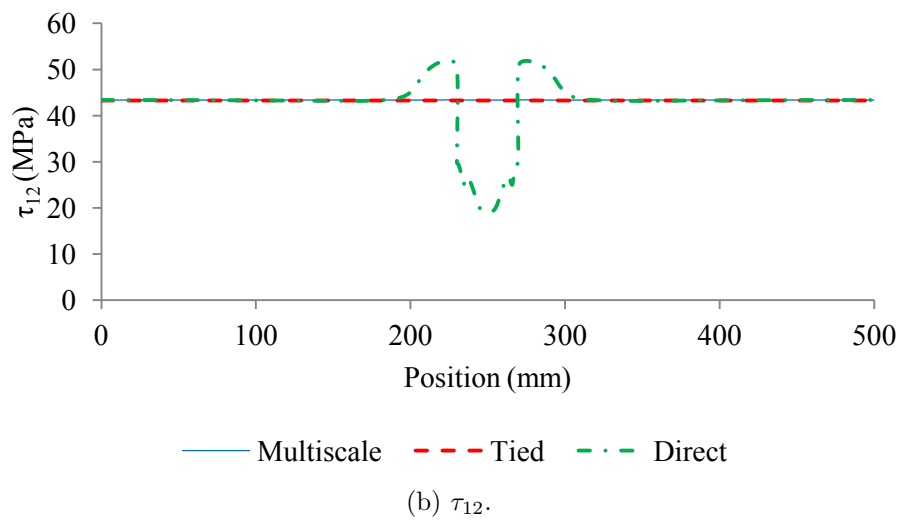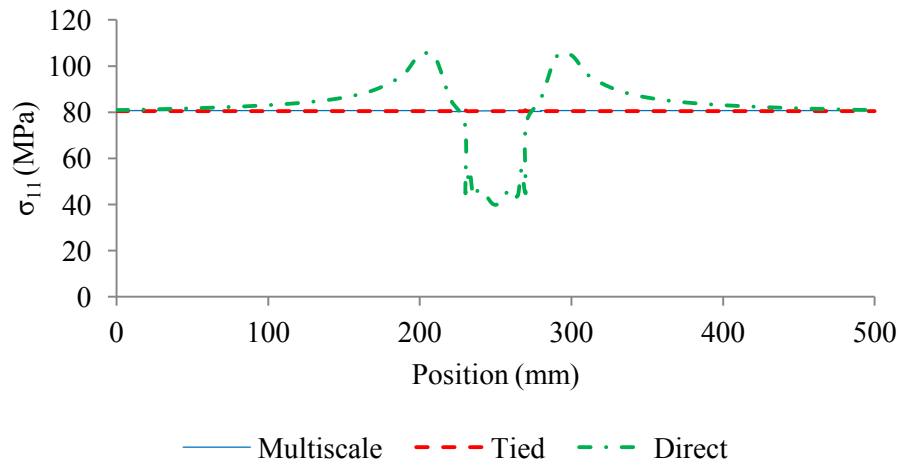
Figure 5.13.: Plots of midplane stress components along the path shown in Figure 5.1 for tied and multiscale approaches for a $\pm 45_{2S}$ layup under the boundary conditions shown in Figure 5.12.

(a) σ_{11}.

(b) τ_{12}.
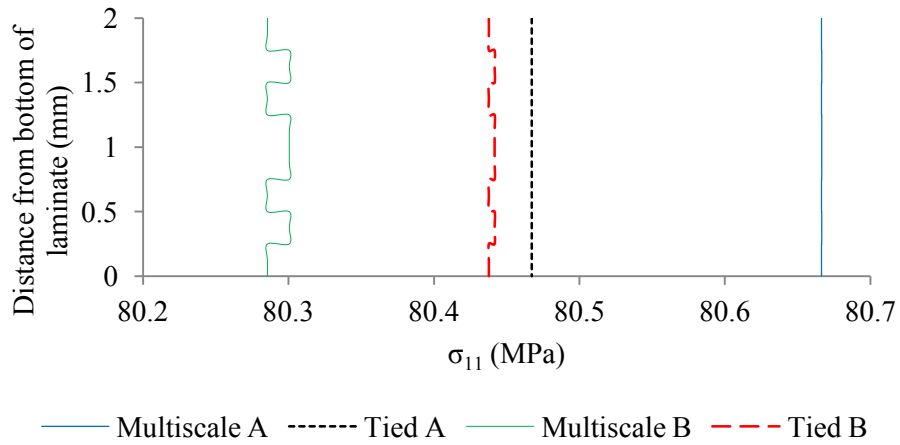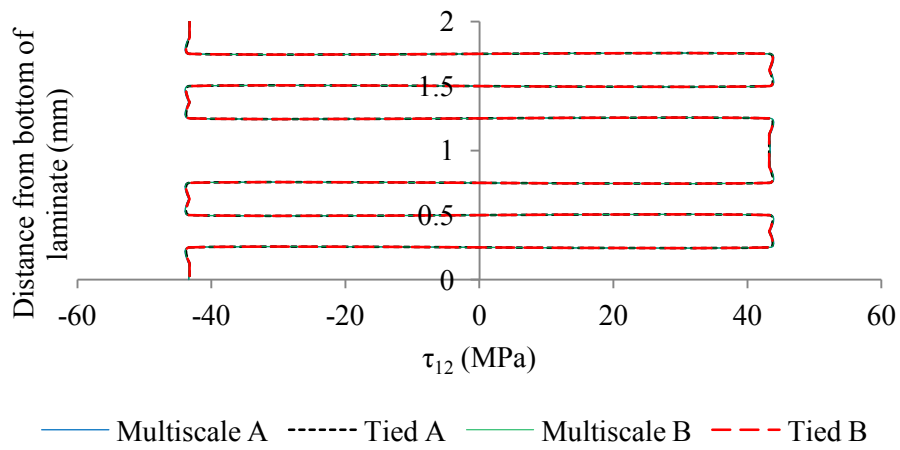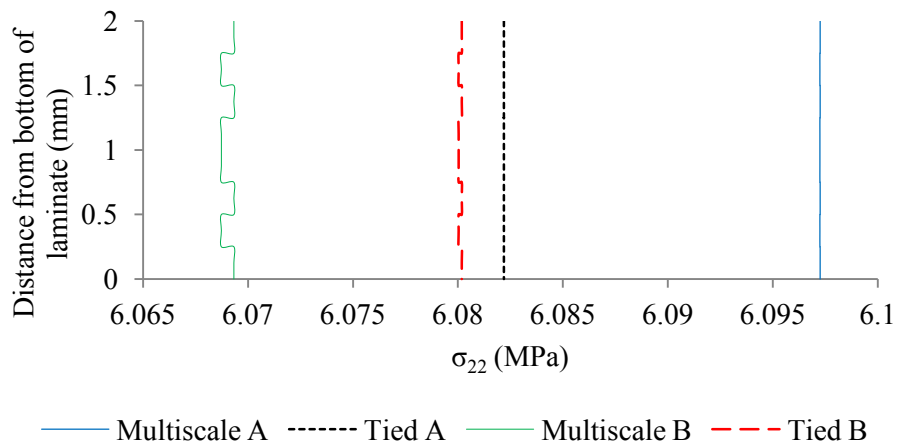
(c) σ_{22}.

Figure 5.14.: Through thickness plots of stress components at selected points (see Figure 5.2) for a $\pm 45_{2S}$ laminateFigure 5.12.

(a) σ_{11}.

(b) τ_{12}.
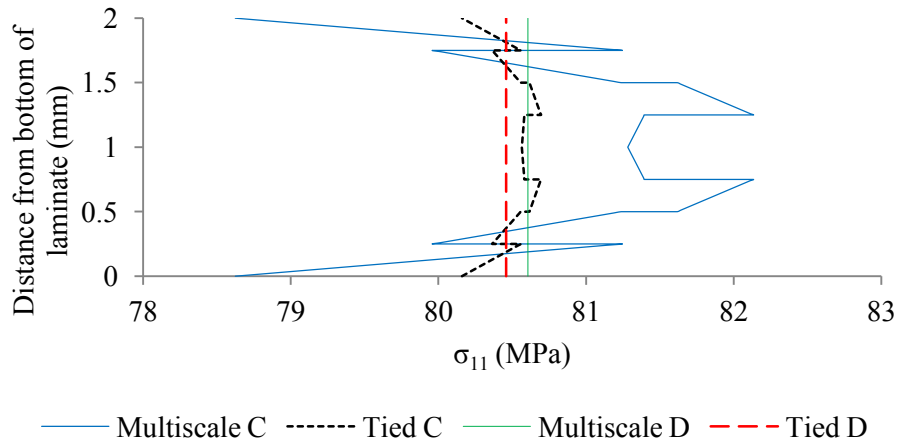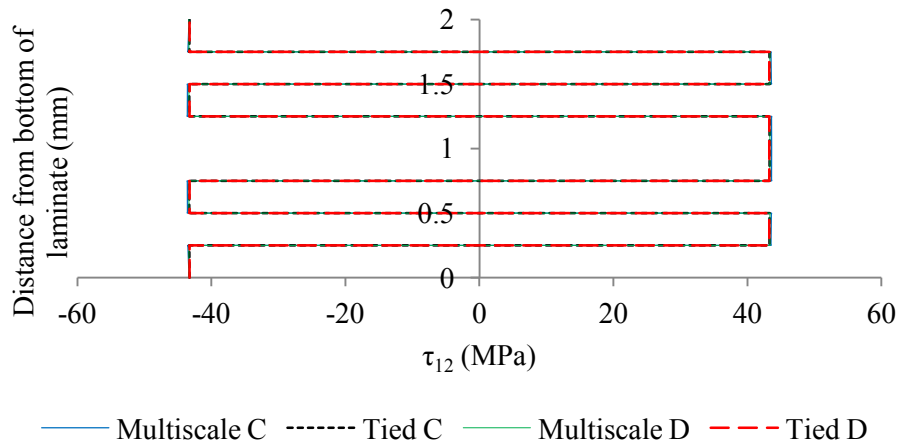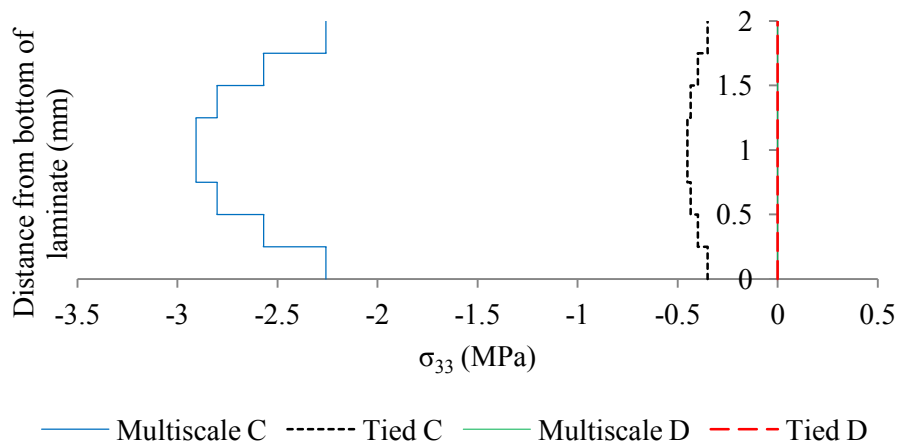
(c) σ_{33}.

Figure 5.15.: Through thickness plots of stress components at selected points (see Figure 5.2) for a $\pm45_{2S}$ laminateFigure 5.12.
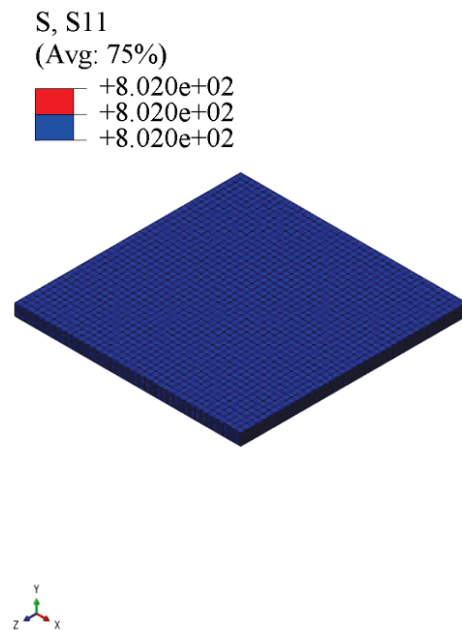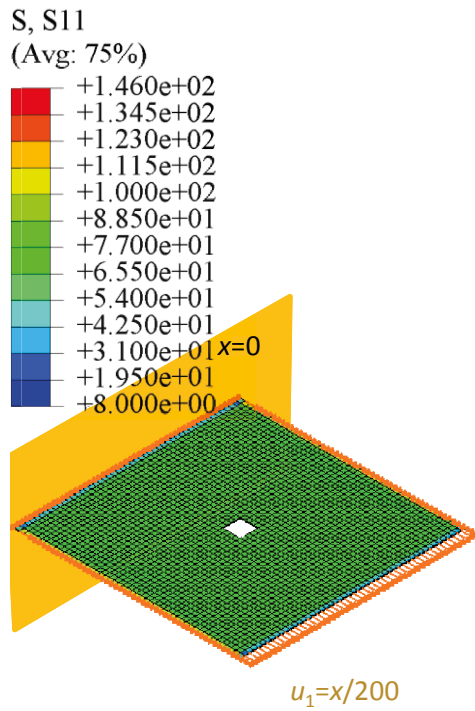
(a) Global model in the multiscale approach.
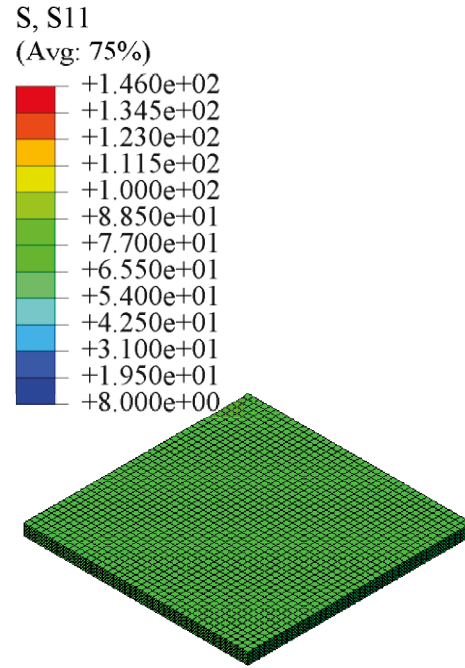
(b) Local model in the multiscale approach.
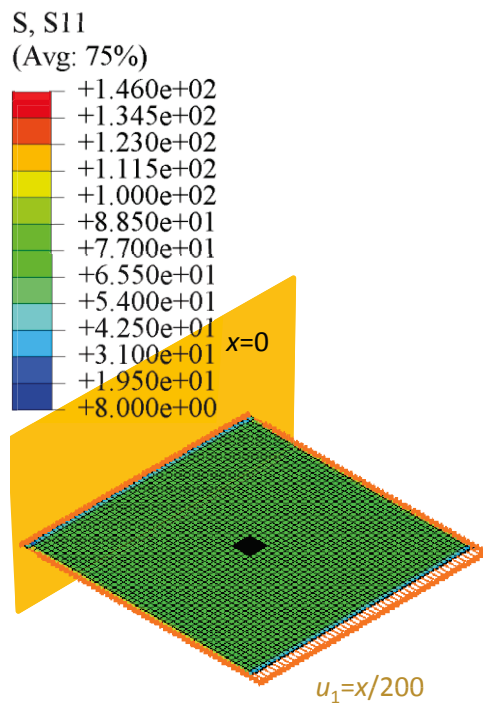
(c) Global model in the tied approach.
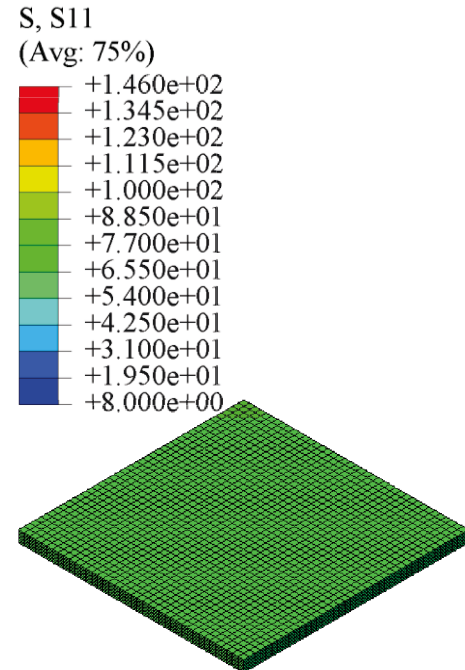
(d) Local model in the tied approach.

Figure 5.16.: Contour plots of σ_{11} using a layup of $[45_4, -45_4]$ under the boundary conditions shown.
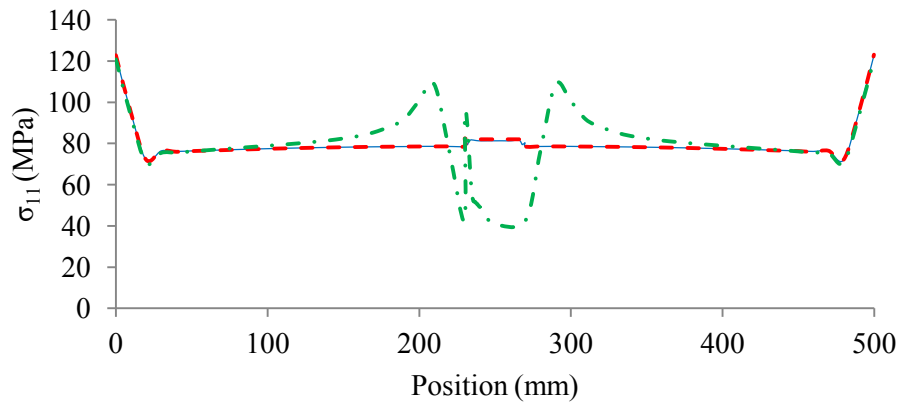
(a) σ_{11}.

(b) τ_{12}.
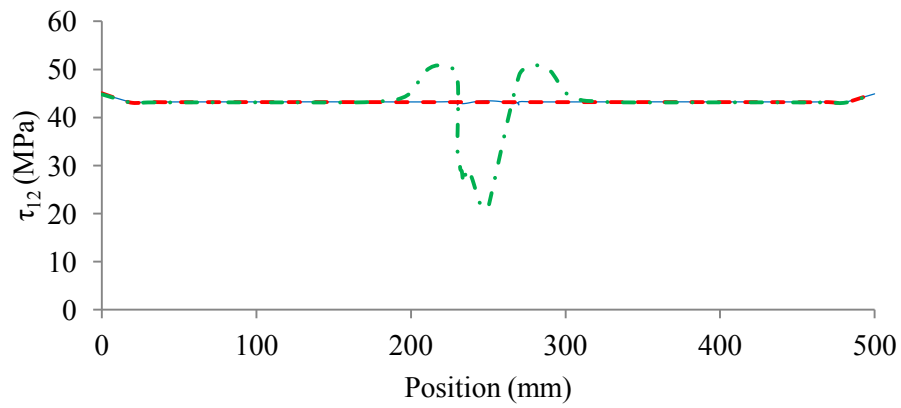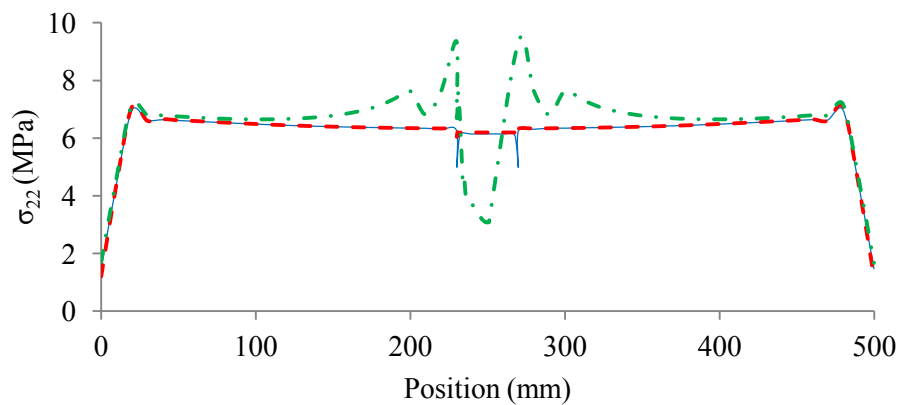
(c) σ_{22}.

Figure 5.17.: Plots of midplane stress components along the path shown in Figure 5.1 for tied and multiscale approaches for a $[45_4, -45_4]$ layup under the boundary conditions shown in Figure 5.16.

(a) σ_{11}.

(b) τ_{12}.
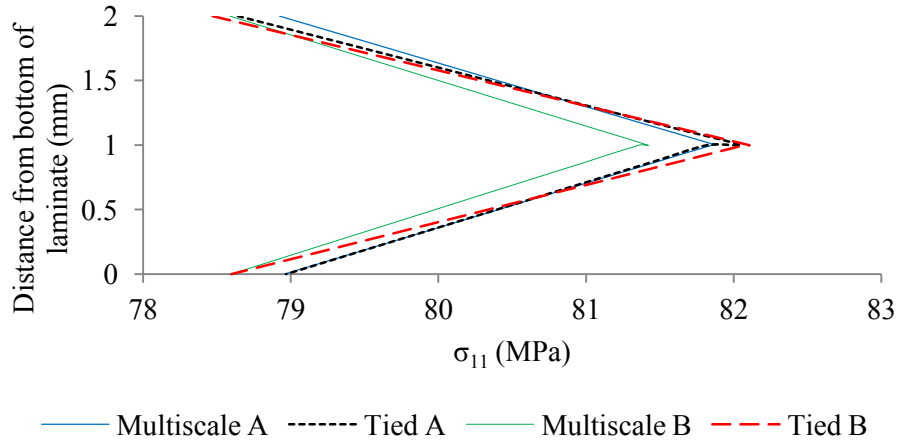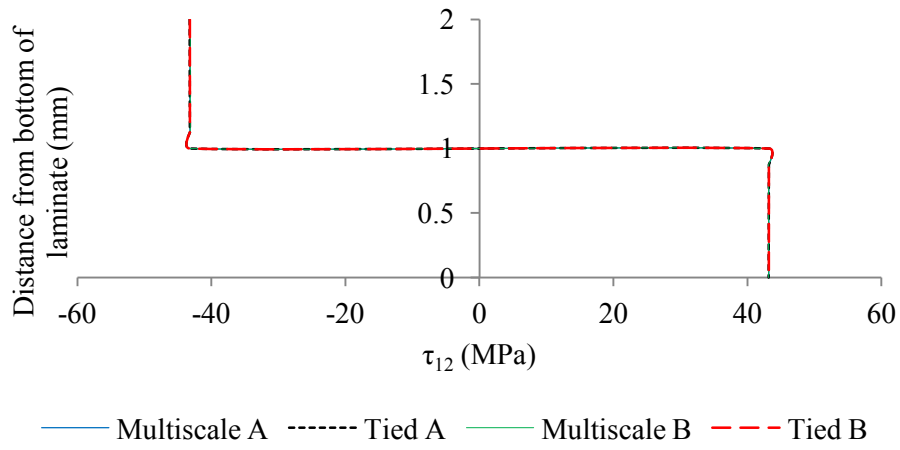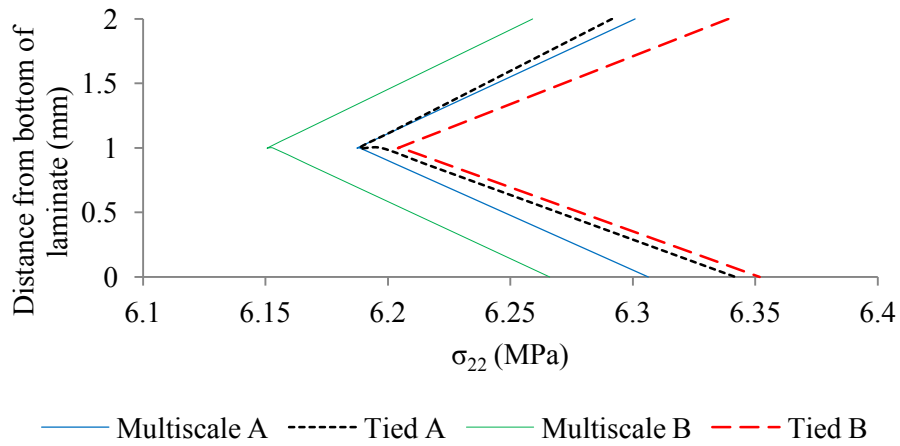
(c) σ_{22}.

Figure 5.18.: Through thickness plots of stress components at selected points (see Figure 5.2) in a $[45_4, -45_4]$ laminate under the boundary conditions shown in Figure 5.16.

(a) σ_{11}.

(b) τ_{12}.
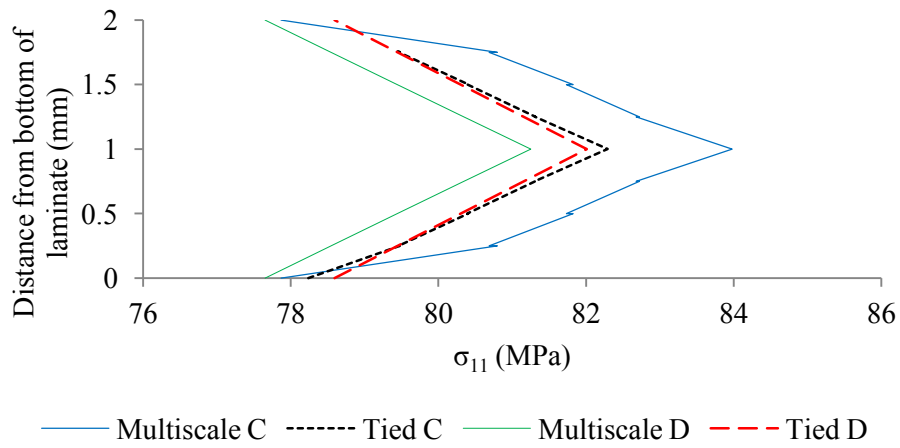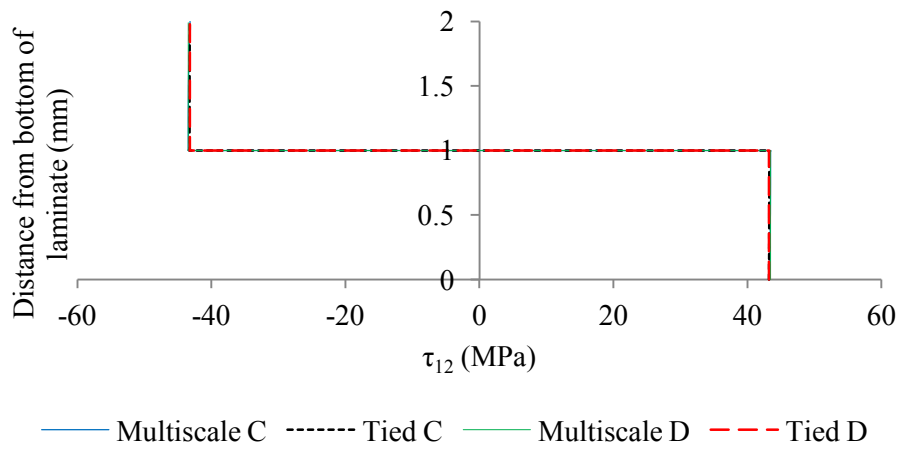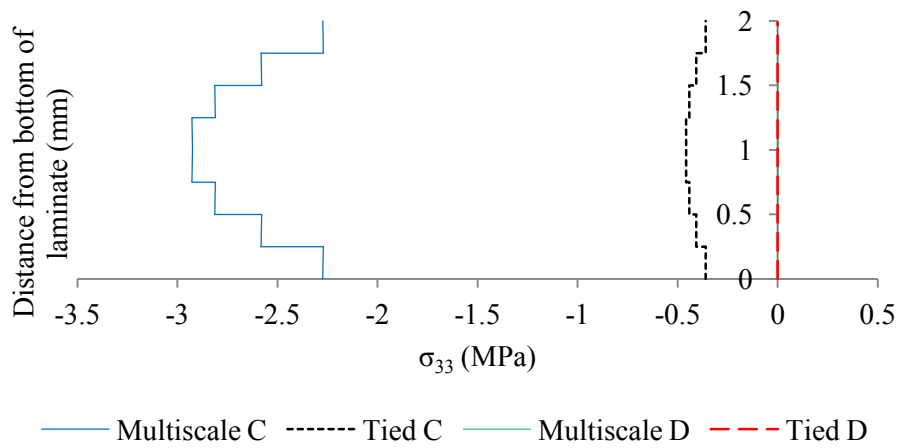
(c) σ_{33}.

Figure 5.19.: Through thickness plots of stress components at selected points (see Figure 5.2) in a $[45_4, -45_4]$ laminate under the boundary conditions shown in Figure 5.16.
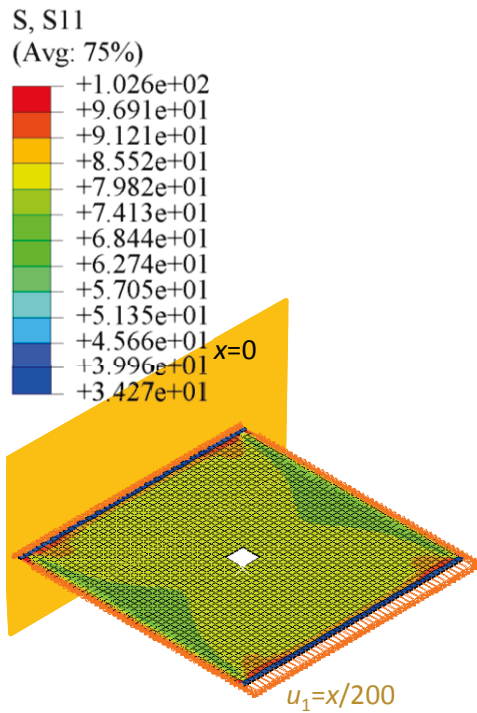
(a) Global model in the multiscale approach.
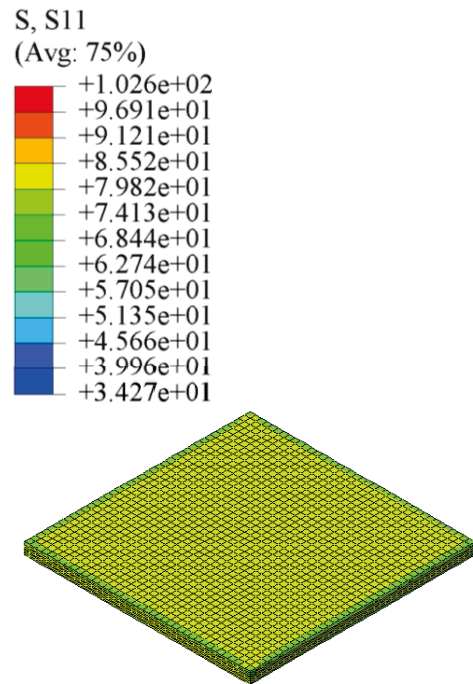
(b) Local model in the multiscale approach.
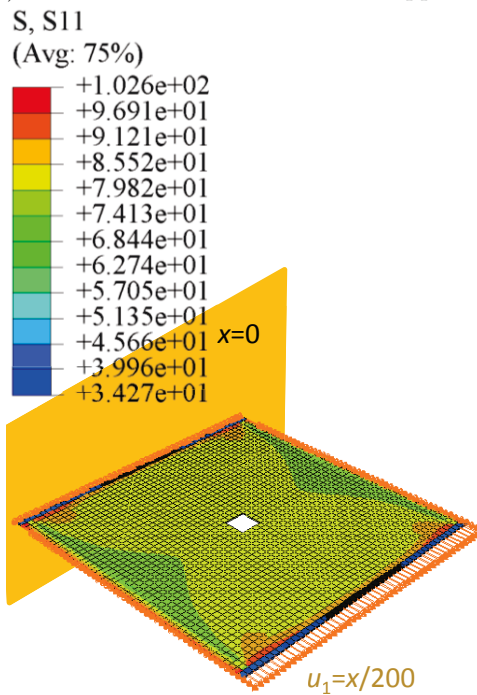
(c) Global model in the tied approach.
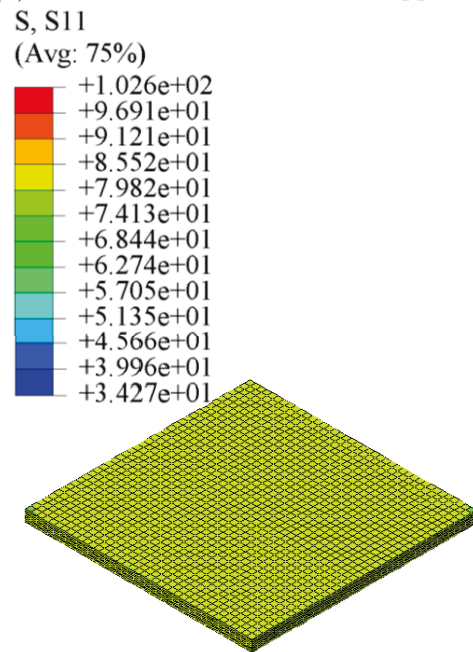
(d) Local model in the tied approach.

Figure 5.20.: Contour plots of σ_{11} using a layup of $[45_4, -45_4]$ under the boundary conditions shown.

(a) σ_{11}.

(b) τ_{12}.
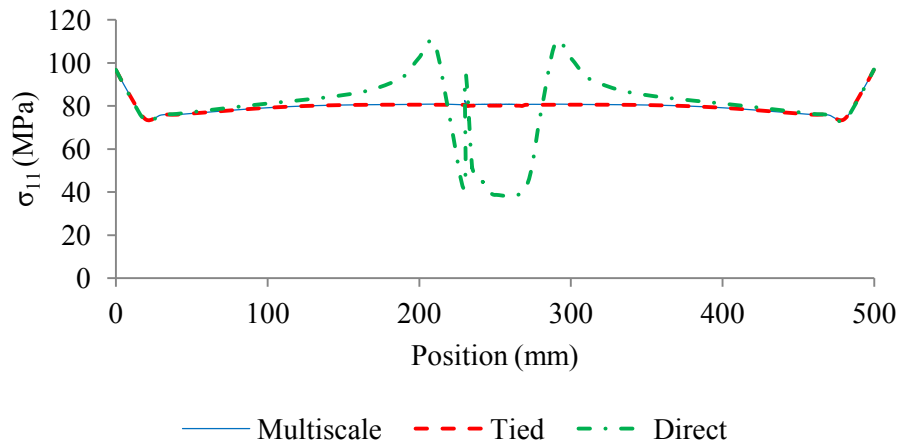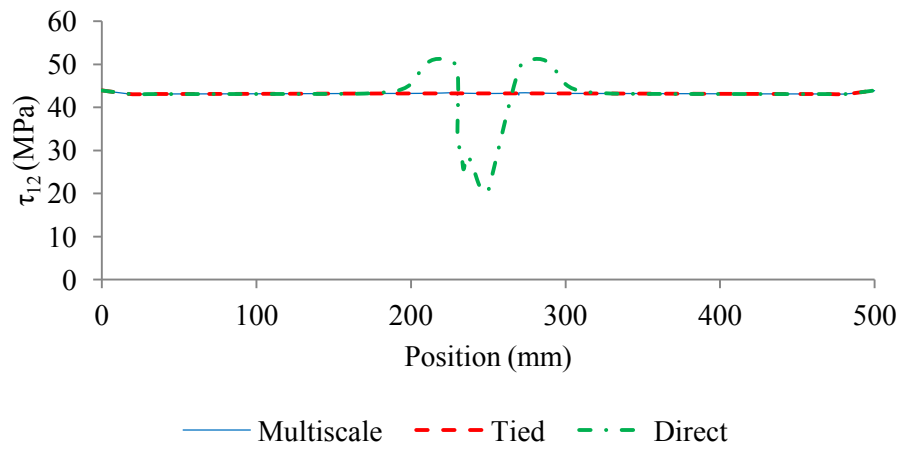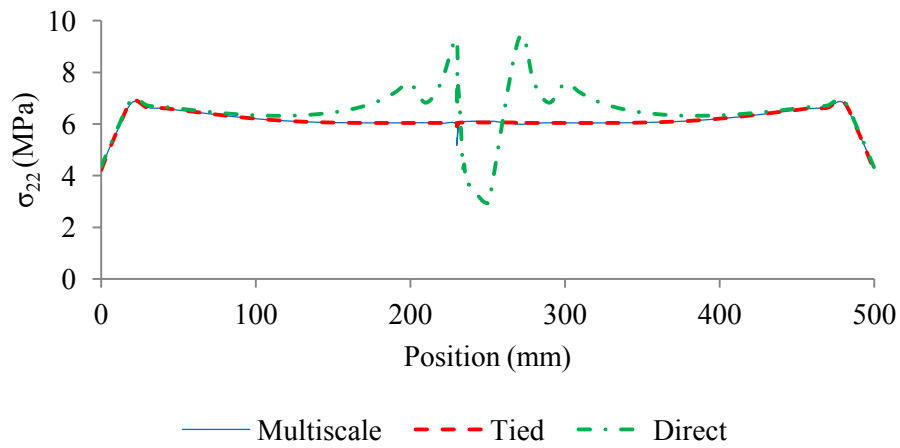
(c) σ_{22}.

Figure 5.21.: Plots of midplane stress components along the path shown in Figure 5.1 for tied and multiscale approaches for a $[45_4, -45_4]$ layup under the boundary conditions shown in Figure 5.20.
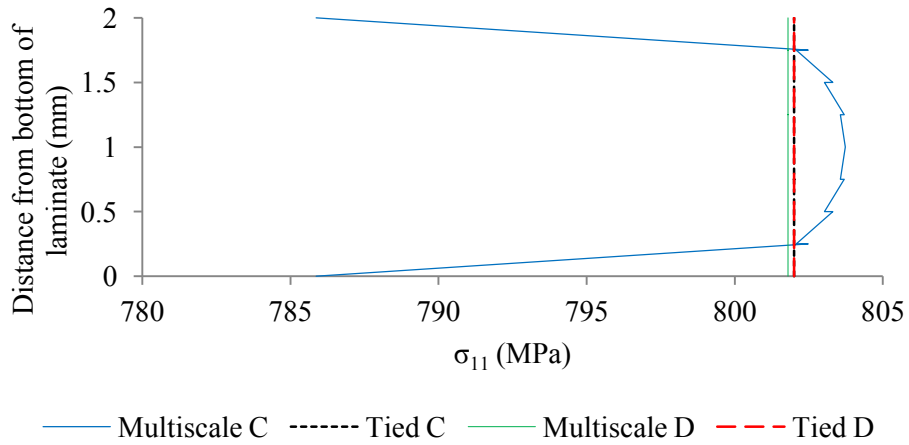
(a) σ_{11}.

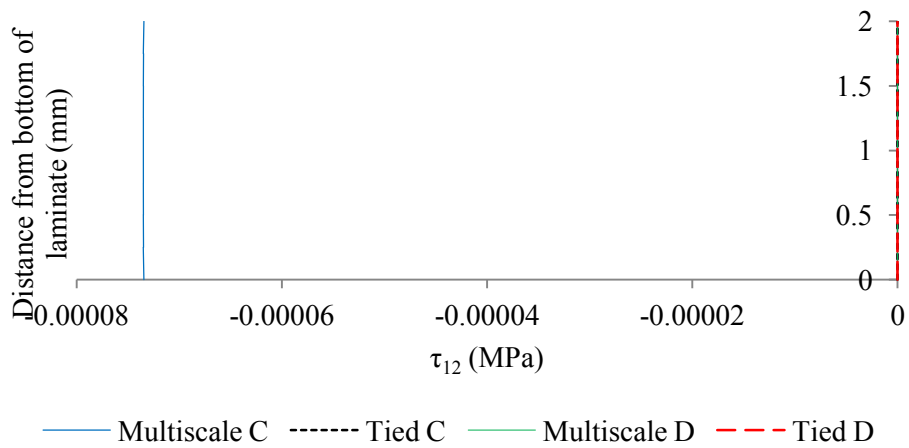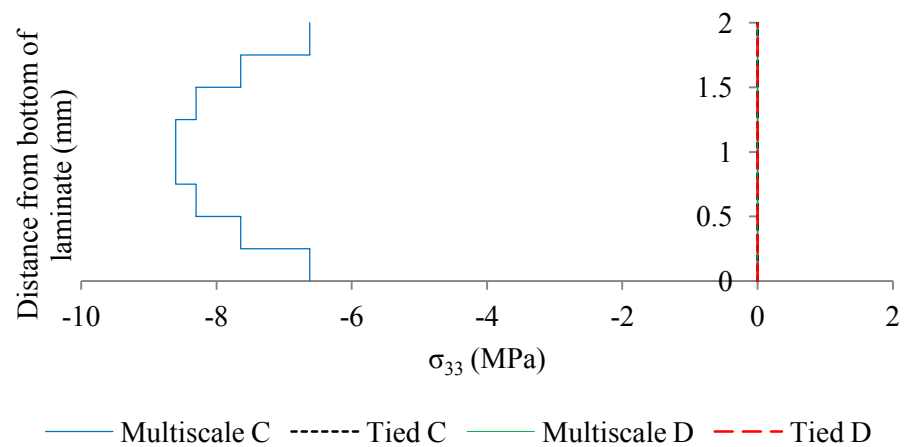(b) τ_{12}.
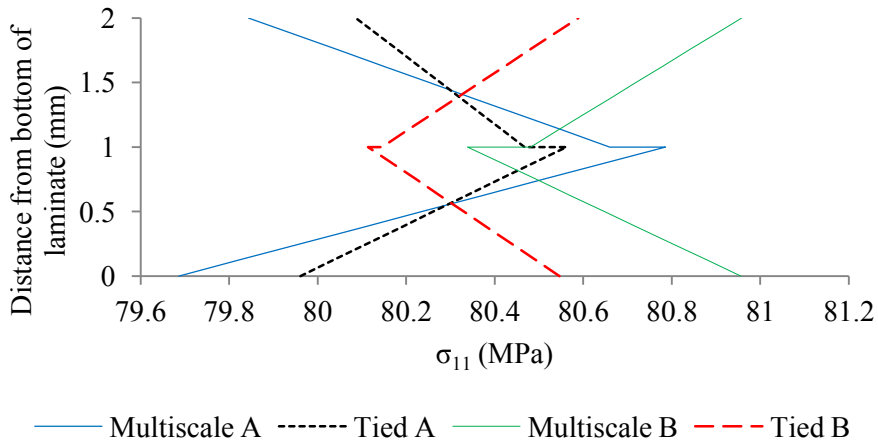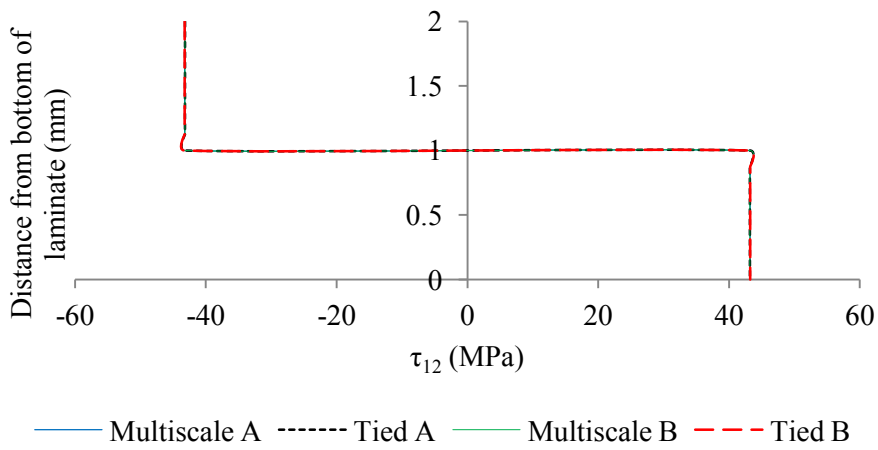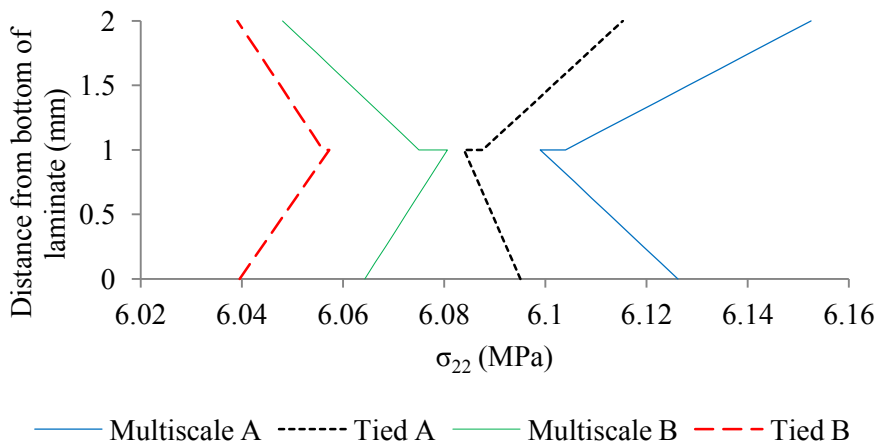
(c) σ_{22}.

Figure 5.22.: Through thickness plots of stress components at selected points (see Figure 5.2) in a $[45_4, -45_4]$ laminate under the boundary conditions shown in Figure 5.20. Nonlinear geometric effects are considered.

(a) σ_{11}.

(b) τ_{12}.
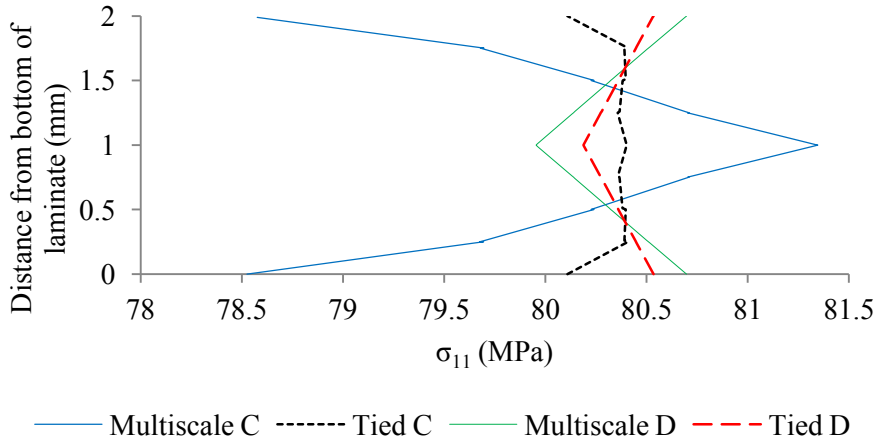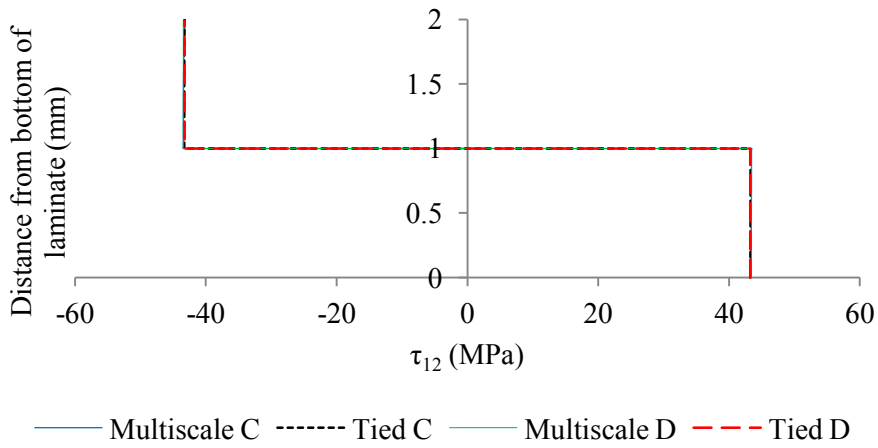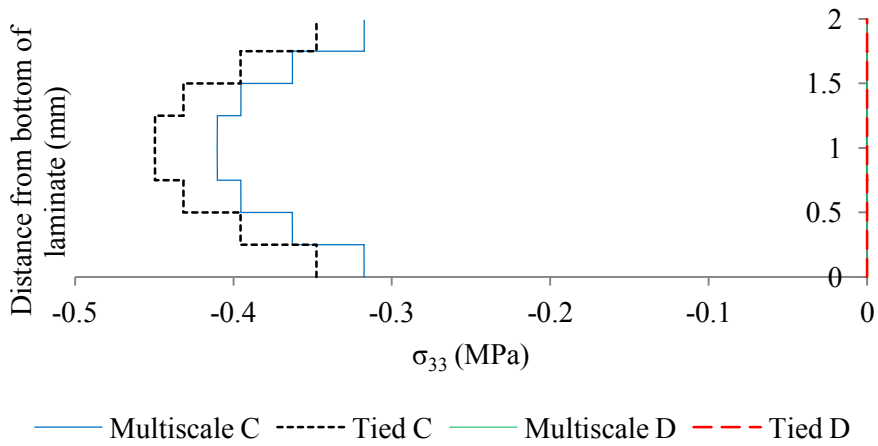
(c) σ_{33}.

Figure 5.23.: Through thickness plots of stress components at selected points (see Figure 5.2) in a $[45_4, -45_4]$ laminate under the boundary conditions shown in Figure 5.20. Nonlinear geometric effects are considered.
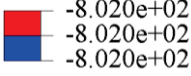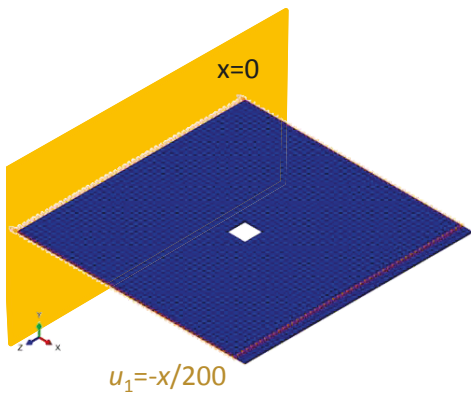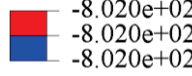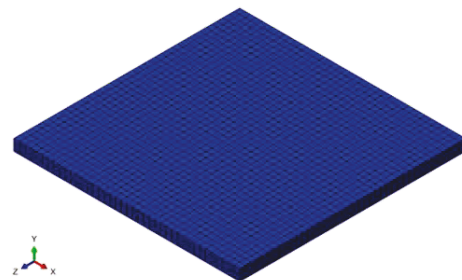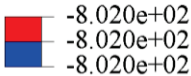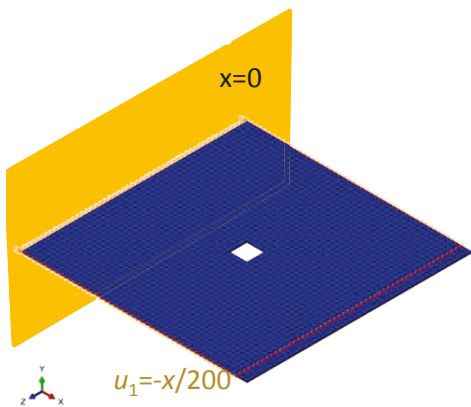
of the corresponding face on the global boundary. Thus the shape of the local boundary is not fully defined before the analysis. Hourglass deformation modes triggered by this additional constraint would explain these local deviations in σ_{22}. Hourglass deformation is a common problem in the finite lement method when linear reduced integration elements are used, and it allows stress free deformation in a regular mesh [75]. As the peaks only affected the first layer of elements, any hourglass deformation modes did not propagate into the model, and this was not considered a serious limitation to the model, as long as care is taken to locate the boundary of the global and local models away from areas where the solution is of interest.

In addition to the stress plots along paths, through thickness plots at various points along this path (Figure 5.2) are presented to provide greater insight into the behaviour of the coupled models. These plots are shown in Figures 5.6, 5.7, 5.10, 5.11, 5.14, 5.15, 5.18, 5.19, 5.22 and 5.23. The test cases involving unidirectional laminates were the simplest, removing any differences in through thickness discretisation of properties between global and local modelling strategies and allowing the coupling method to be examined for fundamental defects. The symmetric $\pm 45_{2S}$ laminate added this complexity to the model while allowing the plate to remain planar, and finally the unbalanced laminates introduced tension-bending and tension-twisting coupling into the model so the method could be evaluated under out of plane deformation modes.

For the local models σ_{11}, τ_{12} and σ_{33} were plotted. σ_{11} and τ_{12} because they were the most significant components and σ_{33} because it provided an insight into how the multiscale approach managed the difference between continuum shell and solid element formulations for through thickness deformation. For the global models, however, through thickness variation of σ_{33} was not available and this is a limitation of continuum shell elements [75]. σ_{22} was plotted instead.

The test cases have demonstrated that the coupling approach is appropriate in unidirectional laminates (Figure 5.4 and Figure 5.8), laminates where stress components vary between plies (Figure 5.12) and cases involving bending and twisting (Figure 5.16). In each of these plots the tied model solution is taken as the control solution, and it should be noted that the control solution does not vary significantly by location for these test cases. It can be seen that for points A and D the multiscale solution is closer to the control solution than for points B and C. This is due to the fact that points B and C are closer to the global-local boundary and hence more greatly influenced by the stronger constraints discussed earlier in this section. It should be noted however that the scales on these plots are very large because the differences between multiscale and control solutions is typically less than 1%. The fact that these effects diminish away from the boundary means that this is not considered a significant limitation.

In Figure 5.7, There are significant σ_{33} stresses at point C which do not exist in the control solution. Note that these stresses are of the order of 1% of σ_{11}. These stresses are most likely due to differences in the way Poisson's ratio effects are accounted for in the continuum shell elements of the global model and the solid elements of the local

110

model. Combined with the constraints on the local boundary discussed earlier this could lead to significant through thickness direct stresses close to the local boundary. Even though the through thickness Young's modulus and Poisson's ratio was specified for the continuum shell elements to match those of the global model, these stresses persisted and it was concluded that this was an unavoidable consequence of the differences in element formulations. These stresses diminished away from the local boundary. In this figure the stepped pattern of stresses is pronounced, but it can be seen in other plots of stress components at points C and D. This is because reduced integration linear elements were used and hence the stress component σ_{33} is constant through an element thickness. The steps correspond to element boundaries.

Discontinuities in σ_{11} may also be seen in Figures 5.7, 5.11, 5.15, 5.19, 5.23 where they would be expected to be continuous. These effects were also attributed to hourglassing but because the magnitude of the discontinuities at element boundaries were small compared to the magnitude of σ_{11}, the effect of hourglassing was not considered significant.

For the case of $\pm45_{2S}$ laminates (Figures 5.14 and 5.15), the sign of τ_{12} reverses between adjacent plies due to the fact that the 2 directions are opposing between plies.

The through thickness stress plots for the geometrically linear and nonlinear cases with unsymmetric laminates should be compared (Figures 5.18, 5.19, 5.22 and 5.23). In both cases through thickness trends in the tied solution are also seen in the multiscale solution. However, while the through thickness distribution of stress components, most notably σ_{11}, remains the same at all points in the geometrically linear case, the through thickness position of peak σ_{11} changes by point in the nonlinear case. At points B and D the peak σ_{11} values are at the top and bottom surfaces of the laminate while at points A and C the peak value of σ_{11} is at the midplane. Note that the boundary conditions applied to the global model effectively restrain the plate against rotation about the z-axis since the displacements in the x direction are specified on the top and bottom surfaces of the continuum shell. Since tension in the x direction of the unbalanced laminate results in rotation about z, this could explain the variation in through thickness σ_{11} distribution within the global model. The further from the boundaries, the more the material may rotate about z. As the 1 direction of a lamina rotates out of the plane, the imbalance in the stiffness of the two halves of the laminate in the loading direction diminishes. The result is a change in through thickness distribution of σ_{11}.

In the local region, the point where the peak σ_{11} values are at the midplane of the laminate is close to the global-local boundary. Within the global region, the fact that there are multiple elements through the thickness of the laminate allows transverse shear flexibility to be captured. However, where the local boundary is coupled to the global model, local boundary nodes are constrained to remain in the plane of their corresponding global element face. This means that the local boundary is effectively rigid in transverse shear and this accounts for the change in through thickness distirbution of σ_{11} within the local model. As can be seen in Figure 5.23, at point D, the through thickness distribution of σ_{11} has returned to a distribution similar to that at point B (Figure 5.22), with the

peak σ_{11} values at the upper and lower surfaces. Since the effect of the constraints against transverse shearing were localised at the global-local interface, this was not considered a major limitation. It only requires that the boundaries are located sufficiently far from regions of interest.

Following this successful testing of the coupled global-local approach, further comparisons against experimental data could be conducted.

5.3. Comparison to experimental data

5.3.1. Model details

Having demonstrated the applicability of the method in Section 5.1 using established modelling techniques, the use of the method to model a component using two local regions for which experimental data is available is presented. The tests in question are those described in Chapter 3. The two runouts closest to the centre of the panel are modelled using local regions. They are close enough to each other that it may be presumed that the failure of one depends on the state of damage in the other. For this reason it may be argued that a fully coupled approach to modelling the two local regions within the global model may be beneficial. It is the aim of this section to demonstrate these benefits.

An implicit dynamics solver was used in the analysis of the runouts. Since much of the deformation was quasi-static, stabilisation in the form of viscous coefficients could be applied to aid convergence.

For the dimensions, layups and material properties, refer to Chapter 3. The global model is meshed with continuum shell elements. Each laminate has one element through the thickness. A global element size of 3mm was specified for the in plane dimensions. Separate meshes were defined for the plate and each L-shaped stiffener half. These meshes were connected with tie constraints.

For the local meshes, each ply was meshed with a single layer of solid elements. Separate meshes were defined for the plate regions, the L-shaped stiffener halves and the filler region. Note that the filler was assumed to have the same properties along its axis as a unidirectional laminate in the fibre direction. The plate was bonded to all other components using cohesive contact (with damage models described in Section 2.2.2. All other interfaces between components were modelled with tie constraints. Dimensions of elements in the plane of the laminae ranged from 2mm away from regions of interest (i.e. where debonding was expected) to 0.25mm at the runouts.

The properties used for one ply in the local models and of the adhesive are summarised in Table 5.2 and Table 5.3 respectively. As discussed in Section 2.2.2, the normal and tangential modes in the cohesive layer are considered independent. For damage initiation a quadratic stress criterion was used, and for evolution the BK law with an exponent of 8 is applied. The division of the domain into global and local regions is illustrated in Figure 4.3.

Table 5.2.: Ply properties used in the stiffened plate model.

Property	Value	Unit
Density, ρ	2.7×10^{-6}	kg mm^{-3}
Longitudinal modulus, E_{11}	160400.0	MPa
Transverse modulus, E_{22}	9290.0	MPa
Out of plane modulus, E_{33}	9290.0	MPa
Shear moduli, G_{12}, G_{13}, G_{23}	4810.0	MPa
Poisson's ratios, ν_{12}, ν_{13}, ν_{23}	0.33	-

Table 5.3.: Adhesive properties used in the stiffened plate model.

Property	Value	Unit
Normal stiffness, K_{nn}	1.0×10^6	MPa mm^{-1}
Tangential stiffness, K_{ss}, K_{tt}	1.0×10^6	MPa mm^{-1}
Critical normal traction, N	50	MPa
Critical in plane traction, S_1, S_2	60	MPa
Normal fracture toughness, G_{NC}	0.9	kJ
Tangential fracture toughness, G_{S1C}, G_{S2C}	2.5	kJ

As seen in Chapter 3, the growth of debonds becomes unstable following a small amount of initial debonding. This can cause problems for a quasi-static solver due to the large amounts of elastic energy which are, in reality converted to kinetic energy. Due to the viscous stabilisation applied in this model however, this elastic energy would be dissipated by artificial mechanisms, resulting in an invalid solution. As a result, only the initial stable part of the deformation was modelled. That is, the applied displacement was limited to 5.75mm. This corresponds to the point where crack jumps begin to occur in the experiments.

5.3.2. Results

The analysis was considered converged in the second iteration. Thus the results presented here are for the zeroth, first and second iteration. In the zeroth iteration the user element stiffnesses are derived from the undamaged component about an undeformed state. The hotspot at the runout of the long stiffener will be refered to as component A, the hotspot at the runout of the short stiffener will be referred to as component B.

The scalar damage variable which is part of the damage model for the adhesive layer (discussed in Section 2.2.2) can be plotted for the interface between the stiffener and the plate for each iteration. It is not plotted for the zeroth iteration as in this case the adhesive layer is undamaged. The damage variable in iterations 1 and the converged iteration for components A and B are shown in Figure 5.24 and Figure 5.25 respectively. Damage initiated earler in the model of the long runout than in the model of the short

runout. It may be noted that in the converged iteration the extent of damage in both runouts has diminished compared to that in iteration 1. Furthermore the adhesive layer in component B shows only a very small area of damage. The fact that the extent of damage in the stiffener runouts decreases from the first to the second iteration is consistent with the beam analogy drawn in Section 3.6. In the first iteration, the global model contains superelement stiffness matrices corresponding to fully bonded stiffeners. This means that the stiffer regions of the beam representation extend for the full length of the stiffeners, while the more flexible region (corresponding to unstiffened lengths of the panel) is at its shortest. The beam therefore has its maximum overall bending stiffness in iteration 1, so this iteration is the one in which the highest bending stresses are expected at the runouts. In iteration 2, the superelement stiffness matrices now correspond to the runouts where some debonding has taken place. In the beam representation, this could be represented by restricting the stiffer sections to regions where the stiffeners are bonded. The result is that the more flexible region is longer and the overall bending stiffness of the beam is reduced. Hence the bending stresses at the runouts decrease, and this is accompanied by a decrease in traction, and thus damage, in the bondline.

The load-displacement curves from the experimental tests have also been compared to those from each iteration of the structural model. These are plotted in Figure 5.26. Note that in the global model, geometric nonlinearities are the only nonlinearies present. The effect of damage can be seen by comparing the results of each iteration. The slope of the load-displacement curve decreases in iterations 1 and the converged iteration compared to iteration 0. This is due to the loss of bending stiffness in the plate when the stiffeners begin to debond (see Section 3.8).

Bending measure (see Section 3.6) is plotted against applied load in Figure 5.27 for both long and short stiffener runouts. The experimental bending measure is also plotted against load for specimens 3, 4 and 5 for comparison. Load data was not availabe for specimens 1 and 2 due to equipment malfunction.

5.3.3. Discussion

It has been seen in Figure 5.26 that the initial gradient of the load displacement curve for the numerical results obtained via the multiscale approach is double that from the experimental results. There are many factors which could lead to this discrepancy. One of the most significant is possibly the filler region, where the fibres were twisted to an unknown extent and were seen to be fairly dry (Figure 3.24), and in the bondline which was seen to contain voids after testing. In Finite element models, the filler region was modelled as a homogeneous region filling the space between the plate and stiffener halves with the properties of the UD laminate, and the fibre direction aligned with the stiffener. This was the most stiff definition of the filler and is likely to account for a significant part of the difference between experimental and numerical results. Note that the initial gradient of the load displacement curve obtained during numerical design in Figure 3.6

Iteration 1:

Scalar damage variable:

+1.000e+00
+8.571e-01
+7.143e-01
+5.714e-01
+4.286e-01
+2.857e-01
+1.429e-01
+0.000e+00

Converged solution:

Scalar damage variable:

+9.993e-01
+8.565e-01
+7.138e-01
+5.710e-01
+4.283e-01
+2.855e-01
+1.428e-01
+0.000e+00
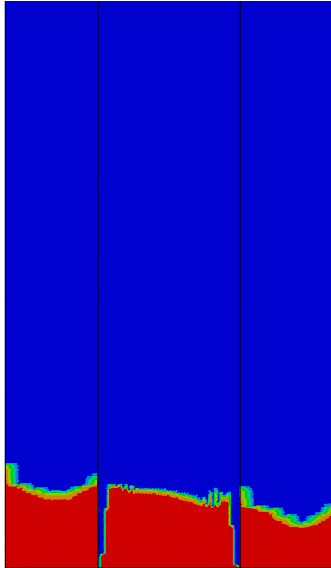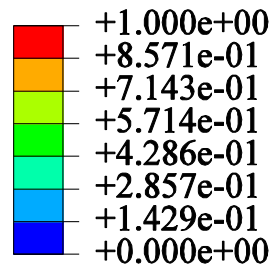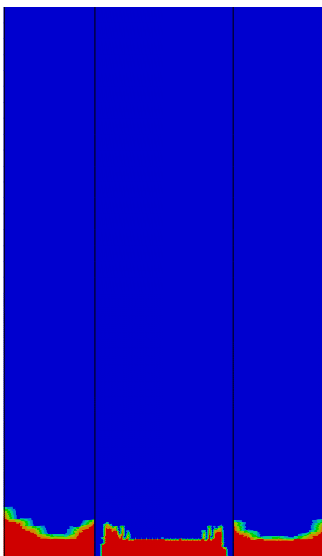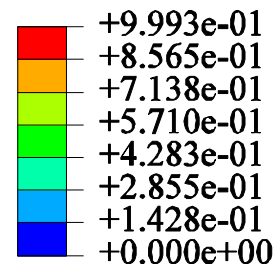
Figure 5.24.: Scalar damage variable at the long stiffener runout for iteration 1 and the converged solution.

Iteration 1:

Scalar damage variable:

+8.598e-01
+7.370e-01
+6.142e-01
+4.913e-01
+3.685e-01
+2.457e-01
+1.228e-01
+0.000e+00

Converged solution:

Scalar damage variable:

+9.977e-01
+8.552e-01
+7.126e-01
+5.701e-01
+4.276e-01
+2.851e-01
+1.425e-01
+0.000e+00
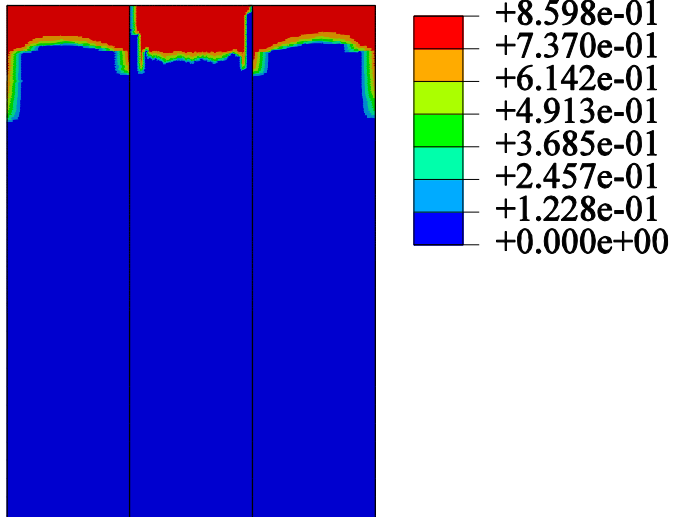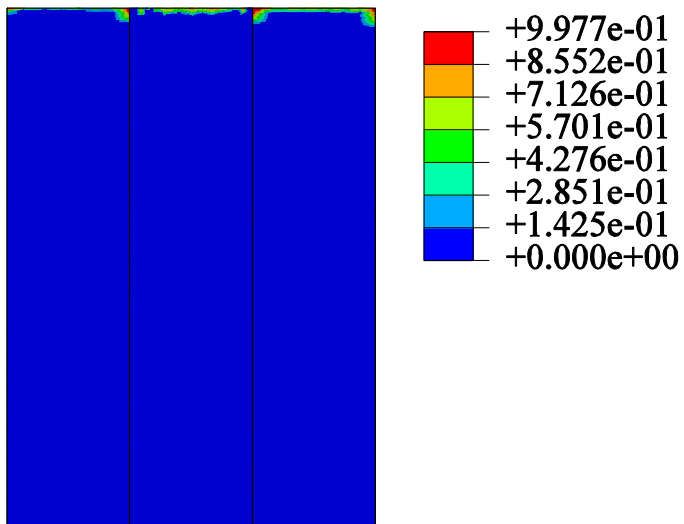
Figure 5.25.: Scalar damage variable at the short stiffener runout for iterations 1 and the converged solution.
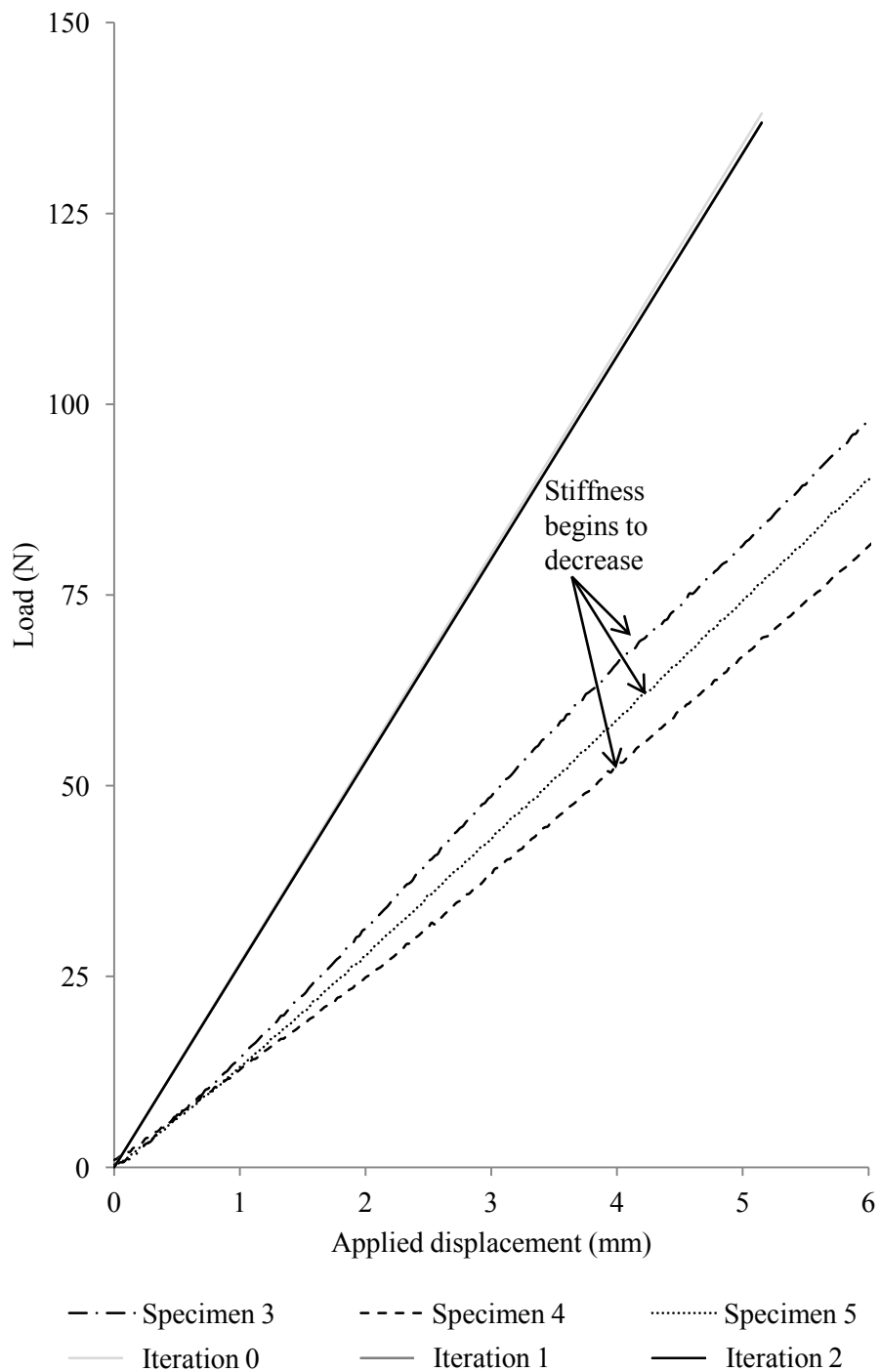
Figure 5.26.: Comparison of experimental load-displacement curves to the coupled global-local results.
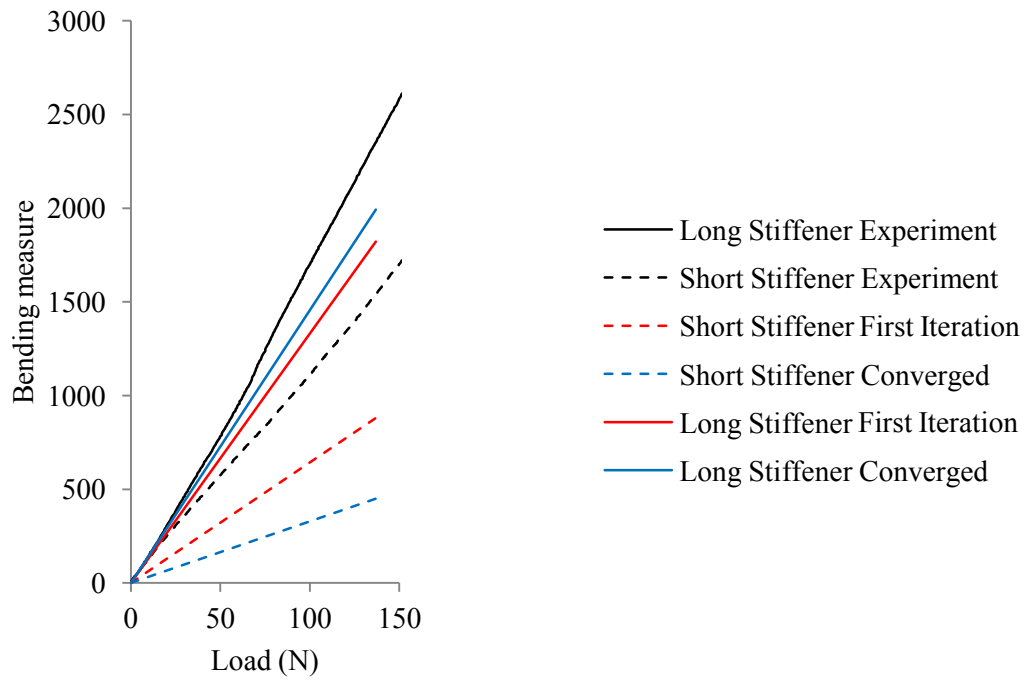
(a) Specimen 3.

(b) Key.
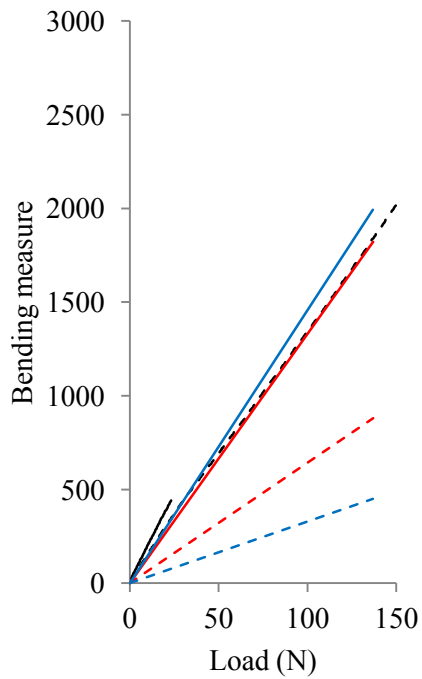
(c) Specimen 4.
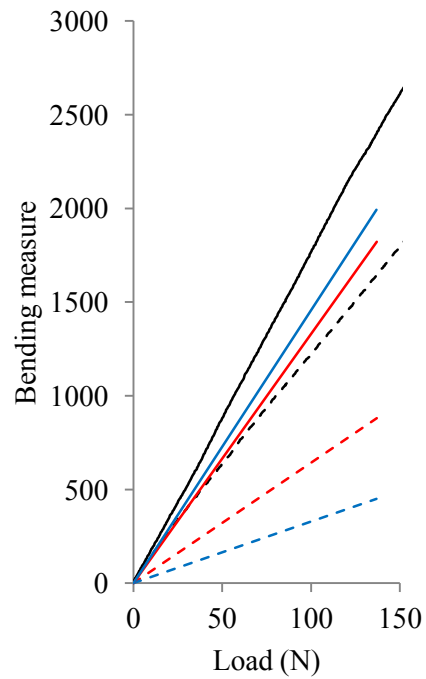
(d) Specimen 5.

Figure 5.27.: Bending measure (see Section 3.6) determined numerically for the first iteration and the converged iteration at the runout of the long and short stiffeners plotted against applied load. Experimental data is included for comparison.

is comparable to that obtained using the multiscale method. Both modelling techniques included the same representation of the filler.

Furthermore, there was a range of 25% in the longitudinal modulus of the laminate between data sources. In addition the modelling of the supporting and load points was idealised to occur at a fixed set of nodes, while in reality there could have been significant slipping of the loading pins relative to the surface of the plate. This, combined with the compliance of the rig mean that there is a large margin of error in the experimentally determined load-displacement curves. As a result the load displacement curves obtained by the multiscale approach are taken to be within the experimental accuracy.

In both Figure 5.24 and Figure 5.25, it is shown that the extent of damage in the converged iteration is lower than that in the first. The fact that the extent of damage differs in iterations 1 and the converged iteration for both runouts may be used as an argument for fully coupled global-local approaches over simple submodelling. The results of iteration 1 are equivalent to the results of simple submodelling - by this point no effects of damage have been passed back to the global model. Comparison with experimental observations, where the damage in the converged iteration agrees well with that measured in the tests suggests that the fully coupled approach is able to capture effects that the simple submodelling approach would miss. Specifically, the redistribution of stresses due to the failure of one component have been shown to significantly affect the solution in an adjacent component.

Since the boundary conditions on the local models correspond to a linear ramp of the final global displacements in the previous iteration, it is not possible to match a time value in the global model to a time value in a local model.

While it is not possible to relate time values between a global and a local model, or indeed between two local models, in the converged numerical solution damage in the short stiffener was only just initiating at the end of the deformation step. Debonding occured earlier in the step for the long stiffener. We are therefore able to say quantatively that the numerical sequence of failure matched the experimental. An incremental global approach could provide more information about failure sequences and is discussed in Section 9.2.

In the range of applied loads plotted in Figure 5.26, there are very small changes in stiffness of the component as debonding begins to occur. The point where the stiffness begins to decrease has been marked for each curve.

Since the stiffness of the component is linearised about its final state in the component level analysis, and the first component iteration is about an undeformed state, it is expected that the load-displacement curve for iteration 0 (at the structural level) should be tangent to the experimental data at the start of the deformation. In fact, as discussed earlier in this section, the gradient of the load-displacement curve for iteration 0 is almost twice the initial experimental gradients. However, the gradients of load displacement curves for iterations 1 and 2 are slightly lower than that for iteration 0 (Figure 5.26), due to damage which has occured in the stiffener runouts.

In the final iteration the stiffness of the component is linearised about the converged

deformed configuration at the final displacement specified in the structural model (5.75 mm). As relatively little plastic deformation is expected, the stresses at the component boundaries should be low on unloading the specimen. This is a requirement as all material properties in the structural model are linear elastic so upon unloading there will be no internal forces in the model. Hence the end point of the load displacement curve from the final iteration should lie on the experimental curve. As seen in Figure 5.26, the end point of the load displacement curve for iteration 2 does not lie within the range of loads observed in the experimental results. This is due to the high stiffness of the finite element models, and experimental factors affecting the recorded loads discussed earlier in this section.

Since the load displacement curves for the finite element model in Figure 5.26 are extracted from the global results, the drop in gradient in this plot shows that damage in the local region may affect the global solution. Demonstrating this was one of the objectives set out in Section 2.7.

Bending measure is plotted against load in Figure 5.27 for both experimental and numerical results. As with the load-displacement curves, the loads for the numerical results were higher than the experimental loads, reflecting the high bending stiffness of the model relative to the specimens. Note that only bending measure determined at the end of the analysis step is meaningful since the multiscale approach uses a single iteration which is converged at the end point of the analysis.

There is a significant difference between bending measures in the first and converged iterations, supporting use of a fully coupled global-local approach. The first iteration is the solution which would be obtained using traditional global-local approached and is not converged. The effect of damage in the runouts can be seen in the changing gradients of the bending measure-load curves.

For the long runout, the gradient of the bending measure-load curve increases from the first to the converged iteration. This signifies a loss in bending stiffness at the runout as the debond in the long stiffener is not present in the first iteration, but it is in the converged one. This is an indicator that the use of coupled global local approaches have advantages, since the effect of this loss of stiffness in the local model would not be present in the global solution of an uncoupled set of models.

For the short runout the gradient is lower in the converged iteration than the first iteration. This signifies a drop in bending moment at the short runout due to the loss in stiffness in the long runout, as discussed in Section 3.6.

In each graph in Figure 5.27, it can be seen that the converged bending moment-load plot agrees more closely with the experimental results. Again this shows the advantages of fully coupled global-local approaches over uncoupled approaches. However, the converged plot for bending moment against load at the short stiffener is a worse match for the experimental data than the first iteration. This is due to the fact that the models had a higher bending stiffness than the specimens, for reasons discussed earlier in this section. As a result the bending measure at the short stiffener is lower than the experimentally measured values. Because of this the increase in bending measure in the first iteration due

to the higher, unconverged extent of damage in the short stiffener makes the first iteration result look like a better match for experimental data. In fact the drop in bending measure at the short stiffener from the first to the converged iteration is expected. The decrease in gradient of the experimental curves for the short stiffeners over the range of loads shown supports this.

5.3.4. Conclusions

In this section it has been shown that the coupling method is suitable for use when modelling a structure with adjacent regions vulnerable to damage. The bending stiffness of the finite element models was significantly higher than that of the specimens. This has been accounted for in the stiff representation of the filler region in the finite element models and initial defects in the bondline of the specimens which could not be modelled. The agreement with the experimental data for the onset of bondline damage provides confidence in the technique. Furthermore, the improved correlation in iteration 2 compared with iteration zero (equivalent to one-way submodelling) means that there is a case for using fully coupled global-local approaches over simple submodelling where failure of one region is likely to lead to a significant redistribution of stresses in the global domain.

6. Coupling local solid meshes with global shell meshes

6.1. Introduction

Shell elements are often used in larger scale models of structures composed of thin plates, with solid models reserved for critical details. This makes a shell to solid coupling routine a natural extension to the method described in Chapter 4. Such a routine has been implemented and is described here following a similar structure to Chapter 4 which detailed the solid to solid coupling approach. An example of a typical global and local mesh is shown in Figure 6.1. The boundary between the local and global regions is labelled Γ. Within the local region, a more refined mesh is generally used. This region is typically one where a more detailed representation of the stress state is required than in the global region.

The flowchart in Figure 4.1 also applies to this coupling process and may be a useful reference in this chapter.

In exactly the same way as with the solid-solid coupling technique, local regions are represented by linearised stiffness and mass matrices relating all global nodes on Γ. The elements in each region of the global model covered by a local model are removed, and replaced by a superelement, the behaviour of which is defined by the linearised mass and stiffness matrices. The displacements at the local boundaries are also determined using displacement field in the global solution.

As with the coupling approach described in Chapter 4, the method may be described by considering the boundary Γ, which exists in global and local level models Figure 6.1. The procedure works by ensuring compatibility of superelements with both global and local level models as follows:

1. Enforcing compatibility of the displacements over the boundary Γ at the global and local levels

2. Iterating between global and local solutions until convergence so that the energy imparted via stresses at the boundary of the superelement is equivalent to that exerted by the local model boundary conditions.

As will be seen in Section 6.4, differences in the way shell and 3D elements represent the thickness of plate-like components mean that a unique displacement field on the 3D boundary cannot be determined from the shell representation. As a result, unlike the

Global
model:

Local
region

Γ

Local
model:

Γ
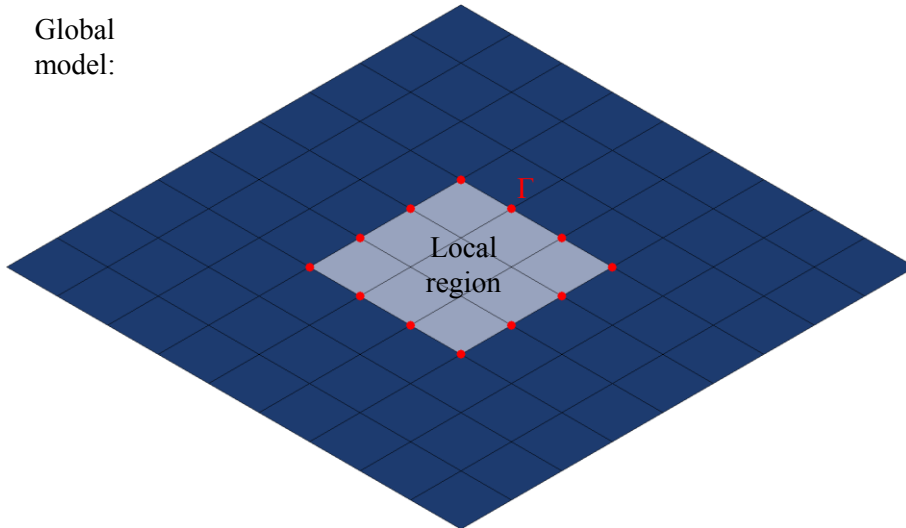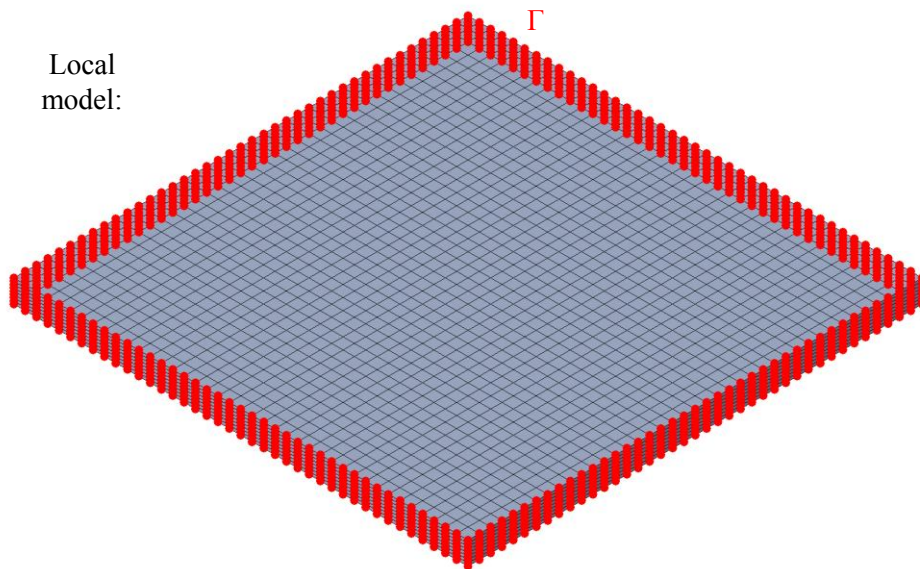
Figure 6.1.: An example of a pair of coupled models where the global model (top) is composed of shell elements and the local model (bottom) is solid element based. Light blue elements represent the local region. Highlighted nodes are the boundary nodes.

method described in Chapter 4, here an approximation of the displacement field at the local boundary must be selected.

6.2. An example of coupled models

Consider the models shown in Figure 6.1. The shell element model is computationally light, and may be analysed very quickly for a large range of boundary conditions, assuming linear material behaviour. Imagine a hypothetical defect, such as an initial delamination at the centre of the plate. The shell model is unable to capture stress gradients involved when a crack propagates from this defect. Hence a more refined solid mesh is required. The increased refinement limits the domain which it is feasible to analyse to a subset of the shell mesh (the light blue region in Figure 6.1). The solution is to couple the two models, with the bulk of the plate meshed in shells and a local region meshed in solid elements.

6.3. Transformation of vectors into a single coordinate system

As discussed in Section 4.3, since the local models are defined separately from the global models, coordinate systems may not be consistent. In order to perform the calculations described in these steps, there needs to be a unified coordinate system in which equivalent points in the global and local models have the same coordinates, and vectors have the same components. Here it is noted that points and vectors have a transformation applied to them, and the details of this transformation may be found in Section 4.3.

6.4. Shape of the deformed boundary

In the case of shell-to-solid coupling, a combination of translations and rotations at the global boundary define the purely translational boundary conditions at the local boundary. This is in contrast with the solid-to-solid coupling technique described in Chapter 4 in which translations at the global level define translations at the local boundary. It should also be noted that since shell elements have no through thickness variation in displacement variables, we are unable to define the relative displacement of component nodes in the thickness direction using these variables. The approach adopted here is to define a straight line passing through each node on the local boundary, and a fixed point on the global boundary (Figure 6.2). The deformed coordinates of this fixed point are set using the translational degrees of freedom at the global boundary. Rotations are then applied to the line and the local boundary node is constrained to lie on the line. In order to apply out of plane translations, a single layer of nodes on the local boundary (the one closest to the mid plane) is assigned 3 displacement boundary conditions rather than a line on which it must lie (Figure 6.3).

In order to simplify the application of boundary conditions, new nodes, not conected to any elements in the local model are defined at the same positions as the global boundary nodes. Later the local boundary nodes will be constrained to linear combinations of the degrees of freedom of these nodes.

The first step in constraining the local boundary is to associate each local boundary node with a shell element edge on the structural boundary. This is achieved by calculating the projection of each local node onto the line defined by each global element edge on the boundary, Γ. If the projection lies on a the shell element edge, the pair of nodes defining the edge is a candidate for the constraint. From the list of candidates the pair leading to the projection at the shortest distance from the original local node is used. If a component boundary node has a position vector $\mathbf{p}$ (see Figure 6.2 for an overview of these vectors), while the shell element nodes have position vectors $\mathbf{q}$ and $\mathbf{r}$, then the position of the component node relative to one shell node is:

$$\mathbf{s} = \mathbf{p} - \mathbf{q} \tag{6.1}$$

The vector connecting the two shell nodes (along the element edge) is:

$$\mathbf{t} = \mathbf{r} - \mathbf{q} \tag{6.2}$$

The projection of the vector $\mathbf{s}$ onto $\mathbf{t}$ is then given by:

$$\mathbf{s}_{projected} = \frac{\mathbf{s} \cdot \mathbf{t}}{||\mathbf{t}||} \tag{6.3}$$

This is the position of the fixed point in the undeformed mesh. The displacement of the fixed point, $\mathbf{u}_p$, may be defined using a linear combination of $\mathbf{u}_q$ and $\mathbf{u}_r$, the translation components of the displacements at the two shell nodes:

$$\mathbf{u}_p = \left(1 - \frac{|\mathbf{s}_{projected}|}{|\mathbf{t}|}\right)\mathbf{u}_q + \frac{||\mathbf{s}_{projected}||}{||\mathbf{t}||}\mathbf{u}_r \tag{6.4}$$

Note that this is the displacement at the same point on the shell element edge as defined by linear shape functions.

For the approach presented here, it is required that one layer of nodes on the component boundary lies on the midplane. These nodes are fixed at the deformed position of their equivalent point on a shell element (Eq. 6.4).

To constrain the remaining points on the local boundary, two approaches are suggested. In the first, all degrees of freedom of all remaining local boundary nodes are constrained according to Eq. 6.5.

$$\mathbf{u}_p = \left(1 - \frac{|\mathbf{s}_{projected}|}{|\mathbf{t}|}\right)\mathbf{u}_q + \frac{||\mathbf{s}_{projected}||}{||\mathbf{t}||}\mathbf{u}_r + \mathbf{u}_\delta \tag{6.5}$$

Where u_δ are additional displacements due to rotations at the driving shell nodes. The
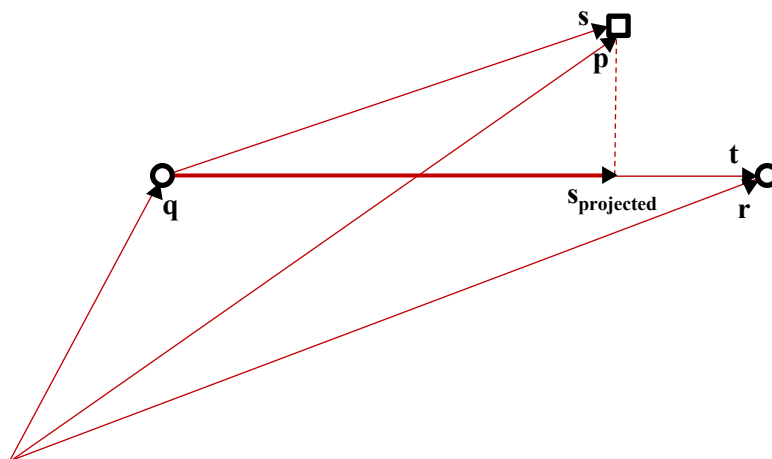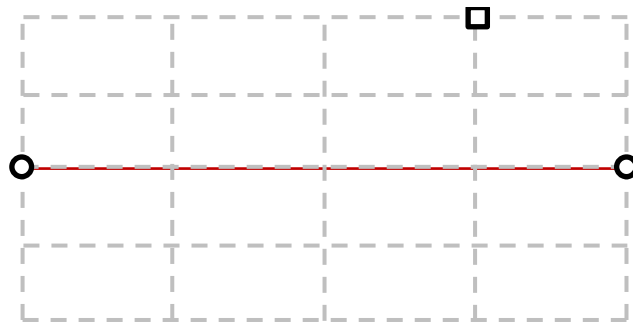
Figure 6.2.: Top: A section of the component boundary superimposed on a shell element edge. Bottom: A summary of the vectors involved in the projection of a component node onto its corresponding shell edge. The points marked with circles are the shell element nodes, and the node marked with a square is the component node.

vector $\mathbf{d}$ between a remaining node and its projection onto the shell edge is given by:

$$\mathbf{d} = \mathbf{p} - \mathbf{q} - \mathbf{s}_{projected} \qquad (6.6)$$

The rotation of point p on the shell element edge is given by:

$$\mathbf{u}_{\theta p} = \left(1 - \frac{|\mathbf{s}_{projected}|}{|\mathbf{t}|}\right) \mathbf{u}_{\theta q} + \frac{||\mathbf{s}_{projected}||}{||\mathbf{t}||} \mathbf{u}_{\theta r} \qquad (6.7)$$

Assuming small rotations $\sin\theta \simeq \theta$ and $\cos\theta \simeq 1$, the additional displacements, $\mathbf{u}_\delta$, may be approximated as the sum of additional displacements due to the rotation about each coordinate direction:

$$\mathbf{u}_\delta = \begin{bmatrix} 0 & -d_3 & d_2 \\ d_3 & 0 & -d_1 \\ -d_2 & d_1 & 0 \end{bmatrix} \mathbf{u}_{\theta p} \qquad (6.8)$$

Where:

$$\begin{bmatrix} d_1 \\ d_2 \\ d_3 \end{bmatrix} = \mathbf{d} \qquad (6.9)$$

This fully constrains all remaining local boundary nodes as a function of the driving global nodes' displacement and rotational degrees of freedom. Note that this fixes the thickness of the laminate at the local boundary. This is due to the fact that the shell formulation does not account for changes in thickness. For all examples presented, this is the approach used.

As an alternative approach to ensure that the component boundary is not overconstrained in the thickness direction, different constraints may be applied to all other component boundary nodes. This approach is outlined in Figure 6.3. The projected point (Eq. 6.4) defines a point through which the sliding axis passes. The rotations at this point on the shell edge (determined by shape function weighted contributions of the nodal rotations) are applied to the sliding axis about this point. The component node is constrained such that it may slide along the axis. Note that this approach has not been implemented here.

At this point it is important to note that if connecting shell elements are not parallel, there will be regions of the component boundary for which points may be projected onto 2 edges, and points which may not be projected onto any element edges (see Figure 6.4). For the purposes of demonstrating that the method works, the following criteria are used:

1. If there are multiple possible projections, the element edge onto which the projected distance is shortest is selected.

2. If there are no possible projections, the projection the smallest distance outside the shell nodes is selected.
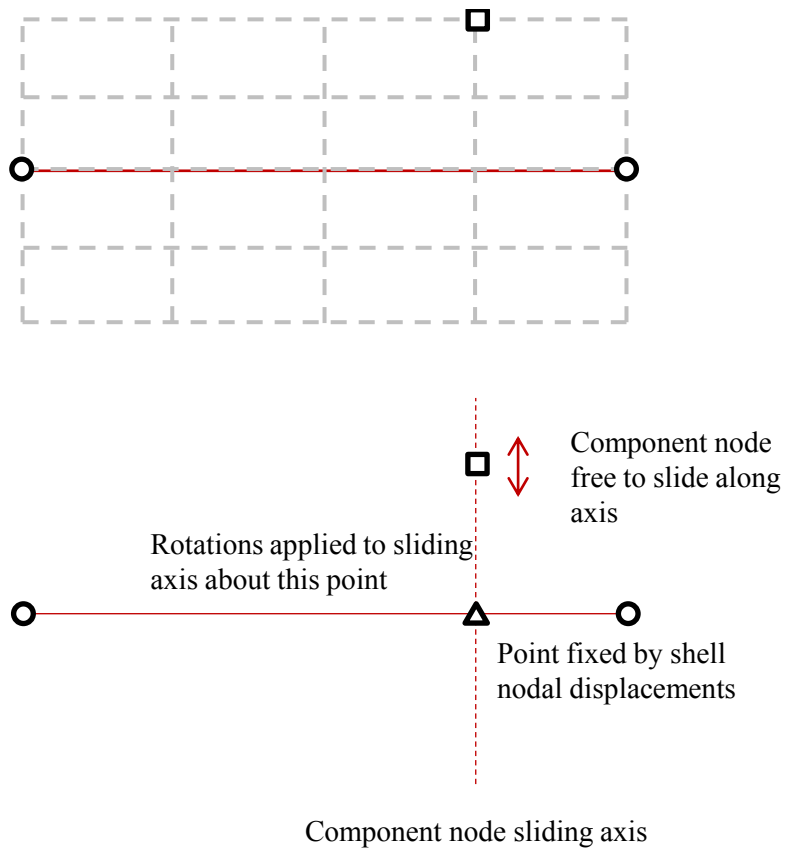
Figure 6.3.: Top: A section of the component boundary superimposed on a shell element edge. Bottom: Definition of a sliding axis for a component boundary node.

No projection onto a shell element edge

Projection onto multiple shell element edges
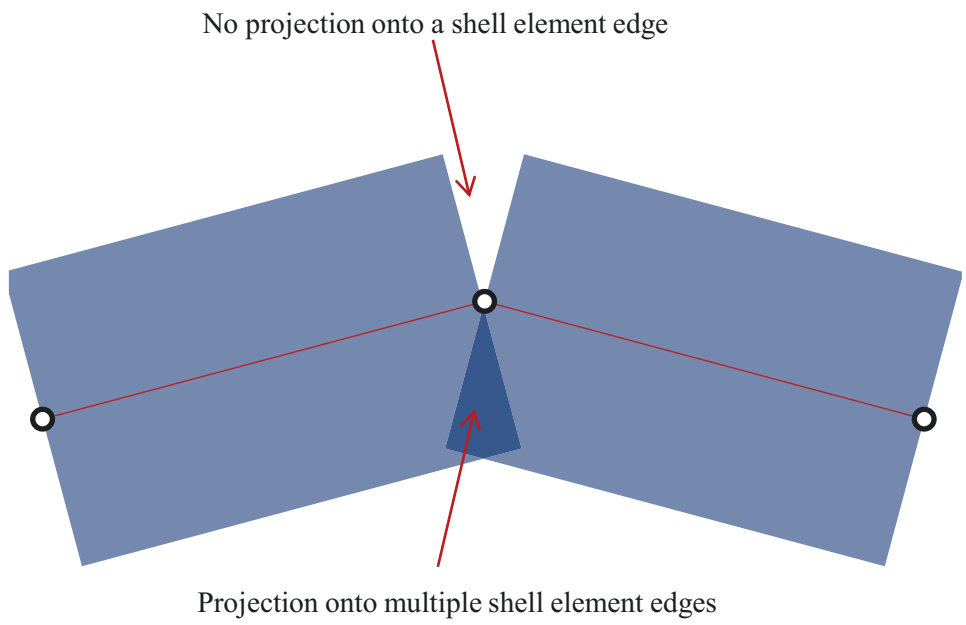
Figure 6.4.: Illustration of issues associated with non-parallel adjacent shell edges on the boundary.

6.5. Forces on the component boundary

Based on the success of the coupling approach described in Chapter 4 and tested in Chapter 5, an analogous approach to application of boundary conditions to the component boundary nodes via "virtual" nodes constrained by Lagrange multipliers satisfying the condition that a node lies on its sliding axis was used. Thus the reaction forces on the component boundary were all calculated at the "virtual" nodes.

6.6. User defined element stiffness matrices

By displacing and rotating the "virtual" nodes' degrees of freedom by a small amount in turn while fixing the others, a stiffness matrix including rotational degrees of freedom could be calculated, as for the solid-solid coupling case described in Section 4.6.

6.7. Transformation of the user defined element stiffness matrix

The inclusion of rotational degrees of freedom in the system does not affect the process by which the stiffness matrix is transformed from the component to the structural coodinate system. The transformation is performed exactly as in Section 4.7.

6.8. User defined element mass matrices

The mass matrix is obtained at a reduced number of degrees of freedom in the same way as for the solid-solid coupling case (Section 4.8). The only difference is that the mass matrix must be extracted at the "virtual" nodes in this case, since it is required to define rotational inertias at the structural nodes, and the only nodes with rotational degrees of freedom in the component model are the "virtual" ones.

6.9. Iterating

As discussed in Section 4.9, in order to obtain a converged solution, multiple iterations may be required depending on the extent of nonlinearity in the component. The effect of updating the component stiffness is measured by comparing the displacement fields in two consecutive iterations. The convergence criterion is the same as that described in Section 4.9.

7. Validation of method of coupling global shell to local solid meshes

7.1. Solid local meshes in shell global meshes

7.1.1. Test Cases

As in Chapter 5, where a demonstration of the solid to solid coupling approach on simple examples was presented, this chapter includes a comparison of the results obtained using the shell to solid coupling methodology and existing modelling techniques. The models selected for the demonstration are flat plates, consisting of 8 plies and varying layups. Details of the model attributes and test cases are given in Figure 7.1 and Table 7.1. The material properties defining a ply are in Table 5.1. The test cases were selected to include a unidirectional laminate, a laminate where the properties vary through the thickness and a laminate with coupling between membrane and twisting/bending deformations. Nonlinear geometry is also considered. Including a laminate where membrane deformation was coupled to bending and twisting ensured that the performance of the coupling technique when rotational degrees of fredom were nonzero was investigated.

   For each test case, three sets of results are plotted. The first is a reference solution obtained using a pre-existing modelling technique consisting of a uniform continuum shell mesh representing the entire domain. In this technique, a single layer of continuum shell elements with 50 elements along each edge was used to discretise the domain. Boundary conditions were applied to all nodes on the edge of the plate. The properties for these elements were defined using the composite layups tool in Abaqus [75], according to the material properties given in Table 5.1 and the stacking sequences in Table 7.1. The second is the global-local technique for coupling shell and solid models. The third is a direct

Table 7.1.: Test cases used to demonstrate the performance of the shell to solid global local approach.

Layup	Nonlinear geometry
0_8°	No
$[+45^\circ, -45^\circ, +45^\circ, -45^\circ]_s$	No
$+45_4^\circ, -45_4^\circ$	No
$+45_4^\circ, -45_4^\circ$	Yes

Structural mesh

Thickness: 2mm

                  1 element

Element type: S4
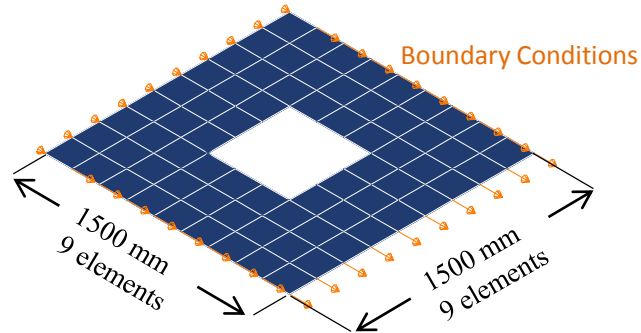
                  shell

Component mesh

Thickness: 2mm

                  1 element

Element type: SC8R

                  continuum shell
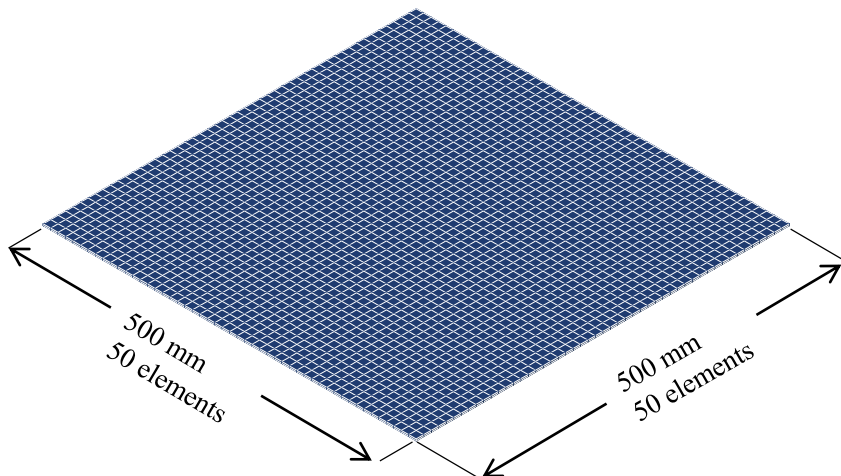
Figure 7.1.: Test case models for shell to solid global local approach. Boundary conditions are applied to the global model (top) at the regions highlighted in orange.

application of the substructure generation technique available in Abaqus [24], combined with a user element in the global model. The latter approach is discussed in Section 5.1.2

In Chapter 5, tied models were used as the reference case. Many finite element packages include an equivalent technique for tying shell to solid models (often called shell-to-solid coupling). In this case, where the tied boundaries were rectangular the shell-to-solid coupling approach gave unexpected values due to incorrect application of coupling constraints at the corners. As a result, models with a uniform mesh were used to obtain the reference solution.

In each case, boundary conditions were applied to the edges of the shell mesh corresponding to a uniform strain in the 0° direction of 0.5%. That is, if the x axis is parallel to the 0° direction, the applied displacement to the edge nodes is $\frac{x}{200}$, where x is the x coordinate of the node. The displacement is enforced parallel to the x axis with all other degrees of freedom unconstrained.

7.1.2. Results

As was the case with the solid to solid coupling approach in Chapter 5, a range of different laminates were considered. For each one plots of stress components along a line perpendicular to the loading direction and along the midline of the plate are shown (Figures 7.3, 7.7, 7.11, 7.15), as well as contour plots for direct stress in the loading directions (Figures 7.4, 7.8, 7.12, 7.16). In addition, plots of various stress components are plotted at a selection of points along ab. The positions of these points, labelled A-D, are shown in Figure 7.2. For each laminate, the results of the coupling simulation are compared to a the results of a full continuum shell model of the entire domain with the same refinement as the component region. The result of the direct application of a substructuring approach with nearest node matching between the scales is also provided for comparison. These approaches are commonly available in commercial finite element software.

7.1.3. Discussion

As was seen in Chapter 5, the direct application of the Abaqus substructuring approach leads to unsatisfactory results. This is due to inappropriate treatment of the component boundary. As discussed in Section 5.1.2, a direct application of substructuring and superelements such as this one results in a superelement which is too flexible and loads being passed into the local region via a subset of the boundary nodes. The result is that stresses are redistributed incorrectly around the superelement within the global model, and within the local bands of high stresses appear between the subset of boundary nodes which are actually driven by the global solution. This effect can be seen clearly in many of the path plots of stress components, such as Figure 7.3a. There are unrealistic peaks in stress within the global model at the local region boundary. Within the local model the stresses are generally too low, although local peaks occur when the path crosses the line between two global shell element nodes on opposing boundaries. This is because there is a load
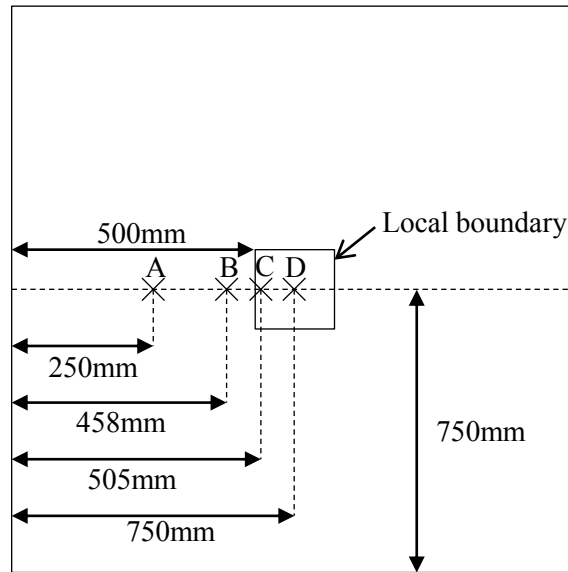
Figure 7.2.: The positions of points A-D, at which through thickness plots of various stress components are presented in this chapter. Point C is 5 mm inside the local region

path between these pairs of nodes, but the stresses are not properly distributed over the plate cross section.

If we compare the results of the global local approach to the reference solution in each case, however, we see a good agreement. At the boundary of the component and structural meshes, there are small irregularities in the stress plots. These may be explained by the transition from displacement fields extrapolated through the thickness using rotations in the structural model and interpolated from nodal displacements in the component model. The fact that no representation of thickness changes are possible in the shell representation may be a significant factor. Furthermore, small angle approximations are used in the global local approach when dealing with nodal rotations. This may also contribute to the irregularities. In all cases, however, if we consider the solutions away from these boundaries, the reference solution and that obtained using the global local approach agree well. This is true for the unbalanced laminate too, so nonzero rotations can be seen to be correctly dealt with. Given the favourable results of these test cases, a demonstration of a three scale application using both the methods detailed in Chapter 4 and Chapter 6, a simultaneous application of both approaches is presented in Section 7.2.

The path plots for all laminates but the unidirectional one (Figure 7.7, Figure 7.11 and Figure 7.15), there were deviations from the control solution in all stress components at the global-local boundary. These deviations were smaller than those in the direct solution and diminished away from the boundary. They may be explained by the constraint on the thickness of the continuum shell elements at the boundary. Since the thickness must remain

(a) σ_{11}.

(b) τ_{12}.
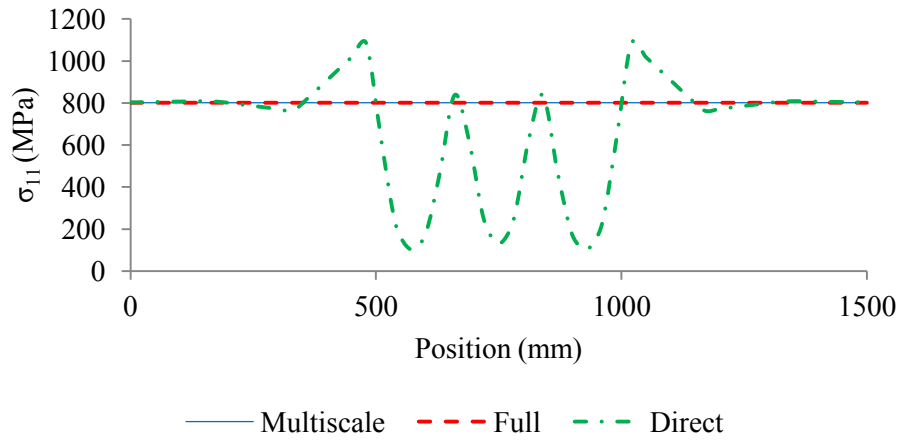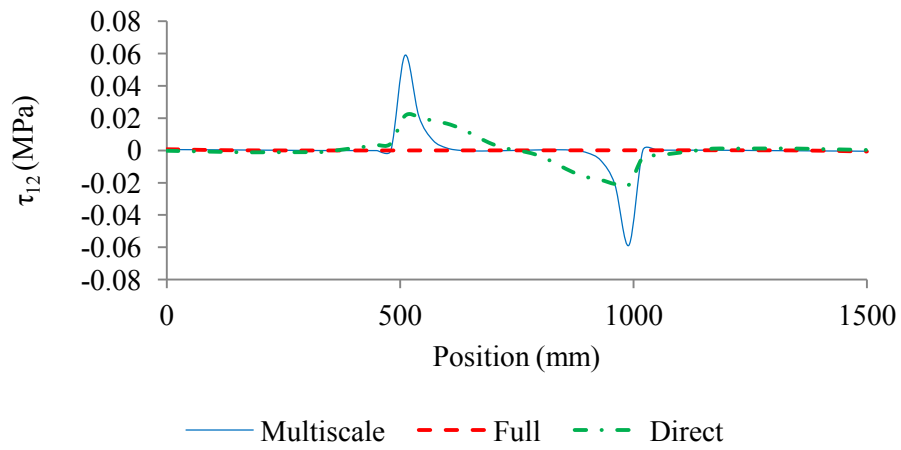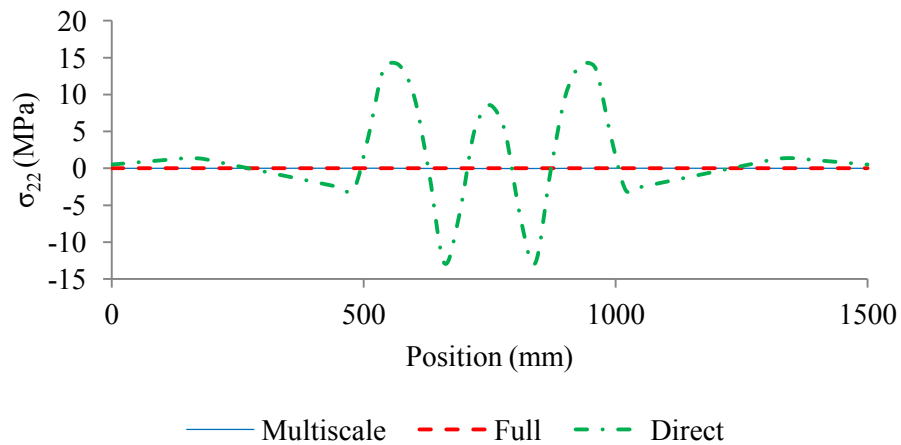
(c) σ_{22}.

Figure 7.3.: Comparison of path plots of stress components for the multiscale approach, direct application of Abaqus substructures and full uniform meshed models for a unidirectional laminate.
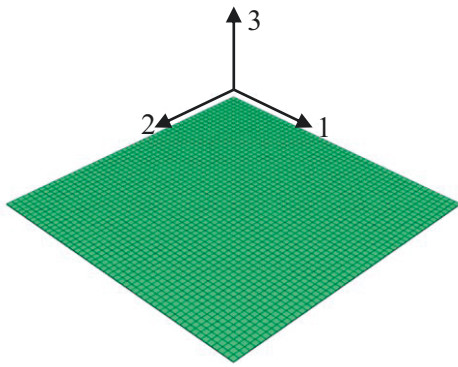
(a) Uniform mesh.
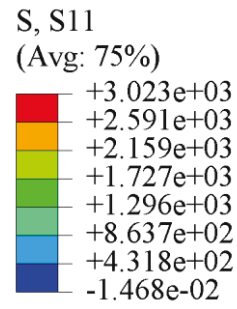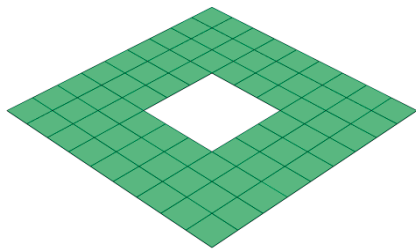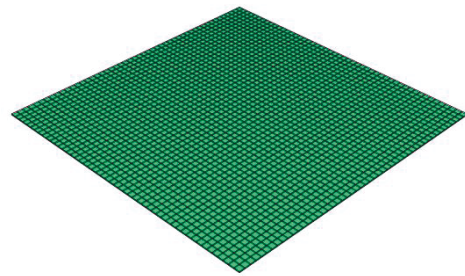
(b) Key for all figures.

S, S11
(Avg: 75%)
+3.023e+03
+2.591e+03
+2.159e+03
+1.727e+03
+1.296e+03
+8.637e+02
+4.318e+02
-1.468e-02

(c) Global model in the global-local approach.

(d) Local model in the global-local approach.
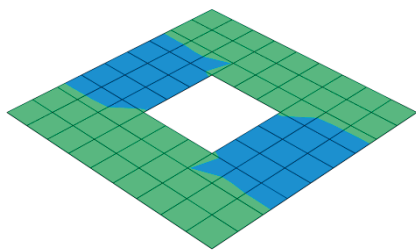
(e) Global model in the direct application of sub-
structuring.
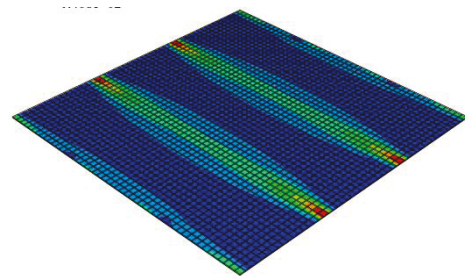
(f) Local model in the direct application of sub-
structuring.

Figure 7.4.: Comparison of contour plots of the direct stress component, σ_{11}, for a unidi-
rectional laminate in the direction of the deformation between a uniform mesh
model, the global-local approach and a direct application of substructuring.

(a) σ_{11}.

(b) τ_{12}.

(c) σ_{22}.
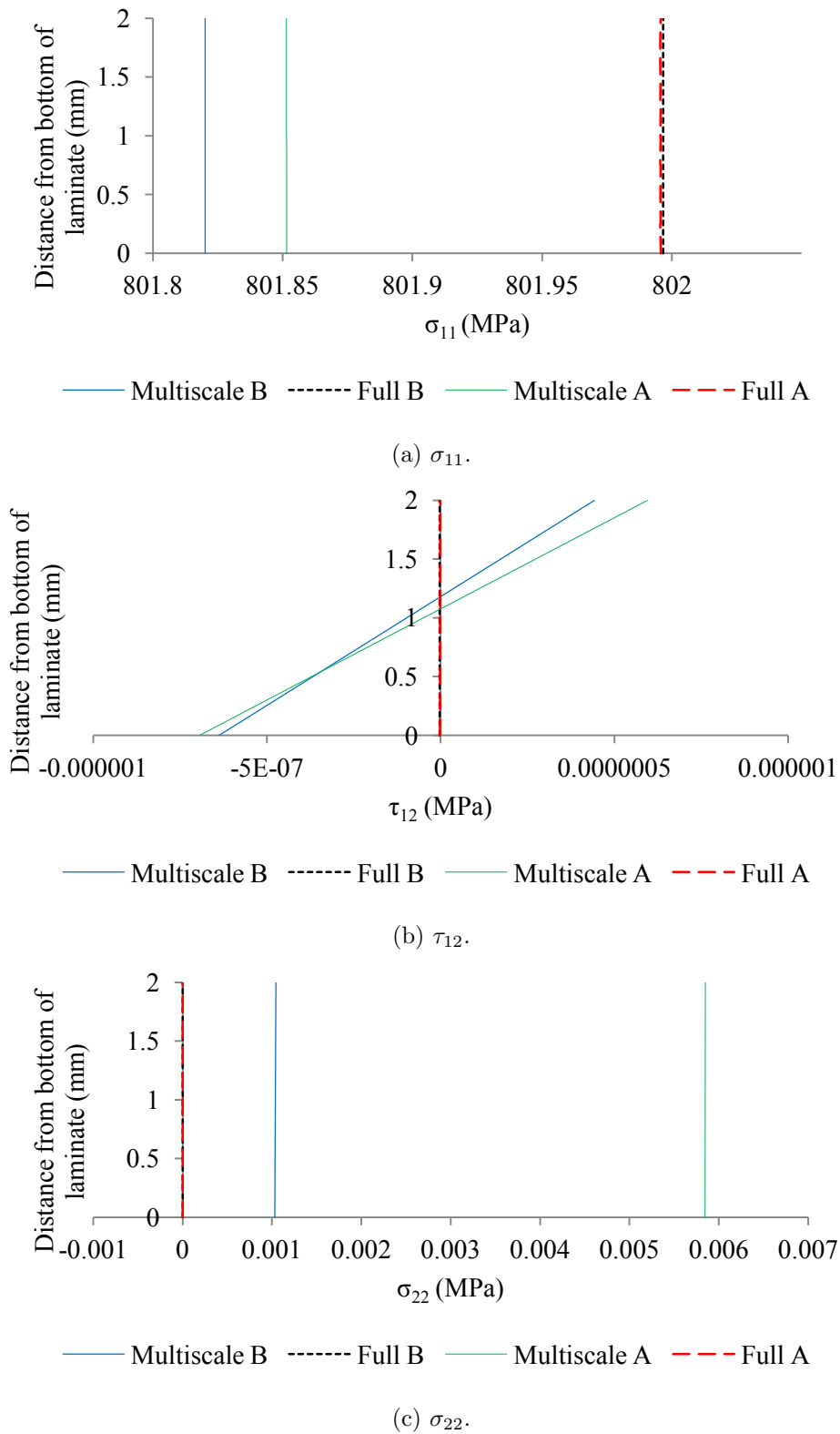
Figure 7.5.: Through thickness plots of stress components at locations A and B specified in Figure 7.2 for the layup and boundary conditions shown in Figure 7.3.

(a) σ_{11}.

(b) τ_{12}.
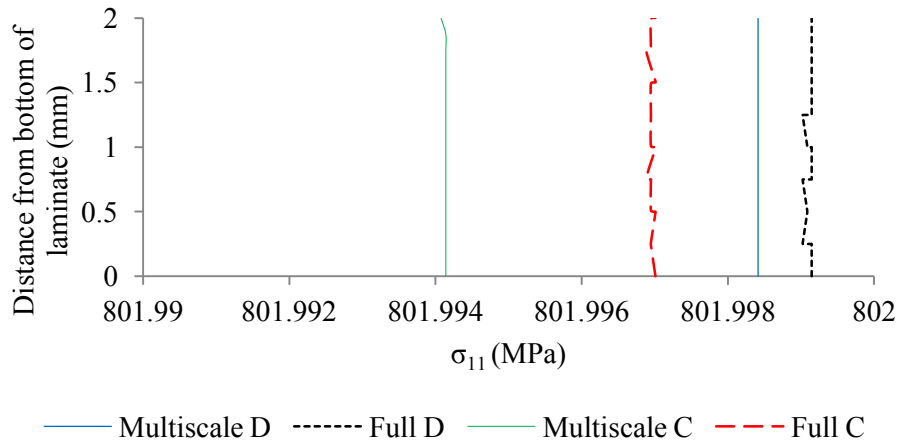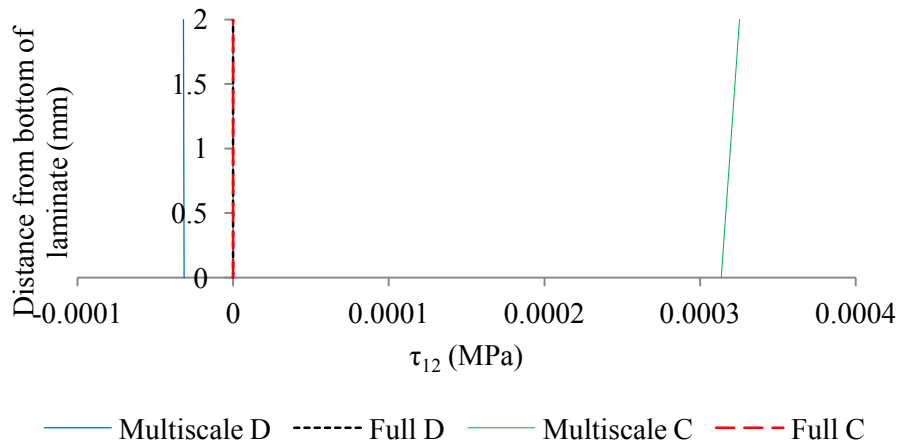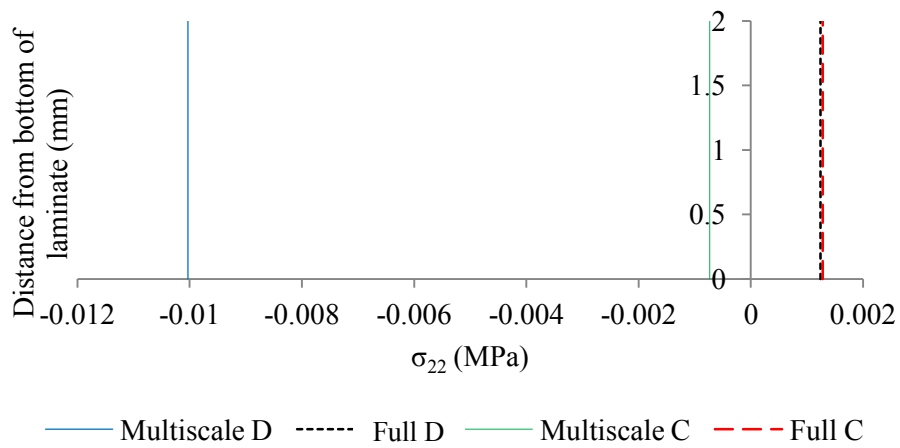
(c) σ_{22}.

Figure 7.6.: Through thickness plots of stress components at locations C and D specified in Figure 7.2 for the layup and boundary conditions shown in Figure 7.3.

(a) σ_{11}.

(b) τ_{12}.
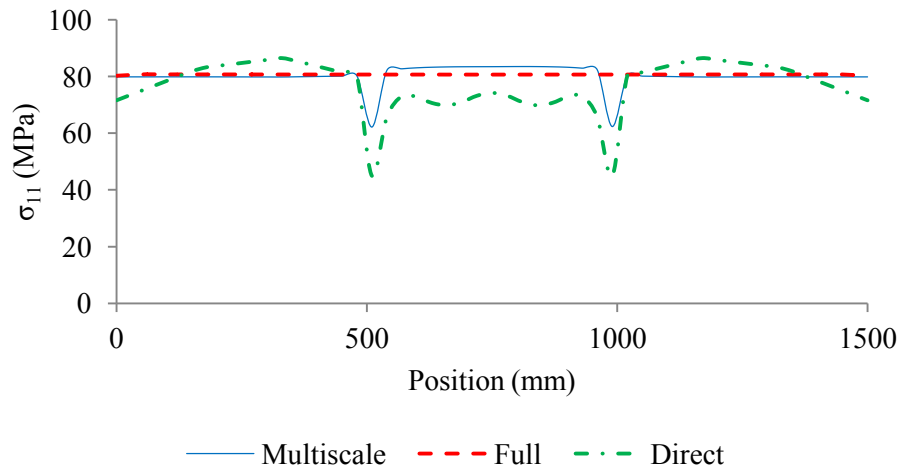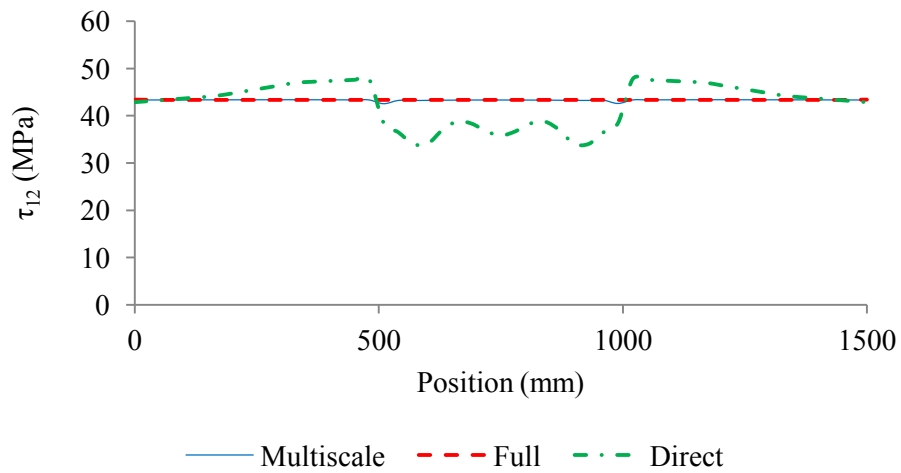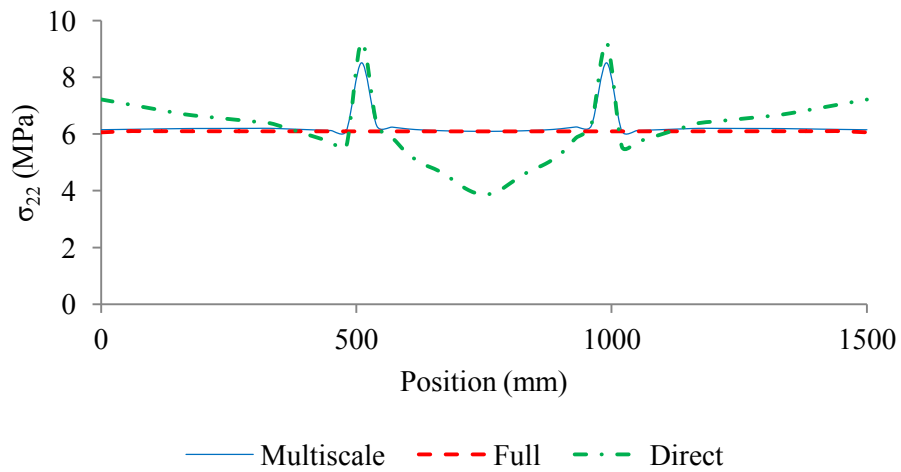
(c) σ_{22}.

Figure 7.7.: Comparison of path plots of stress components for the multiscale approach, direct application of Abaqus substructures and full uniform meshed models for a $[+45°, -45°, +45°, -45°]_s$ laminate.

(a) Uniform mesh.

(b) Key for all figures.

S, S11
(Avg: 75%)
+1.140e+03
+9.495e+02
+7.589e+02
+5.683e+02
+3.776e+02
+1.870e+02
-3.626e+00
-1.943e+02

(c) Global model in the global-local approach.

(d) Local model in the global-local approach.

(e) Global model in the direct application of sub-structuring.

(f) Local model in the direct application of sub-structuring.
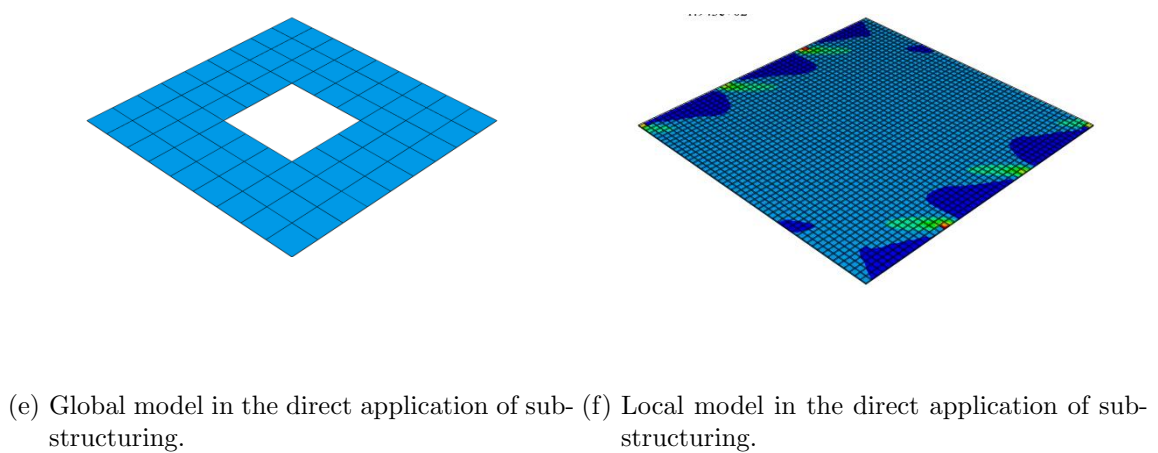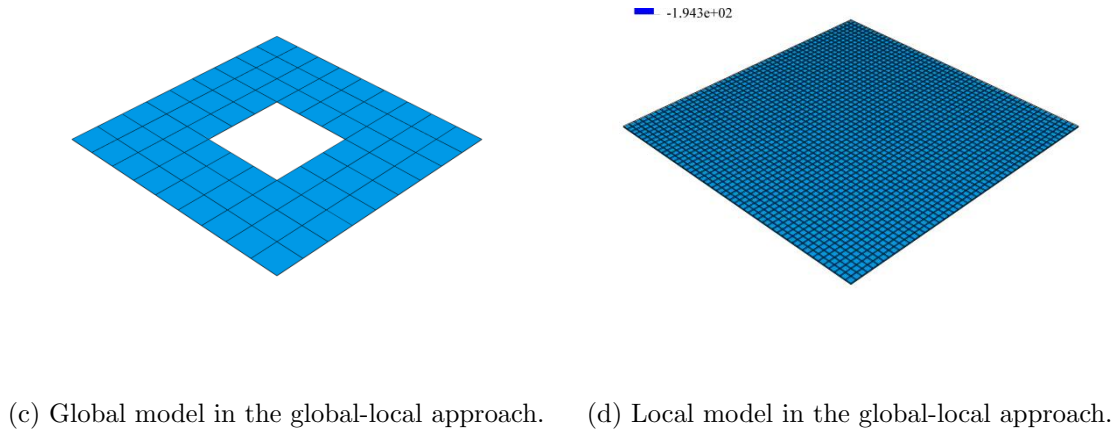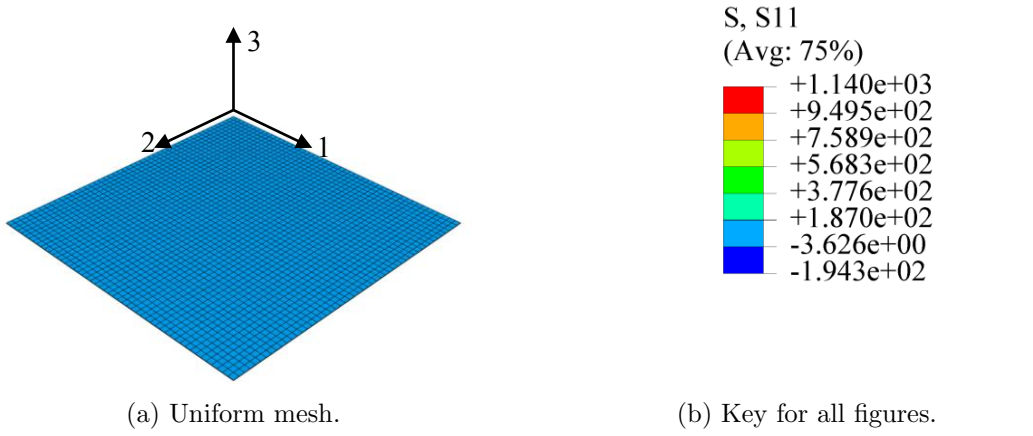
Figure 7.8.: Comparison of contour plots of the direct stress component, σ_{11}, for a $[+45°, -45°, +45°, -45°]_s$ laminate in the direction of the deformation between a uniform mesh model, the global-local approach and a direct application of substructuring.

(a) σ_{11}.

(b) τ_{12}.
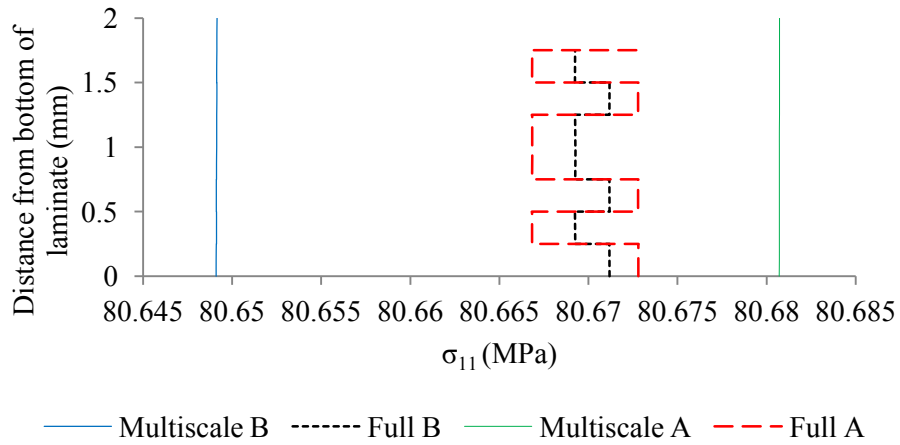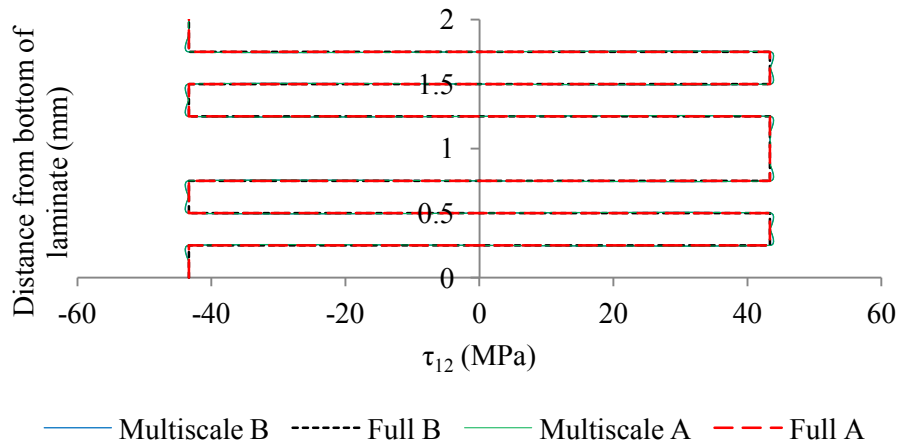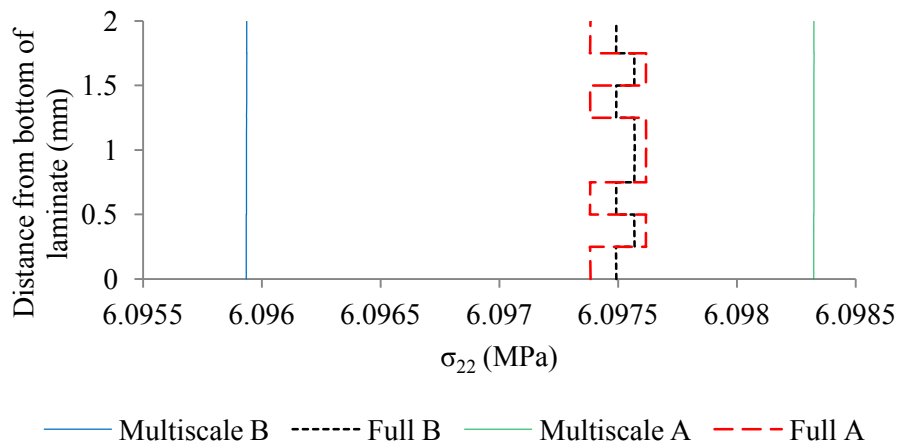
(c) σ_{22}.

Figure 7.9.: Through thickness plots of stress components at locations A and B specified in Figure 7.2 for the layup and boundary conditions shown in Figure 7.7.

(a) σ_{11}.

(b) τ_{12}.
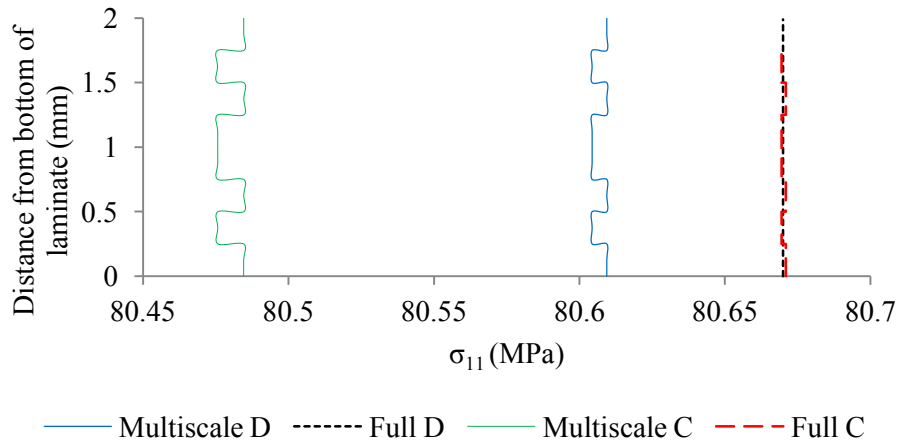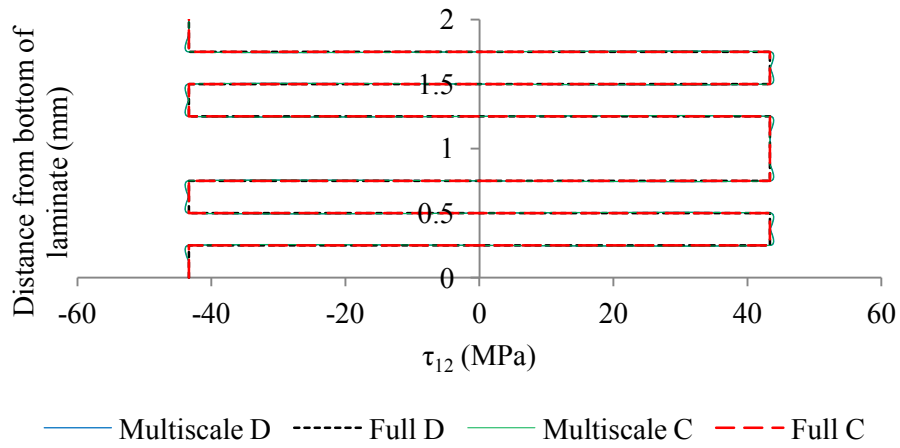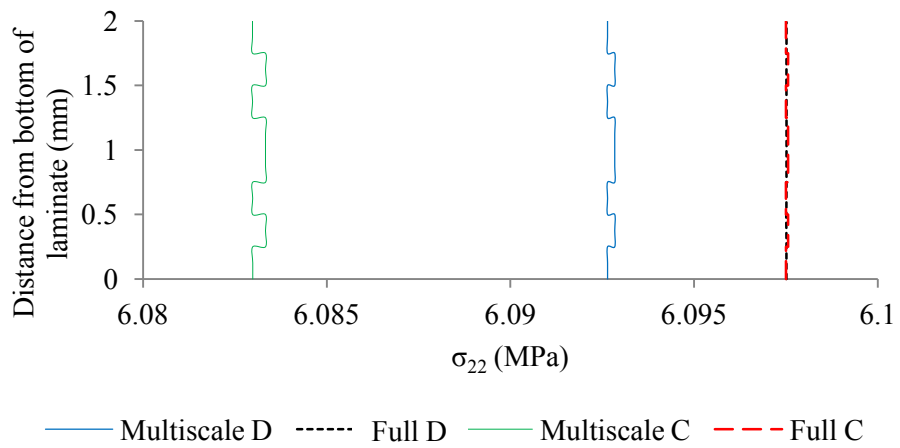
(c) σ_{22}.

Figure 7.10.: Through thickness plots of stress components at locations C and D specified in Figure 7.2 for the layup and boundary conditions shown in Figure 7.7.

(a) σ_{11}.

(b) τ_{12}.

(c) σ_{22}.
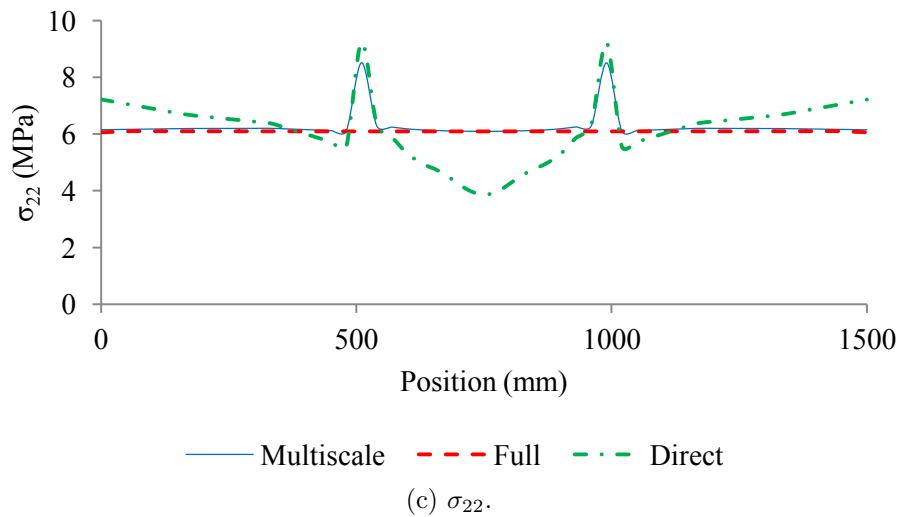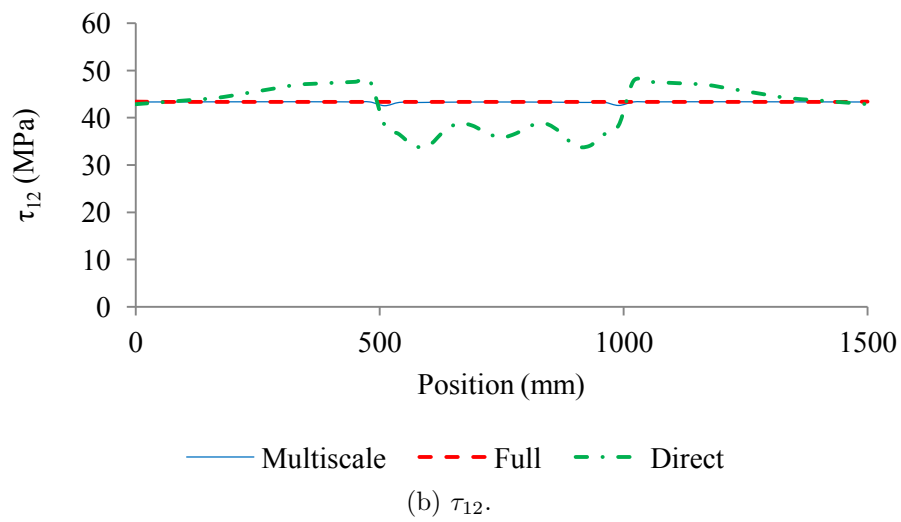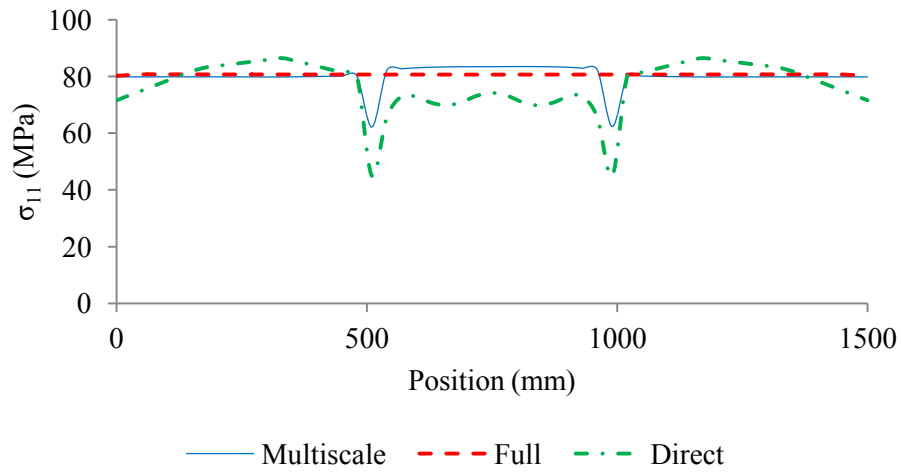
Figure 7.11.: Comparison of path plots of stress components for the multiscale approach, direct application of Abaqus substructures and full uniform meshed models for a $+45_4^\circ, -45_4^\circ$ laminate with nonlinear geometric effects ignored.

(a) Uniform mesh.
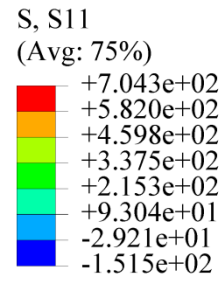
(b) Key for all figures.
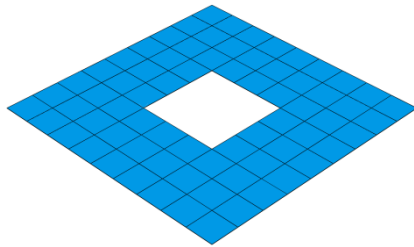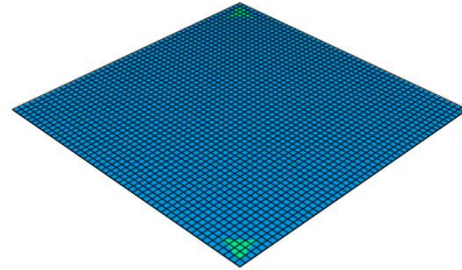
S, S11
(Avg: 75%)
+7.043e+02
+5.820e+02
+4.598e+02
+3.375e+02
+2.153e+02
+9.304e+01
-2.921e+01
-1.515e+02

(c) Global model in the global-local approach.

(d) Local model in the global-local approach.
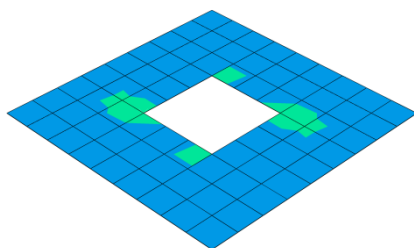
(e) Global model in the direct application of sub-structuring.
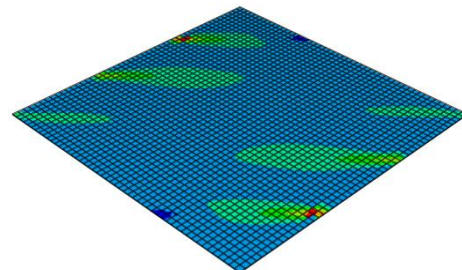
(f) Local model in the direct application of sub-structuring.

Figure 7.12.: Comparison of contour plots of the direct stress component, σ_{11}, for a $+45^\circ_4, -45^\circ_4$ laminate with nonlinear geometric effects ignored in the direction of the deformation between a uniform mesh model, the global-local approach and a direct application of substructuring.

144

(a) σ_{11}.

(b) τ_{12}.
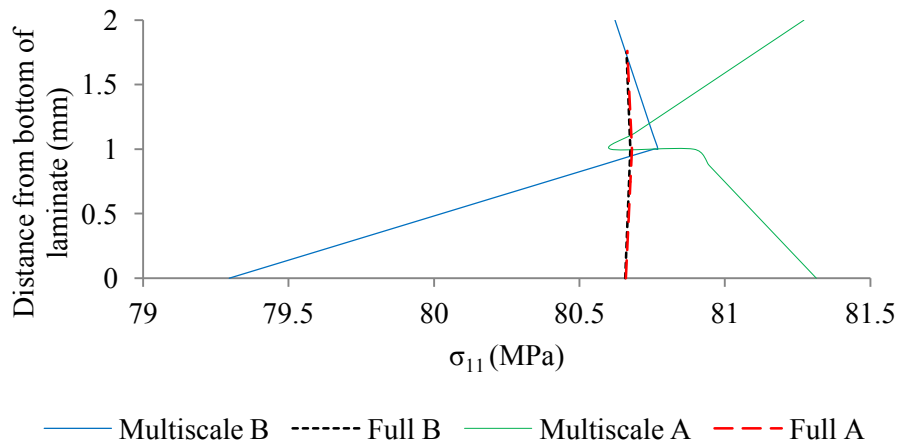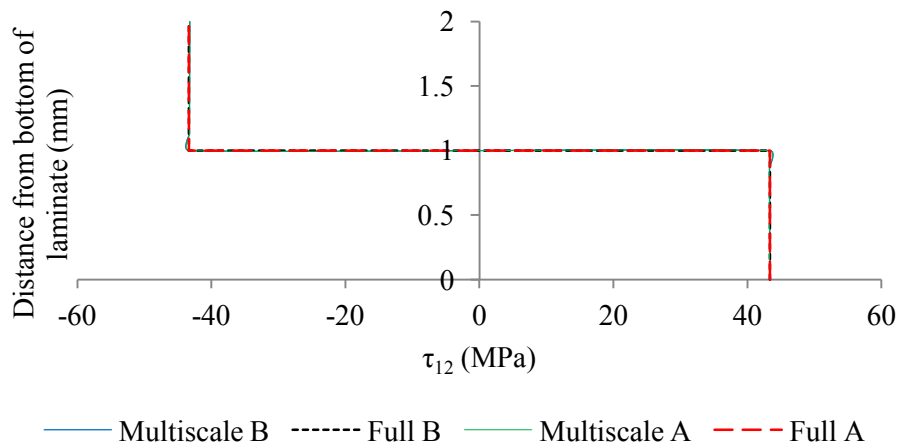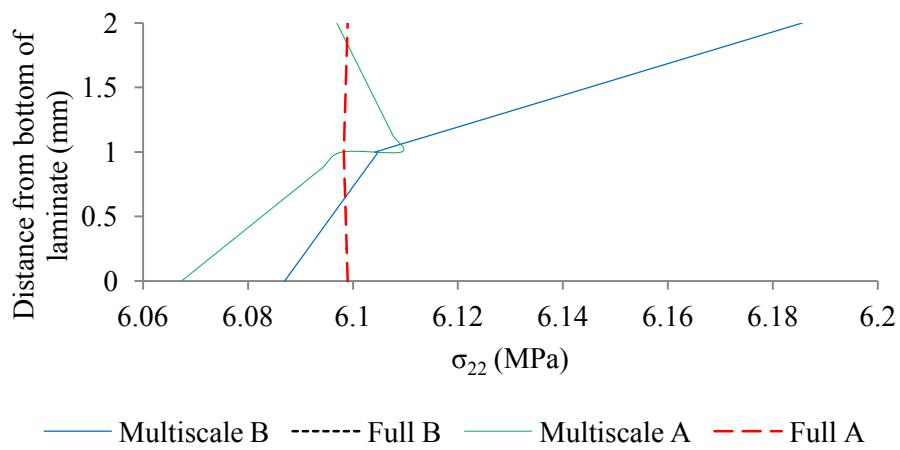
(c) σ_{22}.

Figure 7.13.: Through thickness plots of stress components at locations A and B specified in Figure 7.2 for the layup and boundary conditions shown in Figure 7.11.

(a) σ_{11}.

(b) τ_{12}.
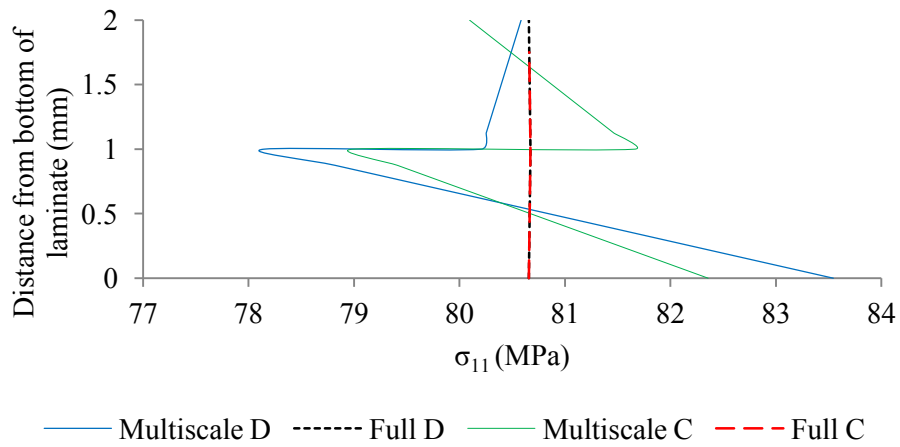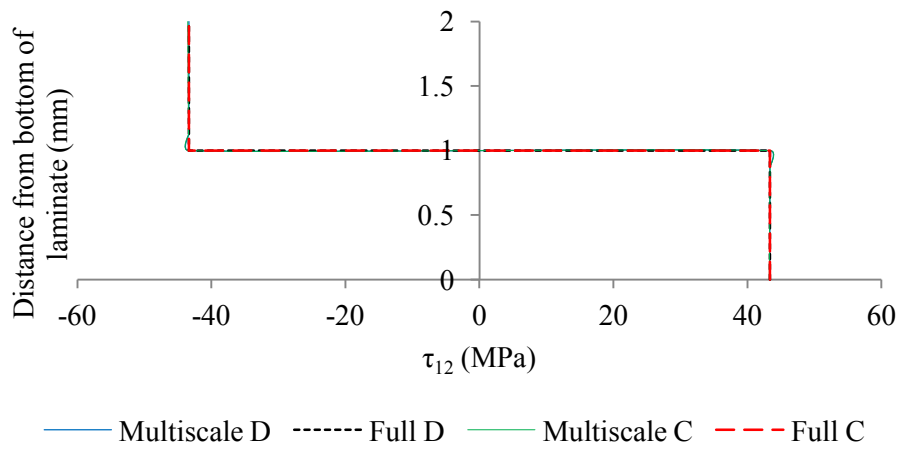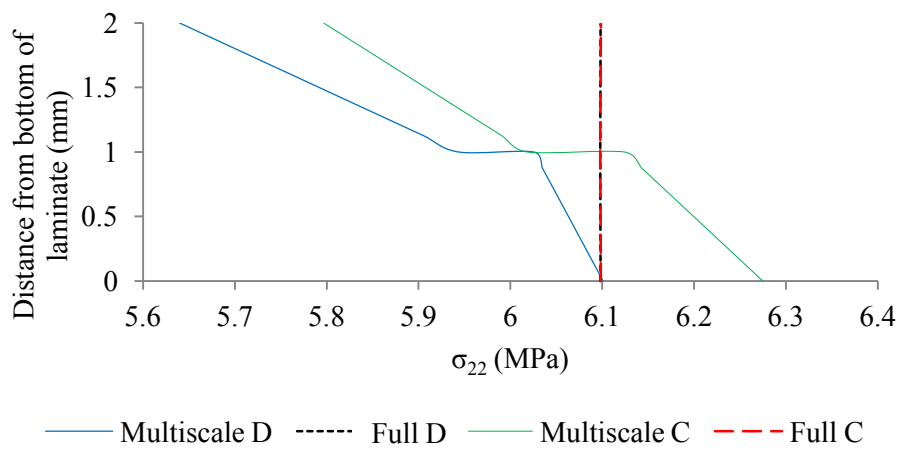
(c) σ_{22}.

Figure 7.14.: Through thickness plots of stress components at locations C and D specified in Figure 7.2 for the layup and boundary conditions shown in Figure 7.11.

(a) σ_{11}.

(b) τ_{12}.
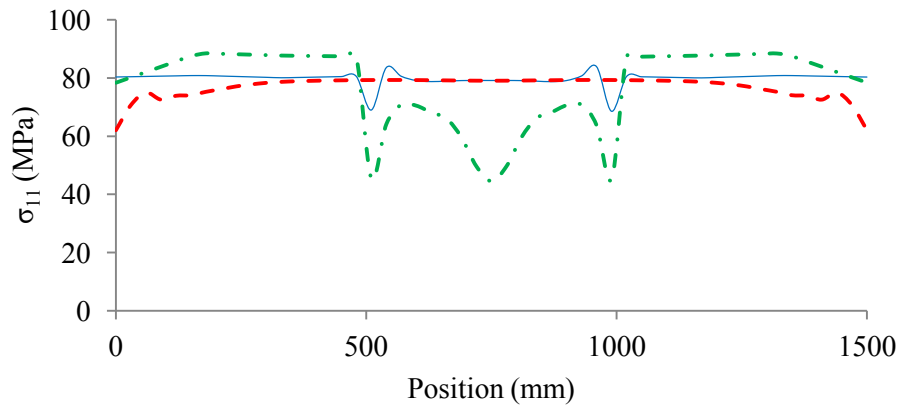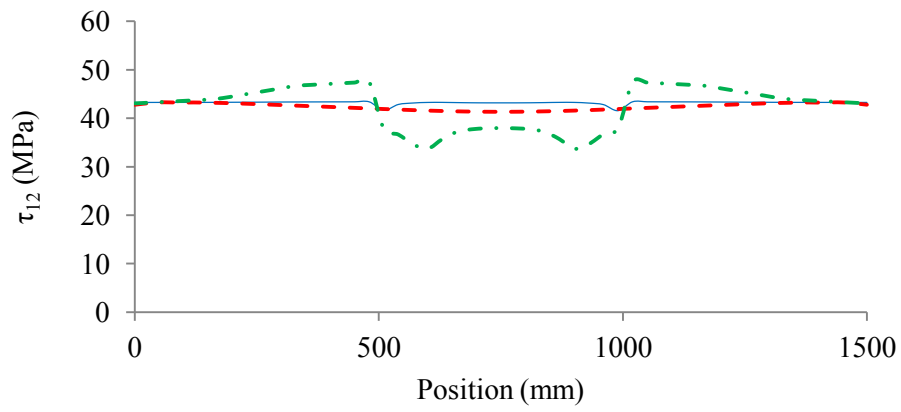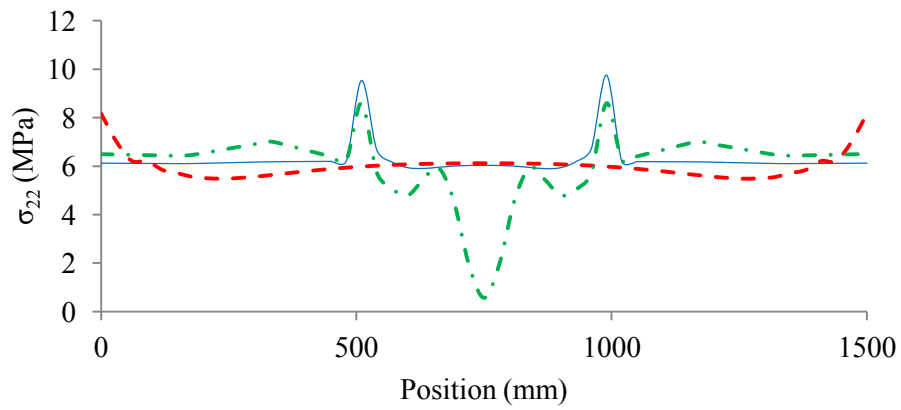
(c) σ_{22}.

Figure 7.15.: Comparison of path plots of stress components for the multiscale approach, direct application of Abaqus substructures and full uniform meshed models for a $+45_4^\circ, -45_4^\circ$ laminate with nonlinear geometric effects included.

(a) Uniform mesh.
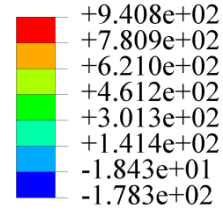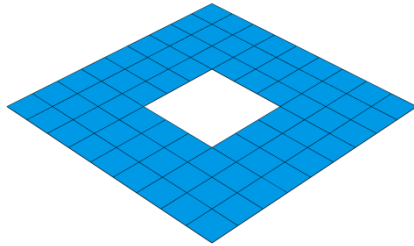
(b) Key for all figures.

S, S11

(Avg: 75%)
+9.408e+02
+7.809e+02
+6.210e+02
+4.612e+02
+3.013e+02
+1.414e+02
-1.843e+01
-1.783e+02

(c) Global model in the global-local approach.
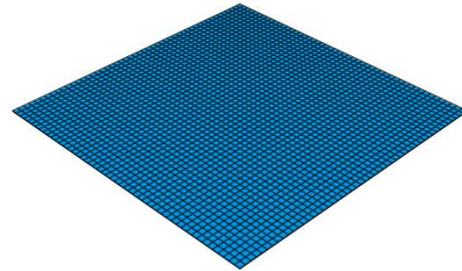
(d) Local model in the global-local approach.
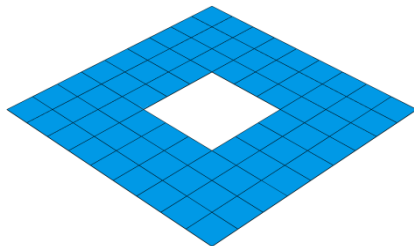
(e) Global model in the direct application of sub-structuring.
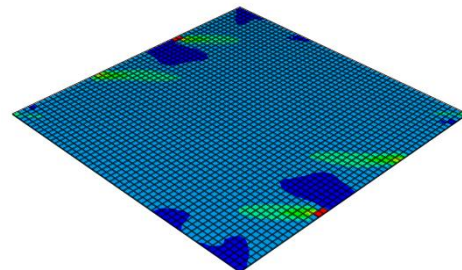
(f) Local model in the direct application of sub-structuring.

Figure 7.16.: Comparison of contour plots of the direct stress component, σ_{11}, for a $+45_4^\circ, -45_4^\circ$ laminate with nonlinear geometric effects included in the direction of the deformation between a uniform mesh model, the global-local approach and a direct application of substructuring.

(a) σ_{11}.

(b) τ_{12}.
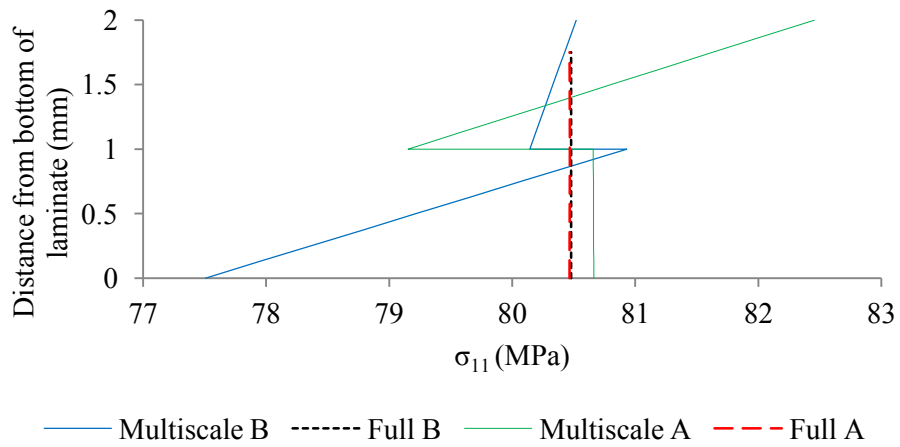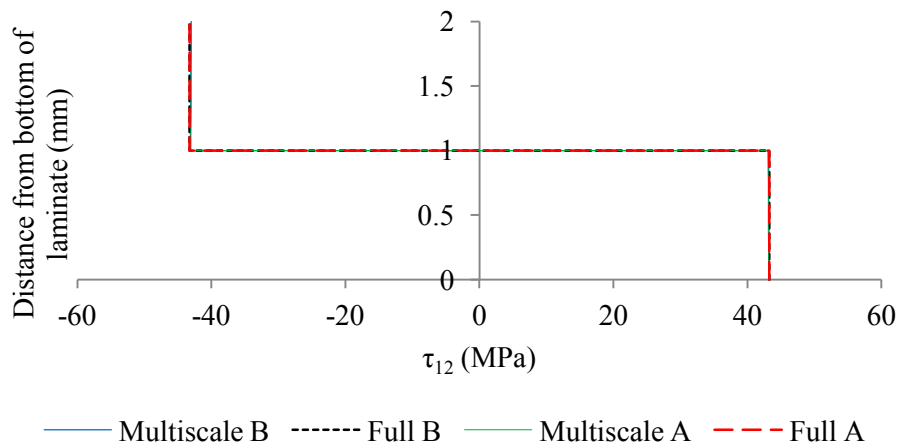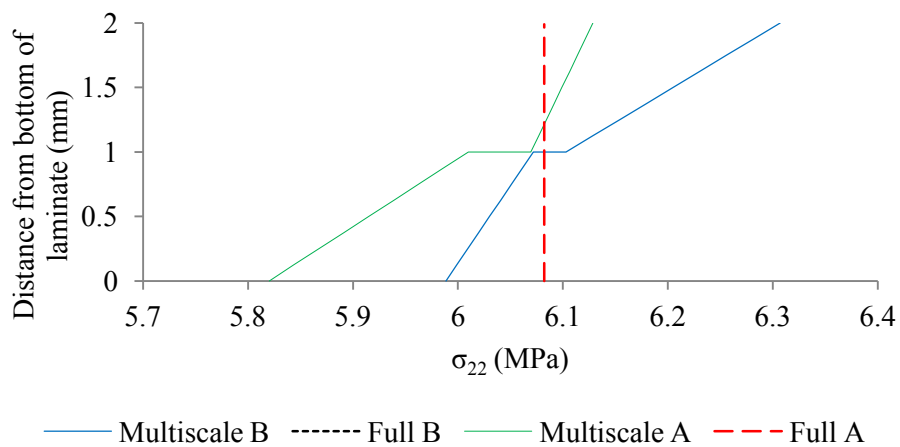
(c) σ_{22}.

Figure 7.17.: Through thickness plots of stress components at locations A and B specified in Figure 7.2 for the layup and boundary conditions shown in Figure 7.15.

(a) σ_{11}.

(b) τ_{12}.
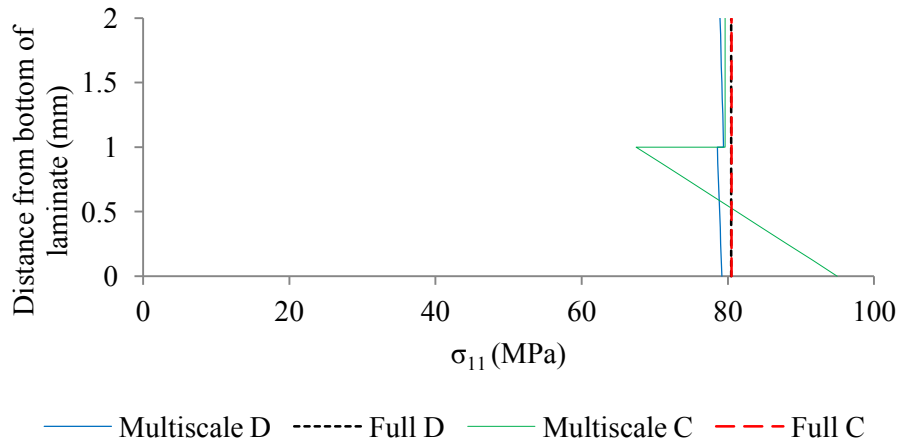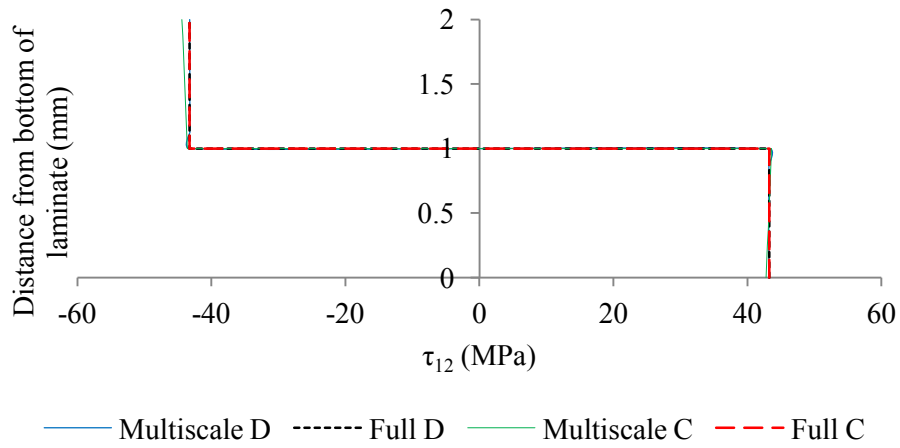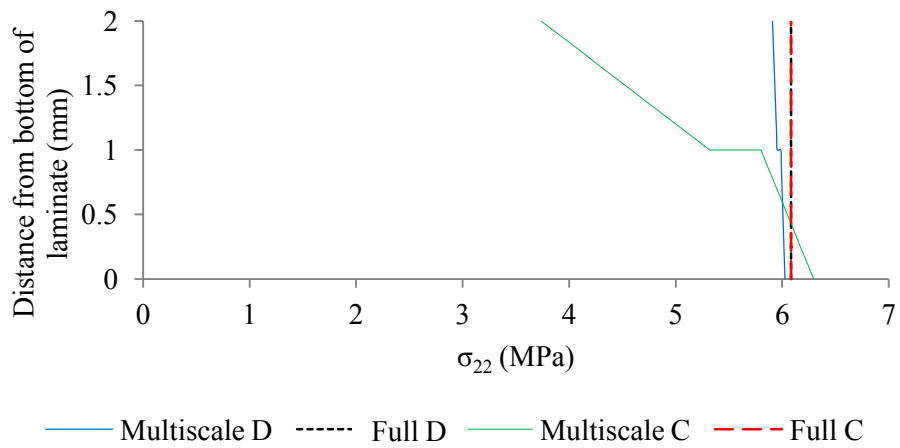
(c) σ_{22}.

Figure 7.18.: Through thickness plots of stress components at locations C and D specified in Figure 7.2 for the layup and boundary conditions shown in Figure 7.15.

constant due to the constraints, stresses due to Poisson's ratio effect are introduced in the thickness direction. These stresses are not available through the thickness of continuum shell elements, but are included in the formulation of the element [75]. This constraint in turn affects the strains due to Poisson's ratio effects in the in-plane directions leading to the discrepancies. Note that there are additional deviations from the control solution in the global model, although they are less pronounced. This is due to the stiffening effect that the through thickness constraint has on the superelement matrix generated from the local model.

In Figure 7.15, the reference solution shows drops in σ_{11} and peaks in σ_{22} at 0 mm and 1500 mm, while the multiscale solution does not. These are the locations at which boundary conditions are applied. In the reference model, these boundary conditions consisted of a displacement in the x-direction at the top and bottom nodes of the continuum shell elements, which effectively constrains rotation about z. The corresponding boundary conditions applied to the multiscale global model were therefore a displacement in x and a zero rotation about z. The deviations in σ_{11} and σ_{22} in the reference solution were attributed to hourglass effects, which were not present in the multiscale model due to the use of different element types. Note that the direct solution appears to show the same effect as the reference solution in the σ_{11} plot. This was in fact caused by the increase in σ_{11} due to the redistribution of stresses around the flexible superelement, compared to the value closer to the reference solution at 0 mm and 1500 mm where the strain in the x direction is held constant by the boundary conditions.

In addition to the path plots, through thickness plots of stress components are also presented for each of the points shown in Figure 7.2. These points were selected such that there was a point far away from the global-local boundary and one adjacent to it, for both the global and local models. This allowed the greatest insight into the effect of the treatment on the global-local boundary on the adjacent stress field, and how the effects diminish away from the boundary. As with the path plots, the full continuum shell model was taken as the control solution. Ideally, σ_{33} would have been plotted through the thickness of the continuum shell elements as it would help in understanding the effects of the constraint on the continuum shell thickness discussed in Section 6.4, but a limitation of these elements is that this quantity is not available. Instead σ_{11}, τ_{12} and σ_{22} were studied.

In each case, the through thickness plots for the global-local approach matched the control solution best at points A and D, the points furthest from the global local boundary. From this result it was concluded that the effects of the overconstraint in the thickness direction diminish away from the global-local boundary. In most cases the maximum deviation from the control solution was much less than 1%, and the most significant deviations for linear geometric problems were of the order of 5% (Figure 7.14c). These deviations were considered minor and as they diminished away from the global-local interface, this was not considered a major limitation.

When nonlinear geometry was considered, the deviations from the control solution were

larger. For example, in Figure 7.18c, the peak deviation from the control solution of σ_{22} at point C was of the order of 20%. This is because, for nonlinear geometric cases, the constraint that the plate thickness remains constant at the boundary affects not only the stresses due to Poisson's ratio effects, but also the stiffness of the deformed elements. These deviations diminish away from the interface, as shown by the corresponding curve for point D. This means that for nonlinear geometric cases involving shell to solid coupling, the global and local models must be defined such that the global-local boundary lies well away from any areas where the solution is of particular interest.

In each case, through thickness shear stress plots matched the control solution well. In the case of the $[+45°, -45°, +45°, -45°]_s$ and $[+45_4°, -45_4°]$ laminates the reversal in shear stress due to the 180° angle between the 2-direction in plies was seen.

For the $[+45°, -45°, +45°, -45°]_s$ laminate, slight differences in σ_{11} and σ_{22} where seen between plies. These differences were small compared to the magnitude of the stress components and could be accounted for by in-plane hourglassing of either the shell or the continuum shell mesh. Note that on the plots where these differences are visible, the scales are extremely large so the differences are much less than 1% of the stress component magnitude.

7.2. Three coupled scales

7.2.1. The three scale model

As noted in Chapter 1, the strictest definition of a multiscale approach requires more than two scales. Following the successful demonstration of the solid to solid coupling methodology in Chapter 5 and of the shell to solid approach earlier in this chapter, the two techniques have been used in conjunction to couple a shell, a continuum shell and a solid model together.

The complete domain is shown in Figure 7.19. The centre points of the shell, continuum shell and solid meshes are coincident. The shell (structural), continuum shell (intermediate) and solid (component) level meshes are shown in Figure 7.20, Figure 7.21 and Figure 7.22 respectively.

The modelled plate is an 8 ply laminate of 0.25mm T800/M21 CFRP. The material properties are given in Table 5.1. The layup is $+45_4°, -45_4°$, which is an unbalanced laminate so nodal rotations are expected at the shell level. Nonlinear geometric effects are considered.

Boundary conditions are applied to the free edges of the shell mesh. Applied displcaments are in the x-direction and proportional to the distance from the x-plane ($u_1 = x/200$). Rotations at these boundaries in the other in-plane direction are constrained. In order to provide results to compare those of the three scale analysis to, the same domain was modelled entirely in continuum shell elements.

152

x=0

1500

1500

500 500

40

40

■ Solid

■ Continuum shell
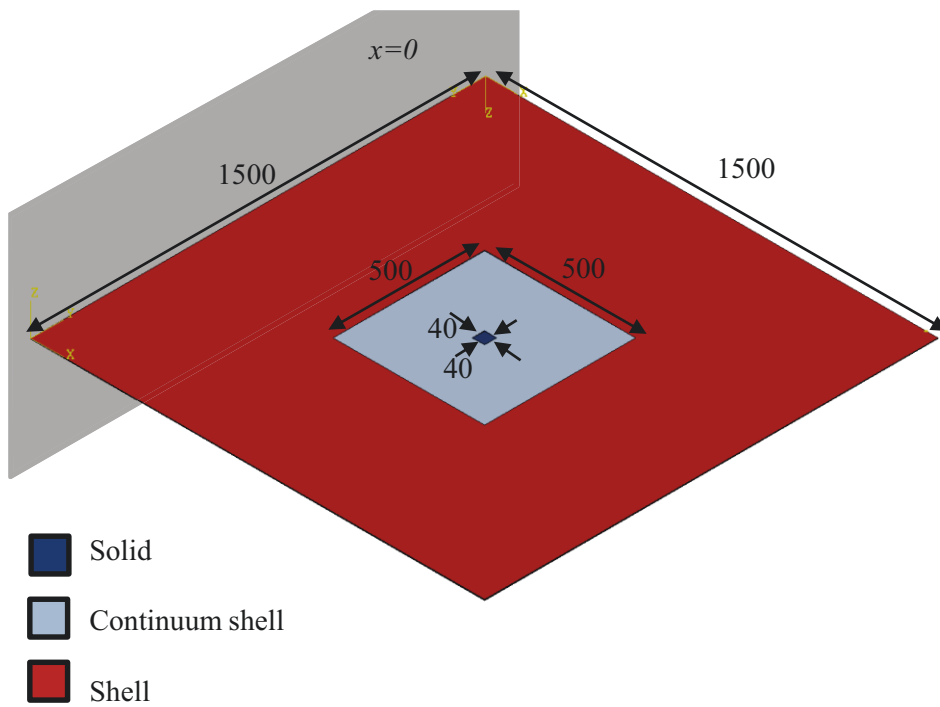
■ Shell

Figure 7.19.: Complete domain of the three scale demonstration model, with the shell, continuum shell and solid regions highlighted in different colours. Dimensions in mm.

Shell level mesh 9×9

Thickness: 2mm
1 element

Element type: S4
shell

1500mm

1500mm
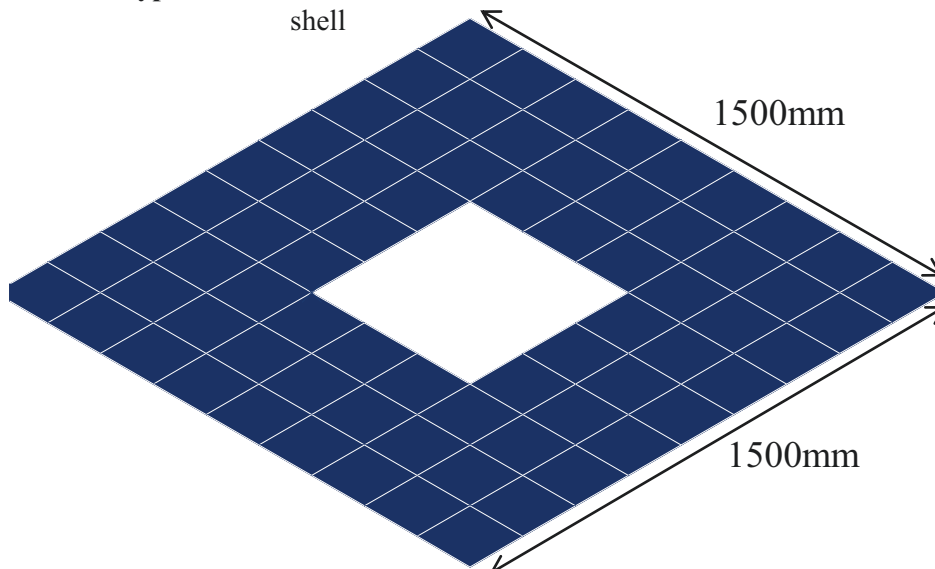
Figure 7.20.: The shell or structural level mesh for the three scale demonstration.

Continuum shell level mesh 50×50

Thickness: 2mm

                    1 element

Element type: SC8R

                    continuum shell

500mm

500mm
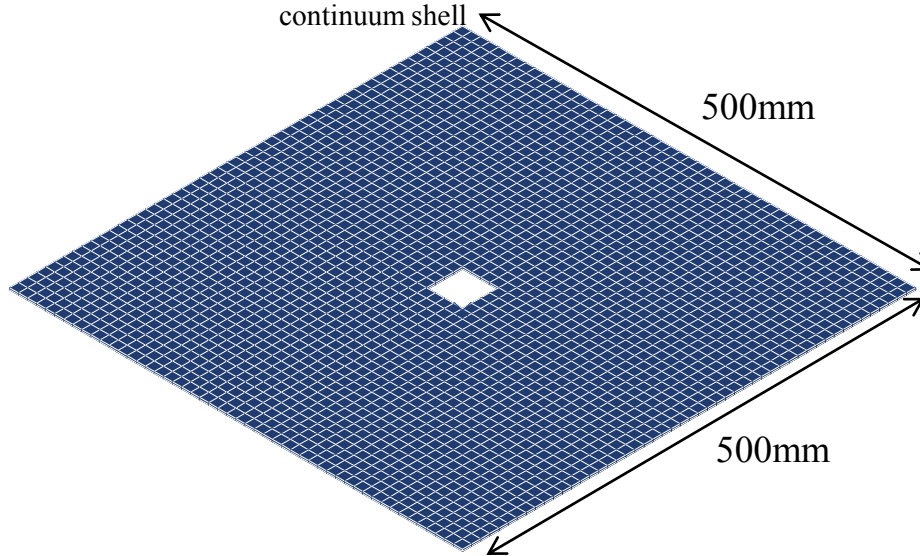
Figure 7.21.: The continuum shell or intermediate level mesh for the three scale demonstration.

Solid level mesh 20×20

Thickness: 2mm

                    8 elements

Element type: C3D8R

                    solid

40mm

40mm
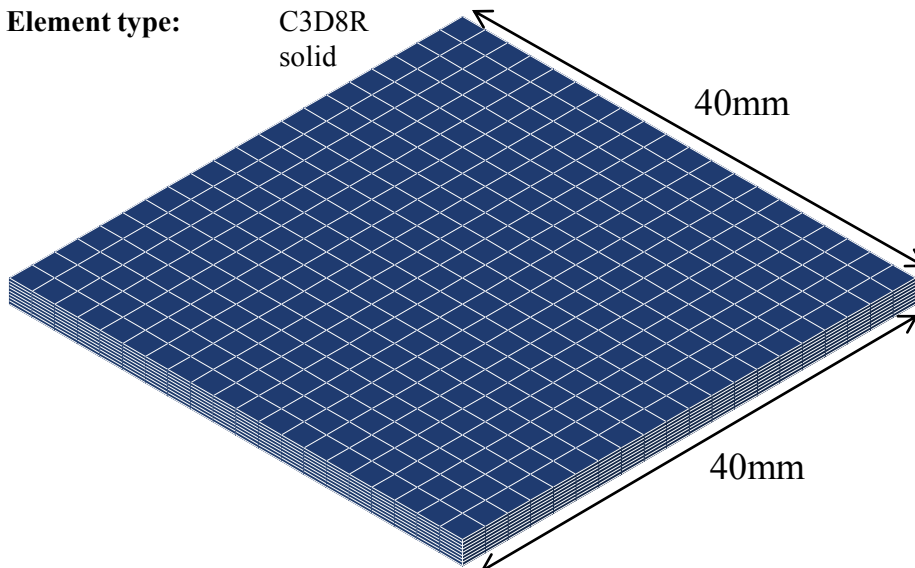
Figure 7.22.: The solid or component level mesh for the three scale demonstration.

7.2.2. Results

Contour plots of σ_{11} using the three scale coupling approach are compared to that obtained using a uniform continuum shell mesh and those using a direct, two scale application of substructuring. The plots are shown in Figure 7.23.

Plots of stress components along a path in the midplane along the centreline in the 2-direction are compared for the three scale coupled approach, the continuum shell model and a direct two scale application of substructuring in Figure 7.24.

7.2.3. Discussion

Both contour and path plots for the coupled three scale approach compare well to the complete continuum shell solution. As this is an established technique for modelling laminates this serves as a control case. There are some small irregularities at boundaries between the scales, but minor deviations from the control solution are to be expected due to changes in modelling technique through the thickness. These deviations, however, are very localised at the boundaries between scales. The solution far from these boundaries approaches the control solution again.

The three scale approach clearly provides an improved solution when compared to the direct application of substructuring.
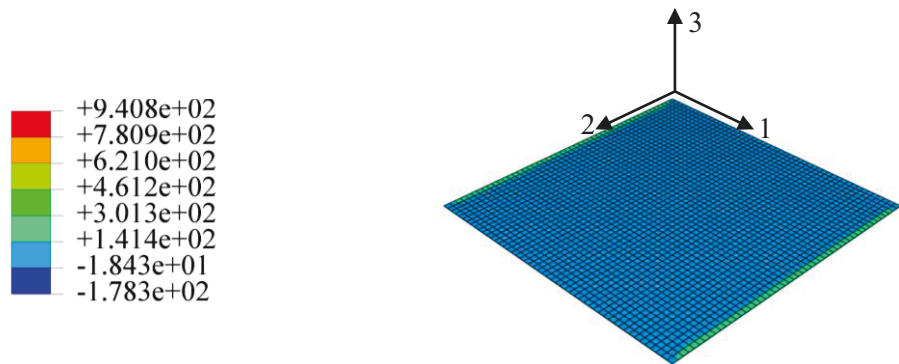
(a) Key
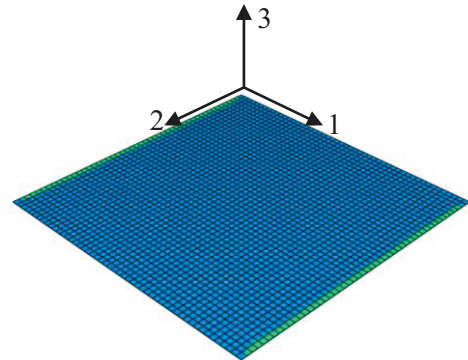
(b) Complete domain modelled using continuum shell elements.
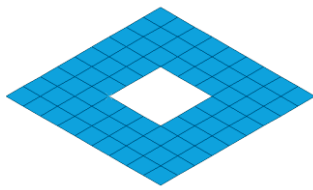
(c) Threescale approach - global domain modelled with shell elements.
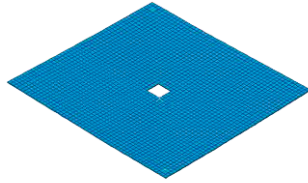
(d) Threescale approach - intermediate domain modelled with continuum shell elements.
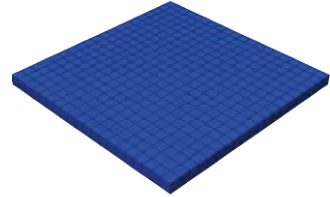
(e) Threescale approach - local domain modelled with solid elements.
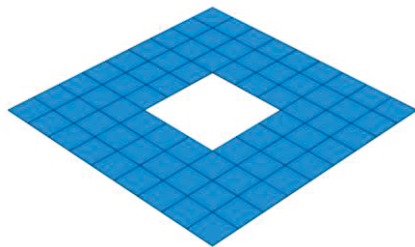
(f) Two scale model using a direct application of substructures - global domain modelled with shell elements.
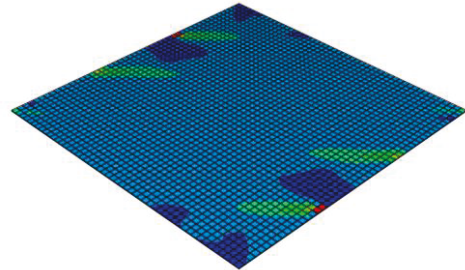
(g) Two scale model using a direct application of substructures - local domain modelled with solid elements.

Figure 7.23.: A comparison of stress component S_{11} (MPa) for equivalent models of a 1500 mm by 1500 mm composite plate of unballanced layup using different modelling strategies.

(a) σ_{11}.

(b) τ_{12}.
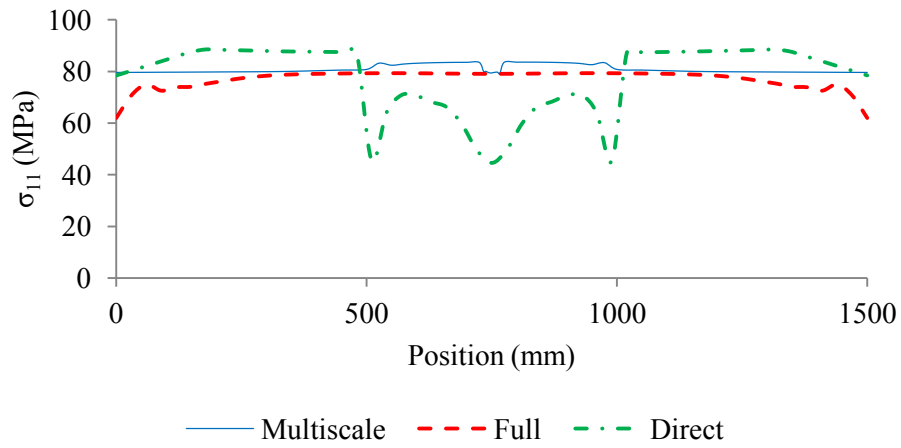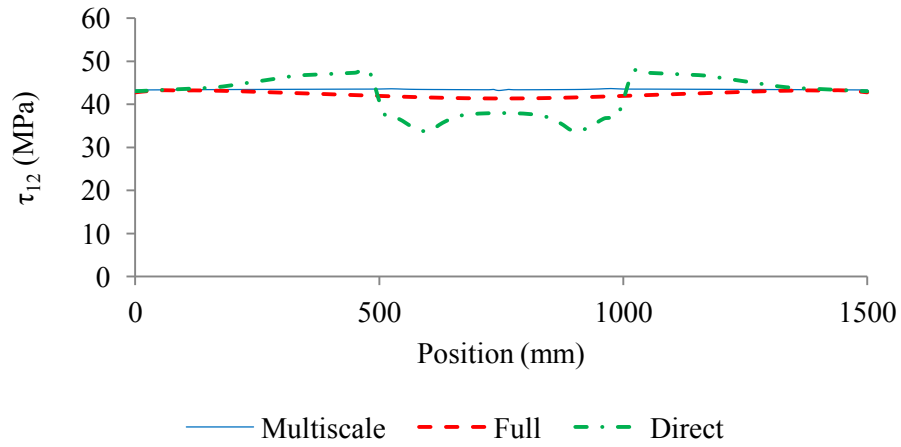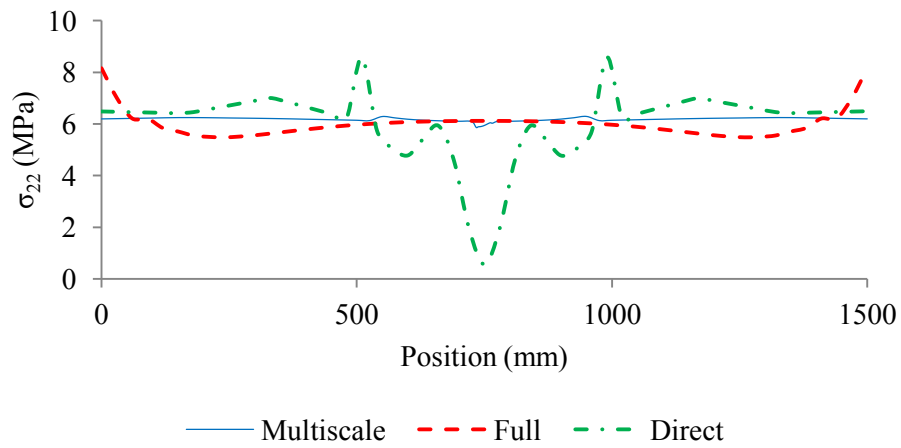
(c) σ_{22}.

Figure 7.24.: A comparison of stress components plotted along a line parallel to the 2 axis at the centreline of the laminate midplane. Plotted results are those obtained by the three scale approach, a direct application of a substructuring method using two scales and a uniform continuum shell mesh.

8. Conclusions

8.1. Review of objectives

In Section 2.7 the following objectives were defined:

1. To develop an appropriate method of extracting damaged properties from a local analysis, such that they may be used in a global analysis.

2. To show that this technique provides results comparable to those obtained by benchmark problems.

3. To justify the use of fully coupled global local approaches over traditional global-local or submodelling processes.

Objective 1 has been addressed by three coupling techniques, the first for coupling solid models, the second for coupling shell global models to solid local models and the third for coupling three scales of model. A brief evaluation of the solid, shell to solid and threescale coupling methods follows in Section 8.2, Section 8.3 and Section 8.4 respectively.

In order to achieve objective 2, solutions obtained using the coupled approaches developed here for simple flat plates were compared to solutions obtained by established finite element techniques. These comparisons are discussed in Chapter 5 and Chapter 7. Specimens were also designed in order that they would fail in two distinct regions during testing, and would provide a test case in which failure in two local models within one global model could be analysed. This would allow coupling methods to be evaluated for a problem representative of a real composite structure. Section 8.5 contains a summary of these tests.

Objective 3 required that advantages over existing multiscale methods, such as traditional global-local approaches were shown. In some traditional approaches no information is passed from the local to the global scale. In others, information is passed in the form of residuals. The limitations of passing residuals are discussed in Section 2.6, and the coupling approaches developed here avoid these by updating the stiffness of the global model according to the damaged state of local models. In addition, analysis of the test case discussed in Section 8.5 showed that the use of a fully coupled technique allowed the influence of damage in one local region on the failure in another to be captured. This would not be the case when using an uncoupled global-local approach.

8.2. Coupling of solid models

Established submodelling techniques where a global solution is used to provide boundary conditions to a local model have been extended to allow information about the state of the local model to be passed to the global model. In Chapter 5 this extended approach has been shown to compare well with tied model results, and to offer improved reliability over a direct application of substructuring approaches without special treatment of boundaries with differing refinement.

Further confidence in the approach was gained by comparison of the numerical results with experimental results from testing benchmark specimens (Section 5.3).

The fully coupled global-local approach has been shown to offer advantages over standard submodelling where information is only passed from the global to the local level. As discussed in Chapter 5.1 the first iteration of the local models corresponds to the local solution which would be obtained via traditional submodelling. The results presented in Section 5.3.2 show improved representation of runout damage compared to the first iteration, thus justifying the use of the fully coupled approach when multiple regions are expeted to undergo damage.

8.3. Coupling of shell models

As discussed in Chapter 1, the design process for a large composite structure often utilises different modelling strategies and elements at different scales. For example, one level of model may use shell elements while the adjacent level uses continuum shell elements. An approach, discussed in Chapter 6, has been developed which allows shell and continuum models to be fully coupled. This approach has been shown to provide comparable results to modelling the entire domain at a single level of refinement in Chapter 7. It has also been shown to provide improved results when compared to a direct application of substructuring approaches without special treatment of boundaries with differing refinement and element type.

8.4. Coupling three scales of model

It has also been demonstrated that nested levels of submodels may be coupled using the techniques. For example a coarse shell mesh may be coupled with a more refined continuum shell mesh, which in turn is coupled to a yet more refined solid element mesh.

The nested technique was applied to an unballanced laminate as described in Section 7.2. The results were shown to match those of the control solution, a complete continuum shell model, well. They were also shown to be an improvement on the direct application of submodels and superelements. This result means that fully coupled global local approaches could be extremely useful in structural design where there are not only two but often many levels of model required [1], as shown in Figure 1.1.

8.5. Design, manufacture, testing and analysis of a benchmark specimen for global/local models

The benchmark specimens were designed to justify the use of a fully coupled global/local approach over standard submodelling. This was achieved by including two regions which were vulnerable to debonding, and where the damaged state of one region could influence the other. It has been shown in Section 3.7.4 that the sequence of failure of these regions was consistent between specimens.

The plots of bending measure showed that the failure of the first vulnerable region resulted in a decrese in the slope of the bending measure against displacement or applied load at the second vulnerable region (Section 3.7.1). This means that the failure of the first region could postpone the failure of the second region, compared to the case where the first region remains intact. This is a phenomenon which would not be captured by a standard global/local approach, and as a consequence the benchmark specimens could be used to demonstrate the merits of using a fully coupled global/local approach.

8.6. General remarks on the methods developed

Another feature of these techniques is that each local model is separate from the others, and from the global model. This allows the analyses to be distributed wherever computational resources are available. There is no requirement for the analyses to be run on the same computer node as information is passed between scales only once each iteration, and the volume of data exchanged is relatively small.

Note that in all applications of the coupling approach, between continuum models only or between shell and continuum models, slight disturbances were noticed in the stress fields close to the boundaries between models. This was true in both global and local regions. The size of the affected regions was small when compared to laminate thicknesses, however, and does not present a problem as long as inter-scale boundaries are located away from regions of interest.

9. Further Work

9.1. Cosimulation

As discussed in Section 2.4, cosimulation methods could be used to implement a fully coupled global-local approach where internal time values in global and local models could be matched. In order to use cosimulation approaches in this way, an appropriate treatment of global-local boundaries is required. The treatment is analogous to that used when calculating superelement stiffness matrices from local models, which was discussed in Chapter 4. A possible extension of this work would be to use cosimulation approaches in place of superelements.

A cosimulation based approach to global-local modelling would remove the flexibility to distribute analyses to available computational resources as frequent communication between global and local solvers is required. This means the analysis will proceed more efficiently if all jobs, global and local are run on the same node.

9.2. Incrementation

Another possible technique to allow internal time points to be matched between global and local models would be to divide the global analysis into increments. For each increment a converged solution could be found and updated superelement matrices calculated.

This method would be useful in the case where boundary conditions on a component were nonlinear. However, changing a superelement's matrices mid-analysis is not a trivial matter in commercial finite element software.

Bibliography

[1] Morten Ostergaard, Andrew Ibbotson, Olivier Roux, and Alan Prior. Virtual testing of aircraft structures. *CEAS Aeronautical Journal*, 1(1):83–103, 2011.

[2] S.T. Pinho, L. Iannucci, and P. Robinson. Formulation and implementation of decohesion elements in an explicit finite element code. *Composites Part A: Applied Science and Manufacturing*, 37(5):778–789, May 2006.

[3] Nicolas Moës, John Dolbow, and Ted Belytschko. A finite element method for crack growth without remeshing. *International Journal for Numerical Methods in Engineering*, 46(1):131–150, 1999.

[4] M.G.D. Geers, V.G. Kouznetsova, and W.A.M. Brekelmans. Multi-scale computational homogenization: Trends and challenges. *Journal of Computational and Applied Mathematics*, 234(7):2175–2182, August 2010.

[5] Somnath Ghosh, Kyunghoon Lee, and Suresh Moorthy. Multiple scale analysis of heterogeneous elastic structures using homogenization theory and voronoi cell finite element method. *International Journal of Solids and Structures*, 32(1):27–62, January 1995.

[6] S. Psarras, S.T. Pinho, and B.G. Falzon. Design of composite stiffener run-outs for damage tolerance. *Finite Elements in Analysis and Design*, 47(8):949–954, August 2011.

[7] P. P. Camanho L. Ianucci P. Robinson S. T. Pinho, C. G. Dávila. Failure models and criteria for FRP under in-plane or three-dimensional stress states including shear non-linearity. *NASA/TM-2005-213530*, 2005.

[8] R. Gutkin, S.T. Pinho, P. Robinson, and P.T. Curtis. Micro-mechanical modelling of shear-driven fibre compressive failure and of fibre kinking for failure envelope generation in CFRP laminates. *Composites Science and Technology*, 70(8):1214–1222, August 2010.

[9] S. Pimenta, R. Gutkin, S.T. Pinho, and P. Robinson. A micromechanical model for kink-band formation: Part I – Experimental study and numerical modelling. *Composites Science and Technology*, 69(7-8):948–955, June 2009.

[10] S. Pimenta, R. Gutkin, S.T. Pinho, and P. Robinson. A micromechanical model for kink-band formation: Part II–Analytical modelling. *Composites Science and Technology*, 69(7-8):956–964, June 2009.

[11] C.B. Hirschberger, S. Ricker, P. Steinmann, and N. Sukumar. Computational multiscale modelling of heterogeneous material layers. *Engineering Fracture Mechanics*, 76(6):793–812, April 2009.

[12] Xue Li, Lope Tabil, and Satyanarayan Panigrahi. Chemical treatments of natural fiber for use in natural fiber-reinforced composites: A review. *Journal of Polymers and the Environment*, 15(1):25–33, 2007.

[13] A. Valadez-Gonzalez, J.M. Cervantes-Uc, R. Olayo, and P.J. Herrera-Franco. Effect of fiber surface treatment on the fibermatrix bond strength of natural fiber reinforced composites. *Composites Part B: Engineering*, 30(3):309–320, April 1999.

[14] J.L. Chaboche, F. Feyel, and Y. Monerie. Interface debonding models: a viscous regularization with a limited rate dependency. *International Journal of Solids and Structures*, 38(18):3127–3160, May 2001.

[15] Penchom Photjanataree, Zheng Liu, and Frank Ralph Jones. The role of a nanoscale interphase from plasma polymers on the micromechanics of fiber composites. *Macromolecular Materials and Engineering*, 297(6):523531, 2012.

[16] D.J Marks and F.R Jones. Plasma polymerised coatings for engineered interfaces for enhanced composite performance. *Composites Part A: Applied Science and Manufacturing*, 33(10):1293–1302, October 2002.

[17] John W. Hutchinson and Henrik M. Jensen. Models of fiber debonding and pullout in brittle composites with friction. *Mechanics of Materials*, 9(2):139–163, September 1990.

[18] G.M. Vyas and S.T. Pinho. Computational implementation of a novel constitutive model for multidirectional composites. *Computational Materials Science*, 51(1):217–224, January 2012.

[19] G.M. Vyas, S.T. Pinho, and P. Robinson. Constitutive modelling of fibre-reinforced composites with unidirectional plies using a plasticity-based approach. *Composites Science and Technology*, 71(8):1068–1074, May 2011.

[20] S Miot, R Done, S.T. Pinho, and A Ibbotson. Analysis of bonded composite structures final report. Technical report, September 2012.

[21] M. Ortiz and A. Pandolfi. Finite-deformation irreversible cohesive elements for three-dimensional crack-propagation analysis. *International Journal for Numerical Methods in Engineering*, 44(9):12671282, 1999.

[22] Viggo Tvergaard. Effect of fibre debonding in a whisker-reinforced metal. *Materials Science and Engineering: A*, 125(2):203–213, June 1990.

[23] C. G. Dávila N. Jaunky V. K. Goyal, E. R. Johnson. An irreversible constitutive law for modeling the delamination process using interface elements. *NASA/CR-2002-211758*, 2002.

[24] *Abaqus User Manual*. Dassault Systémes, 2010.

[25] C. G. Dávila P. P. Camanho. Mixed-mode decohesion finite elements for the simulation of delamination in composite materials. *NASA/TM-2003-212663*, 2003.

[26] M. F De Moura P. P Camanho, C. G. Dávila. Numerical simulation of mixed-mode progressive delamination in composite materials. *Journal of Composite Materials*, 37:1414–1438, 2003.

[27] Stephen W. Tsai. A survey of macroscopic failure criteria for composite materials. *Journal of Reinforced Plastics and Composites*, 3(1):40–62, January 1984.

[28] Y. Mi, M. A. Crisfield, G. A. O. Davies, and H. B. Hellweg. Progressive delamination using interface elements. *Journal of Composite Materials*, 32(14):1246–1272, July 1998.

[29] M.L. Benzeggagh and M. Kenane. Measurement of mixed-mode delamination fracture toughness of unidirectional glass/epoxy composites with mixed-mode bending apparatus. *Composites Science and Technology*, 56(4):439–449, 1996.

[30] M.L. Benzeggagh and M. Kenane. Measurement of mixed-mode delamination fracture toughness of unidirectional glass/epoxy composites with mixed-mode bending apparatus. *Composites Science and Technology*, 56(4):439–449, 1996.

[31] M. Kenane and M.L. Benzeggagh. Mixed-mode delamination fracture toughness of unidirectional glass/epoxy composites under fatigue loading. *Composites Science and Technology*, 57(5):597–605, 1997.

[32] K. B. Katnam, A. D. Crocombe, H. Khoramishad, and I. A. Ashcroft. The static failure of adhesively bonded metal laminate structures: A cohesive zone approach. *Journal of Adhesion Science and Technology*, 25(10):1131–1157, 2011.

[33] C. D. M. Liljedahl, A. D. Crocombe, M. A. Wahab, and I. A. Ashcroft. Damage modelling of adhesively bonded joints. *International Journal of Fracture*, 141(1-2):147–161, September 2006.

[34] T. Belytschko and T. Black. Elastic crack growth in finite elements with minimal remeshing. *International Journal for Numerical Methods in Engineering*, 45(5):601–620, 1999.

[35] T. Belytschko, N. Mos, S. Usui, and C. Parimi. Arbitrary discontinuities in finite elements. *International Journal for Numerical Methods in Engineering*, 50(4):9931013, 2001.

[36] N. Sukumar, N. Mos, B. Moran, and T. Belytschko. Extended finite element method for three-dimensional crack modelling. *International Journal for Numerical Methods in Engineering*, 48(11):15491570, 2000.

[37] Ted Belytschko, Stefan Loehnert, and Jeong-Hoon Song. Multiscale aggregating discontinuities: A method for circumventing loss of material stability. *International Journal for Numerical Methods in Engineering*, 73(6):869–894, 2008.

[38] D. B. P. Huynh and T. Belytschko. The extended finite element method for fracture in composite materials. *International Journal for Numerical Methods in Engineering*, 77(2):214–239, 2009.

[39] O. Bacarreza and M.H. Aliabadi. A novel methodology for fatigue delamination growth analysis of composites. *Key Engineering Materials*, 488-489:763–766, September 2011.

[40] G. Legrain, P. Cartraud, I. Perreard, and N. Mos. An x-FEM and level set computational approach for image-based modelling: Application to homogenization. *International Journal for Numerical Methods in Engineering*, 86(7):915934, 2011.

[41] Toshio Nagashima and Hiroshi Suemasu. X-FEM analyses of a thin-walled composite shell structure with a delamination. *Computers & Structures*, 88(910):549–557, May 2010.

[42] R.D.S.G. Campilho, M.D. Banea, F.J.P. Chaves, and L.F.M. da Silva. eXtended finite element method for fracture characterization of adhesive joints in pure mode i. *Computational Materials Science*, 50(4):1543–1549, February 2011.

[43] José Miranda Guedes and Noboru Kikuchi. Preprocessing and postprocessing for materials based on the homogenization method with adaptive finite element methods. *Computer Methods in Applied Mechanics and Engineering*, 83(2):143–198, October 1990.

[44] H. Moulinec and P. Suquet. A numerical method for computing the overall response of nonlinear composites with complex microstructure. *Computer Methods in Applied Mechanics and Engineering*, 157(1-2):69–94, April 1998.

[45] Somnath Ghosh and Sankar N. Mukhopadhyay. A material based finite element analysis of heterogeneous media involving dirichlet tessellations. *Computer Methods in Applied Mechanics and Engineering*, 104(2):211–247, April 1993.

[46] F.P.T. Baaijens V. Kouznetsova, W.A.M. Brekelmans. An approach to micro-macro modeling of heterogeneous materials. *Computational Mechanics*, 27(PR5):37–48, 2001.

[47] M.G.D. Geers, V. Kouznetsova, and W.A.M. Brekelmans. Gradient-enhanced computational homogenization for the micro-macro scale transition. *Le Journal de Physique IV*, 11(PR5):8, 2001.

[48] V. Kouznetsova, M. G. D. Geers, and W. A. M. Brekelmans. Multi-scale constitutive modelling of heterogeneous materials with a gradient-enhanced computational homogenization scheme. *International Journal for Numerical Methods in Engineering*, 54(8):1235–1260, 2002.

[49] E.W.C. Coenen, V.G. Kouznetsova, and M.G.D. Geers. Novel boundary conditions for strain localization analyses in microstructural volume elements. *International Journal for Numerical Methods in Engineering*, 90(1):121, 2012.

[50] Ted Belytschko and Robert Mullen. Stability of explicit-implicit mesh partitions in time integration. *International Journal for Numerical Methods in Engineering*, 12(10):15751586, 1978.

[51] T. Belytschko, H.-J. Yen, and R. Mullen. Mixed methods for time integration. *Computer Methods in Applied Mechanics and Engineering*, 1718, Part 2:259–275, February 1979.

[52] Thomas J.R. Hughes, Karl S. Pister, and Robert L. Taylor. Implicit-explicit finite elements in nonlinear transient analysis. *Computer Methods in Applied Mechanics and Engineering*, 1718, Part 1:159–182, January 1979.

[53] W.K. Liu and T. Belytschko. Mixed-time implicit-explicit finite elements for transient analysis. *Computers & Structures*, 15(4):445–450, 1982.

[54] M. Brun, A. Batti, A. Limam, and A. Gravouil. Explicit/implicit multi-time step co-computations for blast analyses on a reinforced concrete frame structure. *Finite Elements in Analysis and Design*, 52:41–59, May 2012.

[55] I. Guiamatsia, B. G. Falzon, G. A. O. Davies, and L. Iannucci. Element-free galerkin modelling of composite damage. *Composites Science and Technology*, 69(1516):2640–2648, December 2009.

[56] G. R. Liu. *Meshfree Methods: Moving Beyond the Finite Element Method, Second Edition*. CRC Press, December 2010.

[57] T. Belytschko, Y. Y. Lu, and L. Gu. Element-free galerkin methods. *International Journal for Numerical Methods in Engineering*, 37(2):229256, 1994.

[58] T. Belytschko, Y. Y. Lu, and L. Gu. Crack propagation by element-free galerkin methods. *Engineering Fracture Mechanics*, 51(2):295–315, May 1995.

[59] D.S. Mikhaluk, T.C. Truong, A.I. Borovkov, S.V. Lomov, and I. Verpoest. Experimental observations and finite element modelling of damage initiation and evolution in carbon/epoxy non-crimp fabric composites. *Engineering Fracture Mechanics*, 75(9):2751–2766, June 2008.

[60] C. Levy, M. Perl, and S. Kotagiri. The bauschinger effects influence on the SIFs of multiple longitudinal coplanar cracks in autofrettaged pressurized cylinders. *Engineering Fracture Mechanics*, 73(13):1814–1825, September 2006.

[61] A.Th. Diamantoudis and G.N. Labeas. Stress intensity factors of semi-elliptical surface cracks in pressure vessels by global-local finite element methodology. *Engineering Fracture Mechanics*, 72(9):1299–1312, June 2005.

[62] I. Kizhakkethara AE. Bogdanovich. Three-dimensional finite element analysis of double-lap adhesive bonded joints using submodeling approach. *Composites Part B: Engineering*, 30(6):537–551, 1999.

[63] M Abdel Wahab, I Ashcroft, and A Crocombe. A comparison of failure prediction methods for an adhesively bonded composite beam. *The Journal of Strain Analysis for Engineering Design*, 39(2):173–185, January 2004.

[64] C.T. Sun and K.M. Mao. A global-local finite element method suitable for parallel computations. *Computers & Structures*, 29(2):309–315, 1988.

[65] J.B. Ransom and N.F. Knight Jr. Global/local stress analysis of composite panels. *Computers & Structures*, 37(4):375–395, 1990.

[66] J. D. Whitcomb. Iterative global/local finite element analysis. *Computers & Structures*, 40(4):1027–1031, 1991.

[67] Lionel Gendre, Olivier Allix, Pierre Gosselet, and Franois Comte. Non-intrusive and exact global/local techniques for structural problems with local plasticity. *Computational Mechanics*, 44(2):233–245, 2009.

[68] L. Gendre, O. Allix, and P. Gosselet. A two-scale approximation of the schur complement and its use for non-intrusive coupling. *International Journal for Numerical Methods in Engineering*, 87(9):889905, 2011.

[69] Tony F. Chan and Tarek P. Mathew. Domain decomposition algorithms. *Acta Numerica*, 3:61–143, 1994.

[70] Philippe Cresta, Olivier Allix, Christian Rey, and Stphane Guinard. Nonlinear localization strategies for domain decomposition methods: Application to post-buckling

analyses. *Computer Methods in Applied Mechanics and Engineering*, 196(8):1436–1446, January 2007.

[71] Pierre Gosselet and Christian Rey. Non-overlapping domain decomposition methods in structural mechanics. *Archives of Computational Methods in Engineering*, 13(4):515–572, 2006.

[72] M. Storti, N. Nigro, and S. Idelsohn. Multigrid methods and adaptive refinement techniques in elliptic problems by finite element methods. *Computer Methods in Applied Mechanics and Engineering*, 93(1):13–30, December 1991.

[73] A. Simone L.J. Sluys 0. Lloberas Valls, D.J. Rixen. A domain decomposition approach to multiscale analysis for structures with softening materials. 7th EUROMECH Solid Mechanics Conference, Lisbon, Portugal, 2009.

[74] Julien Pebrel, Christian Rey, and Pierre Gosselet. A nonlinear dual domain decomposition method : application to structural problems with damage. *International Journal for Multiscale Computational Engineering*, 6(3):251–262, 2008.

[75] *Abaqus Analysis User's Guide*. Dassault Systémes, 2010.

[76] C. Hua. An inverse transformation for quadrilateral isoparametric elements: Analysis and application. *Finite Elements in Analysis and Design*, 7:159–166, 1990.

A. Experimental data from stiffened panel tests

In this appendix, abridged experimental data (every 25th sampling point in time) from the tests described in Chapter 3 are presented. For each of the 5 specimens the applied displacement, load and 4 strain values are reported. The measured strains were recorded at the following 4 locations, as illustrated in Figure 3.12:

- Location A: The long stiffener runout on the stiffened side

- Location B: The long stiffener runout on the unstiffened side

- Location C: The short stiffener runout on the stiffened side

- Location D: The short stiffener runout on the unstiffened side

Note that for specimens 1 and 2, load data was not recorded and for specimen 4 the strain gauge at location B failed before the end of the test.

A.1. Specimen 1

Displacement (mm)	Load (N)	Strain at location A	Strain at location B	Strain at location C	Strain at location D
0.0	-	30	-11	49	-61
0.6	-	99	-49	163	-190
1.3	-	171	-83	284	-330
1.9	-	262	-129	417	-489
2.6	-	353	-186	546	-652
3.2	-	444	-239	671	-811
3.8	-	535	-292	796	-978
4.5	-	633	-349	929	-1149
5.1	-	732	-402	1058	-1316
5.7	-	830	-459	1187	-1482
6.4	-	948	-519	1312	-1642
7.0	-	1088	-588	1429	-1797
7.7	-	1228	-656	1551	-1956

8.3	-	1422	-743	1668	-2100
8.9	-	1627	-842	1786	-2241
9.6	-	2173	-1134	1839	-2313
10.2	-	2457	-1338	1941	-2438
10.8	-	2707	-1532	2047	-2567
11.5	-	2984	-1835	2135	-2677
12.1	-	3234	-2332	2191	-2745
12.7	-	3401	-2658	2282	-2851
13.4	-	3579	-3022	2366	-2950
14.0	-	3723	-3249	2483	-3079
14.7	-	3856	-3556	2578	-3177
15.3	-	3973	-3826	2673	-3280
15.9	-	4087	-4030	2791	-3405
16.6	-	4182	-4224	2900	-3515
17.2	-	4254	-4410	3010	-3617
17.8	-	4383	-4561	3143	-3754
18.5	-	4428	-4645	3325	-3894
19.1	-	4535	-4789	3416	-3989
19.8	-	4618	-4902	3484	-4072
20.4	-	4728	-5024	3556	-4159
21.0	-	4846	-5156	3663	-4269
21.7	-	4933	-5259	3735	-4345
22.3	-	5020	-5354	3814	-4421
22.9	-	5100	-5448	3864	-4482
23.6	-	5221	-5574	3970	-4580
24.2	-	5293	-5649	4015	-4629
24.9	-	5388	-5748	4118	-4724
25.5	-	5501	-5869	4212	-4819
26.1	-	5615	-5991	4307	-4914
26.8	-	5729	-6116	4410	-5012
27.4	-	5843	-6226	4508	-5103
28.0	-	5926	-6313	4573	-5164
28.7	-	6025	-6415	4667	-5255
29.3	-	6138	-6533	4755	-5342
30.0	-	6260	-6654	4838	-5429

A.2. Specimen 2

Displacement (mm)	Load (N)	Strain at location A	Strain at location B	Strain at location C	Strain at location D
0.0	-	8	-4	8	0
0.7	-	159	-144	83	-91
1.3	-	345	-318	174	-201
2.0	-	535	-500	262	-315
2.6	-	736	-701	345	-432
3.2	-	971	-929	428	-546
3.9	-	1255	-1194	497	-641
4.6	-	1077	-1096	459	-603
5.2	-	1244	-1270	523	-694
5.9	-	1403	-1441	591	-789
6.5	-	1558	-1611	660	-883
7.2	-	1718	-1782	728	-978
7.8	-	1865	-1941	792	-1069
8.5	-	1991	-2082	842	-1149
9.1	-	2142	-2241	906	-1240
9.8	-	2290	-2400	971	-1331
10.4	-	2434	-2563	1035	-1426
11.1	-	2586	-2719	1107	-1517
11.7	-	2734	-2878	1172	-1604
12.4	-	2874	-3029	1236	-1691
13.0	-	2984	-3151	1289	-1759
13.7	-	3128	-3302	1357	-1850
14.3	-	3264	-3450	1422	-1934
15.0	-	3401	-3594	1482	-2021
15.6	-	3541	-3746	1555	-2112
16.3	-	3682	-3898	1630	-2203
16.9	-	3822	-4046	1706	-2298
17.6	-	3962	-4197	1782	-2389
18.2	-	4102	-4345	1854	-2476
18.9	-	4243	-4497	1930	-2571
19.5	-	4387	-4648	2009	-2662
20.1	-	4531	-4796	2097	-2756
20.8	-	4667	-4944	2184	-2859
21.4	-	4804	-5092	2286	-2969
22.1	-	4944	-5240	2381	-3067
22.7	-	5077	-5384	2483	-3173
23.4	-	5210	-5524	2593	-3283

Displacement (mm)		Strain at location A	Strain at location B	Strain at location C	Strain at location D
24.0	-	5335	-5661	2696	-3382
24.7	-	5471	-5801	2806	-3492
25.3	-	5604	-5941	2904	-3594
26.0	-	5733	-6078	3045	-3716
26.6	-	5850	-6203	3238	-3867
27.3	-	5975	-6339	3374	-3989
27.9	-	6089	-6457	3545	-4110
28.6	-	6207	-6586	3666	-4216
29.2	-	6320	-6707	3788	-4307
29.9	-	6438	-6828	3898	-4402

A.3. Specimen 3

Displacement (mm)	Load (N)	Strain at location A	Strain at location B	Strain at location C	Strain at location D
0.0	0	8	-4	11	0
0.7	8.57	121	-136	125	-110
1.3	18.96	273	-311	254	-227
2.0	30.06	440	-504	375	-353
2.6	41.55	607	-698	504	-474
3.2	52.82	770	-899	622	-595
3.9	63.89	944	-1100	736	-713
4.6	74.13	1149	-1308	834	-823
5.2	84.46	1338	-1517	944	-940
5.9	95.19	1520	-1718	1058	-1058
6.5	105.7	1699	-1911	1175	-1179
7.2	116.25	1877	-2108	1297	-1308
7.8	126.49	2051	-2298	1414	-1426
8.5	137.12	2229	-2487	1536	-1555
9.1	147.24	2400	-2681	1664	-1680
9.8	157.7	2578	-2866	1790	-1809
10.4	168	2753	-3048	1926	-1945
11.1	177.48	2919	-3223	2059	-2082
11.7	187.11	3082	-3397	2214	-2237
12.4	196.86	3246	-3572	2381	-2411
13.0	206.34	3409	-3746	2540	-2582
13.7	215.64	3568	-3913	2696	-2749
14.3	223.87	3708	-4061	2851	-2916
15.0	231.94	3841	-4197	2999	-3079

15.6	238.34	3943	-4300	3177	-3291
16.3	245.05	4049	-4417	3276	-3431
16.9	252.42	4171	-4542	3374	-3549
17.6	260.07	4288	-4671	3473	-3663
18.2	268.15	4421	-4811	3583	-3780
18.9	275.46	4546	-4940	3674	-3882
19.5	281.1	4629	-5043	3750	-3966
20.1	288.94	4747	-5164	3848	-4072
20.8	289.58	4724	-5145	3860	-4083
21.4	295.73	4834	-5266	3951	-4186
22.1	301.89	4940	-5388	4038	-4277
22.7	309.57	5062	-5513	4121	-4364
23.4	316.18	5172	-5630	4224	-4466
24.0	322.31	5282	-5752	4307	-4561
24.7	327.7	5376	-5850	4383	-4641
25.3	334.1	5494	-5972	4474	-4732
26.0	337.06	5528	-6017	4508	-4766
26.6	343.03	5634	-6131	4592	-4857
27.3	349.28	5748	-6252	4683	-4955
27.9	355.41	5858	-6362	4758	-5024
28.6	360.92	5964	-6476	4846	-5122
29.2	367.45	6082	-6597	4925	-5202
29.9	371.59	6154	-6677	4986	-5263

A.4. Specimen 4

Displacement (mm)	Load (N)	Strain at location A	Strain at location B	Strain at location C	Strain at location D
0.0	1	23	-30	23	-15
0.7	9	167	-178	136	-129
1.3	16	311	-326	250	-246
2.0	24	455	-16205	360	-356
2.6	33	603	-16205	474	-478
3.2	42	758	-16205	588	-599
3.9	51	902	-16205	694	-720
4.6	61	1058	-16205	808	-846
5.2	70	1213	-16205	921	-971
5.9	79	1365	-16205	1043	-1100
6.5	89	1520	-16205	1160	-1228

7.2	98	1676	-16205	1282	-1361
7.8	108	1835	-16205	1399	-1490
8.5	117	1991	-16205	1520	-1623
9.1	127	2146	-16205	1646	-1755
9.8	136	2301	-16205	1771	-1896
10.4	146	2461	-16205	1888	-2028
11.1	155	2616	-16205	2013	-2161
11.7	164	2772	-16205	2135	-2298
12.4	173	2931	-16205	2256	-2423
13.0	182	3086	-16205	2381	-2552
13.7	192	3246	-16205	2495	-2684
14.3	201	3397	-16205	2616	-2813
15.0	210	3549	-16205	2730	-2938
15.6	218	3701	-16205	2844	-3056
16.3	227	3848	-16205	2961	-3181
16.9	234	3977	-16205	3033	-3264
17.6	243	4125	-16205	3132	-3371
18.2	252	4273	-16205	3234	-3477
18.9	260	4421	-16205	3333	-3579
19.5	268	4569	-16205	3439	-3685
20.1	277	4713	-16205	3545	-3799
20.8	285	4861	-16205	3644	-3901
21.4	292	4997	-16205	3731	-3992
22.1	300	5137	-16205	3826	-4087
22.7	307	5270	-16205	3913	-4171
23.4	314	5403	-16205	4008	-4269
24.0	315	5414	-16205	4030	-4296
24.7	323	5547	-16205	4121	-4383
25.3	331	5691	-16205	4216	-4478
26.0	337	5820	-16205	4326	-4592
26.6	343	5953	-16205	4428	-4701
27.3	351	6085	-16205	4527	-4804
27.9	357	6207	-16205	4614	-4895
28.6	361	6267	-16205	4667	-4944
29.2	366	6366	-16205	4739	-5016
29.9	372	6480	-16205	4819	-5096

A.5. Specimen 5

Displacement (mm)	Load (N)	Strain at location A	Strain at location B	Strain at location C	Strain at location D
0.0	0	8	-4	11	-4
0.7	7.96	144	-152	125	-114
1.3	17.25	292	-315	246	-235
2.0	26.52	444	-482	368	-360
2.6	36.67	607	-671	482	-489
3.2	46.88	777	-872	591	-610
3.9	57	944	-1077	701	-739
4.6	66.96	1103	-1266	811	-880
5.2	77.27	1270	-1464	925	-1005
5.9	87.48	1433	-1657	1035	-1130
6.5	97.84	1604	-1862	1145	-1255
7.2	107.87	1771	-2063	1247	-1380
7.8	118.2	1945	-2264	1361	-1501
8.5	128.19	2097	-2434	1467	-1627
9.1	137.67	2237	-2593	1570	-1744
9.8	147.46	2389	-2764	1676	-1865
10.4	156.72	2521	-2908	1778	-1983
11.1	166.35	2665	-3071	1888	-2108
11.7	175.59	2791	-3215	2006	-2248
12.4	185.01	2927	-3363	2123	-2381
13.0	194.06	3056	-3503	2241	-2525
13.7	202.87	3185	-3632	2355	-2650
14.3	210.85	3291	-3742	2461	-2772
15.0	219.48	3416	-3879	2567	-2893
15.6	227.74	3545	-4015	2677	-3014
16.3	236.24	3666	-4144	2828	-3185
16.9	244.56	3799	-4292	2954	-3329
17.6	252.73	3928	-4425	3090	-3481
18.2	259.46	4008	-4504	3185	-3591
18.9	267.66	4137	-4645	3302	-3723
19.5	276.47	4262	-4773	3424	-3860
20.1	282.5	4360	-4872	3526	-3977
20.8	290.09	4478	-4993	3647	-4114
21.4	296.25	4569	-5077	3810	-4300
22.1	302.89	4671	-5183	3932	-4436
22.7	308.26	4777	-5289	4046	-4561
23.4	314.54	4883	-5403	4159	-4679

24.0	320.88	4982	-5501	4250	-4777
24.7	325.3	5039	-5547	4349	-4876
25.3	330.66	5134	-5649	4432	-4959
26.0	336.66	5240	-5755	4519	-5058
26.6	342.76	5331	-5839	4614	-5156
27.3	345.23	5392	-5892	4660	-5210
27.9	351.81	5505	-6006	4755	-5308
28.6	357.3	5619	-6116	4853	-5407

B. Top level python script for a coupling technique

```python
#Script to run the trial functions for incorporating
global shell models into the multiscale approach
print "\n ----------------\n|      Start      |\n --------
---------"
print "\n ----------------\n|   Iteration 0   |\n --------
---------"
import subprocess
#remove unnecessary files

kernelcommand="del /q .\*.lck"
subprocess.Popen(kernelcommand,shell=True)
kernelcommand="del /q .\*.rec"
subprocess.Popen(kernelcommand,shell=True)
kernelcommand="del /q .\*.rpy.*"
subprocess.Popen(kernelcommand,shell=True)
kernelcommand="del /q .\*.sim"
subprocess.Popen(kernelcommand,shell=True)
kernelcommand="del /q .\*.simr"
subprocess.Popen(kernelcommand,shell=True)
kernelcommand="del /q .\*.stt"
subprocess.Popen(kernelcommand,shell=True)
kernelcommand="del /q .\*.sup"
subprocess.Popen(kernelcommand,shell=True)
kernelcommand="del /q .\*.prt"
subprocess.Popen(kernelcommand,shell=True)
kernelcommand="del /q .\*.mdl"
subprocess.Popen(kernelcommand,shell=True)
kernelcommand="del /q .\*.mtx"
subprocess.Popen(kernelcommand,shell=True)

loop=0
import shutil
print "\n--> Copying global input file to working
directory\n"
#shutil.copy("c:/Temp/wingmodel.inp","./")

filename="input=wingmodel_%d.inp" %loop
pathname="./wingmodel_%d.inp" %loop
shutil.copy("./wingmodel.inp",pathname)

loopFile=open("loop.txt","w")
loopFile.write(str(loop))
loopFile.close()

import getCoarseGeometry
Geometry=getCoarseGeometry.Coarse()
print "\n--> Geometry extracted for regions:"
```

```python
for region in Geometry["regions"]:
    print " --> "+str(region)
#print Geometry["inOrder"]
#import rewriteCoarse
#rewrite = rewriteCoarse.initial(Geometry["regions"])

import getAxes
Transformed=getAxes.transform(Geometry["coarseLocation"],
Geometry["componentLocation"])
print "\n--> Transformation matrices obtained"

import makeComponent
#print Geometry["coarseNodes"]
reduced=makeComponent.reduce(Geometry["coarseNodes"],
Transformed[2], Transformed[3], Geometry["inOrder"])
print "\n--> Boundary nodes grouped/component models
updated"

import match #Matches the component nodes to pairs of
global shell nodes
matched=match.shellToSolid(reduced["reducedTransformed"],
reduced["boundary"])
print "\n--> Midplane nodes associated with global shell
elements"

import equationsSolid #Write the equations to constrain
component boundary nodes to reduced ones
constrained=equationsSolid.shell2solid(matched)
print "\n--> Equation constraints written to input files:"
for reg in constrained:
    print " --> "+reg

import runRefinedHPC #Run the refined models for each
component
print " \n--> Running the refined models in Abaqus"
AbaqusRefinedInitial=runRefinedHPC.
initial(Geometry["regions"])

#Pausing to wait for the HPC
kernelcommand="e:/tools/winscp/winscp425.exe /console
/script=./checkComplete.sh"
hpcstat="running"
import time
waittime=0
while hpcstat=="running":
    print "Job on hpc for "+str(waittime)+" mins"
    time.sleep(1800)
```

```python
    waittime=waittime+30
    Refined = subprocess.Popen(kernelcommand,
shell=True).wait()
    hpcstatfile=open("list.txt","r")
    noComplete = 0
    for line in hpcstatfile:
        if "Z" in line:
            noComplete=noComplete+1
    if noComplete == len(constrained):
        hpcstat = "complete"
        print "Complete"
    hpcstatfile.close()
time.sleep(120)

kernelcommand="e:/tools/winscp/winscp425.exe /console
/script=./getfiles.sh"
Refined = subprocess.Popen(kernelcommand,shell=True).wait()
#HPC complete after here

import matrix
print " \n--> Extracting matrices from refined model
output"
Mat = matrix.extract(Geometry["regions"],loop)

import transformMatrix
print "\n--> Transforming matrices from component to
global coordinates"
trans=transformMatrix.outer(Transformed[2],loop,
Geometry["regions"])

job="job=wingmodel_%d" %loop
inp="input=wingmodel_%d.inp" %loop
print "\n--> Running coarse wingmodel for iteration
%d"%loop
print "\n--> Start of ABAQUS output\n"
newjob = subprocess.Popen(['abaqus',job,inp,'interactive'],
shell=True).wait()
print "\n--> End of ABAQUS output"

print "\n -----------------\n | End Iteration 0|\n -------
-----------"
import getBCs

while 1:
    print "\n -----------------\n |   Iteration %d   |\n -
----------------" %(loop+1)
    #Write the boundary conditions to the component models
and update matrix paths
```

```python
    print " \n--> Applying boundary conditions to
component models"
    displacements=getBCs.fromCoarse(reduced["pairs"],
Transformed[2])

    if loop > 0:
        print "\n--> Checking convergence"
        import checkConvergence
        converged = checkConvergence.check(displacements,
oldDisplacements)
        if converged == True:
            break

    #Run the component models
    print " \n--> Running the refined models in Abaqus"

AbaqusRefinedInitial=runRefinedHPC.loop(Geometry["regions"])


    #Pausing to wait for the HPC
    kernelcommand="e:/tools/winscp/winscp425.exe /console
/script=./checkComplete.sh"
    hpcstat="running"
    import time
    waittime=0
    while hpcstat=="running":
        print "Job on hpc for "+str(waittime)+" mins"
        time.sleep(1800)
        waittime=waittime+30
        Refined = subprocess.Popen(kernelcommand,
shell=True).wait()
        hpcstatfile=open("list.txt","r")
        noComplete = 0
        for line in hpcstatfile:
            if "Z" in line:
                noComplete=noComplete+1
        if noComplete == len(constrained):
            hpcstat = "complete"
            print "Complete"
        hpcstatfile.close()
    time.sleep(120)

    kernelcommand="e:/tools/winscp/winscp425.exe /console
/script=./getfiles.sh"
    Refined = subprocess.Popen(kernelcommand,
shell=True).wait()
    #HPC complete after here
```

```python
    #Update the loop number
    loop=loop+1
    loopFile=open("loop.txt","w")
    loopFile.write(str(loop))
    loopFile.close()

    #Extract the matrices from the component output
    print " \n--> Extracting matrices from refined model
output"
    Mat = matrix.extract(Geometry["regions"],loop)

    #Transform the stiffness matrices into global
coordinate system
    print "\n--> Transforming matrices from component to
global coordinates"
    trans=transformMatrix.outer(Transformed[2],loop,
Geometry["regions"])

    #Rewrite the global input file so that it looks in the
right place for the matrices
    print "\n--> Updating the coarse model matrix paths"
    Update=getCoarseGeometry.iterate(loop,
Geometry["regions"])

    #Run the coarse model
    job="job=wingmodel_%d" %loop
    inp="input=wingmodel_%d.inp" %loop
    print "\n--> Running coarse wingmodel for iteration
%d"%loop
    print "\n--> Start of ABAQUS output\n"
    newjob = subprocess.Popen(['abaqus',job,inp,
'interactive'],shell=True).wait()
    print "\n--> End of ABAQUS output"

    oldDisplacements = displacements
    print "\n -----------------\n | End Iteration %d |\n -
----------------" %(loop)


print "\n--------------------------------\n|     SOLUTION
CONVERGED        |\n--------------------------------\n"
```

C. Matching component boundary nodes to solid element faces

The process outlined in Figure C.1 is used in order to match local boundary nodes on Γ to a global element face. The first step is to generate a shortlist of possible element faces upon which a component node may lie. For a particular global element face there are 4 nodes each with 3 coordinates, x_i^j, where $i = 1, 2, 3, 4$ represents each of the 4 nodes on the global element face and $j = 1, 2, 3$ represents each of the coordinates. Similarly for each local boundary node there are 3 coordinates x_i^l where l denotes a local node. Global element faces upon which a local node may lie satisfy the criteria:

$$\min_j \left(x_i^j \right) - \frac{\Delta x_i}{10} \leq x_i^l \leq \max_j \left(x_i^j \right) + \frac{\Delta x_i}{10} \ \forall i \tag{A-1}$$

where

$$\Delta x_i = \max_j \left(x_i^j \right) - \min_j \left(x_i^j \right) \tag{A-2}$$

The 10% margins are applied to the criteria since a local boundary node may not lie exactly on the face of an global element due to the increased refinement. As a result there may not be an element face for which

$$\min_j \left(x_i^j \right) \leq x_i^l \leq \max_j \left(x_i^j \right) \ \forall i \tag{A-3}$$

If this yields more than one candidate, which may be the case if element faces are not regular quadrilaterals, then the natural coordinates are determined for the component node in terms of each element face.

The procedure for calculating the natural coordinates is detailed in [76]. Note that in 3D space, three coordinate values must be satisfied with only 2 variables. In order to circumvent this issue, the coordinate direction with the smallest range of values in the 4 structural element face nodes is neglected. Assuming that the component mesh boundary is coincident with the structural one, this does not lead to a loss in accuracy. If the component node does lie on a particular element face then the calculated natural coordinates will be in the range $-1.0 \leq \xi, \eta \leq 1.0$. If the node does not lie on the element face this will not be true. Hence this condition is used to match each component node to an element face.

```
                          ┌──────────┐
                          │  Start   │
                          └──────────┘
                               │
┌──────────────────────────────────────────────────────────────┐
│ For each element face calculate $x^i_{min}$, the minimum value │
│ of the nodal $i$ coordinates, and $x^i_{max}$, the maximum     │
│ value of nodal $i$ coordinates where $i$=1,2,3.                │
└──────────────────────────────────────────────────────────────┘
                               │
┌──────────────────────────────────────────────────────────────┐
│ If any of the component node's coordinates lie outside the     │
│ calculated range for the element face, eliminate the face      │
│ from the shortlist                                             │
└──────────────────────────────────────────────────────────────┘
                               │
┌──────────────────────────────────────────────────────────────┐
│ Determine, for each element face, which is the least           │
│ significant coordinate. This is defined as the coordinate      │
│ direction in which there is the smallest variation over the    │
│ corner nodes of the face                                       │
└──────────────────────────────────────────────────────────────┘
                               │
┌──────────────────────────────────────────────────────────────┐
│ If more than one face remains, calculate the natural           │
│ coordinates of the component node in terms of each face's      │
│ 4 nodes (based on the two most significant coordinates.        │
│ Eliminate any face for which a natural coordinate is           │
│ not between -1.0 and 1.0.                                      │
└──────────────────────────────────────────────────────────────┘
                               │
                          ┌──────────┐
                          │   End    │
                          └──────────┘
```
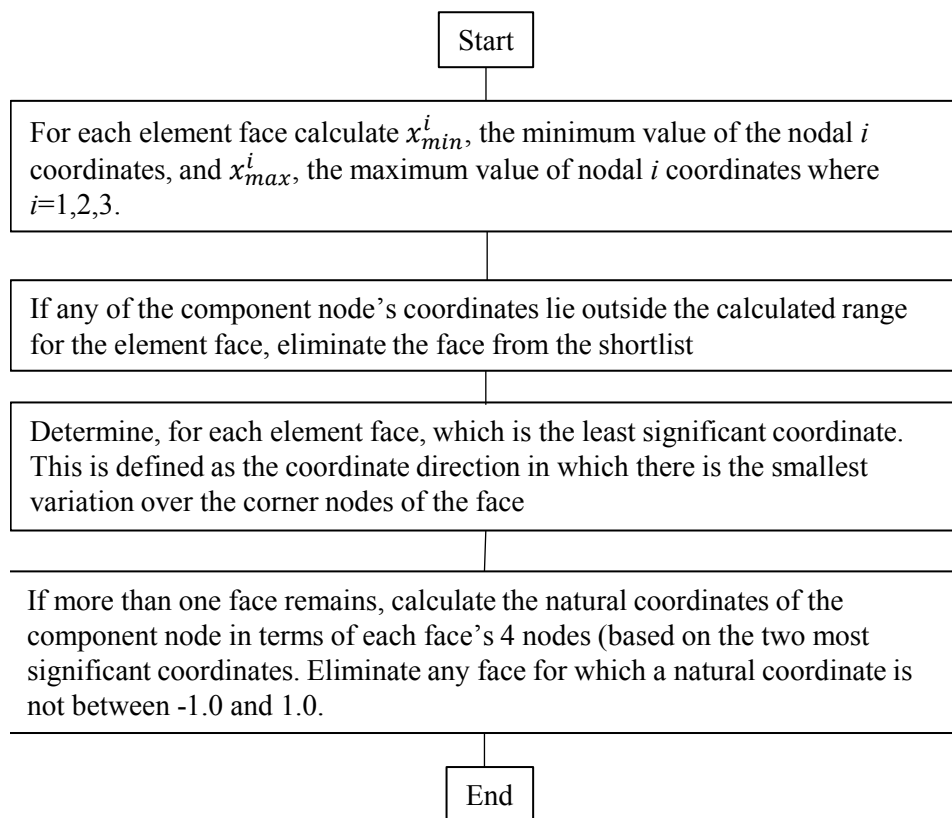
Figure C.1.: Process for matching component nodes on the boundary Γ to the appropriate structural element face.

D. Transformation Method

The Transformation Method (TM) is a technique for enforcing constraints on degrees of freedom (d.o.f.) in the Finite Element Method which is based on the principle that a constraint is a known fact about the system of equations, and this results in one less equation that needs to be solved. TM constraints apply to models where one d.o.f., called a slave is defined by one or more master d.o.f. in the model. Noting that there may be many slave d.o.f. in a model, we may partition all the d.o.f., $\mathbf{u}$, into master ($\mathbf{u}_m$) and slave ($\mathbf{u}_s$) d.o.f..

$$\mathbf{u} = \left[\begin{array}{c} \mathbf{u}_m \\ \mathbf{u}_s \end{array} \right] = \mathbf{T}_{TM}\mathbf{u}_m - \mathbf{L} \tag{A-1}$$

The vector $\mathbf{L}$ is a vector of constants, if any constant terms are involved in the constraint equations. Otherwise $\mathbf{L} = 0$. Note that in the implementation of the coupling methods there are no constant terms in the constraint equations, and so $\mathbf{L}$ is ignored here.

The equilibrium equation of the Finite Element model is rewritten:

$$\mathbf{F} = \mathbf{K}\mathbf{u} = \mathbf{K}\mathbf{T}_{TM}\mathbf{u}_m \tag{A-2}$$

And the potential energy is:

$$\Pi = \frac{1}{2}\left[\mathbf{T}_{TM}\mathbf{u}_m\right]^{\mathrm{T}} \mathbf{K}\mathbf{T}_{TM}\mathbf{u}_m - \left[\mathbf{T}_{TM}\mathbf{u}_m\right]^{\mathrm{T}} \mathbf{F} \tag{A-3}$$

Taking the derivative of this expression with respect to $\mathbf{u}_m$ and requiring that it is zero (minimising the potential energy of the model) provides the new static equilibrium equations:

$$\frac{\partial \Pi}{\partial \mathbf{u}_m} = \mathbf{T}_{TM}^{\mathrm{T}}\mathbf{K}\mathbf{T}_{TM}\mathbf{u}_m - \mathbf{T}_{TM}^{\mathrm{T}}\mathbf{F} = 0 \tag{A-4}$$

Thus:

$$\mathbf{K}_m\mathbf{u}_m = \mathbf{F}_m \tag{A-5}$$

Where:

$$\mathbf{K}_m = \mathbf{T}_{TM}^{\mathrm{T}}\mathbf{K}\mathbf{T}_{TM}, \ \mathbf{F}_m = \mathbf{T}_{TM}^{\mathrm{T}}\mathbf{F} \tag{A-6}$$